# The impact of strong and weak bars on galaxy evolution

Tobias Géron

St Cross College

University of Oxford

A thesis submitted for the degree of

*Doctor of Philosophy*

Hilary 2023

# Abstract

Bars are common structures in disc galaxies that are thought to be long-lived and to have the ability to redistribute matter and angular momentum in their hosts. This implies that bars are important in the evolution of galaxies. Previous studies have traditionally been focussed on strong bars, as they are easier to identify and observe, while the role of weak bars remains relatively unclear. In this thesis, I study the impact that both strong and weak bars have on their hosts, especially in the context of galaxy evolution and quenching.

Bars are typically more common in quiescent galaxies, but it is uncertain whether it is easier to form a bar in a quenched galaxy or if a bar helps to quench its host. In order to answer this question, I use Galaxy Zoo DECaLS to identify a large volume-limited sample of 1,867 galaxies from a wide range of bar types. Using data from SDSS and ALFALFA, I find that the strong bar fraction is higher among quiescent galaxies, consistent with prior work. However, this was not found for weak bars, which seem to be distributed equally between star forming and quiescent galaxies. Additionally, I find that strongly barred star forming galaxies have lower gas masses, higher fibre star formation rates and shorter depletion timescales, compared to unbarred star forming galaxies. Interestingly, this was not found for weakly barred star forming galaxies. I conclude that star forming galaxies with a strong bar are typically rapidly evolving galaxies that quench more efficiently due to the presence of a strong bar. I also find that the differences between weakly and strongly barred galaxies disappear when accounting for bar length and suggest that weak and strong bars are therefore not fundamentally distinct physical phenomena. Instead, I propose that they are part of a continuum of bar types, which ranges from ‘weakest’ to ‘strongest’.

I also study the kinematics of bars, as this can provide insight into their formation and evolution. This is done by applying the Tremaine-Weinberg method on MaNGA IFU data of a sample of 122 strongly barred and 103 weakly barred galaxies identified using Galaxy Zoo DESI, which is the largest sample this method has been applied to so far. I found that strongly barred galaxies have significantly lower values for the bar pattern speed and $\mathcal{R}$, the ratio of the corotation radius to the bar radius, than weakly barred galaxies. As simulations have shown that the bar pattern speed decreases as the bar evolves, these results suggest that strong bars are more evolved structures than weak bars. Additionally, simulations have shown that the ratio $\mathcal{R}$ is correlated with the bar formation mechanism. This implies that strong bars are more likely to be formed by global bar instabilities, while weak bars are more likely triggered by tidal interactions. Ultrafast bars (bars that have $\mathcal{R} < 1$) should theoretically not exist, however, they are repeatedly found in observational studies. I find a much lower fraction of ultrafast bars in my sample compared to the literature: 11% are ultrafast, while only 2% of the sample are confidently within the ultrafast regime. The overall distribution of $\mathcal{R}$ in my sample is higher than what is typically found in other studies, which also decreases the recently claimed tension with $\Lambda$CDM.

I use resolved star formation indicators obtained from MaNGA to study the effect that strong and weak bars, as well as fast and slow bars, have on different regions of their hosts. I found that strongly barred star forming galaxies have significantly more star formation in their centre and region beyond the bar-end, while suppressing star formation in the arms of the bar, compared to weakly barred star forming galaxies. These results are consistent with strong bars facilitating quenching, while weak bars do not. I also found that, while the global star formation rate remains the same between fast and slow bars, slow bars concentrate the star formation along the barred regions more than fast bars. I hypothesise that this is due to the greater difference in velocity between the bar-end region and the gas in the disc for slow bars than for fast bars. I also find preliminary evidence for a synergistic effect between bar strength and kinematics: slow strong bars seem to affect their hosts the most. Based on these results, I suggest to add a second, kinematic, axis to the aforementioned bar continuum. However, an increased sample of barred galaxies with IFU data is needed to study this in more detail. In any case, these results highlight that it is important to study the kinematics of bars in order to fully understand galaxy evolution.

# Statement of Originality

I carried out the work presented in this thesis at the Department of Astrophysics, University of Oxford, between October 2019 and March 2023 under the supervision of Dr. Rebecca Smethurst and Prof. Chris Lintott. I was funded by a combination of the Saven European scholarship and the Oxford Physics Endowment for Graduates (OXPEG) scholarship. I hereby declare that no part of this thesis has been accepted or submitted in support of another degree, diploma or other qualification at the University of Oxford or other higher learning institute. Except where otherwise stated or where reference is made to the work of others, the work in this thesis is entirely my own.

The work presented in Chapter 3 is based on work that has been peer-reviewed and published in Monthly Notices of the Royal Astronomical Society (MNRAS) in Géron et al. (2021). The paper is titled *Galaxy zoo: stronger bars facilitate quenching in star-forming galaxies* and I am the lead author of this work.

The work presented in Chapter 4 is also based on work that has been peer-reviewed and published in MNRAS in Géron et al. (2023). The paper is titled *Galaxy Zoo: Kinematics of strongly and weakly barred galaxies* and I am the lead author of this work.

The work presented in Chapter 5 is in preparation for submission in MNRAS. I will be the lead author of this work.

I was the principal investigator for the observing proposals presented in Chapter 7. However, my supervisors, Dr. Rebecca Smethurst and Prof. Chris Lintott, as well as Dr. Brooke Simmons, have all significantly contributed to these proposals. Futhermore, the actual observations were taken and the data reduction was done collaboratively with another PhD student, David O'Ryan, and my supervisor, Prof. Chris Lintott.

Tobias Géron
*February 2023*

# Acknowledgements

Woah. Where to begin? This all went by too fast and so much has happened in these last few years. I had to face some unexpected hurdles along the way, including a global pandemic and a volcanic eruption. It was a challenge to finish this thesis, but with the help of some amazing people, I am proud to say that I did.

First of all, I want to thank my incredible supervisors, Dr. Becky Smethurst and Prof. Chris Lintott, for their patience, guidance and encouragement over the years. You have both inspired me to become a better scientist and this thesis would not have been possible without your help.

I also want to thank Prof. Karen Masters, Dr. Brooke Simmons, Dr. Sandor Kruk and Dr. Mike Walmsley for all the useful discussions and helpful suggestions for my papers and research in general.

The wonderful people in the department and in my office have made going to work so much more enjoyable, even when things were stressful (especially these last few months). Sarah, Peter, Annabella, Lennart, Joe and everybody else: thanks for all the memories. I also want to specifically thank Jakob for always buying too much food and keeping me fed.

Of course, I also want to thank all the friends I made throughout the years in Oxford for providing endless moral support and the occasional meme. I want to thank Keran and Gustavo in particular, we had a blast in this town and I will always cherish the many pints we shared.

I also want to thank my friends back in Belgium, who I couldn't see as much as I wanted these last couple of years, but who were nevertheless supportive. Thanks for all the adventures that have kept me sane and I hope to climb many more mountains with you in the future.

Finally, I want to thank my incredibly family, especially my parents. They have been a constant source of love and support throughout this journey and have always given me the opportunity to do what I loved.

Oh yeah, I also want to thank the coffee machine in the department, I could not have done this without you. And now, as the last words of this thesis have been written, I am going to the pub for a celebratory pint. Cheers!

Tobias Géron
*February 2023*

*"I may not have gone where I intended to go,*
*but I think I have ended up where I needed to be."*

- Douglas Adams

# Contents

**1 Introduction 1**

1.1 Galaxy bimodality, evolution and quenching . . . . . . . . . . . . . . . 8

1.2 Bars . . . . . . . . . . . . . . . . . . . . . . . . . . . . . . . . . . . . 13

1.2.1 Bar formation mechanisms . . . . . . . . . . . . . . . . . . . . 15

1.2.2 Evolution of bars and their role in galaxy quenching . . . . . . 17

1.2.3 Strong and weak bars . . . . . . . . . . . . . . . . . . . . . . . 19

1.3 Kinematics of bars . . . . . . . . . . . . . . . . . . . . . . . . . . . 21

1.3.1 Orbits of stars in bars and the bar pattern speed . . . . . . . 22

1.3.2 The corotation radius and other important resonances . . . . . 24

1.3.3 Tension with $\Lambda$CDM and $\mathcal{R}$ . . . . . . . . . . . . . . . . . . 26

1.4 Thesis outline . . . . . . . . . . . . . . . . . . . . . . . . . . . . . . 28

**2 Data and Methods 30**

2.1 Data . . . . . . . . . . . . . . . . . . . . . . . . . . . . . . . . . . . 30

2.1.1 Sloan Digital Sky Survey . . . . . . . . . . . . . . . . . . . . . 30

2.1.2 MaNGA survey . . . . . . . . . . . . . . . . . . . . . . . . . . 32

2.1.3 The DESI Legacy Surveys . . . . . . . . . . . . . . . . . . . . 34

2.1.4 ALFALFA . . . . . . . . . . . . . . . . . . . . . . . . . . . . . 34

2.1.5 Galaxy Zoo . . . . . . . . . . . . . . . . . . . . . . . . . . . . 35

2.1.6 Defining the main samples . . . . . . . . . . . . . . . . . . . . 41

2.1.6.1 The GZ DECaLS-SDSS sample . . . . . . . . . . . . 41

2.1.6.2 The GZ DESI-MaNGA sample . . . . . . . . . . . . 47

2.2 Methods . . . . . . . . . . . . . . . . . . . . . . . . . . . . . . . . . 49

2.2.1 Kinematic position angle . . . . . . . . . . . . . . . . . . . . . 49

2.2.2 Bar lengths and bar position angles . . . . . . . . . . . . . . . 51

2.2.3 Inclination . . . . . . . . . . . . . . . . . . . . . . . . . . . . . 53

2.2.4 The Tremaine-Weinberg method . . . . . . . . . . . . . . . . . 55

2.2.4.1 Theoretical derivation . . . . . . . . . . . . . . . . . 57

2.2.4.2 Practical example . . . . . . . . . . . . . . . . . . . . 59
2.2.4.3 Limitations and concerns . . . . . . . . . . . . . . . 62
2.2.4.4 Rotation curves, corotation radii and $\mathcal{R}$ . . . . . . . 64
2.2.4.5 Our measurements . . . . . . . . . . . . . . . . . . . 67
2.2.5 Radius profiles . . . . . . . . . . . . . . . . . . . . . . . . . 70

**3 Strong and weak bars in Galaxy Zoo DECaLS: Stronger bars facilitate quenching in star forming galaxies 76**
3.1 Differences in bar length . . . . . . . . . . . . . . . . . . . . . . . 77
3.2 Properties of strongly and weakly barred galaxies . . . . . . . . . . . 79
3.3 Colour-magnitude diagram and SFR-mass plane . . . . . . . . . . . . 81
3.4 Bars and quenching . . . . . . . . . . . . . . . . . . . . . . . . . . 85
3.5 Bar continuum . . . . . . . . . . . . . . . . . . . . . . . . . . . . 93
3.6 Discussion . . . . . . . . . . . . . . . . . . . . . . . . . . . . . . 94
3.6.1 Strong bars are longer than weak bars . . . . . . . . . . . . . 94
3.6.2 Strong bars are more common in quiescent galaxies . . . . . . 95
3.6.3 Strong bars in star forming galaxies facilitate quenching . . . 96
3.6.4 Bar continuum . . . . . . . . . . . . . . . . . . . . . . . . . 98
3.7 Conclusions . . . . . . . . . . . . . . . . . . . . . . . . . . . . . . 100

**4 Tremaine-Weinberg Method: Kinematics of strongly and weakly barred galaxies 102**
4.1 Effect of slit width . . . . . . . . . . . . . . . . . . . . . . . . . . 104
4.2 Bar pattern speeds, corotation radii and $\mathcal{R}$ . . . . . . . . . . . . . . . . 106
4.3 Relationship between the parameters . . . . . . . . . . . . . . . . . 110
4.4 Quenching . . . . . . . . . . . . . . . . . . . . . . . . . . . . . . . 114
4.5 Comparison with other work . . . . . . . . . . . . . . . . . . . . . . 115
4.6 Discussion . . . . . . . . . . . . . . . . . . . . . . . . . . . . . . 119
4.6.1 Are strong bars older than weak bars? . . . . . . . . . . . . . 119
4.6.2 How are strong and weak bars triggered? . . . . . . . . . . . . 119
4.6.3 Tension with ΛCDM and ultrafast bars . . . . . . . . . . . . . 120
4.6.4 Strong and weak: part of a continuum . . . . . . . . . . . . . 123
4.6.5 Effect on quenching . . . . . . . . . . . . . . . . . . . . . . . 123
4.7 Conclusions . . . . . . . . . . . . . . . . . . . . . . . . . . . . . . 124

5 **Radius profiles: Slow and strong bars affect their hosts the most** **126**

5.1 Strong and weak bars . . . . . . . . . . . . . . . . . . . . . . . . . . . 127

5.1.1 EW[H$\alpha$] along strong and weak bars . . . . . . . . . . . . . . 128

5.1.2 $\mathrm{D_n}$4000 along strong and weak bars . . . . . . . . . . . . . . . 130

5.1.3 Effect of stellar mass . . . . . . . . . . . . . . . . . . . . . . . . 131

5.1.4 Focus on bar-end region . . . . . . . . . . . . . . . . . . . . . 133

5.1.5 Discussion: Strong and weak bars . . . . . . . . . . . . . . . . . 137

5.1.5.1 Star formation in different regions of strong and weak bars . . . . . . . . . . . . . . . . . . . . . . . . . . 137

5.1.5.2 Effect of stellar mass . . . . . . . . . . . . . . . . . . 140

5.1.5.3 Contamination by AGN . . . . . . . . . . . . . . . . 140

5.1.5.4 Strong bars are long-lived . . . . . . . . . . . . . . . 141

5.1.5.5 Implications for bar continuum . . . . . . . . . . . . 142

5.2 Fast and slow bars . . . . . . . . . . . . . . . . . . . . . . . . . . . 143

5.2.1 EW[H$\alpha$] and $\mathrm{D_n}$4000 along fast and slow bars . . . . . . . . . 143

5.2.2 Effect of bar strength . . . . . . . . . . . . . . . . . . . . . . . . 145

5.2.3 Global or local effect? . . . . . . . . . . . . . . . . . . . . . . . 147

5.2.4 Differences in velocity at bar-end . . . . . . . . . . . . . . . . . 149

5.2.5 Discussion: Fast and slow bars . . . . . . . . . . . . . . . . . . 151

5.2.5.1 Star formation in different regions of fast and slow bars151

5.2.5.2 Effect of bar strength . . . . . . . . . . . . . . . . . 152

5.2.5.3 Local, but not global effect . . . . . . . . . . . . . . 153

5.2.5.4 Effect of velocity . . . . . . . . . . . . . . . . . . . . 154

5.2.5.5 A ‘kinematic’ bar continuum . . . . . . . . . . . . . 155

5.3 Conclusions . . . . . . . . . . . . . . . . . . . . . . . . . . . . . . . 157

6 **Conclusions and future perspectives** **160**

6.1 Stronger bars facilitate quenching . . . . . . . . . . . . . . . . . . . 161

6.2 The kinematics of bars . . . . . . . . . . . . . . . . . . . . . . . . . 161

6.3 Fast and slow bars . . . . . . . . . . . . . . . . . . . . . . . . . . . 163

6.4 Bar continuum . . . . . . . . . . . . . . . . . . . . . . . . . . . . . 164

6.5 Future observations . . . . . . . . . . . . . . . . . . . . . . . . . . . 165

7 **Epilogue: A series of unfortunate events** **167**

**Bibliography** **173**

# List of Figures

1.1 Hubble Ultra Deep Field . . . . . . . . . . . . . . . . . . . . . . . . . 2
1.2 Large-scale structure found in the EAGLE simulation . . . . . . . . . 4
1.3 The Hubble tuning fork . . . . . . . . . . . . . . . . . . . . . . . . . 5
1.4 Colour-magnitude diagram . . . . . . . . . . . . . . . . . . . . . . . . 9
1.5 Image of NGC 1300 . . . . . . . . . . . . . . . . . . . . . . . . . . . 13
1.6 Example of bar formation through global bar instabilities . . . . . . . 16
1.7 Comparison of bar lengths and strengths . . . . . . . . . . . . . . . . 20
1.8 Visualisation of multiple bar orbits . . . . . . . . . . . . . . . . . . . 23
1.9 Illustration of the pattern speed and different resonances in a galaxy . 25

2.1 Galaxy Zoo DECaLS decision tree . . . . . . . . . . . . . . . . . . . . 37
2.2 The Galaxy Zoo DECaLS field guide for strong bars . . . . . . . . . . 39
2.3 The Galaxy Zoo DECaLS field guide for weak bars . . . . . . . . . . 40
2.4 DECaLS postage stamps of strongly and weakly barred galaxies . . . 44
2.5 Comparison of bar classifications between Galaxy Zoo 2 and Galaxy Zoo DECaLS . . . . . . . . . . . . . . . . . . . . . . . . . . . . . 46
2.6 DECaLS postage stamps of galaxies where Galaxy Zoo DECaLS disagrees with Nair & Abraham (2010a) . . . . . . . . . . . . . . . . . . 47
2.7 Demonstration of `PaFit` package to obtain kinematic position angles 50
2.8 Comparison of kinematic and photometric position angles . . . . . . . 51
2.9 Comparison of manually measured bar length with the bar lengths from Hoyle et al. (2011) . . . . . . . . . . . . . . . . . . . . . . . . . 54
2.10 Demonstration of how a bar can bias the inclination measurement . . 56
2.11 Example targets for TW method . . . . . . . . . . . . . . . . . . . . 59
2.12 Stellar flux and stellar velocity maps of the TW examples . . . . . . . 60
2.13 The centre offset and systemic correction applied to the TW sample . 62
2.14 The $\langle X \rangle$ vs $\langle V \rangle$ plot of the TW examples . . . . . . . . . . . . . . . . 63
2.15 The rotation curves of the TW examples . . . . . . . . . . . . . . . . 65
2.16 Comparison of the different methods to calculate the corotation radius 67

2.17 The evolution of pattern speed over the 1,000 Monte Carlo iterations of the TW examples . . . . . . . . . . . . . . . . . . . . . . . . . . . . 69
2.18 The posterior distributions of the pattern speed, corotation radius and $\mathcal{R}$ of the TW examples . . . . . . . . . . . . . . . . . . . . . . . . . . . 72
2.19 Demonstration of the method to create the radius profiles . . . . . . . 74
2.20 The distribution of the bar radius . . . . . . . . . . . . . . . . . . . . . . 75

3.1 The bar length against the bar vote fraction . . . . . . . . . . . . . . 78
3.2 Histograms of bar lengths of different bar types . . . . . . . . . . . . 79
3.3 Bar fraction over colour, stellar mass, global SFR and fibre SFR . . . 80
3.4 Histograms of the physical distance corresponding to 3 arcsec . . . . 82
3.5 Colour-magnitude diagram . . . . . . . . . . . . . . . . . . . . . . . . 84
3.6 SFR-stellar mass plane . . . . . . . . . . . . . . . . . . . . . . . . . . 86
3.7 CDFs of HI gas mass, fibre SFR and depletion timescale for the different bar types . . . . . . . . . . . . . . . . . . . . . . . . . . . . . . 88
3.8 CDFs of HI gas mass, fibre SFR and depletion timescale split in bins of $\mathrm{D}_{3\ \mathrm{arcsec}}$ . . . . . . . . . . . . . . . . . . . . . . . . . . . . . . 90
3.9 HI gas mass, fibre SFR and depletion timescale over stellar mass for the different bar types . . . . . . . . . . . . . . . . . . . . . . . . . . 92
3.10 Fibre SFR against bar length . . . . . . . . . . . . . . . . . . . . . . 94
3.11 DECaLS postage stamps of galaxies with intermediate bar lengths . . 95
3.12 Visualisation of the bar continuum . . . . . . . . . . . . . . . . . . . 99

4.1 Comparison of pattern speeds determined using different slit widths . 105
4.2 Histograms of the bar pattern speed estimates for strongly and weakly barred galaxies . . . . . . . . . . . . . . . . . . . . . . . . . . . . . 107
4.3 Histograms of the corotation radius estimates for strongly and weakly barred galaxies . . . . . . . . . . . . . . . . . . . . . . . . . . . . . 108
4.4 Histograms of the estimates of $\mathcal{R}$ for strongly and weakly barred galaxies 109
4.5 Scatter plot of the bar pattern speed against the corotation radius . . 111
4.6 Scatter plot of the corotation radius against the bar radius . . . . . . 112
4.7 The dependence of pattern speed, corotation radius and $\mathcal{R}$ on the bar radius . . . . . . . . . . . . . . . . . . . . . . . . . . . . . . . . . . 113
4.8 The dependence of pattern speed, corotation radius and $\mathcal{R}$ on stellar mass . . . . . . . . . . . . . . . . . . . . . . . . . . . . . . . . . . 114
4.9 Histograms of the pattern speed, corotation radius and $\mathcal{R}$ of star forming and quenching galaxies . . . . . . . . . . . . . . . . . . . . . . 115

4.10 Comparison of the pattern speed, corotation radius and $\mathcal{R}$ estimates calculated here with values found in the literature . . . . . . . . . . . 117
4.11 Comparison of the pattern speed, corotation radius and $\mathcal{R}$ estimates for weakly and strongly barred galaxies calculated here with values found in the literature . . . . . . . . . . . . . . . . . . . . . . . . 118

5.1 Radius profiles of EW[H$\alpha$] for strongly, weakly and unbarred galaxies 129
5.2 Radius profiles of $\mathrm{D_n}$4000 for strongly, weakly and unbarred galaxies . 132
5.3 Radius profiles of EW[H$\alpha$] for strongly, weakly and unbarred galaxies in different stellar mass bins . . . . . . . . . . . . . . . . . . . . . . 134
5.4 Radius profiles of $\mathrm{D_n}$4000 for strongly, weakly and unbarred galaxies in different stellar mass bins . . . . . . . . . . . . . . . . . . . . . . 135
5.5 Radius profiles with slits placed parallel and perpendicular to the bar of strongly and weakly barred galaxies . . . . . . . . . . . . . . . . 136
5.6 Histograms of the difference in EW[H$\alpha$] and $\mathrm{D_n}$4000 in the bar-end region of strong and weak bars . . . . . . . . . . . . . . . . . . . . . 137
5.7 Radius profiles of EW[H$\alpha$] for fast and slow bars . . . . . . . . . . . . 144
5.8 Radius profiles of $\mathrm{D_n}$4000 for fast and slow bars . . . . . . . . . . . . 146
5.9 Radius profiles of EW[H$\alpha$] and $\mathrm{D_n}$4000 for fast and slow bars, split up by bar strength . . . . . . . . . . . . . . . . . . . . . . . . . . . 148
5.10 Histograms of the global star formation rate for fast and slow bars . . 149
5.11 Radius profiles of EW[H$\alpha$] with slits placed parallel and perpendicular to the bar of fast and slow bars, split up by bar strength . . . . . . . 150
5.12 Histograms of the difference in velocity between the bar and the disc at the bar-end region of fast and slow bars . . . . . . . . . . . . . . . 152
5.13 Visualisation of two-dimensional bar continuum, with one morphological and one kinematic axis . . . . . . . . . . . . . . . . . . . . . . . . 156

7.1 Targets for the INT observing run . . . . . . . . . . . . . . . . . . . 168
7.2 The effects of storm Filomena, storm Hermine and the volcanic eruption on la Palma . . . . . . . . . . . . . . . . . . . . . . . . . . . 170
7.3 Spectra for SB_5 . . . . . . . . . . . . . . . . . . . . . . . . . . . 172

# List of Tables

2.1 The classification scheme to assign bar types . . . . . . . . . . . . . . . 43

2.2 Summary of the three main samples used in this thesis . . . . . . . . . 44

2.3 Comparison of the bar classifications in GZ DECaLS with the classifications of Nair & Abraham (2010a) . . . . . . . . . . . . . . . . . . . . 48

2.4 The pattern speeds, corotation radii and $\mathcal{R}$ for 40 randomly selected bars . . . . . . . . . . . . . . . . . . . . . . . . . . . . . . . . . . 71

3.1 The fraction of strong and weak bars found in different types of galaxies 83

4.1 Summary of the fraction of slow, fast and ultrafast bars found in this thesis and in the literature . . . . . . . . . . . . . . . . . . . . . . . . . 121

# Chapter 1

# Introduction

The insight that other galaxies existed beyond our own Milky Way dates back less than 100 years (Hubble, 1925, 1926). Interestingly, multiple nearby and bright galaxies, such as Andromeda, were already present in early catalogues, such as the Messier catalogue (Messier, 1781) and the New General Catalogue (NGC, Dreyer, 1888). However, the exact nature of these objects was unknown for a long time. This was the source of much contention, which is often dubbed 'the Great Debate' (see Hoskin, 1976 and Flório & Freire Júnior, 2021 for a historical review). In the centre of this debate were two astronomers: Shapley and Curtis. Curtis thought that these objects were located far outside the Milky Way and that they were vast structures in their own right (Curtis, 1921). On the other hand, Shapley believed that these objects were relatively small and that they lay within the Milky Way (Shapley, 1921). It was only when Hubble discovered Cepheid variable stars in Andromeda that it became clear that these objects were extragalactic, as these Cepheids can be used to determine the distance to these objects (Leavitt, 1908; Leavitt & Pickering, 1912; Hubble, 1925, 1926). Not even a century after Hubble concluded that other galaxies exist, his namesake, the Hubble Space Telescope, imaged a patch of the sky with a size of 11 arcmin$^2$ for a total exposure time of 11.3 days. The resulting image, referred to as the Hubble Ultra Deep Field, is shown in Figure 1.1, where $\sim$10,000 nearby and faraway ($z > 6$) galaxies are visible (Beckwith et al., 2006; Inami et al., 2017).

The cold dark matter (CDM) theory in contemporary astrophysics is a cosmological theory that explains the formation and evolution of galaxies (Peebles, 1982), such as the ones found in the Hubble Ultra Deep Field. It states that galaxies are thought to form as a result of primordial density fluctuations in the early Universe, which grew larger as the Universe expanded (Guth & Pi, 1982; Hawking, 1982; Blumenthal et al., 1984). The overdense regions had a slightly larger gravitational pull than the underdense regions, and eventually collapsed under their own gravity, forming dark

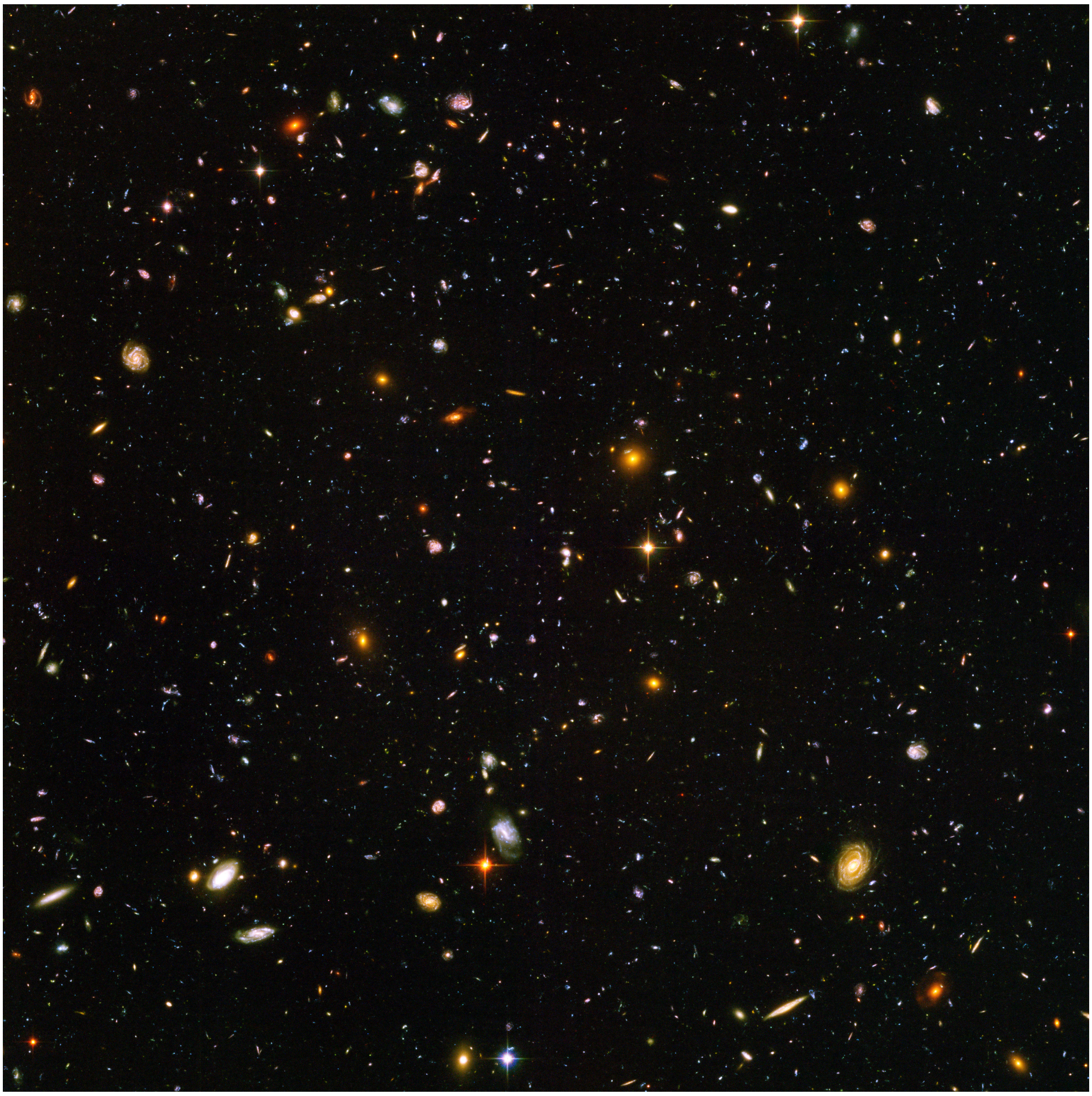

Figure 1.1: The Hubble Ultra Deep Field, imaged by the Hubble Space Telescope. The total region of this image is 11 arcmin$^2$ and Hubble used a total exposure time of 11.3 days taken between September 2003 and January 2004. An estimated number of 10,000 galaxies are visible in this image. Credit: NASA, ESA and Beckwith et al. (2006).

matter (DM) haloes. These DM haloes kept growing through accretion and mergers through a process called hierarchical clustering (White & Rees, 1978; Davis et al., 1985; White & Frenk, 1991). After cooling down, the baryonic matter that initially traced the DM haloes collapsed and formed the first galaxies. A rotating disc will naturally form in the galaxy if sufficient angular momentum is present (Fall & Efstathiou, 1980; Barnes & Efstathiou, 1987). Mergers with other galaxies can change the morphology of the galaxy and can cause the formation of dispersion supported structures such as bulges and elliptical galaxies (Kauffmann, 1996; Mo et al., 1998; Cox & Loeb, 2008).

The CDM theory was later modified to include the acceleration of the expansion of the Universe. This updated form is currently the most generally accepted cosmological theory and is called the $\Lambda$ cold dark matter ($\Lambda$CDM) theory (Perlmutter et al., 1999; Sahni & Starobinsky, 2000; Planck Collaboration et al., 2016, 2020). $\Lambda$CDM has been very successful in explaining the formation and evolution of the large-scale structure in the Universe that we observe today, often measured in the form of correlation functions (Frenk & White, 2012; Sachdeva & Saha, 2016; Bullock & Boylan-Kolchin, 2017). This large-scale structure consisting of clusters, filaments and voids has been reproduced in hydrodynamical simulations of a standard $\Lambda$CDM universe, such as the EAGLE project (Schaye et al., 2015; Crain et al., 2015; McAlpine et al., 2016), which is shown in Figure 1.2.

However, one of the biggest remaining challenges for the $\Lambda$CDM paradigm is found in the morphology of galaxies (Kautsch, 2009; Kormendy et al., 2010; Sachdeva & Saha, 2016; Haslbauer et al., 2022). As galaxies are thought to grow hierarchically through mergers in $\Lambda$CDM (White & Rees, 1978; Davis et al., 1985; White & Frenk, 1991), bulgeless disc galaxies are supposed to be relatively rare. However, a significant population of bulgeless disc galaxies are frequently observed (Kautsch et al., 2006; Carollo et al., 2007; Graham & Worley, 2008; Barazza et al., 2008; Kormendy et al., 2010; Fisher & Drory, 2011; Hoyle et al., 2012; Buta et al., 2015). The observed fraction of bulgeless disc galaxies is much higher than what is predicted by $\Lambda$CDM and cosmological simulations, which implies that there is less hierarchical merger-driven growth of galaxies than what the $\Lambda$CDM framework currently predicts (Abadi et al., 2003; Scannapieco et al., 2009; Trayford et al., 2017; Haslbauer et al., 2022). This tension with $\Lambda$CDM demonstrates the importance of studying the detailed morphology of galaxies in general, as it directly shapes our understanding of the Universe and helps to test $\Lambda$CDM.

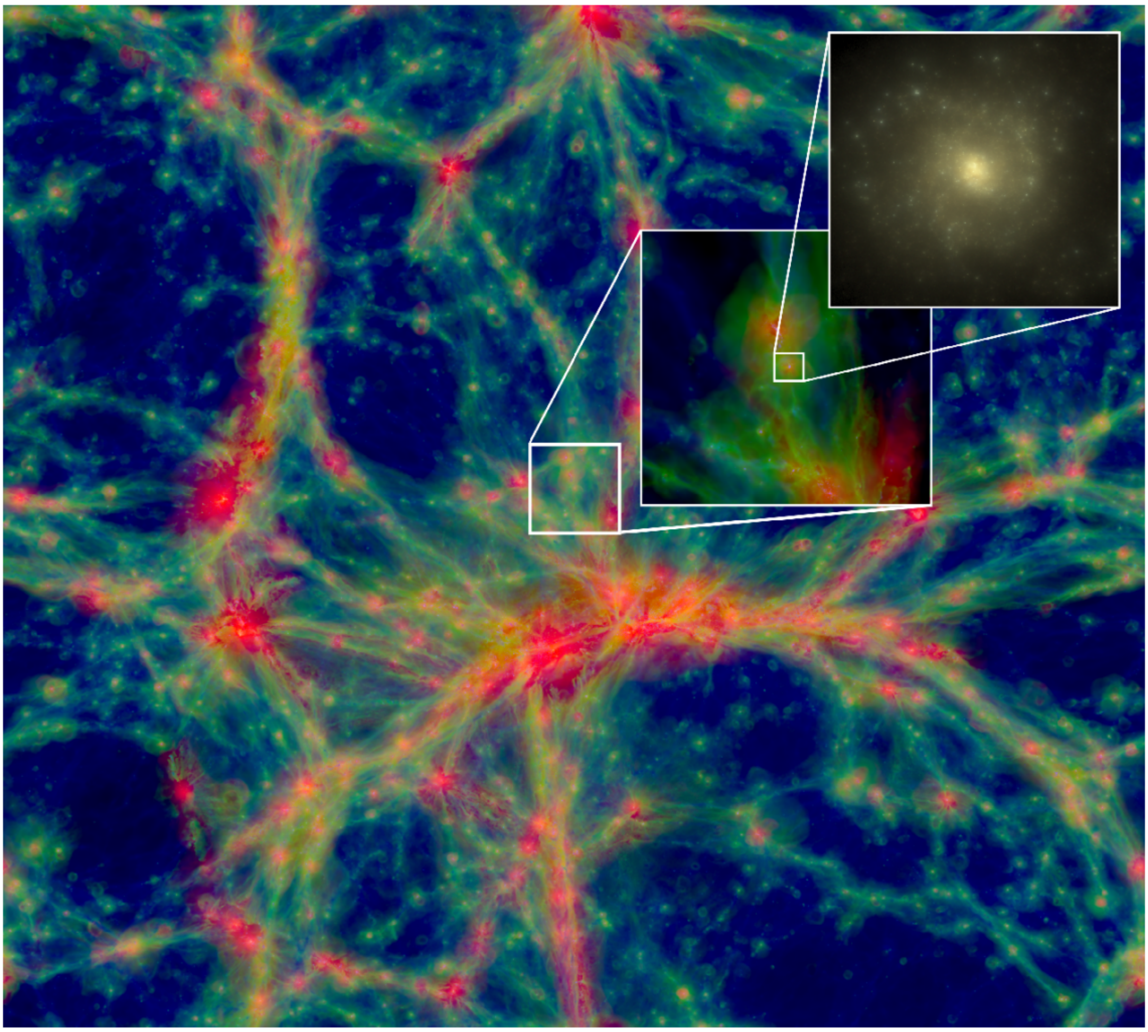

Figure 1.2: This figure shows the large-scale structure found in the EAGLE project, which is suite of a hydrodynamical simulations of a standard $\Lambda$CDM universe. The size of the image is 100 x 100 x 20 comoving Mpc at $z = 0$. The colour represents the temperature of the gas, with blue being cooler (T $<$ 104.5 K) and red being hotter (T $>$ 105.5 K), while the intensity shows the gas density. The inset in the top-left shows the simulated stellar light distribution of one galaxy with the size of 60 x 60 comoving kpc. The original figure is obtained from (Schaye et al., 2015).

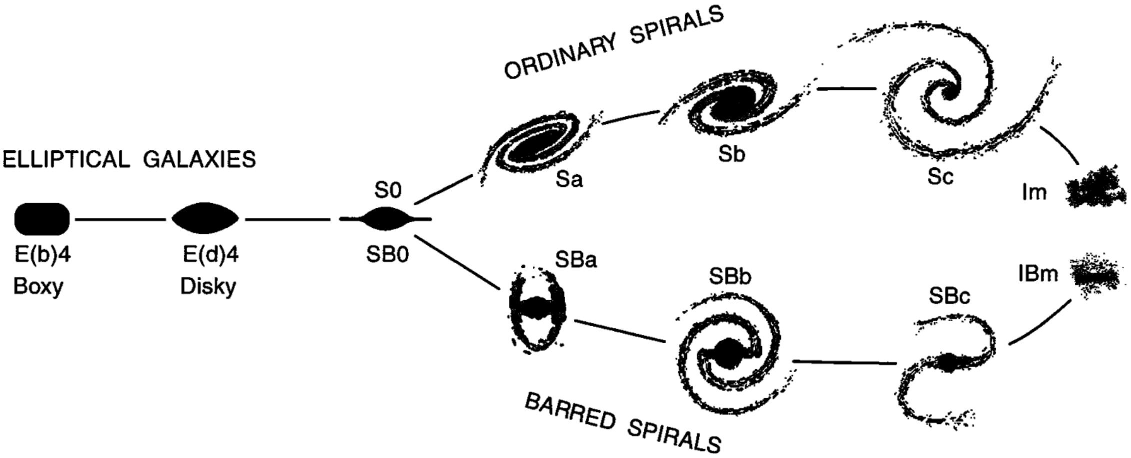

Figure 1.3: A diagram of the Hubble tuning fork. Elliptical galaxies are found on the left side of the tuning fork, while the spiral galaxies are shown on the right, which is separated into two separate branches: unbarred and barred spirals. This figure is obtained from Kormendy & Bender (1996) and is an update to the original tuning fork published in Hubble (1936).

The Universe has produced a great diversity of galaxy morphologies which can be observed in images such as the Hubble Ultra Deep Field. This broad range of morphologies was immediately recognised by Hubble when he was studying low-redshift galaxies during second quarter of the 20$^{\text{th}}$ century, and he created the so-called tuning fork (also known as the Hubble sequence) in order to divide them into separate categories (Hubble, 1926, 1936). The tuning fork, which is shown in Figure 1.3, consists of two halves: the left half contains early-type galaxies, also known as elliptical galaxies, while the right half contains late-type galaxies, which are also known as spiral galaxies[1].

Elliptical galaxies have a smooth ellipsoidal shape and they usually lack any obvious structure, although features like dust lanes (Sadler & Gerhard, 1985; Kaviraj et al., 2012; Davis et al., 2015) and tidal tails (van Dokkum, 2005; Kaviraj, 2010) have been observed in early-type galaxies. In the tuning fork, these systems are denoted as ‘E’ and accompanied by a number, which represents the roundness of the galaxy: E0 are spherical, while E7 are elongated (Hubble, 1926, 1936). Spiral galaxies, shown on the right side of the tuning fork, have a lot of structure. They have a thin flattened disc in which the stars follow nearly circular orbits. The disc also typically contains distinct spiral arms. A spherical central bulge can often be found at the centre of spiral galaxies. They can also contain bars, as shown by the two separate

---

[1] Even though the galaxies are classified as early-type and late-type galaxies, do note that these names do not carry any chronological implications.

branches of the tuning fork, which represent ordinary spirals ('S') and barred spirals ('SB'). This separate branch was made because bars are very common; the bar fraction is 44%-52% in low-redshift disc galaxies at optical wavelengths (Marinova & Jogee, 2007; Barazza et al., 2008; Aguerri et al., 2009; Buta et al., 2019). However, this division is also physically meaningful, as recent evidence has suggested that bars can significantly affect the evolution of their host galaxy (Kormendy & Kennicutt, 2004; Masters et al., 2011; Kruk et al., 2018; Fraser-McKelvie et al., 2020b), which I will elaborate on in Section 1.2.2. By definition, the shape of the spiral arms and the extent of the central bulge varies horizontally over the tuning fork and is noted by the lowercase letter. Traditionally, Sa and SBa galaxies have a large central bulge and tightly wound spiral arms, whereas the bulge in Sc and SBc galaxies is less prominent and their spiral arms are more loosely wound (Hubble, 1926, 1936). However, it is worth noting that more recent work has shown that there is only a weak correlation between bulge prominence and spiral arm tightness, and that galaxies with smaller bulges are able to have a broad range of arm winding (Masters et al., 2019). The tuning fork also includes an intermediate class between elliptical and spiral galaxies, called lenticular galaxies ('S0' or 'SB0'). Although Hubble did predict their existence, he did not originally observed them (Hubble, 1926), but they have been observed since (Spitzer & Baade, 1951; de Vaucouleurs, 1960; Johnson, 1961; Sandage, 1961).

The tuning fork shown in Figure 1.3 is not the original that Hubble created, but rather the updated one presented in Kormendy & Bender (1996). The original tuning fork created by Hubble did not contain irregular galaxies, which are added on the far right of this version. Irregular galaxies can also be barred (abbreviated as 'IBm') or unbarred ('Im'). Additionally, more detail is added regarding the shape of elliptical galaxies, which can have either boxy or discy isophotes (Kormendy & Bender, 1996). Another important change, which is not shown here, was made to the tuning fork in the Comprehensive de Vaucouleurs Revised Hubble-Sandage (CVRHS) system. They introduced three total branches for spiral galaxies: there were now unbarred spirals (SA), strongly barred spirals (SB) and weakly barred spirals (SAB, de Vaucouleurs 1959, 1963). These weakly barred galaxies are an intermediate class between unbarred and strongly barred galaxies. The bars of weakly barred galaxies are small and faint, whereas the bars of strongly barred galaxies are long and obvious (de Vaucouleurs, 1959, 1963). The distinction between weak and strong bars is important for the work presented in this thesis and I will return to this division in Section 1.2.3.

Classifying the morphology of galaxies has traditionally been done by expert classifiers, such as in Hubble (1936) and de Vaucouleurs (1959). More recent examples of experts classifying galaxies include the catalogue of visual morphological classifications of Nair & Abraham (2010a) and the ‘Extraction de Formes Idealisées de Galaxies en Imagerie’ (EFIGI) catalogue presented in Baillard et al. (2011). An alternative approach was explored in the Galaxy Zoo project, which used the efforts of citizen scientists to classify much larger samples of galaxies (Lintott et al., 2008, 2011; Willett et al., 2013). Other studies have also used machine learning techniques to classify the morphology of galaxies (Banerji et al., 2010; Dieleman et al., 2015; Huertas-Company et al., 2015; Hocking et al., 2018; Siudek et al., 2018; Cheng et al., 2020; Martin et al., 2020), which has the advantage of scalability. Such an approach has also been adopted by the Galaxy Zoo team in their latest Galaxy Zoo DECaLS (Walmsley et al., 2022) and Galaxy Zoo DESI catalogues (Walmsley et al., in prep.), where the Galaxy Zoo team (including me) used volunteer classifications to train an ensemble of Bayesian convolutional neural networks to classify the morphology of galaxies.

Another way to describe the morphology of a galaxy is by fitting parametric profiles to its surface brightness. The main advantages of such an approach are reproducibility and the ability to disentangle different components of a galaxy. However, they rely on the validity of the underlying model. One commonly used profile is the generalised Sérsic profile described in Sérsic (1968):

$$I(R) = I_e \exp\left(-b_n\left[\left(\frac{R}{R_e}\right)^{1/n} - 1\right]\right), \tag{1.1}$$

where $R_e$ is the effective radius, which is the radius that contains half of the total light of the model. $I_e$ is the intensity at the effective radius, $b_n$ is a constant dependent on the model and $n$ is the Sérsic index, which describes the shape of the light profile. Galactic discs are typically well described with a Sérsic profile where $n \approx 1$, which is also referred to as an exponential profile (de Vaucouleurs, 1959; Freeman, 1970). In contrast, elliptical galaxies are usually described with a de Vaucouleurs profile, which is a Sérsic profile where $n \approx 4$ (de Vaucouleurs, 1948, 1959). Other quantitative measures of morphology include the concentration (C), asymmetry (A) and clumpiness (S) parameters, also known together as the CAS system (Conselice, 2003). The Gini coefficient (Abraham et al., 2003) and the $\mathrm{M}_{20}$ index (Conselice, 2014) are also frequently used to describe morphology. These parameters are useful when the visual photometric morphologies are not known. However, they generalise the complex morphologies that encode the evolutionary history of a galaxy to a few numbers, which is not ideal for the purposes of thesis thesis and they will therefore not be used. Detailed morphologies are needed to identify and study bars and they are also more sensitive tests of ΛCDM in general.

The kinematics of galaxies can reveal a lot of information about their structure that is otherwise missed by purely photometric studies. For example, Emsellem et al. (2011) and Cappellari et al. (2011b) looked at the stellar kinematics of early-type galaxies and addressed the need for kinematic morphologies. They found that there are well defined categories of early-type galaxies that can be identified through their kinematics, which they called fast and slow rotators, even though both types look very photometrically alike. An alternative to the Hubble tuning fork was proposed based on these insights, in the form of a comb-shaped classification scheme, which made a clear distinction between fast and slow rotators (Cappellari et al., 2011b; Cappellari, 2016). While this is a fundamental and profound method to classify early-type galaxies, it is still important to keep photometric morphologies in mind. This is because individual morphological components can provide information about the formation and evolution of a galaxy and can help to test ΛCDM. In this thesis, I use photometric morphologies to identify specific structures, such as a bar, in galaxies (see Section 2.1.6). However, I return to the kinematics of galaxies and the kinematics of bars in more detail in Section 1.3.

The morphology of a galaxy is closely tied to its evolution, as it depends on the processes that have shaped its history. For example, as mentioned above, it is thought that elliptical galaxies have undergone significantly more mergers than disc galaxies, which generally evolve more in isolation (Fall & Efstathiou, 1980; Barnes & Efstathiou, 1987; Kauffmann, 1996; Mo et al., 1998). The morphology of a galaxy has also been found to correlate with many other physical parameters, such as stellar mass, gas mass, colour, SFR and environment (Strateva et al., 2001; Bundy et al., 2005; Postman et al., 2005; Skibba et al., 2009; Bluck et al., 2014; Smethurst et al., 2015). Given their strong correlation, a study of galaxy evolution, which is covered in more detail in the next section, is incomplete without considering galaxy morphology.

## 1.1 Galaxy bimodality, evolution and quenching

One of the most common tools used to study the evolution of galaxies is the colour-magnitude diagram. An example of a colour-magnitude diagram is shown in Figure 1.4 using nearby galaxies ($0.01 < z < 0.05$) from the Galaxy Zoo DECaLS project (Walmsley et al., 2022), which is covered in more detail in Section 2.1.5. As the name implies, the colour is plotted against the absolute magnitude for all galaxies (in this

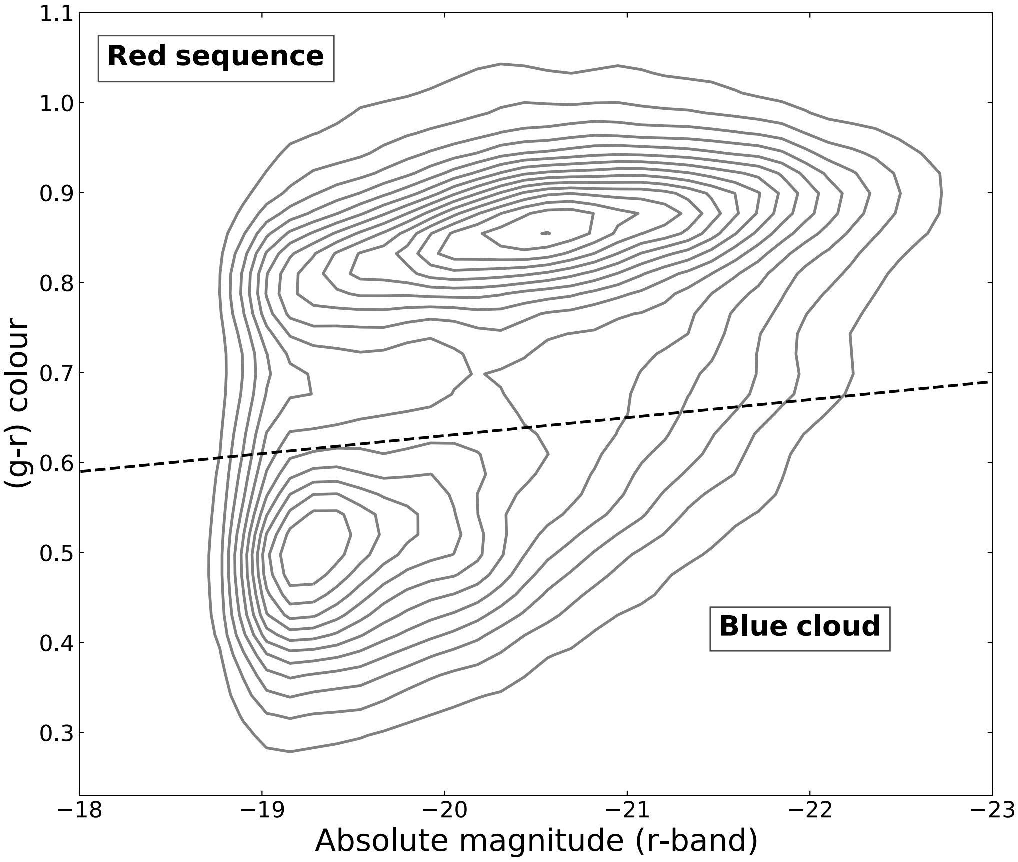

Figure 1.4: The colour-magnitude diagram visualised using a volume-limited sample ($z < 0.05$, $M_{\mathrm{r}} < -18.96$) containing 32,809 galaxies from Galaxy Zoo DECaLS. The colours were obtained from the DECaLS survey (Dey et al., 2019). The dashed line across the diagram is the 'blue edge of the red sequence' defined in Masters et al. (2010).

case it is the ($g$-$r$) colour against the $r$-band absolute magnitude). Large-scale surveys find that galaxies tend to naturally cluster in two separate groups in this diagram, which are commonly referred to as the 'blue cloud' and the 'red sequence', whose positions are labelled on Figure 1.4 (Strateva et al., 2001; Baldry et al., 2004; Dekel & Birnboim, 2006; Masters et al., 2010; Cappellari et al., 2011a). This bimodality represents a underlying dichotomy in galaxy properties. Colour can be interpreted as a proxy for SFR, while the absolute magnitude is a proxy of stellar mass. This suggests that blue cloud galaxies typically have lower stellar masses, higher star formation rates (SFR) and higher gas fractions than red sequence galaxies (Baldry et al., 2004, 2006; Dekel & Birnboim, 2006). Additionally, blue cloud galaxies are mostly spiral or irregular galaxies, whereas the red sequence broadly consists of elliptical galaxies. However there are also significant populations of red spirals and blue ellipticals (Schawinski et al., 2009; Masters et al., 2010; Fraser-McKelvie et al., 2016), implying that the use of colour as a approximation for morphology is not reliable (Smethurst et al., 2022).

Studies have also shown that there is a well defined star forming sequence (SFS) upon which star forming galaxies lie in the stellar mass against SFR plane (Brinchmann et al., 2004; Noeske et al., 2007). The scatter around this sequence is relatively small ($\sigma \approx 0.2$ dex, Speagle et al., 2014), which suggest that most of the star formation in the Universe happens in quasi-steady state (Sparre et al., 2015). Galaxies with very low SFR, also known as quiescent galaxies, are found underneath this SFS. Blue cloud galaxies (and thus the majority of spiral galaxies) tend to lie on the SFS, whereas galaxies in the red sequence (and thus the majority of elliptical galaxies) are usually found well below it (Brinchmann et al., 2004; Noeske et al., 2007; Salim et al., 2007; Elbaz et al., 2011; Renzini & Peng, 2015; Belfiore et al., 2018). Another commonly used tool to study the evolution of galaxies is the UVJ diagram, which can discern quiescent galaxies from star forming galaxies and is typically used at higher redshifts. The rest-frame U-V colour is plotted against the rest-frame V-J colour, where quiescent galaxies typically have high values for the former and low values for the latter (Wuyts et al., 2007; Williams et al., 2009; Whitaker et al., 2010; Brammer et al., 2011; Patel et al., 2011, 2012).

Scaling relations are another important concept used in galaxy evolution. For example, the Tully-Fisher relation describes how the luminosity of spiral galaxies scales with the circular velocity: $L \propto V_c^4$ (Tully & Fisher, 1977). The analogue for elliptical galaxies is the Faber-Jacker relation, which describes the relationship between the luminosity and the velocity dispersion: $L \propto \sigma^4$ (Faber & Jackson, 1976). This relationship was later discovered to be a projection of the fundamental plane that describes the relationship between the luminosity, velocity dispersion and effective radius of elliptical galaxies (Dressler et al., 1987; Djorgovski & Davis, 1987). Cappellari et al. (2013) later showed that the luminosity in the fundamental plane can be replaced by the stellar mass, creating a mass plane.

Whichever tool is used, the goal is similar: to understand the underlying physical processes that shape the evolution of galaxies. For example, as galaxies evolve, they move around on the colour-magnitude diagram. They are thought to transition from the blue cloud to the red sequence, passing over the sparsely populated area in between, in a process called 'quenching' (Bell et al., 2004; Wyder et al., 2007; Martin et al., 2007; Faber et al., 2007; Mendez et al., 2011; Gonçalves et al., 2012; Schawinski et al., 2014). Intermediate galaxies are often called 'green valley' galaxies. Schawinski et al. (2014) have shown that this transition is relatively quick for early-type galaxies ($< 250$ Myr), while this happens more slowly for late-type galaxies ($> 1$ Gyr). However, the exact method by which quenching occurs or why this happens to some galaxies but not others, is not yet fully understood and remains one of the main areas of active research in galaxy evolution (e.g. Trussler et al., 2020; Donnari et al., 2021; Whitaker et al., 2021; Akins et al., 2022; Bluck et al., 2022; Piotrowska et al., 2022; Carnall et al., 2023).

There are many proposed processes that can cause a galaxy to quench. These processes are typically divided into external quenching mechanisms and internal quenching mechanisms. Mergers are a common example of an external quenching mechanism. They can quench galaxies by inducing starbursts that deplete the gas reservoir of the merging galaxies, which quenches the host (Mihos & Hernquist, 1994; Hayward et al., 2014; Sparre & Springel, 2016). A merger also dynamically heats the galaxy, which prevents further star formation (Walker et al., 1996; Kormendy & Kennicutt, 2004). Other external quenching mechanisms include strangulation, which involves halting the supply of gas to the galaxy (Peng et al., 2015; Paccagnella et al., 2016), and the removal of gas in the galaxy through ram pressure stripping, which occurs to infalling galaxies in a cluster (Abadi et al., 1999; Fillingham et al., 2016). Galaxies can also quench due to multiple internal mechanisms. One such example is AGN feedback, where an AGN is thought to heat or expel cold gas from the galaxy (Wyithe & Loeb, 2003; Springel et al., 2005; Somerville et al., 2008; Schawinski et al., 2010; Kaviraj et al., 2011). Bars are also believed to be able to induce quenching (Kormendy & Kennicutt, 2004; Sheth et al., 2005; Athanassoula, 2007; Masters et al., 2011; Cheung et al., 2013; Kruk et al., 2018; Efthymiopoulos et al., 2019), which is a main focus of this thesis and I will return to this topic in much more detail in Section 1.2.2.

The hierarchical clustering paradigm suggests that mergers are common, which, in turn, implies that external mechanisms should be the dominant mechanisms through which galaxies evolve and quench. As mentioned above, this paradigm has been very successful in explaining the large-scale structure of the Universe (Frenk & White, 2012; Sachdeva & Saha, 2016; Bullock & Boylan-Kolchin, 2017). Additionally, simulations of mergers of elliptical galaxies reliably reproduce the aforementioned fundamental plane (Bekki, 1998; Boylan-Kolchin et al., 2005; Hilz et al., 2012; Taranu et al., 2015). However, a lot of evidence suggests that mergers might not be as important as previously thought and that secular processes dominate over external processes. For example, it has been shown that the observed peak of SFR found around $z \sim 1.5 - 2$ (Madau et al., 1998; Hopkins & Beacom, 2006) cannot be explained by mergers alone (Genzel et al., 2008; Shapiro et al., 2008; Cresci et al., 2009; Mancini et al., 2011). Furthermore, Kaviraj et al. (2013) estimate that only 15% of the star formation budget can be attributed to major mergers. There is also a known robust relationship between the black hole mass and the total stellar mass (Marleau et al., 2013; Reines & Volonteri, 2015; Martin et al., 2018). This is found across all morphological types, even in bulgeless galaxies, which suggests that this relationship exists not due to mergers, but due to secular processes (Martin et al., 2018) and that secular processes are fundamental to the coevolution of galaxies and their supermassive black holes (Jiang et al., 2011; Simmons et al., 2013; McAlpine et al., 2020). Finally, as mentioned before, hierarchical clustering fails to explain the high fraction of bulgeless galaxies that are observed (Kautsch, 2009; Kormendy et al., 2010; Sachdeva & Saha, 2016; Haslbauer et al., 2022).

These results suggest that secular processes play a fundamental role in the evolution of galaxies and that it is paramount to study them in detail. As these secular processes are typically interdependent, researching the individual processes with large samples will help to disentangle the different effects they have on galaxies. The impact that bars have on their host, especially with respect to galaxy evolution and quenching, is the main focus of this thesis. Bar formation and evolution is discussed in Section 1.2, while the kinematics of bars are covered in Section 1.3.

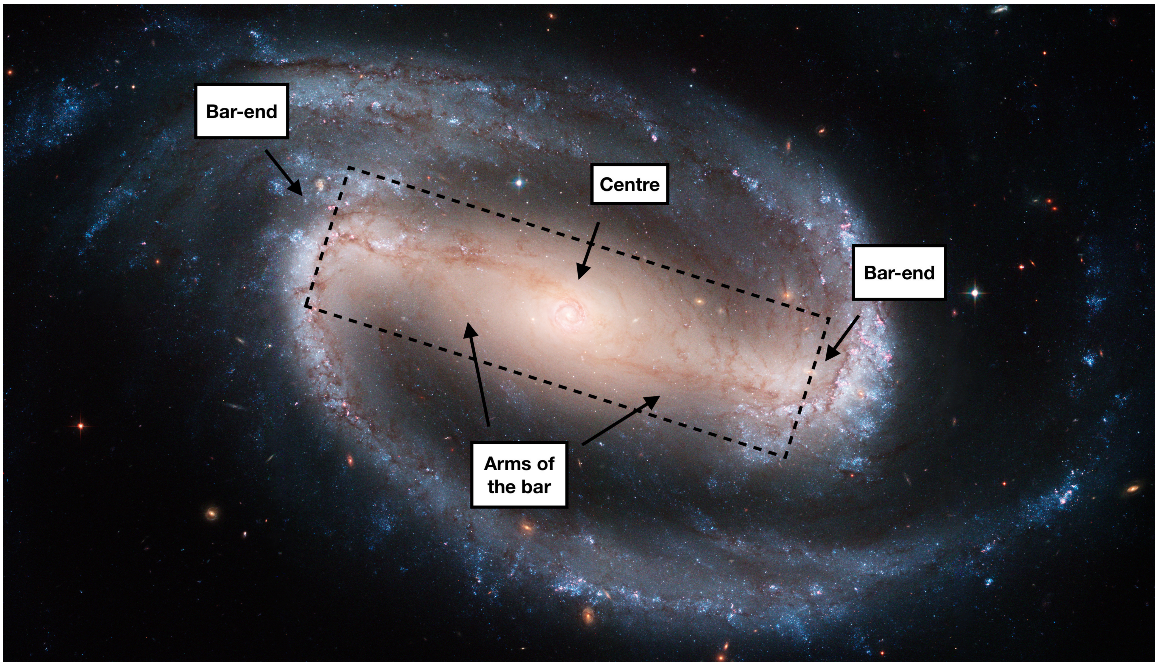

Figure 1.5: NGC 1300 is arguably the most famous barred galaxy. Different important regions of a bar are highlighted in this figure. The centre of the bar usually coincides with the centre of the galaxy. The arms of the bar connect the centre with the bar-end regions. The dust lanes along the arms of the bar are clearly visible and the spiral arms connect directly the the bar-ends. The dashed rectangle delineates the barred region. Credits: NASA, ESA, and The Hubble Heritage Team (STScI/AURA)

## 1.2 Bars

A bar is a central elongated stellar feature that spans across the middle of a galaxy. One of the most well known barred galaxies is NGC 1300, shown in Figure 1.5. It features a very obvious bar that connects to the two spiral arms of the galaxy. There are a few important regions in a bar: the centre, the arms of the bar and the bar-end region. The region between the two bar-ends is referred to as the 'barred region', while everything else is considered 'outside the bar'. These regions are shown in Figure 1.5 and I will refer to these definitions throughout this thesis. The centre of the bar often coincides with the centre of the galaxy, although offset bars have been observed in a small number of galaxies. Kruk et al. (2017) find that only 2% of galaxies with masses similar to the Milky Way ($10^{10.5} - 10^{11.1}$ $M_\odot$) have offset bars. In the case of NGC 1300, the bar-end region connects the bar to the spiral arms, but this is not always the case.

The bar fraction in disc galaxies is around 44%-52% in low-redshift studies at optical wavelengths (Marinova & Jogee, 2007; Barazza et al., 2008; Aguerri et al., 2009; Buta et al., 2019). A lower total bar fraction (between 23.6 - 29.4%) tends to be found in studies using data from Galaxy Zoo 2 (Masters et al., 2011; Skibba et al., 2012; Cheung et al., 2013), although these same studies have noted that the bars identified in Galaxy Zoo 2 tend to be strong bars and leave out a lot of the weaker bars. Interestingly, the bar fraction raises to 59-73% when infrared wavelengths are used (Eskridge et al., 2000; Marinova & Jogee, 2007; Menéndez-Delmestre et al., 2007; Sheth et al., 2008). This higher bar fraction is presumably due to infrared wavelengths not being so affected by dust and star formation (Erwin, 2018).

The bar fraction in disc galaxies has been observed to be lower at higher redshifts ($0.5 < z < 2$), with bar fraction estimates ranging between 10-20% (Sheth et al., 2008; Simmons et al., 2014). Elmegreen et al. (2004) find a constant bar fraction of 23% from $z = 0$ to $z = 1.1$, while Melvin et al. (2014) find that the bar fraction decreases from 22% at $z = 0.4$ to 11% at $z = 1$. Although thought to be less common at higher redshifts, barred galaxies have been observed with the James Webb Space Telescope (JWST) up to $z \sim 2$, which suggests that they were present ~8-10 Gyr ago (Guo et al., 2022). Further analysis of JWST data will help to shed more light on the bar fraction at higher redshifts. It has been suggested that the so-called 'epoch of bar formation' is around $z \sim 0.7$-1, when galaxies started to become dynamically cool and disc dominated, which enables them to form and sustain bars (Kraljic et al., 2012; Melvin et al., 2014; Simmons et al., 2014). This coincides with an observed lower rate of major mergers (Conselice et al., 2003; Ryan et al., 2008; Lotz et al., 2011). From that epoch onwards, secular processes, such as bar quenching, become increasingly more important for the evolution of galaxies (Kraljic et al., 2012; Melvin et al., 2014; Simmons et al., 2014). Additionally, most simulations agree with each other that bars are robust structures that are long-lived (Jogee et al., 2004; Shen & Sellwood, 2004; Debattista et al., 2006; Kraljic et al., 2012; Athanassoula et al., 2013), although some suggest that they might be transient features (Bournaud & Combes, 2002; Bournaud et al., 2005).

In conclusion, bars appear to be relatively common structures in galaxies that are thought to be robust, long-lived and to have affected galaxy evolution for the past ~8-10 Gyr. The different mechanisms that can form a bar are discussed in Section 1.2.1, while the evolution of a bar and how a bar might quench their host is detailed in Section 1.2.2. Finally, Section 1.2.3 discusses the important distinction between weak and strong bars.

### 1.2.1 Bar formation mechanisms

$N$-body simulations of isolated disc galaxies have repeatedly shown that stable bars can spontaneously be formed from instabilities in the disc of the galaxy (Hohl, 1971; Ostriker & Peebles, 1973; Sparke & Sellwood, 1987; Sellwood & Wilkinson, 1993; Polyachenko, 2013). The stability of the disc of a galaxy can be approximated with multiple methods, such as the Toomre stability parameter ($Q$), defined in Toomre (1964):

$$Q = \frac{\kappa \sigma_r}{3.36 G \Sigma} , \tag{1.2}$$

where $\kappa$ is the epicyclic frequency, $\sigma_r$ is the velocity dispersion in the radial direction, $G$ the gravitational constant and $\Sigma$ the surface density of the disc. The disc becomes gravitationally unstable if $Q < 1$, which can result in the formation of a bar, while discs are stable when $Q > 1$. The Toomre stability parameter is still frequently used in simulations to predict bar formation (Fanali et al., 2015; Gavazzi et al., 2015; Spinoso et al., 2017; Seo et al., 2019). Another metric that is used to predict the stability of the disc against bar formation is the ELN-criterion ($\epsilon$), defined in Efstathiou et al. (1982):

$$\epsilon = \frac{V_{\mathrm{max}}}{\sqrt{G M_{\mathrm{d}} / R_{\mathrm{d}}}} , \tag{1.3}$$

where $V_{\mathrm{max}}$ is the maximum rotational velocity, $M_{\mathrm{d}}$ is the total mass of the disc and $R_{\mathrm{d}}$ is the scale length of the disc. Galaxies with $\epsilon < 1.1$ have gravitationally unstable discs that tend to form bars. In contrast, if $\epsilon > 1.1$, the stellar disc is stable and no spontaneous bar formation is typically seen (Efstathiou et al., 1982; Izquierdo-Villalba et al., 2022). The spontaneous formation of a bar in an isolated disc through instabilities is visualised in Figure 1.6 using the self-consistent simulation of a Milky-Way sized disc of Seo et al. (2019). The bar becomes longer and stronger as time goes on, an effect which is visible in both the stellar and gaseous components. Additionally, the gaseous component also clearly shows how bars clear the gas within the bar radius and funnel the gas to the centre of the galaxy, which will be discussed in more detail in Section 1.2.2.

Simulations show that tidal interactions and mergers can also trigger bar formation by disturbing the disc (Noguchi, 1987; Gerin et al., 1990; Elmegreen et al., 1991; Barnes & Hernquist, 1991; Miwa & Noguchi, 1998; Lang et al., 2014). The orbital configuration of the interaction is very important and dictates the properties of the induced bar. For example, simulations have found that prograde encounters usually

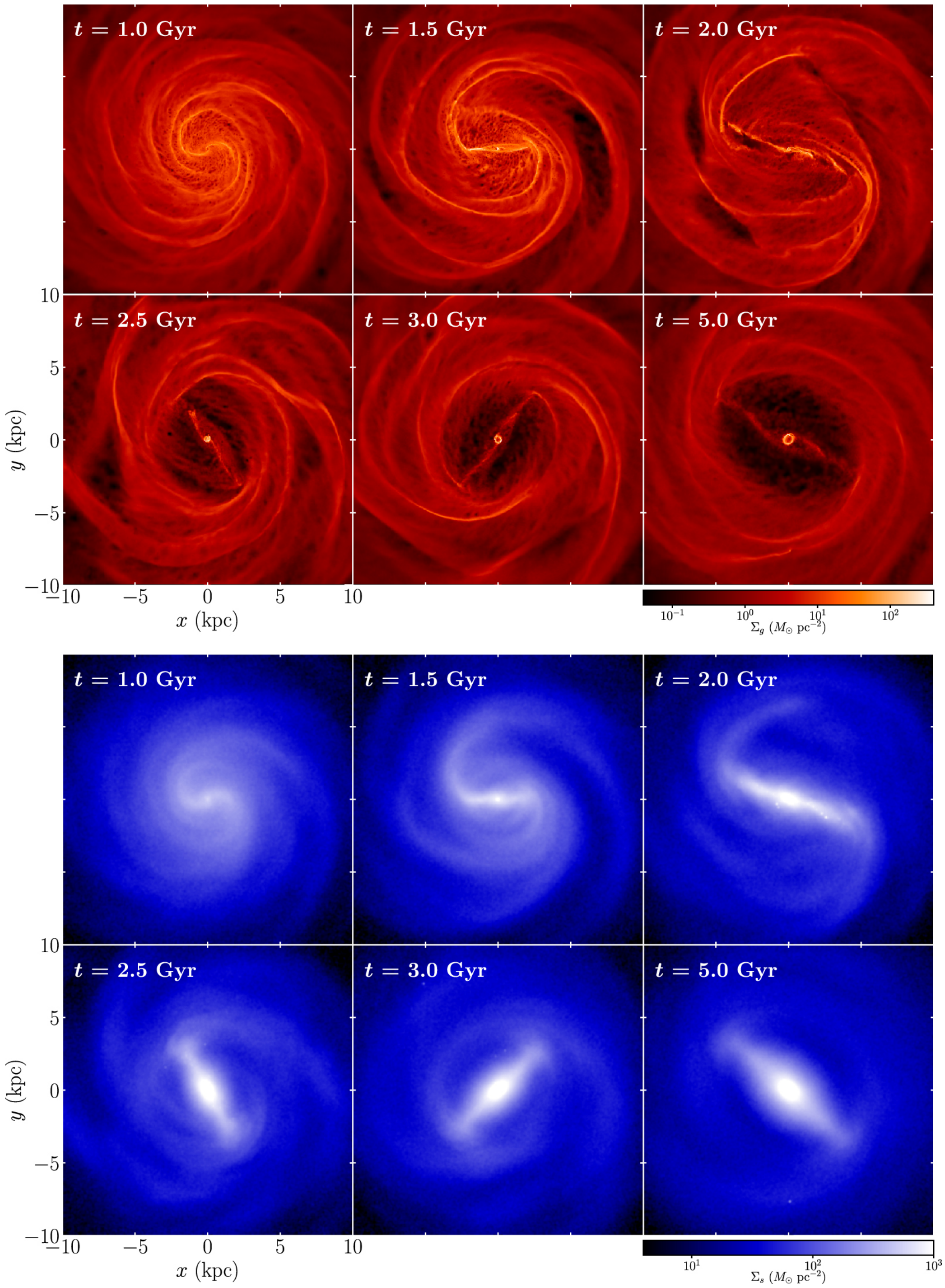

Figure 1.6: Example of bar formation through global bar instabilities in a self-consistent simulation of a Milky-Way sized isolated disc. The top panel shows the gas surface brightness at different epochs of the simulation, while the bottom panel shows the stellar surface brightness. The original figure is obtained from Seo et al. (2019).

form strong bars, whereas retrograde encounters do not trigger bar formation (Lang et al., 2014; Gajda et al., 2017; Łokas, 2018). Interestingly, results from observational studies are not as consistent. Some studies find no, or only weak, evidence for a correlation between the presence of a bar and environment (van den Bergh, 2002; Li et al., 2009; Lin et al., 2014), suggesting that bars are not formed by tidal interactions. However, other studies find a strong correlation (Giuricin et al., 1993; Skibba et al., 2012) or even a negative correlation (Casteels et al., 2013), which suggests that the environment plays an important role in bar formation. Méndez-Abreu et al. (2012) proposed that this contradiction can be resolved by taking the stellar masses of the galaxies into account, as they have found that interactions can form bars in massive galaxies, while bar formation is inhibited in low mass galaxies after tidal interactions. They suggest that this is because the discs of low mass galaxies are susceptible to tidal heating, which prevents bar formation, while the discs of massive galaxies are strong and stable enough to survive close interactions and stay dynamically cold. Once the bar is formed, either through tidal interactions or instabilities in the disc, it will start to grow and influence its host.

### 1.2.2 Evolution of bars and their role in galaxy quenching

Bars evolve and grow over time, during which they affect their hosts in multiple ways. Firstly, they transfer angular momentum outwards from the inner disc to the outer disc and the DM halo (Lynden-Bell & Kalnajs, 1972; Sellwood, 1981; Athanassoula, 2003; Athanassoula et al., 2013). The different resonances of the bar, which are discussed in greater detail in Section 1.3.2, are especially important in this exchange of angular momentum (Lynden-Bell & Kalnajs, 1972; Athanassoula, 2002). By trapping more and more stars in different bar orbits (see Section 1.3.1), the bar grows and becomes longer and stronger over time during this redistribution of angular momentum (Lynden-Bell & Kalnajs, 1972; Sellwood, 1981; Athanassoula, 2003; Martinez-Valpuesta et al., 2006; Athanassoula et al., 2013)). At the same time, the growing bar funnels gas to the centre of the galaxy along the arms of the bar (Sorensen et al., 1976; Athanassoula, 1992b; Davoust & Contini, 2004; Villa-Vargas et al., 2010; Vera et al., 2016; Spinoso et al., 2017; George et al., 2019), often leaving a gas-depleted region behind, which can be seen in the top panel of Figure 1.6 (Fanali et al., 2015; Gavazzi et al., 2015; Spinoso et al., 2017; James & Percival, 2018; George et al., 2019; Seo et al., 2019; Newnham et al., 2020). The inflow of gas to the centre will cause the buildup of a central mass concentration (CMC). Interestingly, it has been argued that the buildup of the CMC can weaken the bar, by interfering with the stellar orbits that make it up (Athanassoula et al., 2005; Bournaud et al., 2005; Villa-Vargas et al., 2010; Athanassoula et al., 2013; Seo et al., 2019), although it has been shown that the mass required for the CMC to completely destroy the bar is much higher than what is usually found in observations (Shen & Sellwood, 2004; Athanassoula et al., 2005). Some studies suggest that this bar-driven inflow of gas could trigger AGN activity (Knapen et al., 2000; Oh et al., 2012; Fanali et al., 2015; Galloway et al., 2015). However, this is still unclear, as other authors suggest that there is no link between the presence of bars and AGN fuelling (Regan & Mulchaey, 1999; Cisternas et al., 2013; Cheung et al., 2015; Cisternas et al., 2015).

It has been suggested that a bar could play a role in galaxy quenching, as multiple studies have shown that the fraction of bars appearing in a galaxy increases in redder, more massive and gas-poor galaxies (i.e. typical quiescent galaxies, Masters et al., 2012; Cervantes Sodi, 2017; Vera et al., 2016; Fraser-McKelvie et al., 2020b). However, these results can be interpreted in two ways: either the bar helps to quench the galaxy, or it is easier to form a bar in a quenched galaxy (Masters et al., 2012). Multiple simulations give weight to the latter option. Villa-Vargas et al. (2010) find that the bar growth is limited in galaxies with a strong gas component and Athanassoula et al. (2013) show that bars in simulations form later if the gas fraction is high in the galaxy. Additionally, the simulations of Seo et al. (2019) show that bars eventually become stronger if the gas fraction is low. One possible mechanism for this anti-correlation is that higher gas fractions will result in a more massive CMC, which is known to weaken bars (Athanassoula et al., 2013; Seo et al., 2019).

However, there is also evidence suggesting that bars help to quench their host. As mentioned above, gas will flow to the centre of the galaxy along the arms of the bar as the bar evolves, creating a CMC. This can trigger a starburst in the centre of the galaxy, which greatly increases the rate of gas consumption and facilitates the quenching process. This increased central star formation has been repeatedly observed (Sheth et al., 2000; Alonso-Herrero & Knapen, 2001; Sheth et al., 2005; Jogee et al., 2005; Hunt et al., 2008; Ellison et al., 2011; Coelho & Gadotti, 2011; Carles et al., 2016; Lin et al., 2020). Another proposed quenching mechanism is that the bar can cause the gas to become too dynamically hot for star formation, by increasing the velocity dispersion or shear in the bar, which lowers the SFR (Athanassoula, 1992b; Reynaud & Downes, 1998; Sheth et al., 2000; Zurita et al., 2004; Haywood et al., 2016; Khoperskov et al., 2018). Lower SFR and SFE are typically observed in the arms of the bar, where the gas flows and resulting shear are greatest (Reynaud & Downes, 1998; Sheth et al., 2000; Maeda et al., 2020b). Fast cloud-cloud collisions can also explain lower SFR and SFE in the arms of the bar (Fujimoto et al., 2014; Maeda et al., 2018; Fujimoto et al., 2020; Maeda et al., 2021). To summarise, while strong evidence has been presented for either case, it is still unclear whether bars cause quenching or whether it is easier to form a bar in a quenched galaxy. This is one of the main topics of this thesis and I will use a large sample of barred galaxies of different bar strengths in order to address this question.

### 1.2.3 Strong and weak bars

There is a large variety in the length and strength of different bars, which is shown in Figure 1.7 using images from the Legacy Survey (Dey et al., 2019). This diversity has to be taken into consideration when studying bars. This can be done by classifying barred galaxies in different subcategories and considering them separately. This was originally done by de Vaucouleurs (1959, 1963), who noted that strong bars are obvious and long, whereas weak bars are faint and small structures. In the catalogue of detailed visual morphological classifications of Nair & Abraham (2010a), a bar is defined to be strong if it dominates the light distribution of the galaxy. In contrast, they define a weak bar as only containing a small proportion of the total flux of the galaxy. However, these definitions leave a lot of room for interpretation by the classifier. This has been noted by Athanassoula (2003): ‘Although the notion of bar strength is clear to everyone, and it is very often easy, when comparing two bars, to say which one is strongest, a precise definition is not trivial’. Other, more quantitative, methods to measure bar strength include estimating the maximum ellipticity (Athanassoula, 1992a; Laurikainen & Salo, 2002; Erwin, 2004) and the boxiness of the bar isophotes (Gadotti, 2011), as galaxies with stronger bars have more pronounced and elongated isophotes. Alternatively, one can approximate the bar strength by estimating the amplitude of the m=2 Fourier mode (Athanassoula, 2003; Garcia-Gómez et al., 2017) or using the torque exerted by the bar (Combes & Sanders, 1981; Buta & Block, 2001; Laurikainen & Salo, 2002; Speltincx et al., 2008). Another approach has been recently explored by Galaxy Zoo DECaLS, which asked citizen scientists to classify bars into weak and strong based on images from DECaLS (Walmsley et al., 2022). The results of Galaxy Zoo DECaLS will be discussed in greater detail in Sections 2.1.5 and 2.1.6.1.

The strength of the bar has been found to correlate with many other physical properties. For example, a positive correlation exists between bar strength and bar length (Hoyle et al., 2011; Díaz-García et al., 2016; Guo et al., 2019), which, in turn,

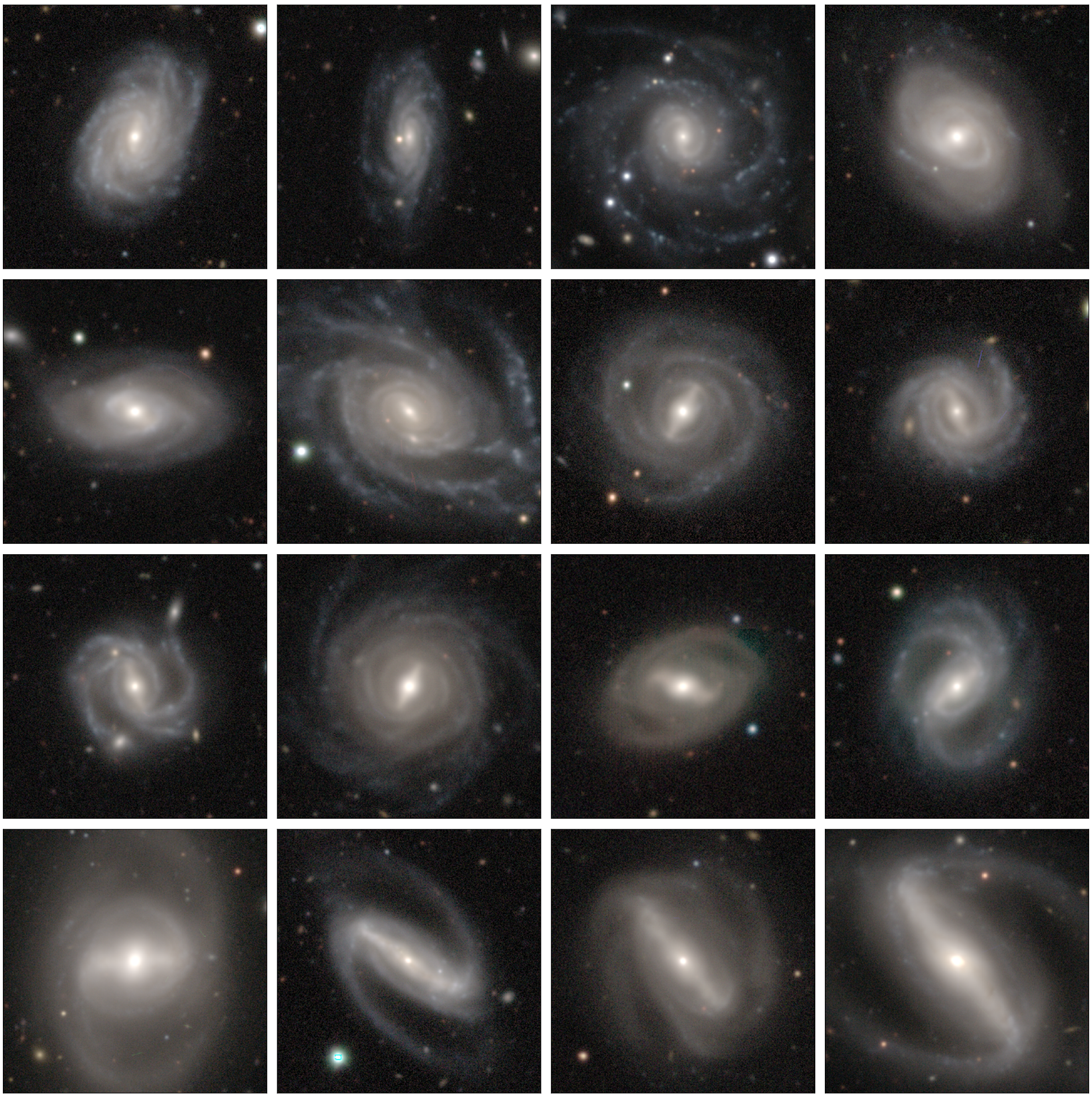

Figure 1.7: Images (95x95 arcsec) obtained from the Legacy Survey (Dey et al., 2019) of barred galaxies. These galaxies were identified by Galaxy Zoo DESI (Walmsley et al., in prep.) and ordered by bar strength from top to bottom and left to right (see Section 2.1.5 for more information on Galaxy Zoo). Note the large variety in bar lengths and strengths in all these barred galaxies.

correlates with the size of the galaxy (Aguerri et al., 2009; Lee et al., 2022). Simulations also show that bars grow to be stronger in gas-poor galaxies (Athanassoula et al., 2013; Seo et al., 2019). Stronger bars also have a higher central concentration of gas (Kuno et al., 2007) and higher SFRs (Martinet & Friedli, 1997; Oh et al., 2012). Additionally, the surface brightness profiles of strong and weak bars seem to differ: weak bars tend to have exponential profiles, while the profiles of strong bars are generally flatter (Elmegreen & Elmegreen, 1985; Elmegreen et al., 1996; Kruk et al., 2018).

However, many open questions remain. This is largely because many studies focus on strong bars, as they are easier to identify and observe. For example, it is ambiguous whether weak and strong bars are fundamentally distinct physical phenomena. Additionally, it is also not certain whether weak and strong bars have similar lifetimes. As mentioned above, bars are more common in quenched galaxies (Masters et al., 2012; Cervantes Sodi, 2017; Vera et al., 2016; Fraser-McKelvie et al., 2020b), but it is unclear whether this is also the case for weak bars. Studies have shown that bars can funnel gas to the centre, which enhances the central star formation, but it is not clear whether this also consistently happens in weakly barred galaxies. As will be discussed in Section 1.4, I will focus on the effects of weak bars in this thesis. Finally, many observational studies have focussed on the kinematics of strong bars, however, observations of the kinematics of weak bars have been sparse. The kinematics of bars is discussed in more detail in the next section.

## 1.3 Kinematics of bars

It is important to look at the kinematics of galaxies, as this is closely related to their evolution. This was shown by the aforementioned fast and slow rotators found in Emsellem et al. (2011) and Cappellari et al. (2011b). It was discovered that fast rotators are rotationally supported and start out as disc galaxies that slowly build up their bulge by the accretion of gas, after which they eventually quench. In contrast, slow rotators are dispersion dominated and form near the centre of massive haloes and have undergone many gas-poor mergers (Emsellem et al., 2011; Bois et al., 2011; Duc et al., 2011; Naab et al., 2014; Cappellari, 2016).

Similarly, the kinematics of bars has also been shown to be important, as it can help to probe a bar's formation mechanism (Martinez-Valpuesta et al., 2016, 2017), their evolution (Debattista & Sellwood, 2000; Athanassoula, 2003; Martinez-Valpuesta et al., 2006; Okamoto et al., 2015), as well as a recently claimed tension with $\Lambda$CDM (Algorry et al., 2017; Peschken & Łokas, 2019; Roshan et al., 2021b), all of which are discussed below.

### 1.3.1 Orbits of stars in bars and the bar pattern speed

The bar of a galaxy consists of stars that are trapped in distinct orbital families. The most important orbits are those that belong to the $x_1$ orbit family and are typically elongated parallel to the bar (Athanassoula et al., 1983; Athanassoula, 1992a; Skokos et al., 2002a; Patsis & Athanassoula, 2019). The orbits in the $x_2$ orbit family are central orbits that are oriented perpendicular to the bar and are usually much smaller than the $x_1$ orbits (Athanassoula, 1992a). There are many different variations of $x_1$ and $x_2$ orbits, depending on the energy of the system (Patsis & Athanassoula, 2019). Other less prevalent orbit families exist too, such as the $x_3$ orbit family, which are similar to the $x_2$ orbit family, but are usually more elongated (Athanassoula, 1992a), retrograde orbits that belong to the $x_4$ orbit family (Contopoulos, 1980; Contopoulos & Papayannopoulos, 1980; Athanassoula et al., 1983) and banana-shaped orbits that orbit around the $L_4$ and $L_5$ Lagrangian points (Skokos et al., 2002a).

The 3D structure of multiple $x_1$ and $x_2$ orbits is shown in Figure 1.8, where the bar is oriented vertically along the (x, y) plane. However, these orbits are shown in the reference frame of the bar. In reality, the bar also rotates around its centre with a certain rotational frequency, also known as the pattern speed of the bar ($\Omega_{\rm bar}$), and these orbits rotate around with it. Simulations show that the bar pattern speed goes down as the bar evolves and grows longer, by exchanging angular momentum with its host (Debattista & Sellwood, 2000; Athanassoula, 2003; Martinez-Valpuesta et al., 2006; Okamoto et al., 2015). However, the redistribution of angular momentum that governs the pattern speed depends on numerous parameters, such as the mass distribution and velocity dispersion of the absorbing and emitting components (Athanassoula, 2003). Observational studies tend to agree with simulations in typically finding that the largest and strongest bars have the lowest pattern speeds (Font et al., 2017; Cuomo et al., 2020), although the sample size of weakly barred galaxies with reliable pattern speed estimates remains relatively low. Although it is expected that this trend remains valid for weakly barred galaxies, measuring the pattern speed for a larger sample of weakly barred galaxies will help to verify whether this is the case.

The pattern speed can be measured observationally in multiple ways. For example, one can subtract a rotation model from the gas velocity field and estimate the pattern speed from the morphology of the residuals (Sempere et al., 1995; Font et al.,

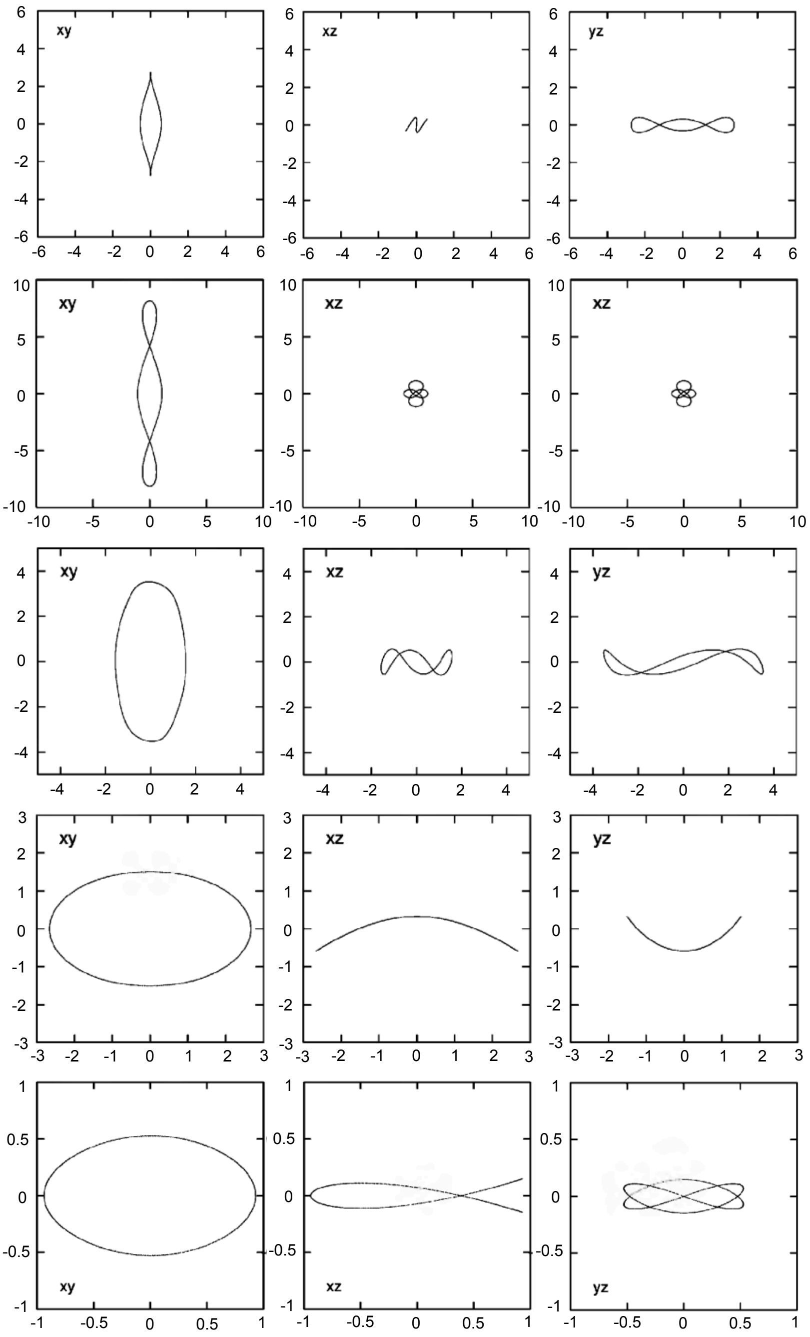

Figure 1.8: Visualisation of the 3D structure of typical stable bar orbits. The top three rows are orbits that below to the $x_1$ family, while the bottom two belong to the $x_2$ orbit family. The bar is oriented vertically along the (x, y) plane (left column), while the (x, z) plane looks on top of the bar-end (middle column). The (y, z) plane is oriented along the side of the bar (right column). This figure is obtained and modified from Skokos et al. (2002a) and Skokos et al. (2002b).

2011, 2017). Alternatively, it is possible to match the observed gas velocity field with simulations that have $\Omega_{\rm bar}$ as a free parameter (Sanders & Tubbs, 1980; Hunter et al., 1988; Lindblad & Kristen, 1996; Weiner et al., 2001; Rautiainen et al., 2008; Treuthardt et al., 2008). Finally, it is also possible to use other morphological features to estimate the bar pattern speed, such as the shape and offset of dust lanes (Athanassoula, 1992b; Sánchez-Menguiano et al., 2015), rings (Buta, 1986; Rautiainen & Salo, 2000; Muñoz-Tuñón et al., 2004; Pérez et al., 2012) or spiral arms (Puerari & Dottori, 1997; Aguerri et al., 1998; Buta & Zhang, 2009; Sierra et al., 2015). However, all these methods are model-dependent. The only reliable model-independent method to estimate the bar pattern speed is the Tremaine-Weinberg method (Tremaine & Weinberg, 1984), which has been used in many studies using long-slit or, more recently, integral-field spectroscopy (Aguerri et al., 2015; Cuomo et al., 2019; Guo et al., 2019; Garma-Oehmichen et al., 2020, 2022). The Tremaine-Weinberg method determines the bar pattern speed based on line-of-sight (LOS) velocity and surface brightness data. I will utilise this method in this thesis and it is described in detail in Section 2.2.4. Once the bar pattern speed is measured, it can be compared to the kinematics of the stars in the disc to estimate another important parameter: the corotation radius.

### 1.3.2 The corotation radius and other important resonances

Stars in the disc of a galaxy will rotate in nearly circular orbits with smaller epicycles when observed from an inertial frame of reference (Binney & Tremaine, 2008). These epicycles are characterised by the epicyclic frequency $\kappa$ and are dependent on the velocity of the star ($v$) and its distance to the centre of the galaxy ($r$, Binney & Tremaine, 2008). These stellar orbits can also be characterised by a pattern speed ($\Omega = v/r$). The epicyclic frequency typically has values $\Omega \lesssim \kappa \lesssim 2\Omega$ (Binney & Tremaine, 2008). However, while the pattern speed of the bar has one value, the pattern speed of stars in the disc changes with the radius of the galaxy (Garma-Oehmichen et al., 2022), as shown in Figure 1.9. These two pattern speeds are important, as they determine where different resonances are located within the galaxy. A resonance occurs when the dynamical parameters $\kappa$, $\Omega$ and $\Omega_{\rm bar}$ are related to each other as follows:

$$l\kappa + m\left(\Omega - \Omega_{\rm bar}\right) = 0 \ , \tag{1.4}$$

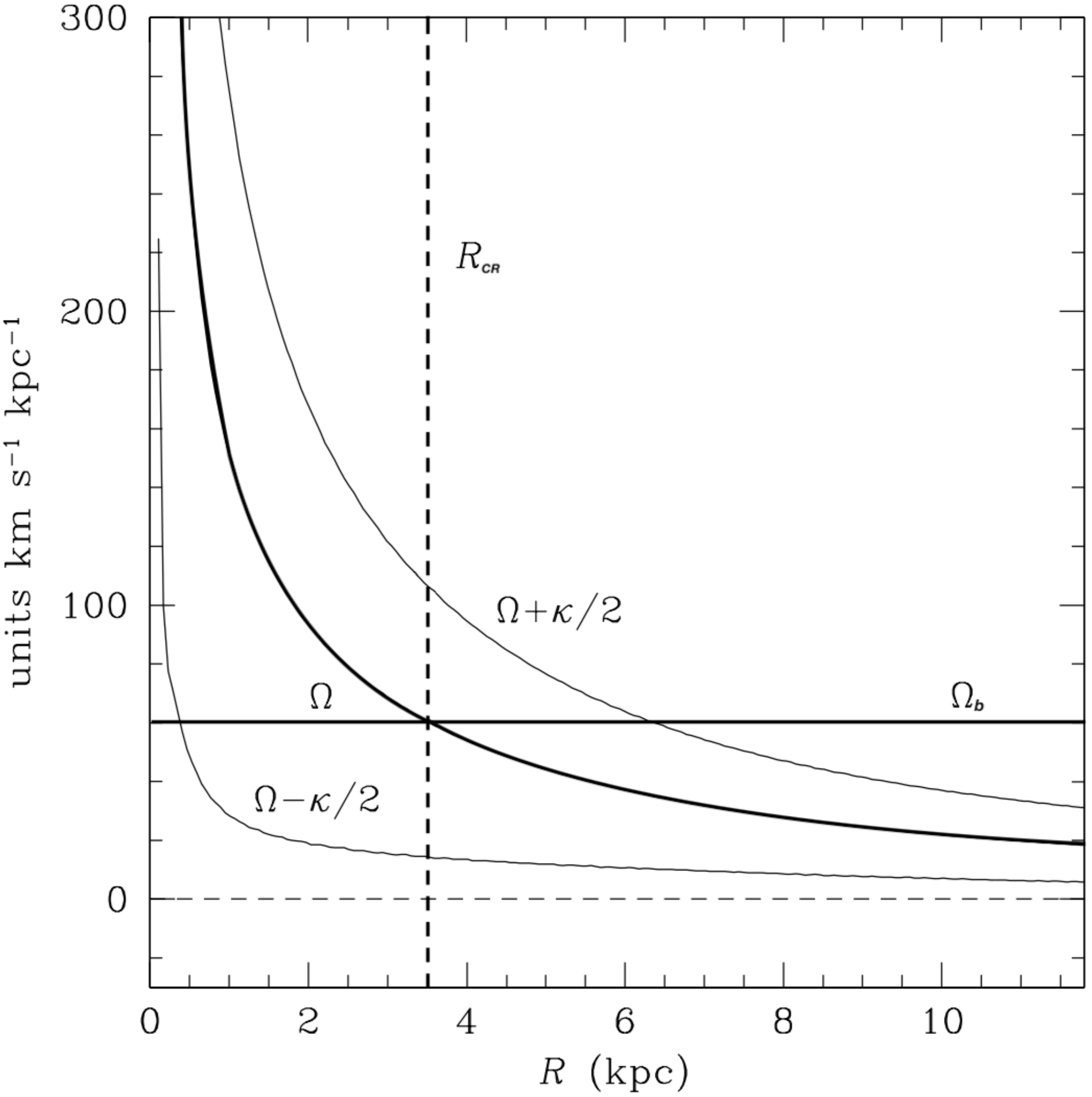

Figure 1.9: This figure shows the pattern speed of the stars in the disc ($\Omega$, thick curved line) against the radius of a typical galaxy model, as well as the behaviour of the $\Omega \pm \kappa/2$ frequencies (thin curved lines). The pattern speed of the bar is shown with the thick horizontal line. The intersection between $\Omega$ and $\Omega_{\text{bar}}$ defines the corotation radius (the vertical dashed line). The inner Lindblad and outer Lindblad resonances occur at the intersection of $\Omega_{\text{bar}}$ and the $\Omega \pm \kappa/2$ curves. This figure is obtained and modified from Binney & Tremaine (2008).

where ($l$:$m$) are a pair of integers (Ceverino & Klypin, 2007). One important resonance is called the inner Lindblad resonance (ILR), which happens when ($l$:$m$) = (-1:2). In this case, Equation 1.4 equals $\Omega_{\rm bar} = \Omega - \kappa/2$. Its counterpart, the outer Lindblad resonance (OLR), occurs when ($l$:$m$) = (1:2) and has $\Omega_{\rm bar} = \Omega + \kappa/2$. Stars in these orbits complete two radial oscillations for every revolution around the centre. When $\Omega$ and $\Omega_{\rm bar}$ are known, the location of these resonances can easily be determined by finding the intersection of the $\Omega_{\rm bar}$ and $\Omega \pm \kappa/2$ curves, as shown in Figure 1.9. These resonances, especially the ILR, are important for the exchange in angular momentum of the bar with its host (Athanassoula, 2003; Ceverino & Klypin, 2007; Kormendy, 2013).

The most important resonance in barred galaxies is called the corotation resonance. This occurs when ($l$:$m$) = (0:1), which changes Equation 1.4 to $\Omega = \Omega_{\rm bar}$. The radius at which the corotation resonance happens is called the corotation radius ($\rm R_{CR}$). Stars orbiting at the corotation radius rotate with a speed equal to the rotation of the bar, i.e. the stars do not move in the rest-frame of the rotating bar. Stars in disc orbits with radii shorter than the corotation radius will rotate faster than the bar, while stars in orbits with radii longer than the corotation radius will rotate slower than the bar. Similarly to the ILR and OLR, it is possible to determine the corotation radius if $\Omega_{\rm bar}$ is known, which is visualised in Figure 1.9. The corotation radius always occurs in between the ILR and OLR. The location of these resonances depend on the bar pattern speed, however, as mentioned above, the bar pattern speed changes as the bar evolves (Debattista & Sellwood, 2000; Athanassoula, 2003; Martinez-Valpuesta et al., 2006; Okamoto et al., 2015), which implies that the location of these resonances and the associated orbits can change over time as well. If the bar pattern speed decreases, then the radius at which these resonances happen will increase (Ceverino & Klypin, 2007). Theoretically, bars cannot grow larger than their corotation radius, as the $x_1$ orbits that make up the bar become unstable at larger radii, so the corotation radius represents a physical upper limit for the length of the bar (Contopoulos, 1980, 1981; Athanassoula, 1992b). The ratio of the corotation radius to the bar radius therefore encodes how close the bar length is to its physical upper limit. This ratio is discussed in more detail in the following section.

### 1.3.3 Tension with $\Lambda$CDM and $\mathcal{R}$

The corotation radius ($\rm R_{CR}$) is often combined with the bar radius ($\rm R_{bar}$) as follows:

$$\mathcal{R} = R_{\rm CR}/R_{\rm bar}\ . \tag{1.5}$$

$\mathcal{R}$ is an important parameter as it has been linked to tensions with ΛCDM and theoretical inconsistencies. For example, $\mathcal{R}$ is used to classify bars into 'slow' ($\mathcal{R} > 1.4$) and 'fast' ($1 < \mathcal{R} < 1.4$). As mentioned above, bars are theoretically not able to grow beyond their corotation radius (Contopoulos, 1980, 1981; Athanassoula, 1992b), which implies that bars with $\mathcal{R} < 1$ should not exist. However, these 'ultrafast' bars have been observed repeatedly (Rautiainen et al., 2008; Aguerri et al., 2015; Font et al., 2017; Guo et al., 2019). For example, Cuomo et al. (2019) find that 44% of their sample are ultrafast bars, while the fraction of ultrafast bars in Garma-Oehmichen et al. (2022) is 39%. More recently, Garma-Oehmichen et al. (2022) have found a lower ultrafast fraction of 11%.

Early observational work typically found that the mean value for $\mathcal{R} \approx 1.2$ (Athanassoula, 1992b; Gerssen et al., 1999; Aguerri et al., 2003). More recent observations with larger sample sizes have shown that most bars have $\mathcal{R} < 1.4$ (Aguerri et al., 2015; Cuomo et al., 2019; Font et al., 2017; Garma-Oehmichen et al., 2020). However, interestingly, simulations predict that at z∼0, the median value of $\mathcal{R}$ should be $\gtrsim 2.5$, which is significantly higher than what is observed (Algorry et al., 2017; Peschken & Łokas, 2019; Roshan et al., 2021b). Simulations predict these high values of $\mathcal{R}$ as they find that bars should slow down due to dynamical friction caused by the DM halo on the bar (Debattista & Sellwood, 1998, 2000; Fragkoudi et al., 2021). This discrepancy has been raised as a tension for the ΛCDM paradigm and much recent work is dedicated to reduce this tension (Algorry et al., 2017; Peschken & Łokas, 2019; Roshan et al., 2021a,b). For example, Fragkoudi et al. (2021) suggests that the DM fraction is too high in simulations, while Beane et al. (2022) show that the gas phase of the disc can act to stabilise the pattern speed and prevent bars from slowing down. Frankel et al. (2022) suggest that simulations do not predict slower bars, but rather shorter bars.

It is also unclear whether ultrafast, fast and slow bars have different effects on their host in terms of inducing star formation and quenching. Finally, simulations have shown that $\mathcal{R}$ is correlated with the formation mechanism of the bar. Bars that are triggered by tidal interactions tend to stay in the slow regime for a longer time, while bars formed by global bar instabilities have lower values for $\mathcal{R}$ (Sellwood, 1981; Miwa & Noguchi, 1998; Martinez-Valpuesta et al., 2016; Gajda et al., 2017; Martinez-Valpuesta et al., 2017). However, it is unclear whether weak and strong bars have significantly different values for $\mathcal{R}$. This implies that studying the kinematics of bars allows us to probe how they are formed, and thus the processes responsible for the evolution of barred galaxies.

## 1.4 Thesis outline

It is clear that secular processes play a major part in galaxy evolution and quenching, alongside mergers (Weinzirl et al., 2009; Kaviraj et al., 2013; Martin et al., 2018; McAlpine et al., 2020; Haslbauer et al., 2022). More specifically, bars seem to be important structures that can drive secular evolution, as they are common (Marinova & Jogee, 2007; Barazza et al., 2008; Aguerri et al., 2009; Buta et al., 2019) and long-lived structures (Elmegreen et al., 2004; Jogee et al., 2004; Shen & Sellwood, 2004; Debattista et al., 2006; Kraljic et al., 2012; Athanassoula et al., 2013) that have the ability to significantly affect their host by redistributing angular momentum and matter (Athanassoula, 1992b, 2003; Villa-Vargas et al., 2010; Athanassoula et al., 2013; Vera et al., 2016; Spinoso et al., 2017). They have also been linked to quenching, as they appear more often among quenched galaxies (Masters et al., 2012; Cervantes Sodi, 2017; Vera et al., 2016; Fraser-McKelvie et al., 2020b). Therefore, it is crucial to understand bars and how they can affect their host galaxies in order to completely understand galaxy evolution.

Nevertheless, several open questions remain. The literature on bars has traditionally been focussed on strong bars, as they are easier to identify and observe, so the role of weak bars is largely uncertain. Are weak bars also preferentially found in quenched galaxies, or is this only the case for strong bars? It is also still ambiguous whether a bar can help to quench a galaxy through secular evolution, or whether it is easier to form a bar in a quenched galaxy. Can additional evidence be found that bars facilitate quenching? If so, is this true for both weak and strong bars? It is also unclear whether weak and strong bars are fundamentally distinct physical phenomena, or whether they are part of a continuum of bar types.

Additionally, the kinematics of bars can quantitatively be described by the pattern speed, corotation radius and $\mathcal{R}$. Are these dynamical parameters similar for weak and strong bars, or do they differ? The pattern speed has been linked to the evolution and lifetime of the bar, which can help address whether both weak and strong bars are long-lived and evolved structures. Meanwhile, $\mathcal{R}$ has been associated with the formation mechanism of the bar, which can help us to probe whether weak and strong bars formed by similar or different mechanisms.

Ultrafast bars are thought to be theoretically impossible, but they have been repeatedly observed. Are ultrafast bars equally prevalent among strong and weak bars? Similarly, the high fraction of observed fast bars has been framed as a tension for $\Lambda$CDM, but it is unknown whether such a high fraction is found for weak and strong bars, or only for strong bars. It is also thought that bars funnel gas to the centre, where it is used to enhance star formation. Does this happen for weak and strong bars? Similarly, the arms of the bar are known to suppress star formation; does this occur in both weak and strong bars? What about evidence for star formation in the bar-end regions? Finally, are there differences in star formation between (ultra)fast and slow bars? These open questions are addressed in this thesis using large samples of strongly and weakly barred galaxies, which did not exist before, identified with Galaxy Zoo (see Section 2.1.6 for more details on the sample selection).

The structure of this thesis is as follows. In Chapter 2, I describe the data used in this thesis, such as SDSS, MaNGA, the DESI Legacy Surveys, ALFALFA and Galaxy Zoo. I also summarise the main samples used in this thesis, as well as the multiple methods that I used. In Chapter 3, I assess whether strong and weak bars have similar effects on their hosts using global galaxy properties. I interpret these results in the context of galaxy quenching and address whether evidence is found for secular evolution in both weakly and strongly barred galaxies. I also test whether strong and weak bars are fundamentally distinct physical phenomena. I study the kinematics of barred galaxies in Chapter 4, by applying the Tremaine-Weinberg method on a sample of weakly and strongly barred galaxies. I test whether there are differences in multiple dynamical parameters between weak and strong bars, which have implications for the formation mechanism and the evolution of the bar. Finally, in this chapter I address the existence of ultrafast bars, as well as the recently claimed tension with $\Lambda$CDM. In order to study how a bar affects their host in more detail, I use resolved data obtained from MaNGA to study star formation indicators in different regions of barred galaxies in Chapter 5. I do this for weak and strong bars, but also for fast and slow bars that were identified in the previous chapter. Finally, the results are discussed and summarised in Chapter 6, where I also elaborate on possible future work that I wish to undertake in order to clarify the remaining questions.

I assume a standard flat cosmological model using $\mathrm{H_0} = 70\ \mathrm{km\,s^{-1}\,Mpc^{-1}}$, $\Omega_\mathrm{m} = 0.3$ and $\Omega_\Lambda = 0.7$ where necessary.

# Chapter 2

# Data and Methods

In this chapter, I will describe all the data and methods used in this thesis. I start with a short description of the Sloan Digital Sky Survey (SDSS) in Section 2.1.1, followed by the Mapping Nearby Galaxies at Apache Point Observatory survey (MaNGA) in Section 2.1.2, the The Dark Energy Spectroscopic instrument (DESI) Legacy Surveys in Section 2.1.3, the Arecibo Legacy Fast ALFA (ALFALFA) survey in Section 2.1.4 and Galaxy Zoo (GZ) in Section 2.1.5. In Section 2.1.6, I review the details of how the two main samples are constructed. Next, I summarise the methods and techniques used throughout this thesis in Section 2.2.

## 2.1 Data

### 2.1.1 Sloan Digital Sky Survey

The Sloan Digital Sky Survey (SDSS, Gunn et al., 1998; York et al., 2000; Blanton et al., 2017a) is a large photometric and spectroscopic survey focussed largely on the northern hemisphere. The data is obtained from Apache Point Observatory (APO), USA, using the Sloan Foundation 2.5-m Telescope and from Las Campanas Observatory (LCO), Chile, using the du Pont Telescope (Abdurro'uf et al., 2022). SDSS commenced observations in 1998 (York et al., 2000), and, astoundingly, by the seventeenth data release (DR17, which is part of SDSS-IV), more than 650 TB of data has been taken cumulatively over the years (Abdurro'uf et al., 2022). Of particular interest to this thesis, SDSS imaged millions of resolved sources over 14,000 deg$^2$, which is more than a third of the Celestial Sphere, in five broad-band filters (*ugriz*, Abazajian et al., 2009; Alam et al., 2015). For point sources, the 50% completeness limit is $r = 22.5$ (Aihara et al., 2011). A small subset of targets, in a region called Stripe 82, were imaged to a depth of $r = 24.6$ (Jiang et al., 2014). Accompanying spectroscopic data exists for most galaxies with an $r$-band Petrosian magnitude of $r \leq 17.77$. However, the fibres used could not be positioned closer together than 55 arcsec. This causes the spectroscopic sample to be incomplete (about ~6% of the targets could not be observed spectroscopically), which was especially problematic for close galaxy pairs (Strauss et al., 2002). The fibres have a diameter of 3 arcsec and are connected to spectrographs that cover a wavelength range of 3800-9200 Å and have a resolution, $\lambda/\Delta\lambda$, between 1850 - 2200 (Strauss et al., 2002). Data from both the photometric and spectroscopic surveys from SDSS DR16 (Ahumada et al., 2020) is used extensively in this thesis.

There are many data products derived from SDSS data. One particularly useful one is the Max Planck Institute for Astrophysics and the Johns Hopkins University (MPA-JHU) value added catalogue (VAC, Kauffmann et al., 2003; Brinchmann et al., 2004; Tremonti et al., 2004). The MPA-JHU catalogue provides stellar mass and star formation rate (SFR) estimates for all galaxies that are in SDSS DR7 (Abazajian et al., 2009). In this thesis, I use the median of the calculated likelihood distributions of stellar mass and SFR. The likelihood distributions of the stellar mass in MPA-JHU are derived from fits to a large grid of star formation histories (SFHs) using photometry from SDSS. These SFHs are based on stellar population synthesis models described by Bruzual & Charlot (2003). Alternative mass estimates that are derived from spectroscopy are also available (Kauffmann et al., 2003), but these estimates are only valid for the centre of the galaxy. This is because the fibre only covers the central 3 arcsec, so additional assumptions need to be made in order to extrapolate them to the rest of the galaxy. Photometric stellar mass estimates are used in this thesis in favour of spectroscopic stellar mass estimates for this reason.

To calculate the SFR, MPA-JHU first classifies galaxies into star forming, AGN or composite using a BPT diagram (Baldwin et al., 1981). The SFR for star forming galaxies is calculated using emission lines and fitting models described by Charlot & Longhetti (2001). The SFR for non-star forming galaxies is inferred using $\mathrm{D_n}4000$ or a conversion factor based on the H$\alpha$ emission line (Brinchmann et al., 2004). These estimates are valid within the 3 arcsec fibre and are called the fibre SFRs.

A correction, called the aperture correction, is needed in order to extrapolate the fibre SFRs to the rest of the galaxy and hence to obtain global SFRs. The original aperture correction applied by MPA-JHU involved determining the empirical relationship between the specific SFR and the ($g$-$r$) and ($r$-$i$) colours inside the fibre. This relationship was then applied to the photometry of the regions outside the fibre to estimate the SFR in the entire galaxy. However, Salim et al. (2007) found that this method introduced significant biases, as it would overestimate the SFR of galaxies with lower SFRs. This is because the empirical relationship between the specific SFR and the ($g$-$r$) and ($r$-$i$) colours inside the fibre is not applicable to some regions outside the fibre. MPA-JHU now avoids these biases by performing an aperture correction by fitting the photometry outside the fibre to stochastic models, similarly to Salim et al. (2007).

### 2.1.2 MaNGA survey

The Mapping Nearby Galaxies at APO (MaNGA) survey (Bundy et al., 2015) is part of SDSS-IV (Blanton et al., 2017b). MaNGA used the Baryon Oscillation Spectroscopic Survey (BOSS) spectrograph, which has a a wavelength coverage of 3600 - 10,000 Å and a resolution of R $\sim$ 2000 (Smee et al., 2013), on the 2.5m Sloan Telescope at APO (Gunn et al., 2006). The great advantage of MaNGA is that it uses integral field units (IFUs), which are able to acquire multiple spectra over the entire area of the galaxy. Each IFU consists of 19-127 individual optical fibers, which are stacked hexagonally (Drory et al., 2015). MaNGA consists of three samples: the Primary sample (47% of MaNGA), the Secondary sample (37% of MaNGA) and the Colour-Enhanced supplement (16% of MaNGA). 80% of the galaxies in the Primary sample are covered to 1.5 effective radii ($R_e$), while 80% of the galaxies in the Secondary sample are covered to 2.5 $R_e$. The Colour-Enhanced supplement targeted galaxies to fill in underrepresented regions in the colour-magnitude diagram, such as high luminosity blue galaxies and low luminosity red galaxies. The targets for MaNGA were selected to have a flat stellar mass distribution (approximated by the absolute $i$-band magnitude). Additionally, it was decided to aim for roughly uniform radial coverage for all targets. This implies that larger and more massive galaxies targeted by MaNGA should have the same angular size as smaller low mass galaxies, which is achieved by sacrificing having identical physical spatial resolution across stellar mass. Finally, targets were selected from the SDSS DR7 spectroscopic survey, as accurate redshift measurements and photometry were needed (Wake et al., 2017). MaNGA has observed $\sim$10,000 galaxies that have redshifts between $0.02 \leq z \leq 0.1$ and stellar masses typically between $10^9 \leq M_*[M_\odot h^{-2}] \leq 10^{11}$ (Wake et al., 2017). Every target in MaNGA has a unique identifier called the plate-ifu, which is a combination of the IDs of the plate and IFU used. A dithering pattern is used to ensure that the whole target is covered uniformly by the hexagonally stacked fibres (Law et al., 2015).

The raw spectra from MaNGA are reduced using the Data Reduction Pipeline (DRP, Law et al., 2016, 2021). The DRP has two distinct stages: for every exposure, the first stage performs a flatfield correction, sky subtraction and a flux and wavelength calibration. Additionally, it identifies cosmic rays and estimates the uncertainty in each pixel. The second stage combines all individual dithered exposures for any given target with astrometric information into a final data cube. Then, the data cubes are processed in the Data Analysis Pipeline (DAP, Westfall et al., 2019) to generate easy-to-use maps of stellar kinematics, gas kinematics and quantities derived from emission and absorption lines. In the DAP, neighbouring spaxels are binned together to achieve a SNR $\geq 10$ in the $g$-band using the Voronoi binning algorithm (Cappellari & Copin, 2003). In this thesis, I use the Voronoi binned maps, unless otherwise specified. The spectra are subsequently analysed with the penalized Pixel-Fitting (pPXF) method (Cappellari & Emsellem, 2004; Cappellari, 2017), which provides best-fit properties of the emission lines and continuum. The Medium resolution INT Library of Empirical Spectra (MILES) stellar-template library (Sánchez-Blázquez et al., 2006; Falcón-Barroso et al., 2011) is used to model the stellar continuum. More information about the observing strategy, survey design, data reduction process, sample selection and the data analysis pipeline can be found in Law et al. (2015, 2016); Yan et al. (2016); Wake et al. (2017); Belfiore et al. (2019); Westfall et al. (2019); Law et al. (2021). For the work in this thesis the MaNGA data was accessed using the *Marvin* software (Cherinka et al., 2019).

Stellar mass and SFR estimates for the MaNGA galaxies are calculated by Pipe3D (Sánchez et al., 2016a,b, 2018). The SFR estimates are based on the H$\alpha$ luminosities in every spaxel, that are dust-corrected using the H$\alpha$/H$\beta$ ratio. However, one caveat is that Pipe3D does not account for H$\alpha$ emission caused by AGN, which may cause it to overestimate the SFR. The stellar mass estimates in Pipe3D are calculated by performing a detailed analysis of the spectra in each spatial bin using single stellar populations (SSPs). An SSP is defined as a collection of stars that are born simultaneously with a given metallicity and initial mass function (Sánchez et al., 2016a). Pipe3D uses a Monte-Carlo approach to find the best linear combination of multiple SSPs for each spectrum, while accounting for non-linear effects induced by kinematics and dust attenuation. This final stellar population model is used to derive the stellar mass (Sánchez et al., 2016a,b).

### 2.1.3 The DESI Legacy Surveys

The Dark Energy Spectroscopic instrument (DESI) Legacy Imaging Surveys are a combination of three unique projects: the Dark Energy Camera Legacy Survey (DECaLS), the Beijing-Arizona Sky Survey (BASS) and the Mayall z-band Legacy Survey (MzLS), which cover $\sim 14,000$ deg$^2$ of the sky in three optical bands ($g$, $r$ and $z$, Dey et al., 2019). These three surveys have very similar imaging standards, which means that they provide similar images. The DESI Legacy Imaging Surveys provide targets for the DESI spectroscopic survey. DECaLS uses the 4m Blanco telescope at the Cerro Tololo Inter-American Observatory with the Dark Energy Camera (DECam, Flaugher et al. 2015). It has the widest footprint in the sky of the three surveys, with a total of $\sim 9,000$ deg$^2$ and images all three $grz$ bands. The PSF depth (defined in Dey et al. (2019) as the median $5\sigma$ detection limit in AB mag for a point source in individual images) for the $g$, $r$ and $z$ bands of DECaLS is 23.95, 23.54 and 22.50, respectively. BASS uses the 90Prime camera (Williams et al., 2004) at the Bok 2.3m telescope located at the Kitt Peak Observatory. BASS images only in the $g$ and $r$ optical bands, with PSF depths of 23.65 and 23.08, respectively, and has a footprint of $\sim 5,000$ deg$^2$. Finally, MzLS uses the Mosiac-3 camera (Dey et al., 2016) at the Mayall Telescope, which is also located at the Kitt Peak National Observatory. MzLS observes the same footprint in the sky as BASS, but complements BASS with observations in the $z$ band, with a PSF depth of 22.60. The sources in the DESI Legacy Surveys are extracted using the *Tractor* (Dey et al., 2019). The complete footprint is analysed in 0.25 deg x 0.25 deg patches and in the latest data release of the Legacy Surveys, DR9, there are approximately 2.0 billion unique sources. Every source is fit with multiple parametric light profiles, such as a PSF and multiple variations on the Sérsic profile (see Equation 1.1). These include disc-like profiles (an exponential profile and a round exponential profile with variable radius) and spheroid-like profiles (a de Vaucouleurs profile). The best-fit model is assigned to the source, which can be used to discern stars from galaxies.

### 2.1.4 ALFALFA

The Arecibo L-band Feed Array (ALFA) is used in the Arecibo Legacy Fast ALFA (ALFALFA) catalogue of extragalactic HI sources used the 305m Arecibo telescope in Puerto Rico and has detected ~31,500 sources with redshifts up to $z < 0.06$ (Giovanelli et al., 2005; Haynes et al., 2011, 2018). The rest-frequency of the atomic hydrogen HI line is at 1,420.4 MHz (or a wavelength of 21 cm). ALFALFA uses ALFA, which has

7 beams and is sensitive to radio frequencies in the L-band (1,225–1,525 MHz). The angular resolution is ∼3.5 arcmin in the L-band, which is typically high enough to correctly identify the optical counterpart of the sources. The ALFALFA catalogue of extragalactic HI sources has a footprint that approximately corresponds to $07^{\mathrm{h}}30^{\mathrm{m}} <$ R.A. $< 16^{\mathrm{h}}30^{\mathrm{m}}$ and $0° <$ Dec. $< +36°$ for the northern hemisphere and $22^{\mathrm{h}} <$ R.A. $< 03^{\mathrm{h}}$ and $0° <$ Dec. $< +36°$ for the southern hemisphere, which corresponds to ∼7000 $\mathrm{deg}^2$, although there is some minor fringing around the edges of the footprint (Haynes et al., 2018). The HI gas masses can be calculated from the HI line flux density using:

$$\mathrm{M_{HI}[M_{\odot}]} = 2.356 \times 10^5\ \mathrm{D}^2\ \mathrm{S}\ , \tag{2.1}$$

where D is the luminosity distance to the galaxy in Mpc and S is the the integrated HI line flux density in Jy km $\mathrm{s}^{-1}$. Unfortunately, not all extragalactic sources have detections, as the chance of detection depends on the width of the HI profile, the integrated HI line flux and the sensitivity of the detectors (Haynes et al., 2011, 2018). However, it is possible to calculate an upper limit for these non-detections by rearranging Equation 4 of Haynes et al. (2018):

$$\mathrm{S} = \mathrm{SNR} \times \mathrm{RMS} \times \mathrm{W}_{50}/\sqrt{\mathrm{w_{smo}}}\ , \tag{2.2}$$

where SNR is the signal-to-noise ratio, RMS is the RMS noise, $\mathrm{W}_{50}$ is the linewidth of the target (assumed to equal 200 km $\mathrm{s}^{-1}$) and $\mathrm{w_{smo}}$ is a smoothing width (which equals $\mathrm{W}_{50}/20$). It is assumed that SNR = 4.5, as the rate of detections drops quickly below this value, and the RMS is extracted from each individual spectrum. The spectra have a spectral resolution of 10 km $\mathrm{s}^{-1}$ at the position of the non-detection (Haynes et al., 2018). The final HI gas mass upper limit can be calculated by using the result from Equation 2.2 in Equation 2.1. Because of the dependence of the upper limit on the distance of the galaxy, targets that are farther away will generally have higher upper limits than nearby galaxies. It is assumed that every target without a gas measurement within the ALFALFA footprint is a non-detection. The upper limits for these non-detections were calculated by a co-author of Géron et al. (2021).

### 2.1.5 Galaxy Zoo

Determining the morphology of galaxies is a crucial, yet time-consuming process if your sample size is large. Galaxy Zoo (GZ) provides a solution to this problem by inviting citizen scientists to help classify targets. The first iteration of Galaxy Zoo (GZ1) was an immense success. More than 100,000 volunteers classified ∼900,000 galaxies (Lintott et al., 2008, 2011) based on images obtained from SDSS (Gunn et al., 1998; York et al., 2000; Blanton et al., 2017a). The volunteers were asked to identify the target as an elliptical galaxy, a spiral galaxy, a merger or as a star. The classifications in GZ1 were also corrected (or 'debiased') for classification bias, which occurs when the observed morphology changes as a function of redshift, independent of any real change in morphology. The cause for this is that galaxies at higher redshifts, on average, are more difficult to classify accurately, as they appear smaller and fainter (Bamford et al., 2009). A much more detailed classification scheme was used in the next version, Galaxy Zoo 2 (GZ2, Willett et al., 2013). This time, volunteers were asked to navigate through an elaborate decision tree, which allowed them to identify bars, bulges, and much more. The primary sample of GZ2 was again sourced from SDSS and consisted of the ∼25% brightest resolved galaxies in the SDSS North Galactic Cap region, which had an apparent r-band magnitude, $m_r$, greater than 17. Over 300,000 galaxies were classified using more than 16 million classifications. Willett et al. (2013) have shown that volunteer classifications from GZ2 agree well with previously existing expert classifications (Nair & Abraham, 2010a; Baillard et al., 2011) and automated classifications (Huertas-Company et al., 2011). One of the interesting features of GZ2 is that it asks volunteers to identify bars. These volunteer bar classifications agree well with the expert bar classifications from the catalogue of visual morphological classifications of Nair & Abraham (2010a), although Willett et al. (2013) show that the bars that are found in GZ2 correspond mostly to the intermediate and strong bars of Nair & Abraham (2010a), while not identifying their weak bars. The GZ2 bar classifications have been extensively used to study bars (Hoyle et al., 2011; Masters et al., 2011, 2012; Skibba et al., 2012; Cheung et al., 2013; Melvin et al., 2014; Simmons et al., 2014; Cheung et al., 2015; Galloway et al., 2015; Kruk et al., 2017, 2018, 2019). However, GZ2 did not attempt to quantify bar strength, it only asked whether the galaxy had one.

The next iteration of Galaxy Zoo was called Galaxy Zoo DECaLS (GZ DECaLS, Walmsley et al., 2022). Around 314,000 galaxies were classified using 7.5 million individual classifications. In GZ DECaLS, the images were sourced from the DECaLS survey, which is part of the larger DESI imaging surveys (Dey et al., 2019). Technically, GZ DECaLS consists of three parts: GZD-1, GZD-2 and GZD-5, which used images from DECaLS DR1, DR2 and DR5, respectively. Most of the galaxies in GZ DECaLS are in GZD-5. DECaLS has deeper and more detailed imaging than SDSS (r = 23.6 and r = 22.5, respectively, Abazajian et al., 2009; Dey et al., 2019), which

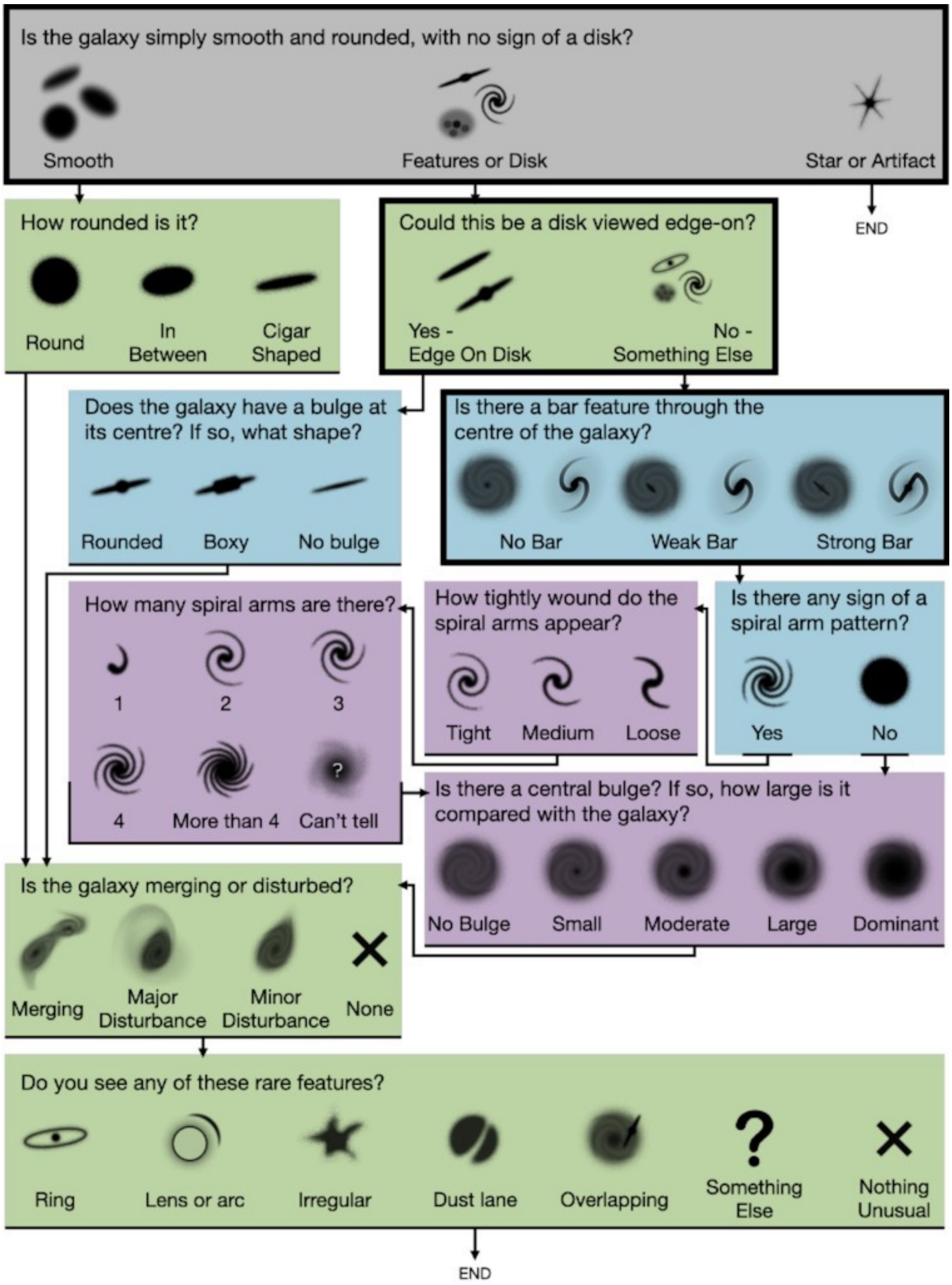

Figure 2.1: The decision tree used for most galaxies in GZ DECaLS. The different colours represent branching in tree and how many dependent questions each question has. Questions coloured in purple have three dependent questions, blue two, green one and grey zero. The path to the bar question is highlighted with black contours. The most important changes compared to the tree in GZ2 are the updated bulge and bar question, as well as the new question about mergers. This figure was adapted from Walmsley et al. (2022).

allows us to probe more detailed structures. Features that were previously undetectable, such as weak bars and tidal features, could now be classified with relative ease. Despite this deeper imaging, GZ DECaLS only included targets that were also in SDSS DR11, which implies that the magnitude limit of GZ DECaLS equals that of SDSS ($m_{\mathrm{r}} = 17.77$, Strauss et al., 2002). The deeper imaging of GZ DECaLS allowed Walmsley et al. (2022) to update the decision tree for GZ DECaLS. The relevant change for this thesis is that GZD-5 not only asked the volunteers whether there was a bar, but also whether the bar is weak or strong, which allows us to probe the strength of the bar. The decision tree of GZD-5 is shown in Figure 2.1. The volunteers had access to a field guide during classification, which provided them with more information and examples about the questions they were asked. The field guide gave a short description of strong bars and weak bars, as well as a couple examples of strongly and weakly barred galaxies using images from SDSS and DESI. Screenshots of the field guide are shown in Figures 2.2 and 2.3. In short, the volunteers were told that strong bars '*extend across a large fraction of the galaxy*' while weak bars are '*smaller and fainter relative to the galaxy*'.

The decision tree shown in Figure 2.1 can be used to explain nomenclature unique to Galaxy Zoo. Every step in the decision tree is called a 'task', which is made up of a 'question' and multiple possible 'answers'. The total number of volunteers that answered a specific question, e.g. 'Is there a bar feature through the centre of the galaxy?', is noted as $N_{\mathrm{bar}}$. Additionally, the fraction of people that voted for a particular answer for a certain question, e.g. 'Strong Bar' for the bar question, is noted as $p_{\mathrm{strong\ bar}}$ and is called the vote fraction. Additionally, please note the different branching options of the tree. A volunteer can only be asked the bar question if they answered *'Is the galaxy simply smooth and rounded, with no sign of a disc?'* with *'Features or Disc'* and *'Could this be a disc viewed edge-on?'* with *'No - Something Else.'*.

Another big change in GZ DECaLS was the introduction of machine classifications. An ensemble of Bayesian convolutional neural networks were trained on the classifications made by humans in GZD-5. An active learning system was used to focus volunteer efforts on targets which are most informative for the neural network. The most informative targets were seen by at least 30 volunteers, while the remaining galaxies were seen by $\sim$5. Walmsley et al. (2022) show that these machine classifications are $\sim 99\%$ accurate when compared to confident volunteer classifications (which are defined as volunteer classifications with vote fractions below 0.2 or above 0.8).

**Strong Bar**

Strong bars are clearly visible straight features. They extend across a large fraction of the galaxy, and they're bright enough to be pretty obvious. They are usually in the center of the galaxy, but not always.

Figure 2.2: A screenshot from the field guide from GZ DECaLS that the volunteers have access to during classification. This section of the field guide gives a brief description of strong bars and provides a few examples of strongly barred galaxies using images from SDSS and DESI.

**Weak Bar**

Weak bars are the little siblings of strong bars. They are the same shape, but smaller and fainter relative to the galaxy. Since they don't stand out quite as much they can look a little more oval, but they are still longer in one direction than the other.

Figure 2.3: A screenshot from the field guide from GZ DECaLS that the volunteers have access to during classification. This section of the field guide gives a brief description of weak bars and provides a few examples of weakly barred galaxies using images from SDSS and DESI.

The next and currently latest version of Galaxy Zoo is called Galaxy Zoo DESI (GZ DESI, Walmsley et al., in prep.). GZ DESI expands on GZ DECaLS by also including the other DESI surveys from DESI DR8, such as BASS and MzLS (see Section 2.1.3, Dey et al., 2019). Additionally, GZ DESI includes fainter ($m_\mathrm{r} = 19.0$) and higher redshift ($z = 0.4$) targets than GZ DECaLS. It must also be noted that GZ DESI consists only of automated classifications, as it takes full advantage of the deep learning models developed in Walmsley et al. (2022). The models are trained on volunteer classifications obtained in all the GZ DECaLS subsections (GZD-1, GZD-2 and GZD-5), as well as new volunteer classifications of galaxies based on images from DESI DR8. There are 8.67 million galaxies with automated classifications provided in GZ DESI. There were no changes made to the decision tree shown in Figure 2.1 that are relevant for this thesis. At the time of writing, GZ DESI has been completed, but has not yet been made publicly available.

As part of my DPhil, I helped with the creation of the GZ DECaLS and GZ DESI catalogues. My responsibilities included downloading the appropriate images from DECaLS and DESI, uploading them to the Galaxy Zoo platform and aggregating the volunteer classifications into a final catalogue. The GZ DECaLS and GZ DESI catalogues are presented in Walmsley et al. (2022) and Walmsley et al. (in prep.), respectively.

Similarly, I led the development of a value added catalogue (VAC) for MaNGA, where morphological classifications from Galaxy Zoo are provided for almost all targets in MaNGA, which was released as part of SDSS-IV DR17 (Abdurro'uf et al., 2022). We provide volunteer classifications from multiple iterations of Galaxy Zoo (Lintott et al., 2008, 2011; Willett et al., 2013) for 9,622 galaxies in MaNGA and machine classifications from GZ DECaLS (Walmsley et al., 2022) for 3,620 galaxies in MaNGA. The VAC can be accessed here[1].

### 2.1.6 Defining the main samples

#### 2.1.6.1 The GZ DECaLS-SDSS sample

There are two main samples in this thesis. The first one is called the GZ DECaLS-SDSS sample, which is used in Chapter 3 and is largely a combination of SDSS data (see Section 2.1.1) and the volunteer classifications of GZ DECaLS (so not the automated machine classifications, see Section 2.1.5). I opted to work with the version of GZ DECaLS with the most updated decision tree, which is GZD-5. Additionally,

---

[1] `sdss4.org/dr17/data_access/value-added-catalogs/`

I only used galaxies that had received more than 30 total votes in the final catalogue to guarantee reliable classifications. This threshold was put in place because $\sim$76% of galaxies in GZ DECaLS GZD-5 were only seen by $\sim$5 volunteers in GZ DECaLS in order to speed up the training process of the automated classifications (see Section 2.1.5 and Walmsley et al. 2022 for more details). However, the vote fractions of galaxies with such a small number of volunteer vote classifications are likely to be untrustworthy, so this threshold was used in order to avoid contaminating the sample with galaxies with unreliable morphological classifications and to guarantee that the resultant conclusions are robust. This resulted in a sample size of 57,562 targets. This set of galaxies with more than 30 votes is a randomly sampled subset from the entire GZ DECaLS sample, so no biases are introduced by using this threshold, except for one caveat. Due to the active learning scheme employed by GZ DECaLS, a minority (6,939 in total) of the galaxies with more than 30 votes were uploaded specifically because they were considered most informative for the neural network to learn from during the training of the automated classifications (Walmsley et al., 2022). However, the results presented in this thesis that use the GZ DECaLS-SDSS sample remained qualitatively the same when these specific galaxies are excluded.

I also cross-matched the targets to MPA-JHU for stellar mass and SFR estimates, and ALFALFA (I include the detections and non-detections, see Section 2.1.4) for gas mass estimates. The cross-match against ALFALFA substantially lowered the sample size to 3,521 galaxies. In order to minimise selection effects, additional thresholds are placed on the redshift ($0.01 < z < 0.05$, spectroscopic redshift estimates are from SDSS) and absolute r-band magnitude ($M_{\rm r} < -18.96$, dereddened magnitude estimates are obtained from DECaLS), which results in a volume-limited sample with 2,391 galaxies. Finally, I want to only work with galaxies that have robust bar classifications. Due to the decision tree nature of the classifications in GZ, this is achieved by applying additional limits on the percentage of people that voted that the galaxy has 'features or a disc' ($p_{\rm features/disc}$), the percentage of people that voted that the galaxy was not edge-on ($p_{\rm not\ edge\text{-}on}$) and the number of people that were asked the bar question ($N_{\rm bar}$), as advised in Section 3.3 of Willett et al. (2013). These thresholds aim to remove galaxies with high vote fractions for the preceding responses, but are unreliable due to a low total number of votes. For example, if only one person voted for the question *'Could this be a disc viewed edge-on?'*, then $p_{\rm not\ edge\text{-}on}$ for that galaxy will equal either 1.0 or 0.0, but this classification is not reliable due to the low total number of votes. As explained in Willett et al. (2013), these thresholds are calculated by finding the lowest value for the vote fraction of the

Table 2.1: The vote fractions of the bar question of each target are used to determine the bar type of the galaxy using the scheme shown here. The possible bar types are: no bar, weak bar or strong bar.

| Condition 1 | Condition 2 | Result |
|---|---|---|
| $p_{\text{strong bar}} + p_{\text{weak bar}} < 0.5$ | N/A | No bar |
| $p_{\text{strong bar}} + p_{\text{weak bar}} \geq 0.5$ | $p_{\text{strong bar}} < p_{\text{weak bar}}$ | Weak bar |
| $p_{\text{strong bar}} + p_{\text{weak bar}} \geq 0.5$ | $p_{\text{strong bar}} \geq p_{\text{weak bar}}$ | Strong bar |

previous question, while still keeping >99% of targets in the sample with $N_{\text{votes}} \geq N_{\text{crit}}$, where $N_{\text{crit}} = 20$ is chosen. However, the thresholds quoted in Willett et al. (2013) are based on GZ2, so new values are calculated based on GZ DECaLS. The new thresholds are: $p_{\text{features/disc}} \geq 0.27$ and $p_{\text{not edge-on}} \geq 0.68$ for $N_{\text{bar}} \geq 20$. These thresholds will effectively limit the sample to disc galaxies which are not edge-on that could contain bars. It is worth noting that although it is only required that $p_{\text{features/disc}} \geq 0.27$, the actual value for $p_{\text{features/disc}}$ will be significantly higher for most targets: the median $p_{\text{features/disc}}$ of the final sample is equal to 0.82. Applying these thresholds further reduced the sample size to a final total of 1,867 galaxies.

Every galaxy in this sample was assigned one of three bar types: strong, weak or no bar. This was done by comparing the relevant vote fractions. If $p_{\text{strong bar}} + p_{\text{weak bar}} < 0.5$ (i.e. more than half of the volunteers voted that the galaxy had no bar), then the galaxy was classified as unbarred. If this condition was not met and if $p_{\text{strong bar}} \geq p_{\text{weak bar}}$, then the galaxy had a strong bar. Otherwise, it has a weak bar. This classification scheme is summarised in Table 2.1. This approach was chosen over a simple majority vote, as the vote for 'a bar' was diluted by providing two separate options. It was found that, using this scheme, 15.5% of the galaxies (289/1,867) have a strong bar and 28.1% (525/1,867) have a weak bar, which results in a total barred fraction of 43.6%. This is in general agreement with the literature, as total bar fractions of 44%-52% are typically found in studies using optical wavelengths at low redshifts (Marinova & Jogee, 2007; Barazza et al., 2008; Aguerri et al., 2009; Buta et al., 2019). As noted in Section 1.2, bar fractions found in GZ2 are usually lower (between 23.6 - 29.4%; Masters et al., 2011; Skibba et al., 2012; Cheung et al., 2013) than the bar fractions found in other studies. This confirms that the bars found in GZ2 are mostly strong bars, as was suspected, since the inclusion of weak bars removes this discrepancy. A summary of this sample can be found in the first row of Table 2.2 and is used in Chapter 3.

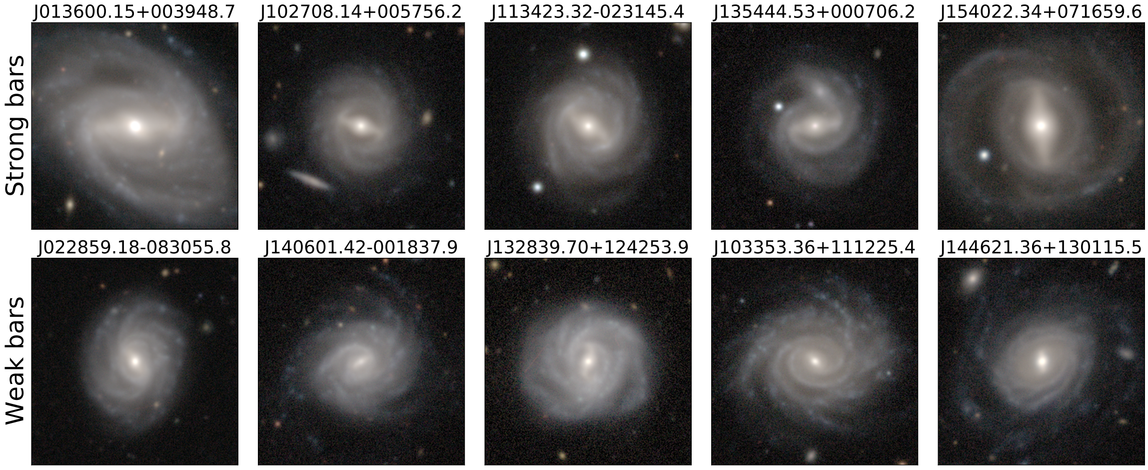

Figure 2.4: DECaLS postage stamps (72x72 arcsec) of five randomly selected galaxies with high strong bar vote fractions ($p_{\text{strong bar}} > 0.6$, top row) and weak bar vote fractions ($p_{\text{weak bar}} > 0.6$, bottom row) and with high Petrosian radii (> 18 arcsec) in GZ DECaLS. The IAU names are displayed above every target. The main difference between the strong and weak bars appears to be the bar length and strength, as is expected from instructions given to volunteers.

Table 2.2: Summary of the three samples used in this thesis. For every sample, the sample size is listed, as well as the total number and fraction of strongly barred galaxies, weakly barred galaxies and galaxies without bars. The first sample, GZ DECaLS-SDSS, is used in Chapter 3 and is described in Section 2.1.6.1. The GZ DESI-MaNGA sample is used in Chapter 5 and described in Section 2.1.6.2. Finally, the TW sample is used in Chapter 4 and described in Section 2.2.4.5.

| Name | Sample size | Strong bars | Weak bars | No bar |
|---|---|---|---|---|
| GZ DECaLS-SDSS | 1,867 | 289 (15.5%) | 525 (28.1%) | 1,053 (56.4%) |
| GZ DESI-MaNGA | 2,125 | 363 (17.0%) | 796 (37.5%) | 966 (45.5%) |
| TW | 225 | 122 (54.2%) | 103 (45.8%) | 0 (0%) |

To make sure that the bar classifications are robust and consistent, the bar types in this sample are compared to bar types obtained from GZ2. A total of 1,160 galaxies overlap in both samples after applying the same thresholds to the raw vote fractions of GZ2. I opt to use the raw vote fractions from GZ2, as opposed to the debiased ones, as the votes from GZ DECaLS are also not debiased. The bar fraction from GZ2 is plotted, as well as the strong bar, weak bar and total bar fractions from GZ DECaLS, against redshift in the left panel of Figure 2.5. The bars in GZ2 were identified using the commonly used threshold of $p_{\text{bar, GZ2}} > 0.5$ (Masters et al., 2011, 2012; Cheung et al., 2015; Kruk et al., 2017, 2018). It is very clear that GZ DECaLS identifies many more bars compared to GZ2. This is unsurprising, as the deeper imaging provided by DECaLS should reveal structures previously hidden in SDSS. Additionally, the updated decision tree in GZ DECaLS allows for more detailed classification. The right panel of Figure 2.5 shows the GZ2 vote fraction $p_{\text{bar, GZ2}}$ plotted against the different GZ DECaLS bar fractions. It is clear that the total GZ DECaLS bar fraction increases with $p_{\text{bar, GZ2}}$, which can be expected. However, interestingly, the GZ DECaLS weak bar fraction rises initially, but drops again at higher values for $p_{\text{bar, GZ2}}$. This behaviour can be explained by assuming that, as a bar becomes stronger, a user in GZ2 is more likely to vote that it is a bar. Due to the more shallow imaging used in GZ2, some volunteers are not as confident that a weak bar is a bar, as it might not be clearly visible in SDSS.

The vertical dashed line is placed at $p_{\text{bar, GZ2}} = 0.5$, which is a threshold commonly used to detect bars in GZ2 (Masters et al., 2011, 2012; Cheung et al., 2013, 2015; Kruk et al., 2017, 2018). It is clear that most strongly barred galaxies in GZ DECaLS were already identified in GZ2. Conversely, most of the new bars found in GZ DECaLS are weak bars, which is what is expected. This is what is typically found in the literature as well: previous work using GZ2 data noted that their barred sample mainly consisted of strongly barred galaxies (Masters et al., 2011; Cheung et al., 2013, 2015; Kruk et al., 2017, 2018). Masters et al. (2012) noted that >90% of the strong and intermediate bar types from Nair & Abraham (2010a) have $p_{\text{bar, GZ2}} > 0.5$.

To conclude the comparison with GZ2: GZ DECaLS identifies more barred galaxies in compared to GZ2, due to deeper imaging and an improved decision tree. Most bars identified in GZ2 turn out to be strong bars, while most of the newly identified bars in GZ DECaLS are weak bars. The use of the updated decision tree in GZ DECaLS over the one in GZ2 is a great improvement. The new tree allows for a more detailed classification, which helps to identify more bars (most of which are weak) and to probe the strength of the bar.

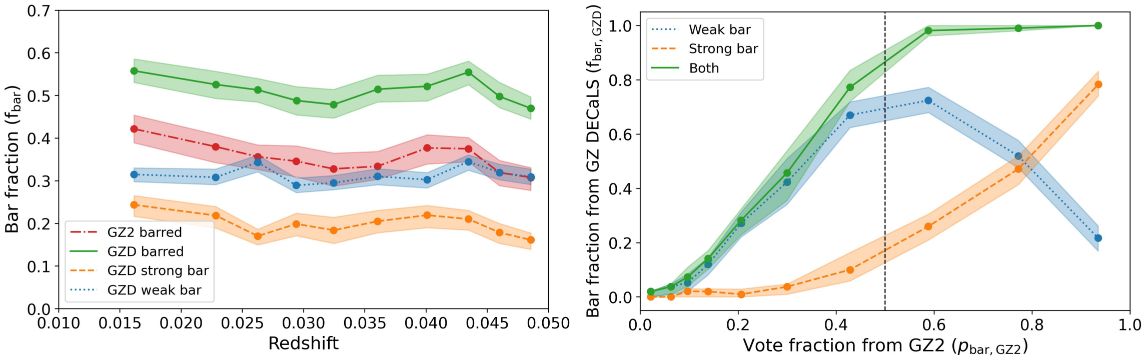

Figure 2.5: The classifications from GZ DECaLS are compared to GZ2. In the left panel, all the different bar fractions are plotted against redshift. All the galaxies are binned in equal-sized bins. In the right panel, I plot the GZ2 vote fraction ($p_{\text{bar, GZ2}}$) against different bar fractions in GZ DECaLS ($f_{\text{bar, GZD}}$). The shaded regions show the $3\sigma$ region after bootstrapping the data 10,000 times and retaining 90% of the data for each iteration. The vertical dashed line is placed at $p_{\text{bar, GZ2}} = 0.5$, which is a threshold commonly used to separate barred and unbarred galaxies in GZ2 (e.g. Masters et al., 2011, 2012; Cheung et al., 2013, 2015; Kruk et al., 2017, 2018). This shows that GZ DECaLS finds more bars than GZ2, with most of the newly identified bars are weak bars.

The classifications from GZ DECaLS-SDSS sample are also compared against the catalogue of visual morphological classifications of Nair & Abraham (2010a). Please note that Nair & Abraham (2010a) use images from SDSS, while deeper DECaLS images were used in GZ DECaLS. There are a total of 589 overlapping galaxies in both samples. Nair & Abraham (2010a) classify bars into being strong, intermediate, weak, ansae, peanut, nuclear, unsure or no bar. However, the ansae, peanut, nuclear and unsure categories are not common and in this comparison, they were combined into one category called ‘others’. The comparison is shown in Table 2.3. Although this did not occur frequently, it is worth clarifying that a single galaxy could belong to multiple categories in Nair & Abraham (2010a), while this is not possible in the classification scheme used here. The two samples largely agree with each other. 25 of the 27 galaxies classified by Nair & Abraham (2010a) as strongly barred are also identified in GZ DECaLS as being strongly barred. Conversely, 306 out of 338 of the galaxies GZ DECaLS determined as being unbarred were also classified by Nair & Abraham (2010a) as having no bar. There is a small subset of galaxies (23 in total, which are shown in Figure 2.6) that GZ DECaLS classifies as being strongly barred, while they are classified as being unbarred in Nair & Abraham (2010a). After closer visual inspection of these galaxies, it is concluded that most of them do actually have a strong bar. This apparent contradiction can be caused by Nair & Abraham (2010a)

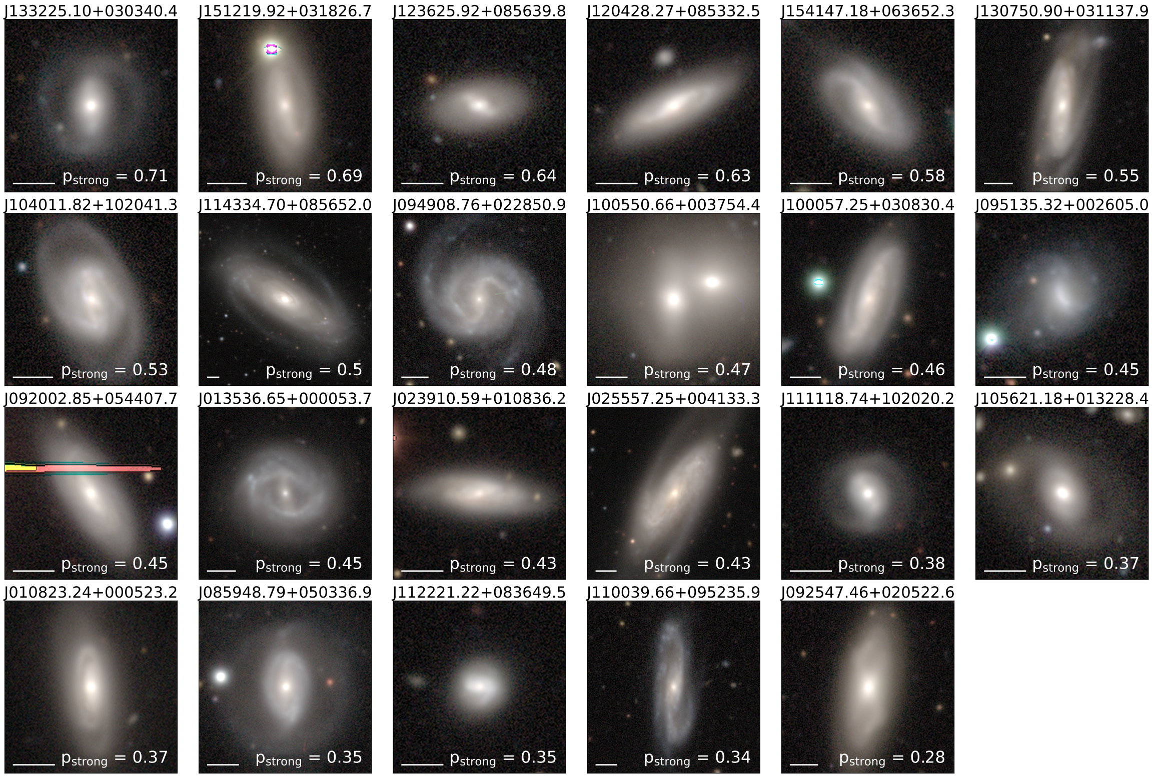

Figure 2.6: DECaLS postage stamps of the 23 galaxies classified by GZ DECaLS as strongly barred, while they are classified by Nair & Abraham (2010a) as unbarred. The IAU name of every galaxy is shown up top of the image. The galaxies are ordered based on $p_{\text{strong bar}}$, which is shown in the bottom right corner in each image. The horizontal line on the bottom left corner of each image represents 10 arcsec. The mask over galaxy J092002.85+054407.7 is due to a very bright foreground star. The majority of these galaxies do have a strong bar, especially at higher $p_{\text{strong bar}}$. Please note Nair & Abraham (2010a) use SDSS images to classify galaxies, while GZ DECaLS used deeper images from DECaLS.

using SDSS images, while the GZ DECaLS used deeper and more detailed DECaLS images.

#### 2.1.6.2 The GZ DESI-MaNGA sample

The second main sample used in this thesis is called the GZ DESI-MaNGA sample. I use the automated classifications from GZ DESI (see Section 2.1.5) and cross-match them against MaNGA (see Section 2.1.2), producing a set of 9,812 galaxies. Similarly to the previous sample, thresholds are applied to create a volume limited sample ($0.01 < z < 0.05$, spectroscopic redshift estimates are from NSA) and absolute r-band magnitude ($M_{\text{r}} < -18.96$, also from NSA). This reduces the sample to 5,810 galaxies. Additional thresholds are placed on the vote fractions of the previous questions in the

Table 2.3: GZ DECaLS is compared to the catalogue of visual morphological classifications of Nair & Abraham (2010a). Every cell indicates the percentage of a given GZ DECaLS bar type that are classified by Nair & Abraham (2010a) as having a certain feature (i.e. the percentages sum to 100 along each row). The total sample size is always given in parentheses. E.g.: 21.4% of galaxies with a strong bar in GZ DECaLS are also identified as strongly barred by Nair & Abraham (2010a).

| GZ DECaLS \ NA10 | Strong bar | Intermediate bar | Weak bar | No bar | Others |
|---|---|---|---|---|---|
| Strong bar | **21.4% (25)** | **43.6% (51)** | 8.5% (10) | 19.7% (23) | 6.8% (8) |
| Weak bar | 1.3% (2) | **27.1% (42)** | **23.9% (37)** | **42.6% (66)** | 5.2% (8) |
| No bar | 0.0% (0) | 1.2% (4) | 5.3% (18) | **90.5% (306)** | 3.0% (10) |

Galaxy Zoo decision tree to guarantee reliable classifications. These are identical to the ones used in the GZ DECaLS-SDSS sample: $p_{\text{features/disc}} \geq 0.27$, $p_{\text{not edge-on}} \geq 0.68$ and $N_{\text{bar}} \geq 0.5$. However, please note that as I am using automated classifications, the meaning behind these vote fractions is different. Instead of them representing the fraction of people that voted for a particular answer, it is the estimated fraction of people that would have voted for a certain answer. Additionally, $N_{\text{bar}}$ is no longer the number of people that have been asked the bar question, but rather the estimated fraction of people that would have been asked the question. Applying these thresholds on $p_{\text{features/disc}}$, $p_{\text{not edge-on}}$ and $N_{\text{bar}}$ further reduces the sample size to 2,125 galaxies. The same scheme was used to assign bar types to every target as for the GZ DECaLS-SDSS sample, which is shown in Table 2.1. This results in a strong bar fraction of 17.0% (363/2,125) and a weak bar fraction of 37.5% (796/2,125). This combines to a total barred fraction of 54.5%. Note that these bar fractions are different from the ones found for the GZ DECaLS-SDSS sample. In particular, the weak bar fraction here is much higher. This is due to the sample selection employed in MaNGA (see Section 2.1.2. As this sample consists of MaNGA galaxies, accurate stellar mass estimates are available from Pipe3D (see Section 2.1.2), which are used in this thesis. This sample is used in Chapter 5 and summarised in the second row of Table 2.2.

The automated classifications from GZ DESI are trained on the volunteer classifications of GZ DECaLS (see Section 2.1.5 for more details). As the GZ DECaLS-SDSS sample is consistent with GZ2 and Nair & Abraham (2010a), it is expected that this is also the case for the GZ DESI-MaNGA sample.

## 2.2 Methods

### 2.2.1 Kinematic position angle

In order to calculate the bar pattern speed (see Section 2.2.4.1), I need robust estimates of the position angle for the entire GZ DESI-MaNGA sample. There are photometric approaches to obtaining the position angle, such as fitting isophotes to the galaxy (Aguerri et al., 2015; Cuomo et al., 2019; Guo et al., 2019). The outermost ellipses can then be averaged to probe the position angle. However, this approach is not ideal. Firstly, one has to decide arbitrarily how many and which outer isophotes to use. Secondly, and most importantly, the presence of a bar, especially a strong bar, will skew the isophotes dramatically. Other structures, such as spiral arms, rings, foreground stars and companion galaxies will introduce a similar bias.

Another approach is to use the kinematic position angle instead, which does not suffer from these problems. I calculate global kinematic position angles for the entire GZ DESI-MaNGA sample using the Python package `PaFit`[2] with the stellar velocity maps from MaNGA. To avoid biasing the kinematic position angle with any small-scale disturbances, the stellar velocity maps are first smoothened by using a 10x10 pixel sliding window that calculates the median in every position. The method that this package is based on is described in Appendix C of Krajnović et al. (2006). Here, a bi-anti-symmetric map based on the smoothened input is constructed by averaging the velocity in the four quadrants of the map. The angle which minimises the difference between the symmetrised map and the original velocity map is considered the global kinematic position angle. This is illustrated in Figure 2.7 for a random strongly barred galaxy from MaNGA. The top-left panel shows the original stellar velocity field for this target, while the top-right panel shows the smoothened version. The bottom-left panel shows the velocity map symmetrised around 34.5 degrees (east of north), which is the angle at which the difference between the original and the symmetrised map is minimal. The bottom-right panel shows the velocity map symmetrised around a different angle. It is very obvious that the difference of this map with the original will be much higher. The $3\sigma$ confidence limit on the kinematic position angle can be found by taking the range of angles for which the difference in $\chi^2$ with the best-fit angle is less than 9 (Krajnović et al., 2006).

Many other papers have successfully used `PaFit` before (Cappellari et al., 2007; Krajnović et al., 2011). While the kinematic position angle is less biased by the presence of bars, there are still some pitfalls to be aware of. The inner parts of the

---

[2] `www-astro.physics.ox.ac.uk/~cappellari/software#pafit`

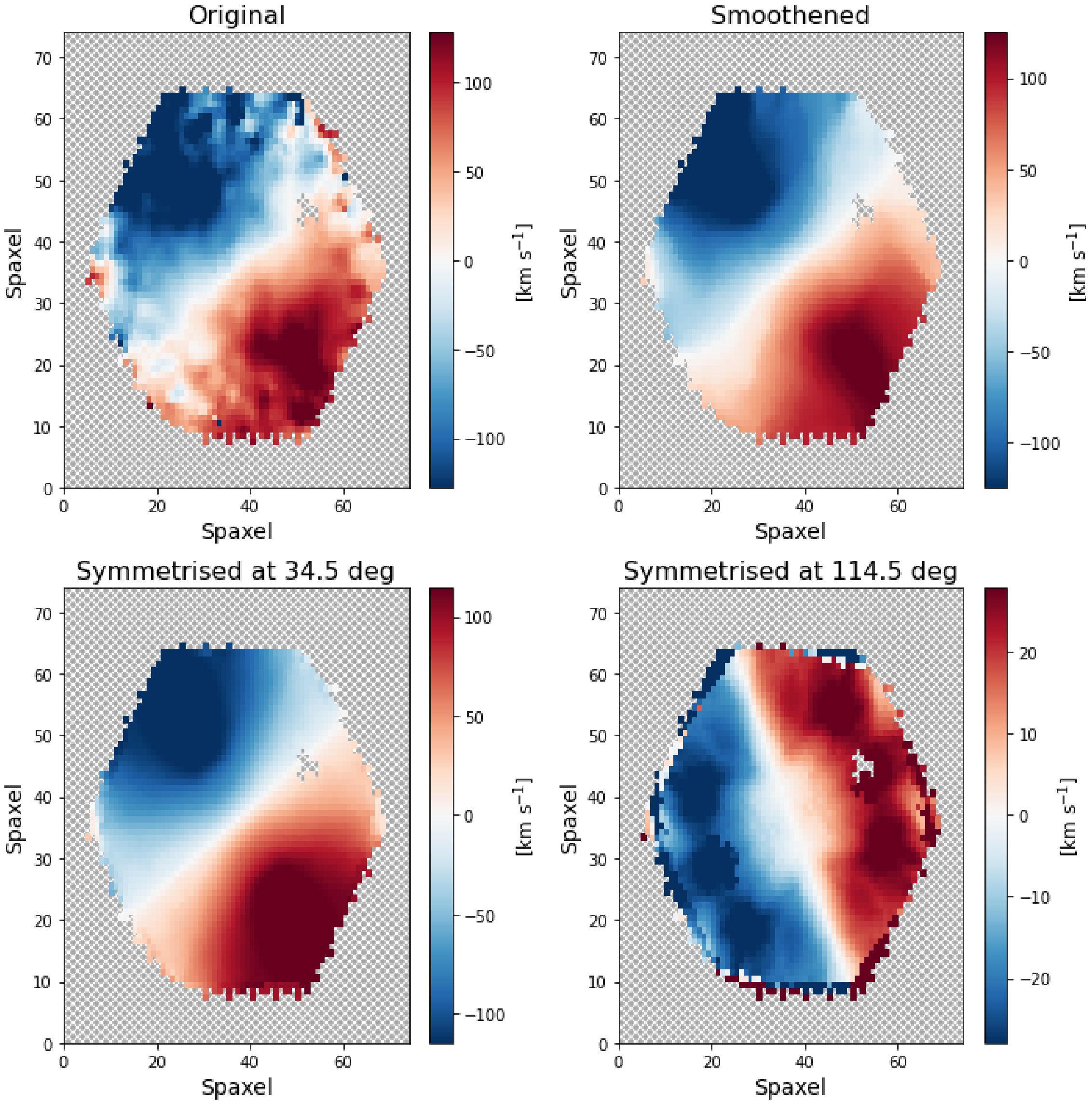

Figure 2.7: I demonstrate how the `PaFit` package obtains the global kinematic position angle using bi-anti-symmetric velocity maps for a strongly barred galaxy (plate-ifu: 9042-12703). The top-left panel shows the original velocity field, while the top-right panel visualises the smoothened version. The bottom-left panel shows the symmetrised map at 34.5 degrees, which is the angle at which the difference between the smoothened and the symmetrised map is minimal. The bottom-right panel shows a symmetrised map for a different angle, which is not the kinematic position angle.

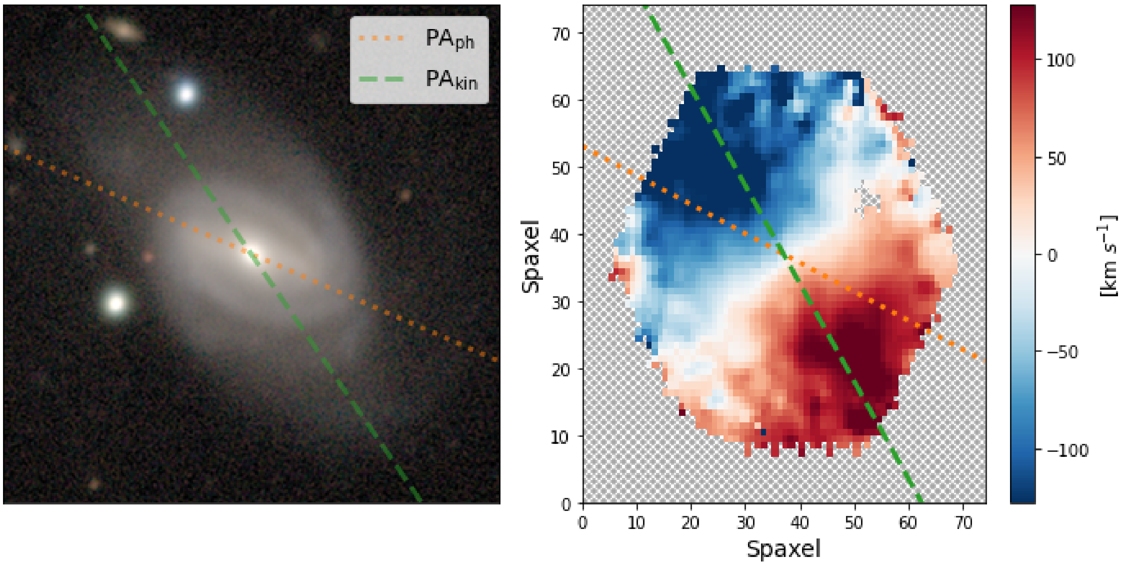

Figure 2.8: The left panel shows a DECaLS postage stamp (64x64 arcsec) of a strongly barred galaxy (plate-ifu: 9042-12703), while the right panel shows its velocity field, obtained from MaNGA. I overlay both panels with the kinematic position angle estimated here (dashed green line), as well as a photometric position angle obtained from the NSA catalogue (dotted orange line). The photometric position angle is clearly biased by the presence of the strong bar, while the kinematic position angle is not.

disc velocity field can be twisted by a bar. The inclination of the galaxy, the coverage of the IFU and the difference in position angle between the disc and bar will all have an effect. These biases are described in more detail in Appendix A3 of Guo et al. (2019). Nevertheless, the kinematic position angle remains more robust than the photometric position angle. This is demonstrated in Figure 2.8, where the kinematic position angle is shown on top of a DECaLS postage stamp and the velocity field of a strongly barred galaxy. A photometric position angle, retrieved from the NASA-Sloan Atlas (NSA), which is calculated from Sérsic fits in the $r$-band, is also shown. It is clear that the photometric position angle is biased significantly by the presence of the bar, as it traces the bar almost perfectly, while the kinematic one is not.

### 2.2.2 Bar lengths and bar position angles

I want to obtain robust bar length and bar position angle measurements for both the GZ DECaLS-SDSS and GZ DESI-MaNGA samples. Multiple methods exist to determine the length of the bar. For example, fitting isophotes to the galaxy is frequently done, (Laine et al., 2002; Erwin, 2005; Marinova & Jogee, 2007; Aguerri et al., 2009), but this method is prone to inconsistencies, as bars are associated with spiral arms, ansae and rings (Aguerri et al., 2009; Kormendy, 2013; Laurikainen et al., 2013; Hilmi et al., 2020). Alternatively, one can use Fourier decomposition (Aguerri et al., 2000) or use explainable artificial intelligence and saliency mapping techniques (Bhambra et al., 2022).

However, these automated measurements do not always work for smaller and weaker bars. Manually measuring bar lengths is a viable alternative to automated measurements and they have been used successfully before in multiple studies, such as in Erwin (2019). Díaz-García et al. (2016) show that bar lengths measured with multiple automated techniques agree with their manual measurements. Manually measuring bars can also be done by the public. For example, Hoyle et al. (2011) describes a citizen science project focussed on measuring bar lengths for GZ2 galaxies[3]. They also show that manual measurements between different volunteers agree within 10% of each other and they demonstrate that manual bar length measurements can be unbiased and robust against systematic effects. Finally, the Galaxy Zoo:3D project has bar masks for galaxies in MaNGA. These bar masks can be used to approximate the bar length (Masters et al., 2021). However, both citizen science projects are based on SDSS images, which lack the depth to identify many weak bars. Additionally, while there is an overlap, neither project completely covers both the GZ DECaLS-SDSS and GZ DESI-MaNGA samples.

Thus, I manually measured the bar length of all galaxies in the samples myself[4]. A few additional galaxies were measured that also have measurements in Hoyle et al. (2011) to better compare to their catalogue. The bar lengths were measured on composite *grz*-images obtained from the Legacy Survey. I put multiple measures in place to guarantee that my measurements were performed as correctly and consistently as possible. For example, the order of measurements was completely randomised, so that it was impossible to know whether the bar was classified by Galaxy Zoo as a weak or strong bar. The measurements were done in DS9 (Joye & Mandel, 2003), which provides a measurement tool that records the distance automatically. Additionally, every galaxy had its bar length measured twice and the mean was taken as the final value. The final bar length distribution is modelled by a Gaussian centered on this final value and with an uncertainty equal to half the difference between the two measurements. Finally, all individual measurements were inspected again to guarantee

---

[3] The bar length measurements in Hoyle et al. (2011) are shown in units of kpc/h. However, after closer inspection it was found that this is incorrect, and the bar lengths given by Hoyle et al. (2011) are actually in kpc, while assuming h = 0.7. I have applied this correction throughout this thesis.

[4] When talking about the bar length, I refer to the entire length of the bar, i.e. twice the bar radius, unless otherwise specified.

that no obvious mistakes were made while measuring. The bar length measurements are deprojected using the method described by Gadotti et al. (2007):

$$R_{\mathrm{b,deproj}} = R_{\mathrm{b,obs}} \sqrt{\cos^2 \phi + \sin^2 \phi / \cos^2 i}\,, \tag{2.3}$$

where $\mathrm{R_{b,deproj}}$ and $\mathrm{R_{b,obs}}$ are the deprojected and observed bar lengths, respectively, $\phi$ is the difference between the position angle of the bar and of the galaxy and $i$ is the inclination of the galaxy.

I manually measured the length of 2,151 bars in the manner described above[5]. I now have a reliable bar length measurement for all the barred galaxies in the GZ DECaLS-SDSS and GZ DESI-MaNGA samples. There are 238 galaxies in common with Hoyle et al. (2011), which are compared to each other in Figure 2.9. They agree relatively well, the bar lengths measured here are, on average, ~88% the length of those in Hoyle et al. (2011). This difference is possibly caused by the different images that were used; I used more detailed and deeper DECaLS images to measure bar length, whereas the volunteers in Hoyle et al. (2011) measured the bars on images from SDSS DR6 (Adelman-McCarthy et al., 2008) using a Google Maps interface.

The relative bar length, defined as the radius of the bar divided by the radius of the galaxy, is also calculated for the entire sample. The Petrosian radii from SDSS-IV DR16 (Blanton et al., 2017a; Ahumada et al., 2020) are used as a metric of the radius of the galaxy. The DESI Legacy surveys also provide estimates for the radius of the galaxy, but after visual inspection, it was found that they are not as reliable as the ones in SDSS. The position angle of the bar is also computed using these manual measurements. They are also modelled as a Gaussian centered around the mean of the measurements and with an uncertainty equal to half the difference between the two measurements.

### 2.2.3 Inclination

It is not straightforward to correctly estimate the inclination of a (strongly) barred galaxy. If you are not careful to account for the bar, it could bias the inclination measurement, for example by making it seem more inclined than it actually is. Therefore, I measure the inclinations of the barred galaxies in the GZ DESI-MaNGA sample myself. I use the Python package `photutils`[6] to perform the elliptical isophote analysis technique described by Jedrzejewski (1987). This method works by fitting multiple

---

[5] Yikes.

[6] `https://photutils.readthedocs.io/en/stable/index.html`

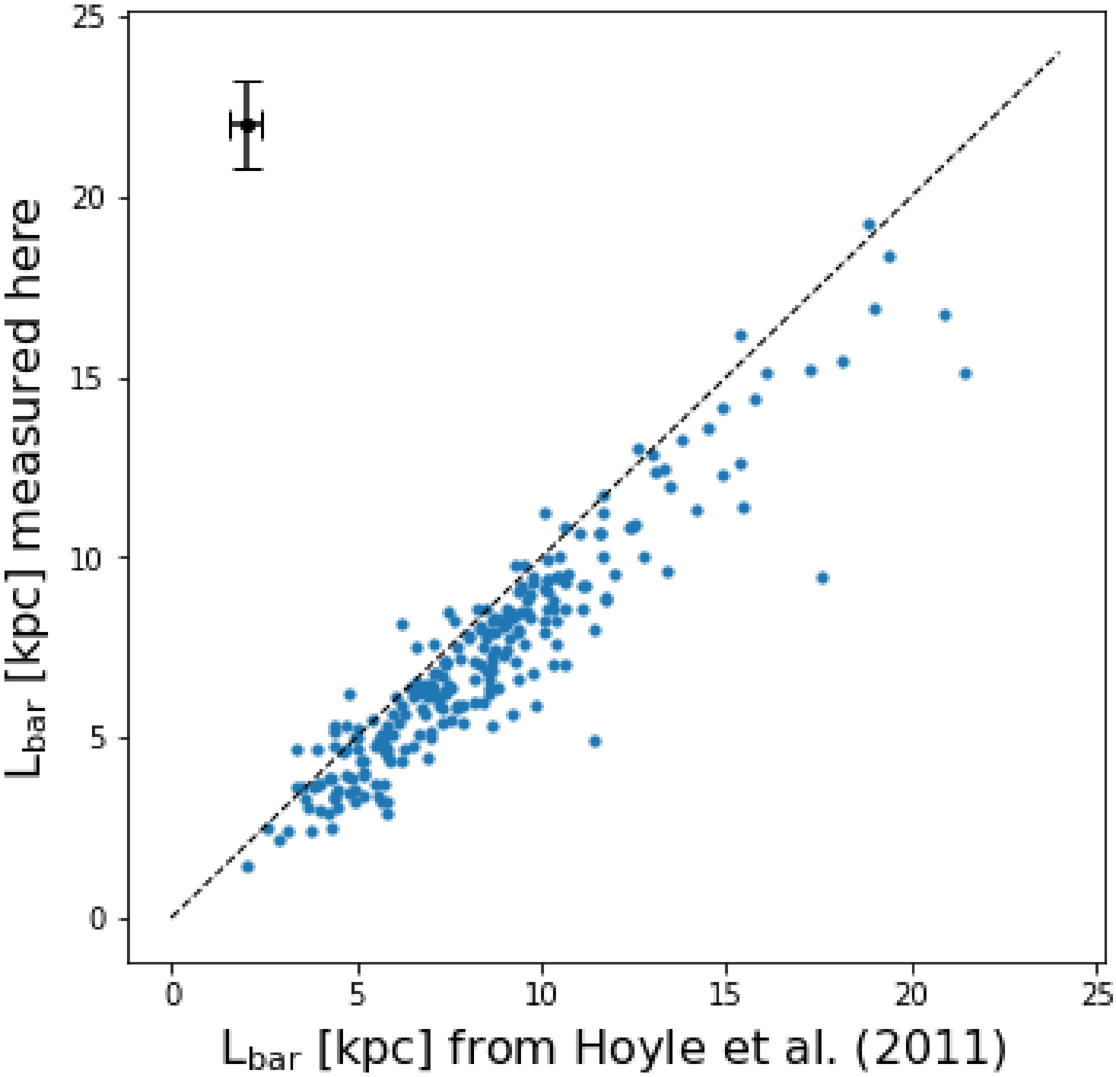

Figure 2.9: The bar lengths measured here are compared to the bar lengths from Hoyle et al. (2011). There are 238 galaxies measured in both samples. The dashed line shows where the measurements would be identical. The bar lengths measured here are, on average, ~88% the length of those measured in Hoyle et al. (2011). Please note that the bar lengths in neither sample is deprojected here.

ellipses to $r$-band images from the Legacy Survey. The ellipticity of the outermost ellipses is averaged, which should trace the inclination of the galaxy. The median of the ellipticity of the outermost 5% of fitted isophotes, which usually corresponded to 5 isophotes, was typically used to obtain a final value for ellipticity. However, any isophotes that are within the bar region (which were measured as explained in Section 2.2.2) were excluded, which guarantees that the bar does not affect the measurement. This implies that fewer than 5 isophotes were used for some targets with long bars. To make sure that the final inclination was correct, I manually inspected the ellipticity profiles and $r$-band images of all the targets. Nevertheless, foreground stars, rings and spiral arms will all bias this measurement to some degree. The errors associated with the outer isophotes were combined to calculate the error on the ellipticity. Ellipticity can be converted to inclination using: $\cos{(i)} = 1 - \epsilon = b/a$, where $i$ is the inclination, $\epsilon$ the ellipticity, $b$ the length of the minor axis and $a$ the length of the major axis of the galaxy. This approach does assume that the galaxy has a thin disc. It is possible to account for the thickness of the disc using the intrinsic thickness parameter q, which is typically assumed to be equal to 0.2 for disc galaxies (e.g. Stark et al., 2021; Price et al., 2022; Rathore et al., 2022). However, this correction only makes a significant difference in edge-on galaxies, which are excluded from the GZ DESI-MaNGA sample (see Section 2.1.6.2). Thus, in this thesis, I decided to work with the simplified thin disc (q = 0) model instead, as is frequently done (e.g. Aguerri et al., 2015; Cuomo et al., 2019; Guo et al., 2019). Figure 2.10 demonstrates the importance of accounting for the bar when measuring inclinations using photometry. It shows the ellipticity profile of a clearly face-on strongly barred galaxy. Figure 2.10 also shows ellipticity estimates obtained from the NSA catalogue, which are based on Sérsic and elliptical Petrosian fits to $r$-band images from SDSS. It is clear that the NSA ellipticities are biased by the strong bar, as these ellipticities are much higher and do not represent the galaxy properly. The inclination measured here equals $\sim 25$ deg, while the NSA values are $\sim 57$ deg and $\sim 45$ deg, respectively. Interestingly, a strong bar does not always necessarily cause an overestimate of the inclination. In some cases, a strong bar can cause a galaxy to appear more face-on. This happens in edge-on galaxies where the bar position angle is perpendicular to the position angle of the galaxy.

### 2.2.4 The Tremaine-Weinberg method

In this section, I introduce the Tremaine-Weinberg (TW) method, which is used to determine the bar pattern speed of a galaxy. The theoretical derivation and background of the TW method is given in Section 2.2.4.1. I apply the TW method on

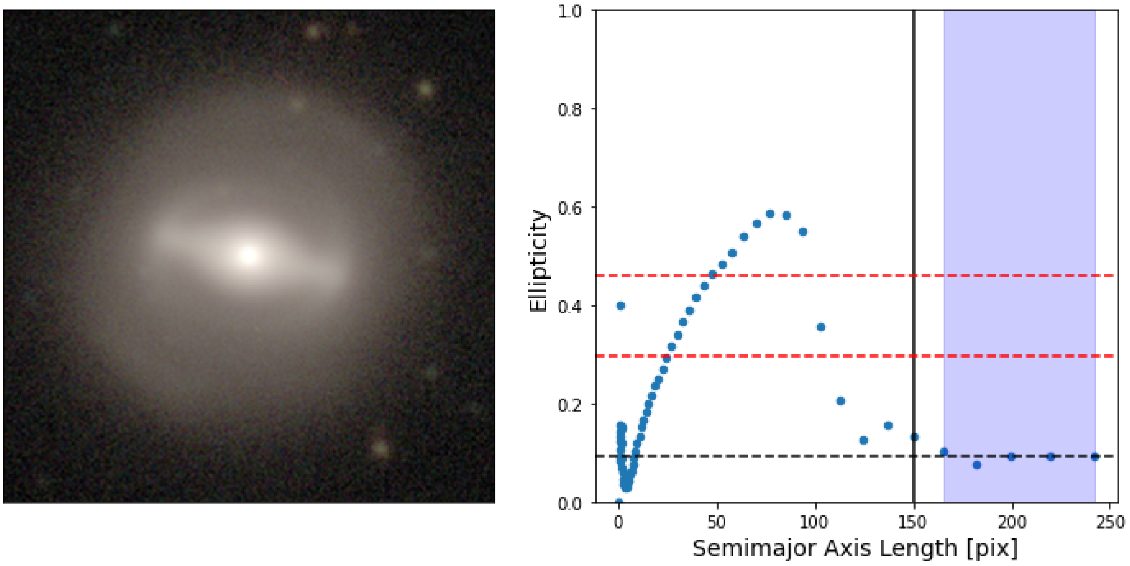

Figure 2.10: This figure shows the importance of account for the bar when using photometry to measure ellipticity. The left panel shows a DECaLS postage stamp (59x59 arcsec) of a galaxy (plate-ifu: 8622-12701), while the right panel shows the ellipticity profile of that galaxy. Every blue dot is an ellipse fitted to the photometry. The vertical black line delineates the bar radius. The blue shaded region are the ellipses used to calculate the ellipticity, which is shown by the black horizontal dashed line. The red horizontal dashed lines are ellipticity estimates obtained from the NSA catalogue, which are based on Sérsic and elliptical Petrosian fits of the SDSS $r$-band. It is obvious that they are biased by the presence of a strong bar.

two example galaxies in Section 2.2.4.2. Some practical concerns on the TW method are raised in Section 2.2.4.3. In Section 2.2.4.4, I go a step further and illustrate how the corotation radius and the dimensionless ratio $\mathcal{R}$ can be obtained from the pattern speed. Finally, the TW method is applied to all the galaxies in the GZ DESI-MaNGA sample in Section 2.2.4.5.

#### 2.2.4.1 Theoretical derivation

The Tremaine-Weinberg (TW) method is a model-independent method to determine the pattern speed of a galaxy (Tremaine & Weinberg, 1984). The TW method assumes that there is a well-defined pattern speed and that the continuity equation is satisfied by the tracer (i.e. stars or gas). The first assumption implies that the surface brightness of the tracer is constant in a frame rotating at a fixed pattern speed $\Omega_\mathrm{b}$. This can be written down as:

$$\Sigma(x, y, t) = \tilde{\Sigma}(r, \phi - \Omega_\mathrm{b} t) \ , \tag{2.4}$$

where $\Sigma$ is the surface brightness of the tracer at time $t$ using Cartesian coordinates ($x$, $y$) in the disc plane of the galaxy and $\tilde{\Sigma}$ is the surface brightness of the tracer in polar coordinates ($r$, $\phi$), where $x = r\cos\phi$ and $y = r\sin\phi$. The second assumption implies that, in theory, the tracer cannot be created or destroyed. This assumption is obviously an approximation of reality, as gas is converted into stars.

I outline the derivation of the TW method below, closely following Tremaine & Weinberg (1984). The continuity equation for the tracer can be written down as:

$$\frac{\partial\Sigma(x, y, t)}{\partial t} + \frac{\partial}{\partial x}\left[\Sigma(x, y, t) v_x(x, y, t)\right] + \frac{\partial}{\partial y}\left[\Sigma(x, y, t) v_y(x, y, t)\right] = 0 \ , \tag{2.5}$$

where $v$ is the mean velocity of the tracer in the disc. The leftmost term in the equation above can be rewritten using Equation 2.4:

$$\frac{\partial\Sigma}{\partial t} = -\Omega_\mathrm{b}\frac{\partial\tilde{\Sigma}}{\partial\phi} = \Omega_\mathrm{b}\left(y\frac{\partial\Sigma}{\partial x} - x\frac{\partial\Sigma}{\partial y}\right) \ . \tag{2.6}$$

This is substituted in Equation 2.5, after which both sides are integrated over $x$ from $-\infty$ to $+\infty$:

$$\Omega_\mathrm{b} y\int_{-\infty}^{+\infty}\frac{\partial\Sigma}{\partial x}dx - \Omega_\mathrm{b}\int_{-\infty}^{+\infty} x\frac{\partial\Sigma}{\partial y}dx + \int_{-\infty}^{+\infty}\frac{\partial\left(\Sigma v_x\right)}{\partial x}dx + \int_{-\infty}^{+\infty}\frac{\partial\left(\Sigma v_y\right)}{\partial y}dx = 0 \ . \tag{2.7}$$

The first and third terms are equal to 0, since $\Sigma \to 0$ as $|x| \to \infty$. After integrating over $y$ and reshuffling the terms:

$$\Omega_{\rm b} \int_{-\infty}^{+\infty} \Sigma(x,y,t) x dx = \int_{-\infty}^{+\infty} \Sigma(x,y,t) v_y(x,y,t) dx \ . \tag{2.8}$$

It is now possible to imagine a Cartesian coordinate system $(X, Y)$ in the sky plane with the origin in the centre of the galaxy and the $X$-axis aligned with the line of nodes (LON), which is defined as the intersection of the sky plane and the disc plane (i.e. the major axis of the galaxy). This sky plane is related to the disc plane as follows: $(X,\, Y) = (x,\, y \cos i)$, where $i$ is the inclination of the disc. Additionally, the line of sight velocity can be expressed as $V_{\rm LOS} = v_y \sin i$. Equation 2.8 is rewritten in terms of the sky plane:

$$\Omega_{\rm b} \sin{(i)} \int_{-\infty}^{+\infty} \Sigma(X,Y) X dX = \int_{-\infty}^{+\infty} \Sigma(X,Y) V_{\rm LOS}(X,Y) dX \ . \tag{2.9}$$

In the last step, both sides are multiplied by a weight function $h(Y)$, the terms are rearranged and both sides are integrated over $Y$:

$$\Omega_{\rm b} \sin{(i)} = \frac{\int_{-\infty}^{+\infty} h(Y) dY \ \int_{-\infty}^{+\infty} \Sigma(X,Y)\, V_{\rm LOS}(X,Y)\, dX}{\int_{-\infty}^{+\infty} h(Y) dY \ \int_{-\infty}^{+\infty} X\, \Sigma(X,Y)\, dX} \ . \tag{2.10}$$

More details can be found in Tremaine & Weinberg (1984). When working with IFU data, a delta function like $h(Y) = \delta\,(Y - Y_0)$ is usually used as a weight function, so that the integration happens in pseudo-slits across the IFU parallel to the LON. It is possible to perform multiple integrations using different offset distances $Y_0$ to ensure a robust measurement of the pattern speed. In this case, Equation 2.10 can be simplified to:

$$\Omega_{\rm b} \sin{(i)} = \frac{\langle V \rangle}{\langle X \rangle} \ , \tag{2.11}$$

where $\langle V \rangle$ is called the kinematic integral and $\langle X \rangle$ the photometric integral. They can be written down as:

$$\langle X \rangle = \frac{\int_{-\infty}^{+\infty} X \Sigma {\rm d}\Sigma}{\int_{-\infty}^{+\infty} \Sigma {\rm d}\Sigma} \ ; \ \langle V \rangle = \frac{\int_{-\infty}^{+\infty} V_{\rm LOS} \Sigma {\rm d}\Sigma}{\int_{-\infty}^{+\infty} \Sigma {\rm d}\Sigma} \ . \tag{2.12}$$

$\langle V \rangle$ is effectively the luminosity-weighted mean line of sight velocity and $\langle X \rangle$ the luminosity-weighted mean position. It is helpful to note that the kinematic and photometric integrals for a perfectly axisymmetric disc will equal zero. This suggests

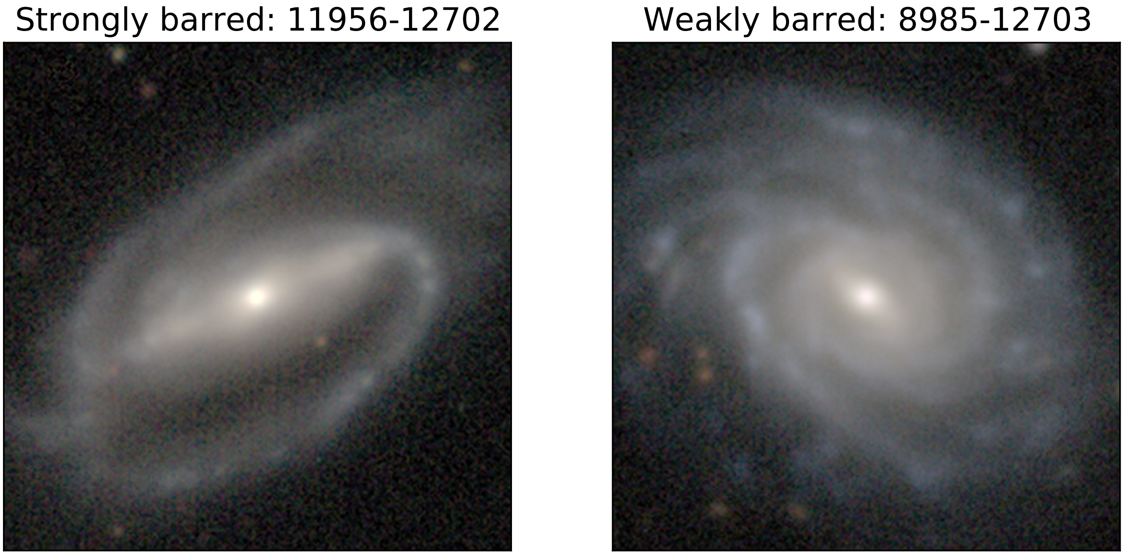

Figure 2.11: DECaLS postage stamps (64x64 arcsec) of a strongly barred galaxy (left, plate-ifu: 11956-12702) and weakly barred galaxy (right, plate-ifu: 8985-12703), which I will use to demonstrate the steps in the Tremaine-Weinberg method throughout this chapter.

that any additional structures, such as the bar, will be the cause of any non-zero values in these integrals.

#### 2.2.4.2 Practical example

To illustrate the different steps of the TW method described in the section above, I will apply it to one strongly barred galaxy and one weakly barred galaxy, shown in Figure 2.11, using stellar flux and velocity data from MaNGA.

As shown by Equation 2.11, the bar pattern speed can be determined by calculating the kinematic and photometric integrals. These integrals are determined for multiple different pseudo-slits across the IFU with different offsets from each other. In Figure 2.12, these multiple pseudo-slits are shown on top of the MaNGA stellar flux and velocity maps for these targets. I placed the pseudo-slits carefully next to each other so that they do not overlap and each slit should be centered on the disc minor axis. In order to make optimal use of the data, the length of every individual pseudo-slit is as long as the data allows. This means that different pseudo-slits for the same target can theoretically have different lengths. In practice, this difference is minimal, and such an approach has been used in other work (Garma-Oehmichen et al., 2020, 2022). To ensure that no signal from outside the bar is picked up, no slits are placed outside the bar. However, inside the bar, as many slits are placed as

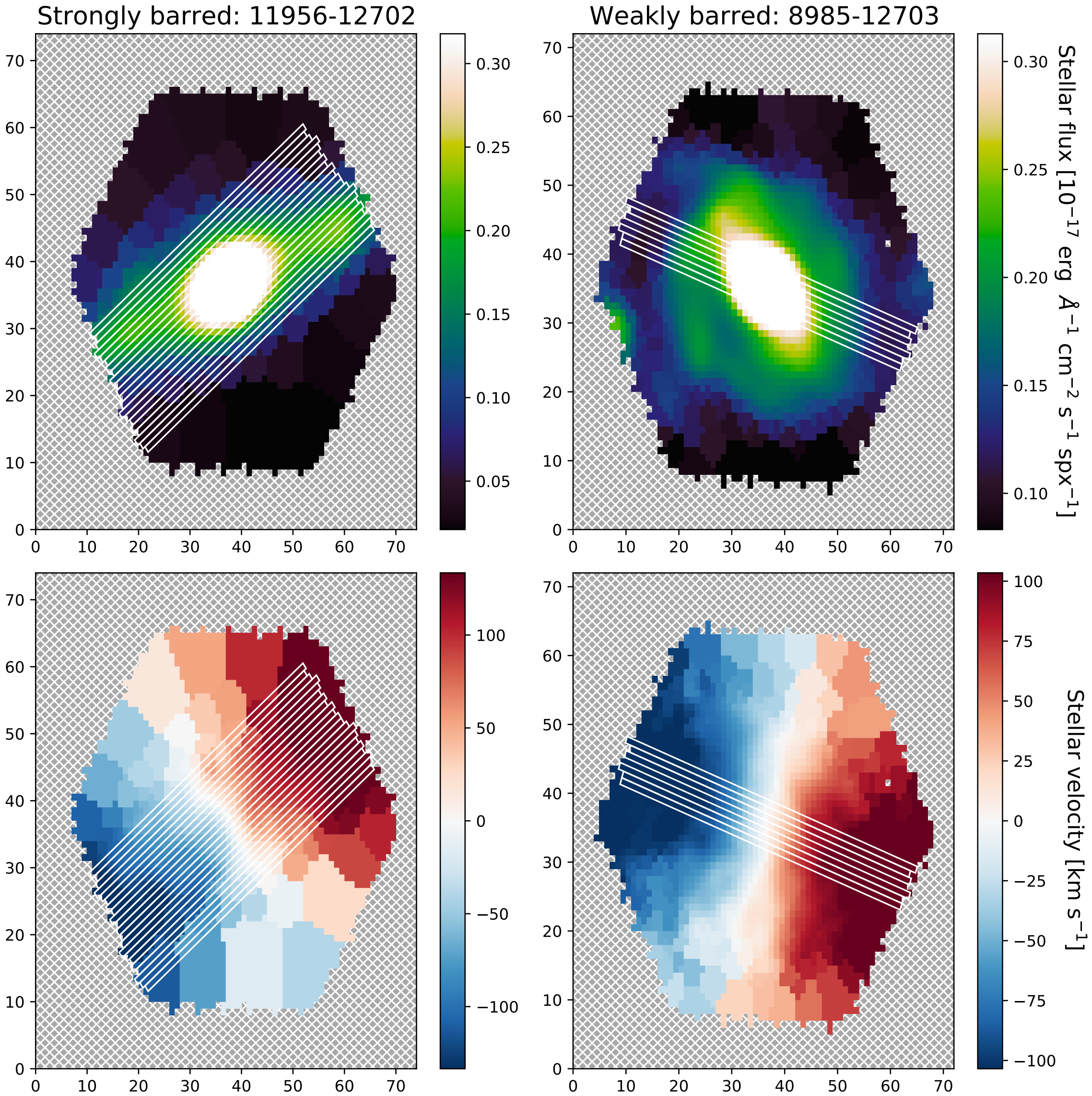

Figure 2.12: The stellar flux (top row) and stellar velocity (bottom row) for a strongly barred (left column) and weakly barred (right column) example galaxies. The multiple pseudo-slits for each target are shown on top of the maps in white outlines. These pseudo-slits are using to calculate the kinematic and photometric integrals, which are needed to determine the bar pattern speed.

possible. A minimum of 3 slits is used to make sure that the pattern speed measurement is robust. The median number of pseudo-slits placed is 10, while the maximum number is 48. A slit width of 0.5 arcsec is used, which is similar to the slit width used in Guo et al. (2019). Other studies usually use a slit width of 1 arcsec (Aguerri et al., 2015; Cuomo et al., 2019). However, in order to determine the pattern speed of weakly barred galaxies, a smaller slit width is needed, so that enough pseudo-slits can be placed inside weak bars. Additionally, Guo et al. (2019) and Zou et al. (2019) have found that the width of the pseudo-slit does not have a significant impact on the final measurement.

As shown in Equation 2.12, the limits of the integration technically go from $-\infty$ to $+\infty$. However, this is not possible when working with real data. This means that additional precautions need to be taken to ensure that the data has sufficient coverage to apply the TW method. Zou et al. (2019) suggest only using targets with coverage out to at least 1.3 $R_e$ to ensure convergence of the pattern speed measurement. As noted in Section 2.1.2, MaNGA typically covers their targets out to 1.5 - 2.5 $R_e$, which satisfies the above criterion. Nevertheless, as advised by Zou et al. (2019), every individual pseudo-slit is tested on its convergence, by systematically increasing the length of each pseudo-slit by 1 pixel until it reaches its maximum length ($\mathrm{L_{max}}$). It was decided that a slit has converged if the median of the absolute value of the change in $\Omega_\mathrm{b} \sin(i)$ among the last 5 lengths tested (so from $\mathrm{L_{max}} - 5$ until $\mathrm{L_{max}}$) is less than 1 km s$^{-1}$ arcsec$^{-1}$. Only slits that have converged were used to determine the final value of the pattern speed.

The TW method is sensitive to centering errors and incorrect estimates of the systemic velocity (Guo et al., 2019; Garma-Oehmichen et al., 2020). It is not possible to assume that the center of the galaxy is in the centre of the MaNGA map. Instead, I convolve the stellar flux map with a two-dimensional Gaussian kernel with a standard deviation of 3. Then, it is assumed that the brightest pixel of the convolved image corresponds to the galaxy centre. On average, this deviated only 1 pixel from the centre of the MaNGA map. MaNGA has already estimated and subtracted the systemic velocity from their data. However, this was not always perfect. Therefore, the systemic velocity correction that was applied was relatively low, with a median value of 9.6 km s$^{-1}$, but for a minority of targets this could go up to $\sim$40 km s$^{-1}$. The correction was calculated by averaging the stellar velocities in the 5 arcsec centre of the galaxy. The values for these corrections are shown for our entire sample in Figure 2.13.

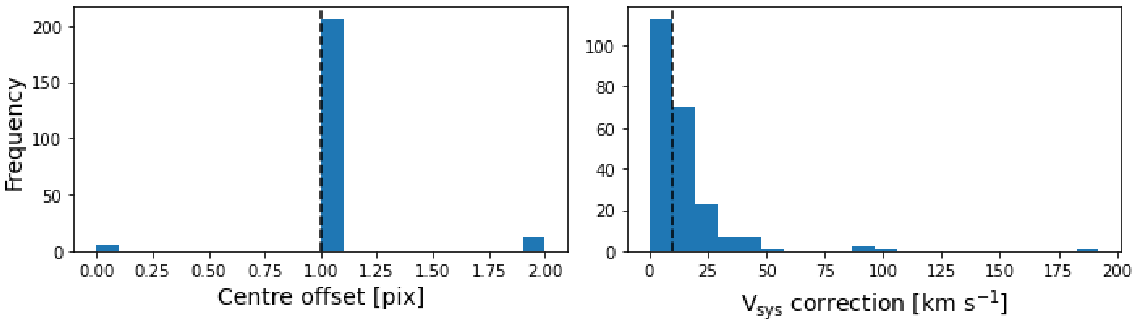

Figure 2.13: The centre offset (left) and systemic velocity correction (right) that was applied to the final sample. The median value is indicated by the striped black line. For most targets, these corrections were minimal. However, they were not negligible for a small subset of galaxies.

The kinematic and photometric integrals of all slits that have converged are calculated. However, to determine the pattern speed, the ratio of $\langle V \rangle$ and $\langle X \rangle$ is not calculated directly. Rather, the values of $\langle V \rangle$ against $\langle X \rangle$ are plotted for every individual pseudo-slit in the target. The slope of the best-fit line going through these points is then equal to $\Omega_\mathrm{b} \sin(i)$. This is visualised in Figure 2.14. While this might seem like an unnecessary step, it helps to make the measurements even more robust to centering errors and incorrect estimates of the systemic velocity (Guo et al., 2019). I find that $\Omega_\mathrm{b} \approx 12.4$ km $\mathrm{s}^{-1}$ $\mathrm{arcsec}^{-1}$ for the strongly barred example and $\Omega_\mathrm{b} \approx 13.2$ km $\mathrm{s}^{-1}$ $\mathrm{arcsec}^{-1}$ for the weakly barred example.

The code used in this thesis to calculate the bar pattern speed has been made publicly available and released under an open source license here[7].

#### 2.2.4.3 Limitations and concerns

As mentioned in Section 2.2.4.1, it is possible to apply the TW method to any tracer as long as it satisfies the continuity equation. Multiple studies have chosen gas as the tracer to determine the pattern speed using the TW method (Zimmer et al., 2004; Hernandez et al., 2005; Emsellem et al., 2006; Fathi et al., 2009; Gabbasov et al., 2009). Alternatively, one could also choose stars as the tracer, as I did in Section 2.2.4.2. Many other studies have used stars as their tracer as well (Merrifield & Kuijken, 1995; Debattista et al., 2002; Aguerri et al., 2003; Corsini et al., 2007). There was initially some concern that you could only use stars as tracers in early-type barred galaxies, as star formation and dust obscuration could cause the surface brightness to not trace the underlying mass distribution correctly (Binney &

---

[7] `https://doi.org/10.5281/zenodo.7567945`

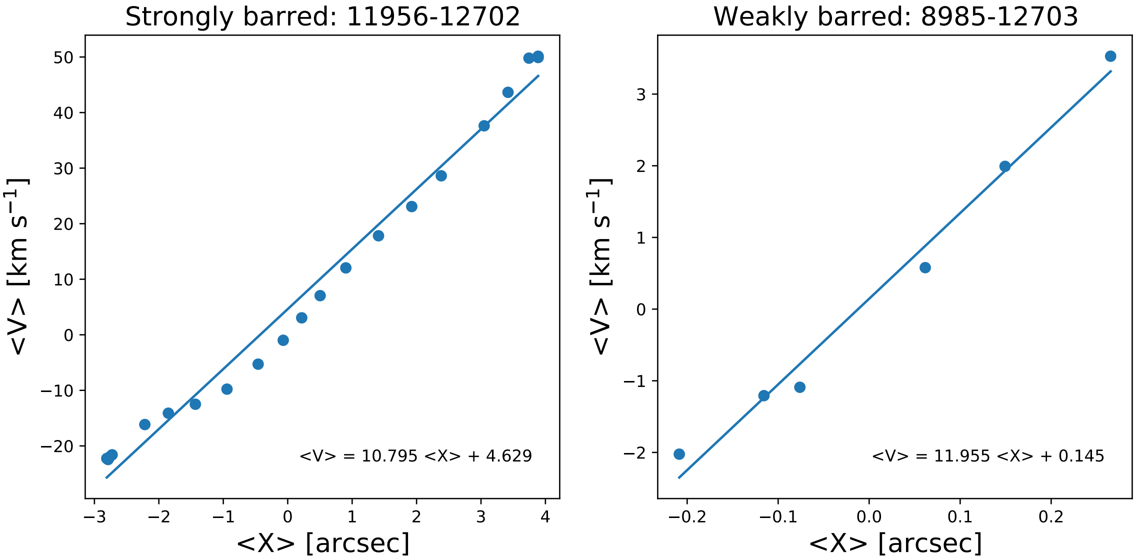

Figure 2.14: $\langle V \rangle$, the kinematic integral, is plotted against $\langle X \rangle$, the photometric integral, for all the pseudo-slits for a strongly barred galaxy (left) and a weakly barred galaxy (right). The equation of the best-fit line is shown in each plot and the slope of this line is equal to $\Omega_{\rm b} \sin(i)$.

Tremaine, 2008). However, other work has shown that this is not a concern, as these effects are minimal, and that it is entirely possible to use the TW method on late-type galaxies (Gerssen et al., 2003; Gerssen & Debattista, 2007; Treuthardt et al., 2007; Aguerri et al., 2015; Cuomo et al., 2019; Guo et al., 2019; Garma-Oehmichen et al., 2020). More recently, Williams et al. (2021) applied the TW method to stellar and gaseous tracers (using both CO and H$\alpha$) using data from the PHANGS-MUSE and PHANGS-ALMA surveys (Leroy et al., 2021a,b; Emsellem et al., 2022). Interestingly, they found significantly different results from both types of tracers, with discrepancies between $\sim 20\%$ and $\sim 40\%$. They ascribe these differences to the clumpy nature of the gaseous tracers and advise not to use them. Thus, it was decided to use stars as the tracer in this thesis.

There are a few additional limitations on the TW method one must be aware of. Firstly, the TW method is only applicable to galaxies with regular kinematics that have a well-defined pattern speed. Additionally, only targets with intermediate inclinations, e.g. $20^\circ < i < 70^\circ$, can be used (Tremaine & Weinberg, 1984; Aguerri et al., 2015; Cuomo et al., 2019; Garma-Oehmichen et al., 2020). Both high-quality spatial and velocity data is needed, and the former is not available for edge-on galaxies, while the latter is not well constrained in face-on galaxies. There is also the added concern that detecting bars in edge-on galaxies is difficult and unreliable. Furthermore, one of the biggest sources of uncertainty for the TW method is incorrect estimates of the PA of the galaxy (Debattista, 2003; Debattista & Williams, 2004; Zou et al., 2019; Garma-Oehmichen et al., 2020). Debattista (2003) have shown that an error of 5 degrees in the PA of the galaxy can result in errors as large as 48% in pattern speed. This means that a reliable and robust estimate of the position angle is crucial. Another constraint is that the bar cannot be aligned with the major or minor axis of the galaxy, as otherwise all non-axisymmetric regions due to the bar will disappear and the kinematic and photometric integrals will not detect anything (Garma-Oehmichen et al., 2020). Finally, one also needs to be able to place a sufficient number of pseudo-slits along the bar. If not enough pseudo-slits can be placed, then the best-fit line in the $\langle V \rangle$ over $\langle X \rangle$ plot (see Figure 2.14) is not well constrained, which prevents a robust measurement of the pattern speed. As mentioned above, one should only place pseudo-slits on top of the bar. It is therefore important to remember that this method is less applicable for the shortest and weakest bars, for which it will be less accurate.

#### 2.2.4.4 Rotation curves, corotation radii and $\mathcal{R}$

In the sections above, I outlined how pattern speed estimates are obtained using the TW method. With these measurements, one can also calculate the corotation radius ($R_{\mathrm{CR}}$). This is the radius at which the centrifugal and gravitational forces balance each other in the rest frame of the bar. This means that, at this radius, the stars in the disc will have the same angular velocity as the bar pattern speed (Cuomo et al., 2019; Guo et al., 2019). It is common to approximate the corotation radius by $R_{\mathrm{CR}} = V_{\mathrm{c}}/\Omega_{\mathrm{b}}$, where $V_{\mathrm{c}}$ is the circular velocity in the flat part of the rotation curve (Aguerri et al., 2015; Cuomo et al., 2019; Guo et al., 2019). However, this method assumes that the corotation radius lies in the region where the rotation curve has flattened, which is not necessarily the case, and assuming this can lead to incorrect measurements of $R_{\mathrm{CR}}$. A more flexible approach is to look at the rotation curve of the galaxy, which can be obtained by using stellar velocity data from MaNGA. In order to do derive the rotation curve, I need to calculate the true stellar velocity $\mathrm{V}_{\mathrm{rot}}$ from the observed stellar velocity $\mathrm{V}_{\mathrm{obs}}$:

$$V_{\mathrm{rot}} = V_{\mathrm{obs}} / \left(\sin i \times \cos\phi\right) \ , \tag{2.13}$$

where $i$ is the inclination of the galaxy and $\phi$ is the azimuthal angle measured relative to the position angle of the galaxy. The deprojected distances to the galaxy are also needed, which can be obtained by applying Equation 2.3. These true stellar

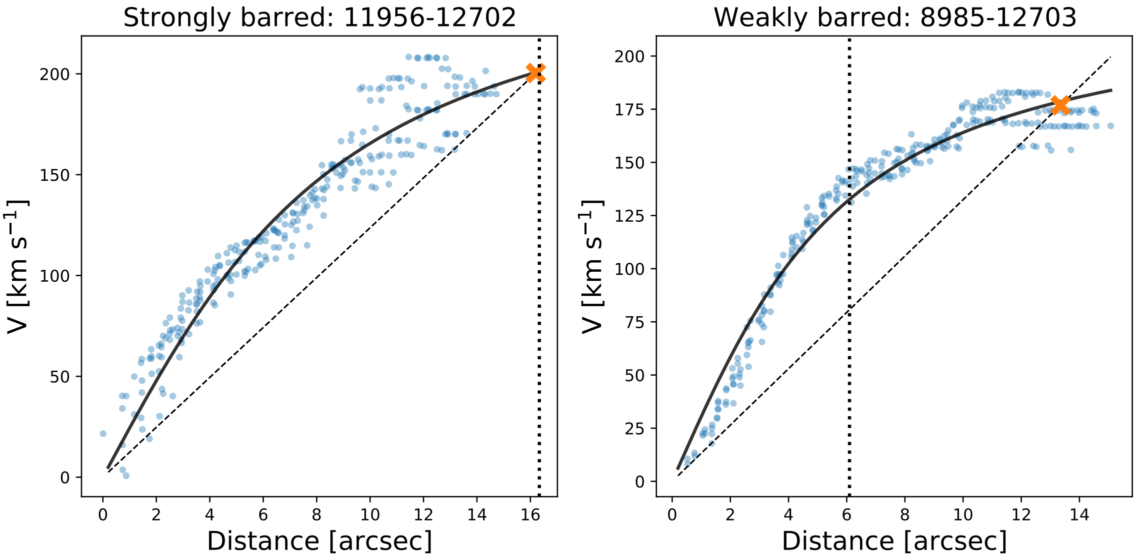

Figure 2.15: Visualisation of the rotation curve (black line) of a strongly barred galaxy (left) and weakly barred galaxy (right). The rotation curve is modelled by a two parameter arctan function described in Courteau (1997), using stellar velocity measurements from MaNGA in a 5 arcsec aperture along the major axis of the galaxy (blue dots). The black dashed line is obtained by multiplying the bar pattern speed, $\Omega_b$, with the distance from the centre of the galaxy. The distance where this line and the rotation curve intersect (indicated by the orange cross), defines the corotation radius. The dotted vertical line is the deprojected bar radius. The ratio of the corotation radius to the bar radius is defined as $\mathcal{R}$.

velocities and deprojected distances are calculated for spaxels in a 5 arcsec aperture along the position angle of the galaxy, in order to minimise the effect of the corrections described above. Finally, the rotation curve of the galaxy is modelled by a two parameter arctan function, described in Courteau (1997):

$$V_{\rm rot} = V_{\rm sys} + \frac{2}{\pi} V_{\rm c} \arctan\left(\frac{r - r_0}{r_t}\right), \tag{2.14}$$

where $V_{\rm sys}$ is the systemic velocity, $V_{\rm c}$ is the asymptotic velocity, r is the distance, $r_0$ is the spatial centre of the galaxy and $r_t$ is the transition radius. This model is fit using a least squares algorithm. In this model, the rotation curve flattens at $r_t$ and goes towards $V_{\rm c}$. Here, $r_0$ and $V_{\rm sys}$ are assumed to equal zero. The resulting models for the strongly and weakly barred example galaxies are shown in Figure 2.15.

The rotation curve can be combined with the bar pattern speed to estimate the corotation radius. First, the bar pattern speed is multiplied by the distance from the centre of the galaxy, which effectively indicates how fast the tracer moves for that particular pattern speed at any given distance from the centre. The distance at which the rotation curve of the galaxy intersects with this curve is the corotation radius. This is shown for the example targets in Figure 2.15, where I find that $R_{\mathrm{CR}} \approx 16.2$ arcsec for the strongly barred example and $R_{\mathrm{CR}} \approx 13.4$ arcsec for the weakly barred example. Figure 2.16 highlights the importance of using the rotation curve of the galaxy and not assuming that the corotation radius lies in the region where the velocity curve has flattened. In the left panel, the corotation radius is calculated using $R_{\mathrm{CR}} = V_{\mathrm{c}}/\Omega_{\mathrm{b}}$, and subtracted by value measured above. The right panel shows the fraction of the corotation radii calculated with both methods. I find that the former method consistently overestimates the corotation radius, with a median overestimate of 3.3 arcsec (or 27.1%). This is equal to 2.1 kpc for the sample used here, which corresponds to 47.9% of the half-light Petrosian radius obtained from NSA. Garma-Oehmichen et al. (2020) performed an analogous analysis on their data and found similar results, which indicates that the simplified approach introduces a significant bias.

It must be noted that the observed stellar velocity is not identical to the circular velocity of stars on perfectly circular orbits. The circular velocity is typically higher than the observed stellar velocity, which increases the final value of the corotation radius. This difference in velocity is caused by an effect called asymmetric drift ($\mathrm{V}_{\mathrm{AD}}$, Binney & Tremaine, 2008). Asymmetric drift scales with radial velocity dispersion, which is typically highest at lower radii. This implies that the effects of asymmetric drift are significantly more important in the centre of galaxies than at higher radii (Debattista et al., 2002; Aguerri et al., 2003; Binney & Tremaine, 2008). Additionally, because of the shape of a typical rotation curve (initially sharply rising and flattening after the transition radius, $\mathrm{r}_t$), the magnitude of the effect of asymmetric drift on the corotation radius depends on where the corotation radius lies relative to the rotation curve. If the corotation radius lies within part of the rotation curve that has started flattening (if $R_{\mathrm{CR}} \gtrsim \mathrm{r}_t$), the increase in corotation radius is roughly equal to the difference in velocity caused by asymmetric drift at that radius divided by the bar pattern speed ($\mathrm{V}_{\mathrm{AD}}$ / $\Omega_{\mathrm{b}}$). However, if the corotation radius lies within the sharply rising part of the rotation curve (if $R_{\mathrm{CR}} \lesssim \mathrm{r}_t$), then the corotation radius will increase with $\mathrm{V}_{\mathrm{AD}}$ / $\Omega_{\mathrm{b}}$ plus an additional term proportional to the slope of the rotation curve. These two combined effects suggest that the consequences of asymmetric drift will be minimal at higher radii. For the sample presented here, the median ratio of $R_{\mathrm{CR}}/\mathrm{r}_t$ equals 2.84. This shows that the typical corotation radius is above the transition radius and that an asymmetric drift correction will only have a minimal effect on these targets. Therefore, I did not correct for asymmetric drift in this work.

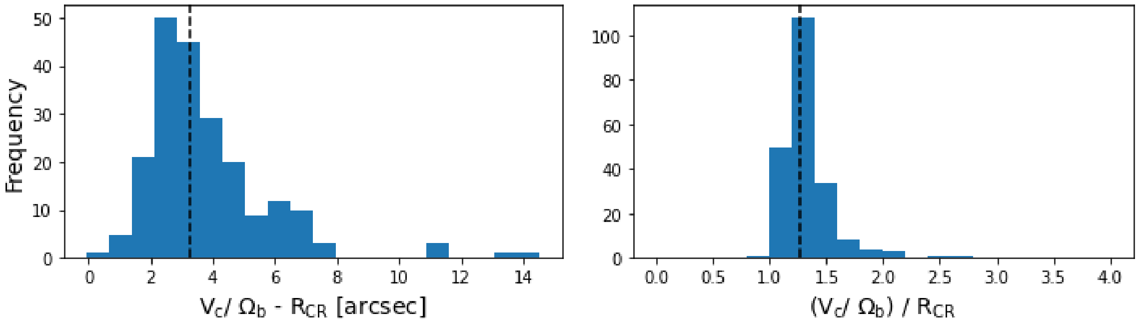

Figure 2.16: The left panel shows the difference between the two methods to calculate the corotation radius, while the right panel shows their fraction. It is clear that calculating the corotation radius by assuming $R_{\mathrm{CR}} = V_{\mathrm{c}}/\Omega_{\mathrm{b}}$ consistently overestimates it. I find a median overestimate of 3.3 arcsec, or 27.1%.

As mentioned in Section 1.3.3, the corotation radius can be used to calculate the dimensionless parameter $\mathcal{R}$, which is defined as the ratio of the corotation radius to the bar radius ($\mathcal{R} = R_{\mathrm{CR}}/R_{\mathrm{bar}}$). The ratio $\mathcal{R}$ is important, as it can be used to classify bars into fast ($1.0 < \mathcal{R} < 1.4$) and slow ($\mathcal{R} > 1.4$) bars (Debattista & Sellwood, 2000; Rautiainen et al., 2008; Aguerri et al., 2015). This implies that fast bars end near the corotation radius, whereas slow bars have bar radii that are shorter than the corotation radius. Additionally, the bar-ends of fast bars rotate with a velocities similar to the stars in the disc, whereas the bar-ends of slow bars rotate much slower with respect to the disc. I find $\mathcal{R} \approx 1.00$ and $\mathcal{R} \approx 1.88$ for the strongly and weakly barred examples, respectively. Furthermore, it is not expected to see bars with $\mathcal{R} < 1.0$, as it is believed that it is not possible for bars to extend beyond corotation, i.e. bars whose bar-ends have a velocity greater than the stellar disc should not exist (Contopoulos, 1980, 1981; Athanassoula, 1992b). However, multiple studies have measured these so-called ultrafast bars (Buta & Zhang, 2009; Aguerri et al., 2015; Cuomo et al., 2019; Guo et al., 2019; Garma-Oehmichen et al., 2020).

#### 2.2.4.5 Our measurements

I applied the TW method described above to estimate bar pattern speeds, corotation radii and $\mathcal{R}$ for the GZ DESI-MaNGA sample, which has 2,125 galaxies. However, it is not possible to do this for every galaxy in the GZ DESI-MaNGA sample. Most obviously, I have to throw away all the unbarred galaxies, which brings the sample size down to 1,159. Additionally, as described in Section 2.2.4.3, the TW method is not suitable for galaxies with irregular kinematics, as one of the assumptions of the method is that the galaxy must have a well-defined pattern speed. The stellar velocity field of every galaxy was inspected by eye and 474 galaxies with irregular kinematics were removed.

Additionally, the bar cannot align with the disc major or minor axis. Thus, galaxies where the PA of the bar was within 10° of the major or minor axis of the galaxy were removed from the sample, which affected 193 galaxies. The position angle of the disc and the bar are measured as explained in Sections 2.2.1 and 2.2.2, respectively. The TW method only works on galaxies with intermediate inclination, so the sample is limited to galaxies with inclinations between 20° and 70°, which removed a further 32 galaxies. The inclination values used here are calculated as explained in Section 2.2.3.

The position angle of the disc is one of the biggest sources of uncertainty for the TW method (Debattista, 2003; Zou et al., 2019; Garma-Oehmichen et al., 2020). A Monte Carlo simulation is performed to correctly propagate this uncertainty. To ensure a robust posterior distribution whilst optimising computer time, 1,000 iterations are done where the inclination, position angle of the disc, bar length and position angle of the bar are resampled in every iteration, by assuming Gaussianity over these parameters. The median of the posterior distribution was taken as the final value, while the $16^{\rm th}$ and $84^{\rm th}$ percentiles of the distribution are taken as the $1\sigma$ errors. The evolution of the pattern speed of the strongly barred and weakly barred example is shown in Figure 2.17, where the pattern speed estimate for every iteration is shown, as well as the median value of the posterior distribution of the pattern speed using all prior iterations. The median change in the last 50 iterations of the median of the posterior distribution is calculated for the entire sample. The maximum change is $\sim 0.027$ km s$^{-1}$ arcsec$^{-1}$, while the median is $\sim 0.003$ km s$^{-1}$ arcsec$^{-1}$. This suggests that 1,000 iterations is enough to obtain robust estimates of the pattern speed.

As the TW method requires us to reliably perform a linear fit in the $\langle V \rangle$ against $\langle X \rangle$ plots, every galaxy needs to have a minimum of at least 3 pseudo-slits. 87 galaxies were removed from the sample because of this threshold. The pseudo-slits can only be placed on top of the bar region and the bar length measurements used here are detailed in Section 2.2.2. The reliability of the linear fit is ensured by calculating the normalised root mean squared error (NRMSE) to estimate the fit quality. Targets that had a median NRMSE greater than 0.2 over all the MC iterations were removed, which affected 36 targets. Additionally, the NRMSE of the fit to the two-parameter arctan model used to describe the rotation curve of the galaxy is calculated, as some galaxies are not described correctly by this model. A threshold of 0.2 was used here as well, which affected only 1 additional galaxy. These threshold values were chosen

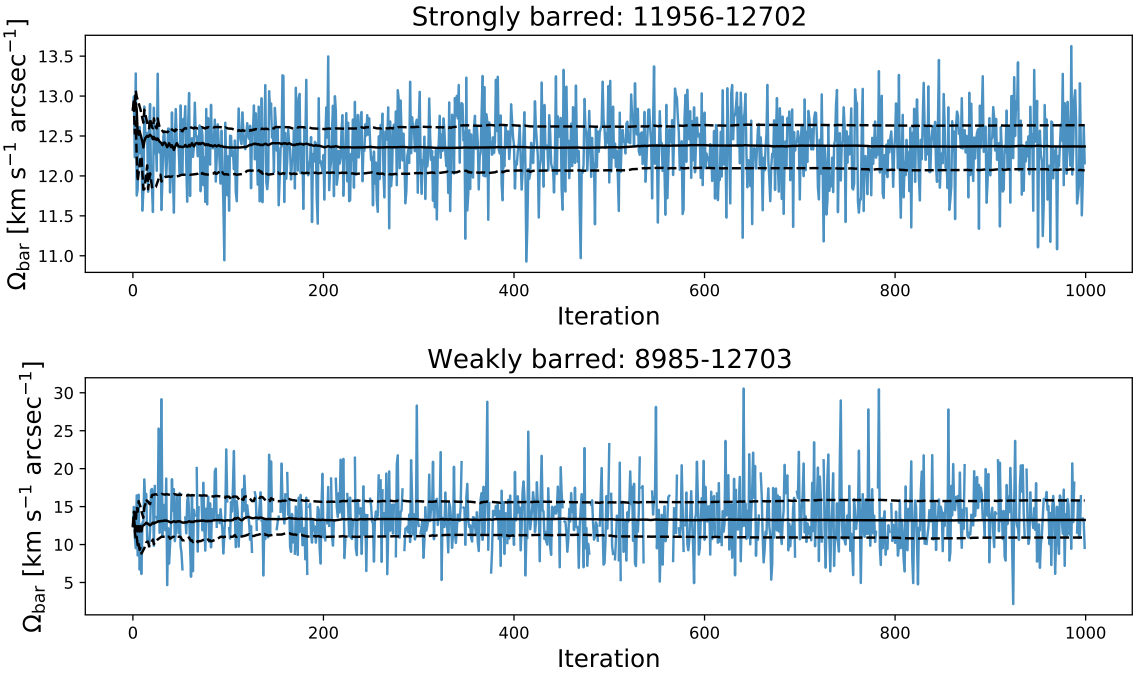

Figure 2.17: The evolution of the pattern speed over the 1,000 MC iterations for the strongly barred example (top panel) and weakly barred example (bottom row). The blue curve tracks the calculated pattern speed in each iteration, while the full black line is the median value of the posterior distribution of the pattern speed using all prior iterations. The dashed lines are the 25th and 75th percentiles.

after careful visual inspection of all the fits. Finally, all targets where the TW method was unable to calculate a value for the pattern speed (e.g. due to not being able to place enough slits) for more than 10% of all MC iterations were removed as well. The final sample consists of 225 galaxies, with 122 strongly barred and 103 weakly barred galaxies. This sample is called the TW sample and is summarised in the bottom row of Table 2.2. Please note that this is only ∼19% of all the barred galaxies in the GZ DESI-MaNGA sample. This low success rate is attributed to the high sensitivity of the TW method and, as explained above, the need for robust data to accurately measure the pattern speed. Nevertheless, this is still the largest sample size the TW method has been applied to so far and the only one with a substantial amount of weak bars.

I have determined reliable bar pattern speed estimates for all these targets. However, calculating the corotation radius proved difficult for a small subset of these galaxies, usually if the pattern speed was low. A lower pattern speed will result in a higher corotation radius, which sometimes fell far outside the MaNGA field of view. It was decided that extrapolating the rotation curves too much endangers the reliability of the corotation estimates. Thus, targets where I had to extrapolate by more than a factor of two were excluded. This affected 15 of the 225 galaxies. The final posterior distributions of the weakly and strongly barred example can be found in Figure 2.18. The values for the bar pattern speeds, corotation radii and $\mathcal{R}$ of 40 randomly selected galaxies can be found in Table 2.4. The complete table is available online here[8] and is used in Chapter 4 to investigate the kinematics of weakly and strongly barred galaxies.

### 2.2.5 Radius profiles

In Chapter 5, I will analyse how a bar affects different regions (such as the centre, the arm of the bar and the bar-end) of galaxy. This is done by generating radius profiles for every target over any particular map from MaNGA (see Section 2.1.2) along any given PA (e.g. the PA of the bar). An median profile can be created taking the median of individual profiles of galaxies that belong to any given group (i.e. for all strongly barred galaxies).

This process is visualised in Figure 2.19. The top left panel shows a DECaLS image of a random strongly barred star forming galaxy. The bottom left panel shows its Gaussian-fitted equivalent width measurement of H$\alpha$ (EW[H$\alpha$]) obtained from

---

[8] `https://doi.org/10.5281/zenodo.7567945`

Table 2.4: The bar pattern speeds, corotation radii and $\mathcal{R}$ for 40 randomly selected bars. The full table can be found online here.

| Plate-ifu | $\Omega_b$ [km s$^{-1}$ arcsec$^{-1}$] | $\Omega_b$ [km s$^{-1}$ kpc$^{-1}$] | R$_{CR}$ [arcsec] | R$_{CR}$ [kpc] | $\mathcal{R}$ [-] |
|---|---|---|---|---|---|
| 11014-12705 | $9.4^{+0.99}_{-1.2}$ | $27.8^{+2.9}_{-3.5}$ | $15.2^{+2.9}_{-2.1}$ | $5.12^{+0.98}_{-0.70}$ | $1.60^{+0.50}_{-0.29}$ |
| 9504-3704 | $34^{+14}_{-11}$ | $37^{+15}_{-11}$ | $3.7^{+2.2}_{-1.1}$ | $3.5^{+2.1}_{-1.1}$ | $0.85^{+0.57}_{-0.28}$ |
| 8245-12702 | $15.4^{+0.85}_{-1.7}$ | $22.5^{+1.2}_{-2.5}$ | $19.0^{+3.2}_{-1.5}$ | $13.0^{+2.2}_{-1.0}$ | $1.09^{+0.74}_{-0.21}$ |
| 11979-12703 | $14.5^{+4.4}_{-4.4}$ | $20.5^{+6.2}_{-6.2}$ | $13.8^{+6.8}_{-3.8}$ | $9.7^{+4.8}_{-2.7}$ | $2.1^{+1.1}_{-0.65}$ |
| 9027-12704 | $5.5^{+2.9}_{-0.9}$ | $8.0^{+4.2}_{-1.3}$ | $13.3^{+3.6}_{-6.7}$ | $9.2^{+2.5}_{-4.6}$ | $0.82^{+0.26}_{-0.30}$ |
| 8079-9101 | $13.2^{+1.9}_{-1.9}$ | $28.1^{+4.1}_{-4.1}$ | $17.3^{+4.2}_{-3.1}$ | $8.1^{+2.0}_{-1.5}$ | $1.84^{+0.65}_{-0.43}$ |
| 8624-9102 | $12.5^{+4.0}_{-6.8}$ | $22^{+7.1}_{-12}$ | $16^{+21}_{-4.6}$ | $9^{+12}_{-2.6}$ | $2.5^{+5.1}_{-0.86}$ |
| 10220-9101 | $20.5^{+2.1}_{-3.4}$ | $28.4^{+2.9}_{-4.6}$ | $11.1^{+3.1}_{-1.5}$ | $8.0^{+2.2}_{-1.1}$ | $1.60^{+0.69}_{-0.31}$ |
| 11979-9101 | $20.8^{+4.3}_{-5.3}$ | $23.9^{+5.0}_{-6.0}$ | $9.9^{+4.4}_{-2.2}$ | $8.7^{+3.8}_{-2.0}$ | $1.37^{+0.65}_{-0.36}$ |
| 8723-12701 | $19.7^{+2.8}_{-2.8}$ | $25.6^{+3.6}_{-3.6}$ | $11.2^{+2.3}_{-1.8}$ | $8.6^{+1.8}_{-1.4}$ | $1.85^{+0.55}_{-0.37}$ |
| 9881-12704 | $6.7^{+2.5}_{-1.1}$ | $12.5^{+4.6}_{-2.0}$ | $14.1^{+4.1}_{-5.7}$ | $7.6^{+2.2}_{-3.1}$ | $1.00^{+0.32}_{-0.31}$ |
| 11868-12703 | $8.5^{+3.7}_{-4.4}$ | $9.8^{+4.3}_{-5.1}$ | $16^{+21}_{-5.9}$ | $14^{+18}_{-5.0}$ | $1.2^{+1.6}_{-0.67}$ |
| 11965-9102 | $16.30^{+0.66}_{-0.72}$ | $25.3^{+1.0}_{-1.1}$ | $8.93^{+0.69}_{-0.58}$ | $5.77^{+0.45}_{-0.37}$ | $1.34^{+0.35}_{-0.23}$ |
| 10492-12702 | $18.3^{+1.0}_{-0.96}$ | $33.6^{+1.9}_{-1.8}$ | $6.82^{+0.36}_{-0.39}$ | $3.72^{+0.20}_{-0.22}$ | $1.43^{+0.12}_{-0.10}$ |
| 8257-3703 | $23.4^{+1.9}_{-2.1}$ | $46.5^{+3.8}_{-4.2}$ | $6.00^{+0.95}_{-0.75}$ | $3.02^{+0.48}_{-0.38}$ | $0.92^{+0.17}_{-0.14}$ |
| 8602-12705 | $7.9^{+1.4}_{-3.4}$ | $12.5^{+2.2}_{-5.4}$ | $23^{+20}_{-4.1}$ | $15^{+13}_{-2.6}$ | $1.8^{+2.1}_{-0.42}$ |
| 8323-12705 | $14.5^{+1.9}_{-2.6}$ | $21.4^{+2.9}_{-3.8}$ | $23.5^{+8.7}_{-5.0}$ | $15.8^{+5.9}_{-3.3}$ | $1.4^{+1.2}_{-0.52}$ |
| 8442-9102 | $13.1^{+4.6}_{-3.1}$ | $28.2^{+9.8}_{-6.8}$ | $7.9^{+2.2}_{-1.9}$ | $3.7^{+1.0}_{-0.88}$ | $1.06^{+0.33}_{-0.28}$ |
| 10492-6102 | $23.1^{+4.5}_{-4.4}$ | $38.7^{+7.5}_{-7.4}$ | $11.1^{+3.3}_{-2.3}$ | $6.6^{+1.9}_{-1.4}$ | $1.9^{+1.2}_{-0.54}$ |
| 11956-12702 | $12.37^{+0.42}_{-0.46}$ | $15.63^{+0.53}_{-0.59}$ | $16.20^{+0.80}_{-0.71}$ | $12.82^{+0.63}_{-0.56}$ | $1.00^{+0.11}_{-0.11}$ |
| 10226-3704 | $28.3^{+7.7}_{-8.3}$ | $35^{+9.7}_{-10}$ | $8.9^{+5.4}_{-3.2}$ | $7.1^{+4.3}_{-2.5}$ | $1.7^{+1.0}_{-0.63}$ |
| 8145-3704 | $25.9^{+3.1}_{-2.5}$ | $46.7^{+5.5}_{-4.4}$ | $10.9^{+1.8}_{-2.0}$ | $6.0^{+1.0}_{-1.1}$ | $1.71^{+0.26}_{-0.29}$ |
| 8456-6101 | $16.7^{+3.0}_{-2.9}$ | $35.7^{+6.5}_{-6.2}$ | $9.8^{+4.4}_{-3.3}$ | $4.6^{+2.1}_{-1.6}$ | $0.97^{+0.44}_{-0.31}$ |
| 12651-9101 | $18.0^{+7.3}_{-1.3}$ | $20.3^{+8.2}_{-1.5}$ | $10.3^{+0.99}_{-3.6}$ | $9.1^{+0.88}_{-3.2}$ | $0.70^{+0.12}_{-0.15}$ |
| 8324-9101 | $12.5^{+3.3}_{-2.5}$ | $21.7^{+5.7}_{-4.3}$ | $13.3^{+4.3}_{-3.9}$ | $7.7^{+2.5}_{-2.2}$ | $3.5^{+2.1}_{-1.3}$ |
| 8084-6101 | $14.5^{+1.5}_{-1.5}$ | $34.8^{+3.7}_{-3.6}$ | $10.3^{+1.7}_{-1.4}$ | $4.29^{+0.69}_{-0.58}$ | $1.52^{+0.40}_{-0.27}$ |
| 11004-12704 | $11.6^{+3.9}_{-3.8}$ | $23.6^{+7.9}_{-7.7}$ | $11.5^{+7.2}_{-3.5}$ | $5.7^{+3.5}_{-1.7}$ | $1.45^{+0.93}_{-0.45}$ |
| 9886-12701 | $8.8^{+3.0}_{-3.8}$ | $18.9^{+6.5}_{-8.3}$ | $17^{+17}_{-5.4}$ | $7.9^{+7.7}_{-2.5}$ | $3.1^{+4.5}_{-1.1}$ |
| 8602-12701 | $15.9^{+4.4}_{-2.5}$ | $29.6^{+8.2}_{-4.6}$ | $16.6^{+2.5}_{-2.7}$ | $8.9^{+1.4}_{-1.5}$ | $1.40^{+0.33}_{-0.29}$ |
| 9190-12703 | $15.7^{+1.7}_{-4.5}$ | $35^{+3.7}_{-10}$ | $13.0^{+7.2}_{-1.8}$ | $5.8^{+3.2}_{-0.8}$ | $1.5^{+1.0}_{-0.34}$ |
| 8978-9101 | $19.2^{+3.0}_{-6.3}$ | $32^{+5.0}_{-10}$ | $8.6^{+6.3}_{-1.8}$ | $5.2^{+3.8}_{-1.1}$ | $1.5^{+1.2}_{-0.35}$ |
| 8137-9102 | $15.2^{+2.1}_{-3.6}$ | $24.4^{+3.3}_{-5.7}$ | $11.8^{+8.4}_{-4.1}$ | $7.3^{+5.2}_{-2.5}$ | $1.2^{+1.2}_{-0.44}$ |
| 8596-12702 | $36^{+11}_{-3.0}$ | $48^{+14}_{-3.9}$ | $6.2^{+0.7}_{-1.8}$ | $4.7^{+0.53}_{-1.4}$ | $1.34^{+0.16}_{-0.16}$ |
| 12495-6102 | $12.7^{+2.9}_{-5.3}$ | $23.6^{+5.4}_{-9.7}$ | $17^{+14}_{-4.4}$ | $8.9^{+7.3}_{-2.4}$ | $2.9^{+2.0}_{-1.4}$ |
| 9028-12702 | $15.2^{+1.5}_{-1.5}$ | $25.3^{+2.5}_{-2.5}$ | $14.4^{+2.0}_{-1.6}$ | $8.6^{+1.2}_{-0.99}$ | $1.89^{+0.25}_{-0.22}$ |
| 8619-12701 | $19.4^{+1.9}_{-1.8}$ | $33.1^{+3.2}_{-3.1}$ | $15.6^{+2.9}_{-3.1}$ | $9.1^{+1.7}_{-1.8}$ | $1.40^{+0.28}_{-0.29}$ |
| 11834-12705 | $12.4^{+2.0}_{-3.4}$ | $14.8^{+2.4}_{-4.0}$ | $19.5^{+8.3}_{-3.2}$ | $16.3^{+7.0}_{-2.7}$ | $2.8^{+1.4}_{-0.71}$ |
| 8982-6104 | $19.9^{+3.6}_{-2.6}$ | $28.4^{+5.1}_{-3.7}$ | $8.6^{+1.6}_{-1.2}$ | $6.1^{+1.1}_{-0.87}$ | $1.85^{+0.91}_{-0.59}$ |
| 7962-12704 | $9.0^{+3.4}_{-3.3}$ | $19.9^{+7.6}_{-7.2}$ | $13.4^{+9.7}_{-4.4}$ | $6.0^{+4.4}_{-2.0}$ | $3.0^{+3.2}_{-1.1}$ |
| 9095-9102 | $20^{+11}_{-7.8}$ | $31^{+18}_{-12}$ | $7.9^{+6.0}_{-3.4}$ | $5.1^{+3.9}_{-2.2}$ | $2.0^{+2.5}_{-0.87}$ |
| and 185 more rows... | | | | | |

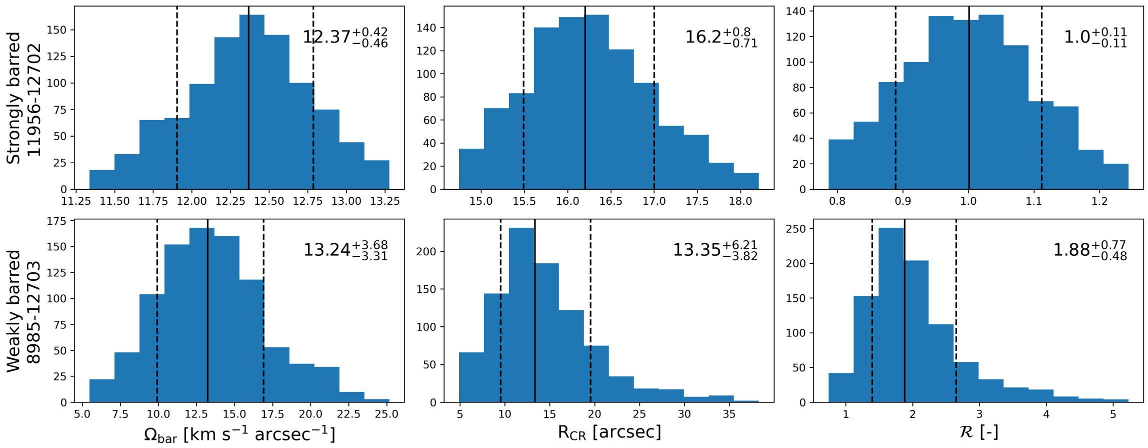

Figure 2.18: The final posterior distributions of the pattern speed (left column), corotation radius (middle column) and $\mathcal{R}$ (right column) for a strongly barred galaxy (top row) and weakly barred galaxy (bottom row). The posterior distributions were obtained by performing Monte Carlo (MC) simulations of 1,000 iterations in order to characterise the uncertainty on each measurement. The median value is shown in every plot by a black vertical line, while the 16th and 84th percentile are shown by the dashed vertical lines. These values are also indicated in the top-right corner of each subplot.

MaNGA, overlaid with an aperture positioned along the PA of the bar and with a width of 3 arcsec. The distance to the centre of the galaxy is calculated for every spaxel whose centre falls within the aperture, as well as the distance normalised to the bar radius. These are plotted against EW[H$\alpha$] in the top and bottom middle panels, respectively. Next, the radius profile for this galaxy is calculated by binning these spaxels into bins that have a width of 1 arcsec and 0.15 $R_{\rm bar}$ for the top middle and bottom middle panel, respectively, and taking the median in every bin. The radius profile of this particular galaxy has an interesting shape. The EW[H$\alpha$] seems to peak in the centre, after which it goes down until ∼2 arcsec or ∼0.6 $R_{\rm bar}$. The EW[H$\alpha$] rises again and reaches a second peak around ∼4.5 arcsec or ∼1.2 $R_{\rm bar}$, after which it falls again. Interestingly, this second peak reaches its maximum right behind the end of the bar. In this particular example, it seems like EW[H$\alpha$] is high in the centre and bar-ends, while being lower in the bar arms and outside the bar.

If all galaxies are binned in the same way, it is possible to generate a median profile of any sample of galaxies by taking the median of all profiles. This is shown in the top-right and bottom-right panels of Figure 2.19 for the two different metrics of distance. Here, the median radius profiles for all strongly barred star forming galaxies in the GZ DESI-MaNGA sample have been generated, which are shown by the faint grey lines in the background. The median value in every bin is calculated and shown by the thicker orange line. This is the median radius profile of EW[H$\alpha$], which is representative of the population of strongly barred star forming galaxies in the GZ DESI-MaNGA sample.

In some situations (e.g. to facilitate comparison with barred galaxies), I want to generate radius profiles normalised to $R_{\mathrm{bar}}$ for unbarred galaxies. In order to achieve this, the bar length distribution of all barred galaxies was fitted with a log-normal distribution, shown in Figure 2.20. Every unbarred galaxy was assigned a bar length to normalise with, which was randomly drawn from this distribution. However, it must be noted that this was done just to provide a benchmark to compare the barred galaxies with and that any trends with $R_{\mathrm{bar}}$ found for unbarred galaxies do not have any physical meaning.

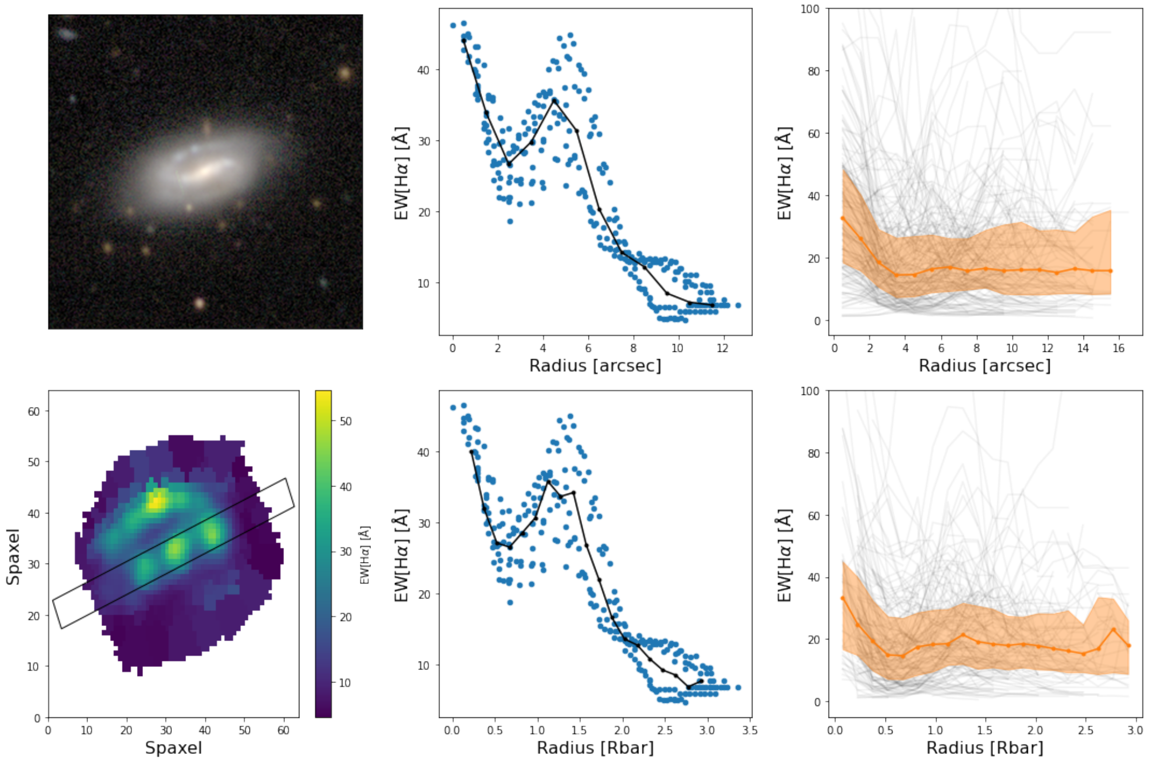

Figure 2.19: This figure shows demonstrates how the radius profiles are constructed using a random strongly barred star forming galaxy (plate-ifu: 12622-9101), visualised in the top left panel. The bottom left panel shows the EW[H$\alpha$] map obtained from MaNGA. This panel is overlaid with an aperture positioned along the PA of the bar. All the spaxels whose centre lie within the aperture are extracted from the map. The EW[H$\alpha$] of those spaxels is plotted against the distance to the centre of the galaxy in the top middle panel. The same plot is shown in the bottom middle panel, but the distance is normalised to the bar radius of this galaxy. The radius profile of this particular galaxy is shown by the black line. Finally, if multiple galaxies are binned in the same way, it is possible to create an median profile of any sample of galaxies by taking the median value in each bin. The top and bottom right panels show the radius profiles of all strongly barred star forming galaxies in the GZ DESI-MaNGA sample using the faint grey lines. The thicker orange line shows the median radius profile of EW[H$\alpha$] for strongly barred star forming galaxies. The shaded regions represent the $25^{\text{th}}$ and $75^{\text{th}}$ percentile in every bin.

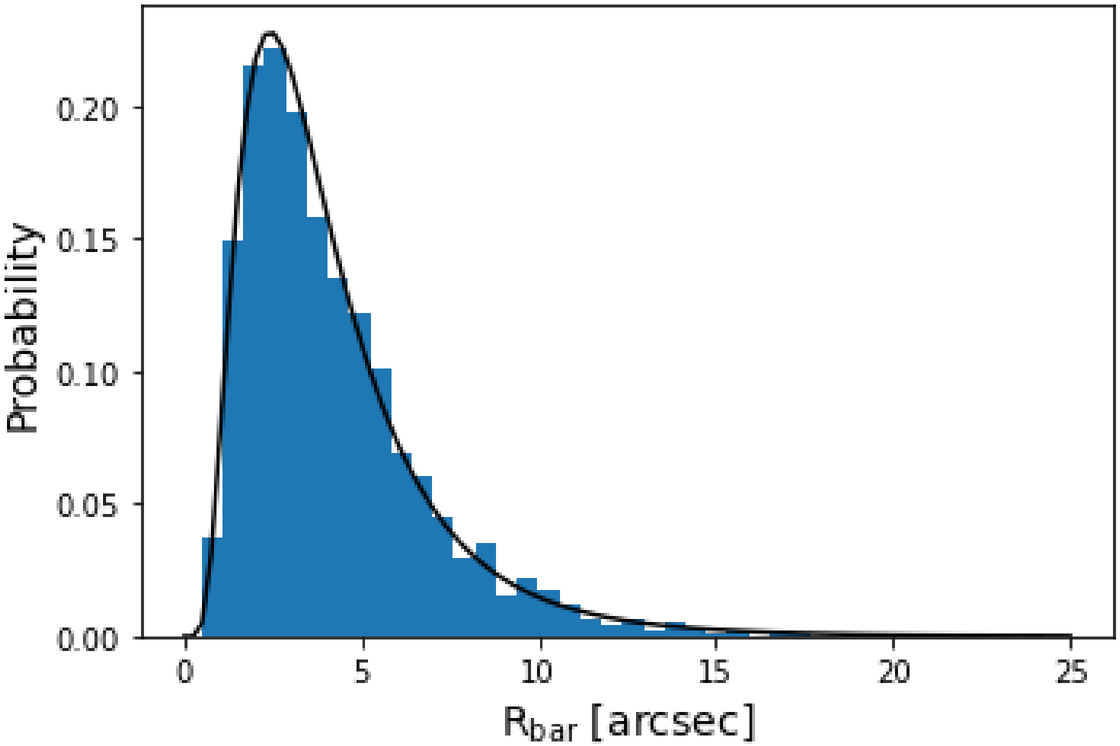

Figure 2.20: The bar radius distribution for all barred galaxies (blue histogram) is fitted with a log-normal distribution (black line).

# Chapter 3

# Strong and weak bars in Galaxy Zoo DECaLS: Stronger bars facilitate quenching in star forming galaxies

*The contents of this chapter have been published in Géron et al. (2021).*

In this chapter, I contrast the properties of strong and weak bars in the GZ DECaLS-SDSS sample, which contains 1,867 galaxies and is described in Section 2.1.6.1. As noted before, the stellar masses and star formation rates (SFRs) used in this chapter were obtained from MPA-JHU (Kauffmann et al., 2003; Brinchmann et al., 2004; Tremonti et al., 2004, see Section 2.1.1), while gas mass estimates were taken from ALFALFA (Giovanelli et al., 2005; Haynes et al., 2011, 2018, see Section 2.1.4). The GZ DECaLS-SDSS sample is unique as it has a large number of weakly barred galaxies. GZ DECaLS was able to identify these weak bars due to the deep imaging and detailed decision tree used during classification. This allows me to study the effects of that bars, strong and weak, have on their host.

Observational studies have shown that bars are more common in massive, red and gas-poor galaxies (Masters et al., 2012; Cervantes Sodi, 2017; Vera et al., 2016; Fraser-McKelvie et al., 2020b). However, as suggested by Masters et al. (2012), it is not clear whether this observation means that it is easier to form a bar in a quiescent galaxy, or that a bar helps to quench its host through a type of slow or 'secular' evolution. Bars are thought to funnel gas to the centre (Debattista & Sellwood, 2000; Athanassoula, 2003; Martinez-Valpuesta et al., 2006; Okamoto et al., 2015) and after the gas is concentrated in the centre, it is available to increase star formation.

Multiple studies have observed enhanced star formation in barred galaxies (Alonso-Herrero & Knapen, 2001; Hunt et al., 2008; Ellison et al., 2011; Coelho & Gadotti, 2011; Hirota et al., 2014; Janowiecki et al., 2020; Magaña-Serrano et al., 2020; Lin et al., 2020). A galaxy with increased star formation will use up its gas quicker, which could cause it to eventually quench, assuming that the gas is not replenished (Kormendy & Kennicutt, 2004; Sheth et al., 2005; Athanassoula, 2007; Masters et al., 2011; Cheung et al., 2013; Kruk et al., 2018; Efthymiopoulos et al., 2019). In this chapter, I shall test whether evidence of secular evolution caused by bars is found in the GZ DECaLS-SDSS sample. Most importantly, I will look at whether this secular evolution can be caused by both weak and strong bars, or only by one bar type.

First, in Section 3.1, I describe the differences in bar length between weak and strong bars identified in GZ DECaLS. In Section 3.2, I investigate the general properties of strongly and weakly barred galaxies. Afterwards, in Section 3.3, I look at the location of strongly and weakly barred galaxies on the colour-magnitude diagram and SFR-mass plane. In Section 3.4, I provide evidence for secular quenching observed in strongly barred galaxies. Finally, I ask the fundamental question of whether strong and weak bars actually are distinct physical phenomena in Section 3.5. The results are discussed and summarised in Sections 3.6 and 3.7, respectively.

## 3.1 Differences in bar length

One of the characteristics of a strong bar is that it is typically longer than a weak bar (de Vaucouleurs, 1959, 1963). During classification, volunteers are told that strong bars "*extend across a large fraction of the galaxy*" while weak bars are "*smaller and fainter relative to the galaxy*". This is reflected in Figure 3.1, where the average vote fraction ($p_{\text{no bar}}$, $p_{\text{weak bar}}$ and $p_{\text{strong bar}}$) is plotted against the length of the bar, which are measured manually as explained in Section 2.2.2. The length of the bar is shown in kpc, as well as relative to the Petrosian $r$-band diameter ($2\text{R}_p$). This last metric, which I will refer to as the 'relative bar length' from now on, is used to quantify the length of the bar in relation to its host. However, do note that the estimate of the SDSS Petrosian diameter can be biased by the presence of a bar, especially a strong bar. As the bar becomes longer, volunteers are more likely to classify it as a strong bar. There are more strong than weak bars above a relative bar length of ∼35% (or an absolute bar length of ∼6 kpc). However, it is interesting to note that there is still a great overlap between weak and strong bars, such that there is no distinct threshold in bar length where volunteers switch between from voting for weakly barred

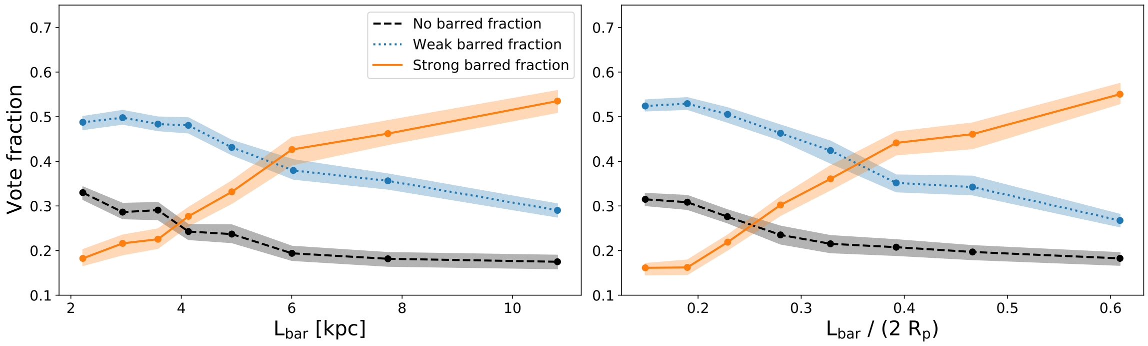

Figure 3.1: The absolute bar length (in kpc, left panel) is plotted against the average strong (orange), weak (blue) and unbarred (grey) vote fraction. The right panel shows the relative bar length (obtained by dividing the absolute length by the SDSS $r$-band Petrosian diameter) against the different average vote fractions. It is clear that volunteers become increasingly confident that a bar is strong as the length of the bar increases. The shaded regions represent the $3\sigma$ region after bootstrapping the data 10,000 times and retaining 90% of the data for each iteration.

to strongly barred. However, as established in Section 2.1.6.1 and discussed in Willett et al. (2013) and Walmsley et al. (2022), the volunteer classifications from GZ2 and GZ DECaLS agree very well with expert classifications. This implies that the overlap in bar length between strong and weak bars is not a consequence of using volunteer classifications, but rather an intrinsic property of strong and weak bars.

Figure 3.2 shows the bar length distributions for the weak and strong bars in the GZ DECaLS-SDSS sample. It shows that strong bars are longer than weak bars, as expected, in terms of absolute and relative bar length. A weak bar will, on average, cover 20-30% of the Petrosian diameter, whereas a strong bar will cover over, on average, 40-45% of the Petrosian diameter. However, there is still a big overlap between the two bar types. Nevertheless, there are very few short strong bars and long weak bars. Only $\sim 7\%$ of strong bars have a relative bar length shorter than the median of the weak bars. Similarly, only $\sim 12\%$ of weak bars have a relative bar length longer than the median of the strong bars.

The galaxies in Figure 3.2 are also separated into 'star forming' (SF) and 'quiescent' groups, by using the star formation sequence defined by Belfiore et al. (2018):

$$\log\left(\mathrm{SFR}/\mathrm{M}_{\odot}\,\mathrm{yr}^{-1}\right) = (0.73 \pm 0.03)\log\left(\mathrm{M}*/\mathrm{M}_{\odot}\right) - (7.33 \pm 0.29)\ , \tag{3.1}$$

where we assume that anything that is $1\sigma$ (= 0.39 dex) below this line is quiescent and everything above is SF. It is interesting to note that, in terms of absolute bar

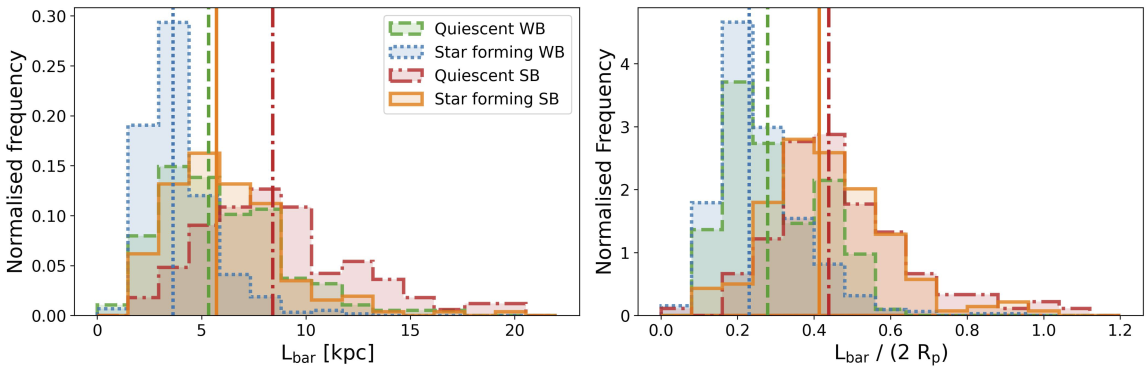

Figure 3.2: The left panel shows the distribution of bar lengths for the different bar types in kpc. The right panel shows the distribution of relative bar length for the different bar types. The bar types are additionally split into SF and quiescent, using Equation 3.1. The vertical lines represent the median of every sample. Strong bars are typically longer than weak bars. Similarly, when looking at the bar lengths in kpc, bars in quiescent galaxies are typically longer than their counterparts in SF galaxies. In terms of relative bar length, a strong bar will, on average, cover 40-45% of the Petrosian diameter of its host, while a weak bar will span 20-30%.

length, bars in quiescent galaxies are longer than their SF counterparts. The longest bars are typically strong bars in quiescent galaxies, whereas the shortest bars are weak bars in SF galaxies. Interestingly, the difference in length between SF and quiescent galaxies seems to disappear when considering relative bar length, which suggests that the bar co-evolves with the entire galaxy, regardless of whether there is ongoing star formation.

In conclusion, Figures 3.1 and 3.2 show that **strong bars are longer than weak bars**. However, there is still a significant overlap in bar length between the two bar types. Volunteers (and, indeed, expert classifiers) become more confident that a bar is strong if it is longer, as was expected due to the information provided to them during classification.

## 3.2 Properties of strongly and weakly barred galaxies

Multiple studies have shown that bars are more frequently found in massive, red, and quiescent galaxies (Masters et al., 2012; Cervantes Sodi, 2017; Vera et al., 2016; Fraser-McKelvie et al., 2020b). Here, I will explore whether that statement holds for our general GZ DECaLS-SDSS sample, and whether it applies to both weak and strong bars. In Figure 3.3, I show how the weak and strong bar populations change with

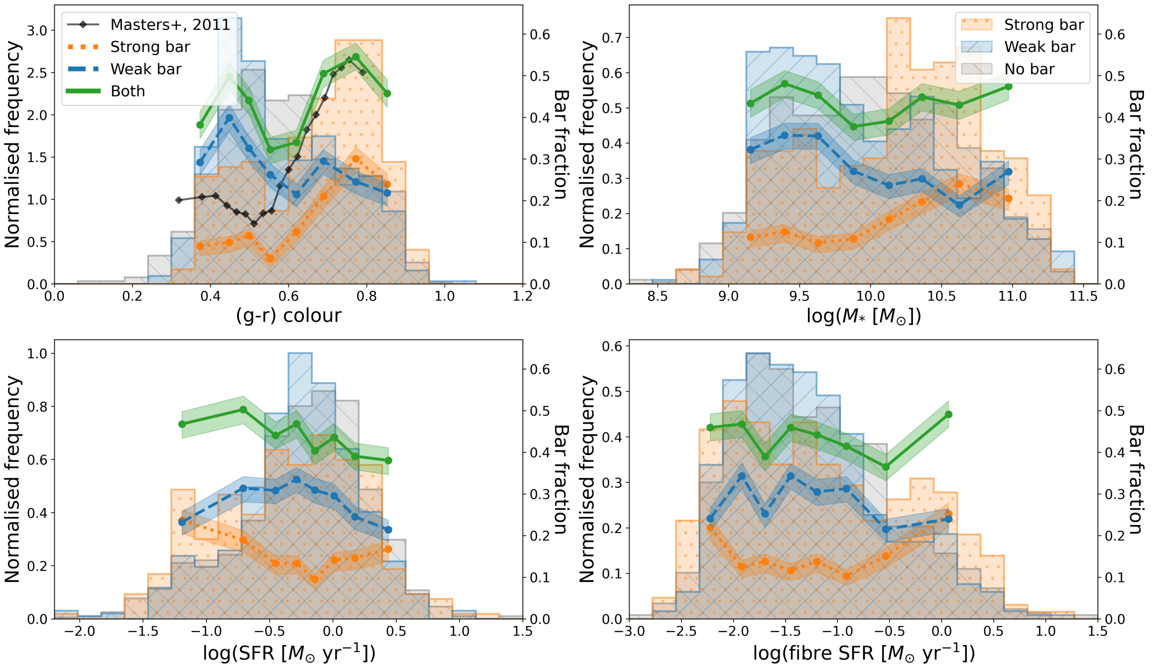

Figure 3.3: The top-left panel shows the effect of (g-r) color on weak (blue), strong (orange), and combined (i.e. strong and weak; green) bar fractions (secondary y-axis). All galaxies are binned in equal-sized bins, while the contours represent the $3\sigma$ region after bootstrapping the data 10,000 times and retaining 90% of the data for each iteration. The histograms in the background show the normalised frequencies of galaxies with a strong bar, a weak bar, and no bar (primary y-axis). This is repeated for the stellar mass in the top-right panel, the SFR in the bottom-left panel, and the fibre SFR in the bottom-right panel. This figure suggests that strong bars drive the consensus that bars are found more often in massive, red and quiescent galaxies. In contrast, the weak bar fraction actually decreases with redder colours and increasing stellar mass.

respect to ($g$-$r$) colour, stellar mass, global SFR and fibre SFR. The primary y-axis shows the absolute number of bars, visualised with the histograms (the histograms are normalised so that the area under each histogram equals one). The secondary y-axis indicates the bar fraction, which is the number of barred galaxies of a particular bar type divided by the total number of galaxies in that bin, shown by the different lines. The dependence of the bar types on the ($g$-$r$) colour is shown in the top-left panel. The strong bar fraction is higher at redder colours, while the weak bar fraction decreases as the colour becomes redder. The results from Figure 3 from Masters et al. (2011), who also studied the relationship between colour and bar fraction, are also shown in this panel. The results presented here seem to agree with theirs, especially at redder colours.

The top-right panel of Figure 3.3 shows the distribution of stellar mass for the different bar types. The strong bar fraction rises with stellar mass, while this is not the case for weak bars. Our sample contains a lot of weak bars in low-mass galaxies, which is in agreement with Elmegreen & Elmegreen (1985), who found a similar result.

The SFR distributions shown in the bottom-left and bottom-right panels also provide interesting insights. The strong bar fraction appears highest at lower global SFRs. However, the histograms show that most strong bars are actually in the middle global SFR range (SFR $\sim$1 $M_{\odot}$ $yr^{-1}$). The 'combined' bar fraction decreases with SFR. The strong bar fraction seems lowest in the middle fibre SFR ranges. There is no clear trend here for the weak and 'combined' bar fractions in terms of fibre SFR.

The fibre SFR is included in this analysis because it measures the SFR in the central 3 arcsec of the galaxy. This region is of particular interest when studying the effects of bars, as it is believed that the bar drives gas to the centre of the galaxy (Sorensen et al., 1976; Athanassoula, 1992b; Davoust & Contini, 2004; Athanassoula et al., 2013; Villa-Vargas et al., 2010; Vera et al., 2016; Spinoso et al., 2017; George et al., 2019), where it can enhance star formation. However, the physical size of the 3 arcsec region that the fibre probes will vary depending on the redshift of the galaxy, which ranges between 0.69 and 2.93 kpc for our sample. Figure 3.4 shows the distributions of the physical distance corresponding to the 3 arcsec fibre for every bar type. A KS test for every comparison shows that they are not significantly different (all three comparisons are $< 1.5\sigma$). This suggests that the redshift distributions of the three samples are similar. Additionally, this shows that this effect applies to the different populations equally and that it can be ignored.

The data presented in this section shows that **the consensus that bars are found more often in massive, red and quiescent galaxies is driven by strongly barred galaxies**. The trends for the weak bars are different: the weak bar fraction actually decreases with redder colours and increasing stellar mass.

## 3.3 Colour-magnitude diagram and SFR-mass plane

It is also possible to investigate the bar fraction across the colour magnitude diagram, where galaxies are typically divided into the 'blue cloud' and 'red sequence'. We use the 'blue edge of the red sequence' defined by Masters et al. (2010) to divide our

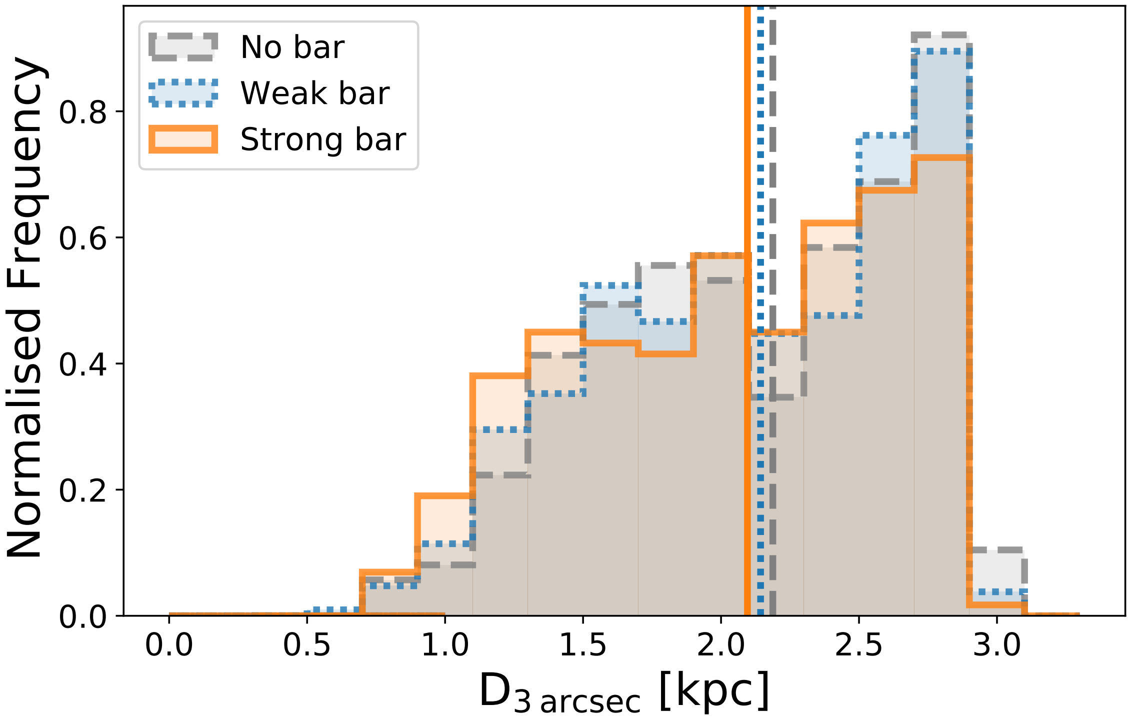

Figure 3.4: The histograms show the distribution of the physical distance corresponding to the 3 arcsec fibre ($D_{3\ \mathrm{arcsec}}$) for the three bar types. The dashed line indicated the median value for each bar type. The three distributions do not significantly differ from each other, as indicated by the results of a KS test for the three comparisons, which is always $< 1.5\sigma$.

Table 3.1: The fraction of each bar type present in each galaxy type (the percentages sum to 100 down every column). The total number of every group is always shown in parentheses. The galaxies are divided into blue cloud or red sequence using Equation 3.2 and into star forming or quiescent using Equation 3.1. The colour-magnitude diagram and SFR-mass plane are shown in more detail in Figures 3.5 and 3.6.

| | Blue cloud | Red sequence | Star forming | Quiescent |
|---|---|---|---|---|
| Strong bar | 9.6% (111) | 24.9% (178) | 13.0% (176) | 22.0% (113) |
| Weak bar | 29.9% (345) | 25.2% (180) | 29.3% (397) | 25.0% (128) |
| No bar | 60.5% (697) | 49.9% (356) | 57.7% (781) | 53.0% (272) |

sample in these respective categories:

$$(g - r) = 0.63 - 0.02(M_r + 20) \ , \tag{3.2}$$

where $M_r$ is the $r$-band absolute magnitude. This threshold is used in order to identify all galaxies that are clearly in the red sequence. The colour-magnitude diagram for the disc galaxies in the GZ DECaLS-SDSS sample is plotted in Figure 3.5, where it is shown that the weak bar fraction is slightly higher in the blue cloud than in the red sequence, but not by a wide margin (29.9% and 25.2%, respectively). Conversely, the strong bar fraction is noticeably higher in the red sequence (24.9%) than in the blue cloud (9.6%). These percentages are summarised in Table 3.1. The colour distribution of galaxies with strong bars is also significantly different from the underlying colour distribution of unbarred galaxies (the p-value of a KS test, p-value$_{\mathrm{KS}}$, is lower than $10^{-15}$, which corresponds to $>8\sigma_{\mathrm{KS}}$). This suggests that a strong bar may influence the colour of its host, and possibly its evolution. The colour distribution of weakly barred galaxies compared to unbarred galaxies is less significantly different (p-value$_{\mathrm{KS}}$ = 0.012; $2.5\sigma_{\mathrm{KS}}$). Interestingly, the absolute magnitude distributions of galaxies with weak bars and no bars are more significantly different (p-value$_{\mathrm{KS}}$ = 0.009; $2.6\sigma_{\mathrm{KS}}$) than the distributions of galaxies with strong bars and no bars (p-value$_{\mathrm{KS}}$ = 0.98; $0.03\sigma_{\mathrm{KS}}$), but both comparisons are still $< 3\sigma$.

A similar analysis is shown on the SFR-stellar mass plane in Figure 3.6. The plane divides the sample into 'star forming' and 'quiescent' using Equation 3.1. The weak bar fractions are similar in the quiescent and SF group, (25.0% and 29.3%, respectively), whereas the strong bar fraction is much higher among quiescent disc galaxies than in the SF disc galaxies (22.0% and 13.0%, respectively). These percentages are also shown in Table 3.1. However, please note that in absolute numbers, there actually seem to be more strong bars in SF galaxies (176 galaxies) than in quiescent galaxies (113 galaxies). The stellar mass distributions of weakly barred and

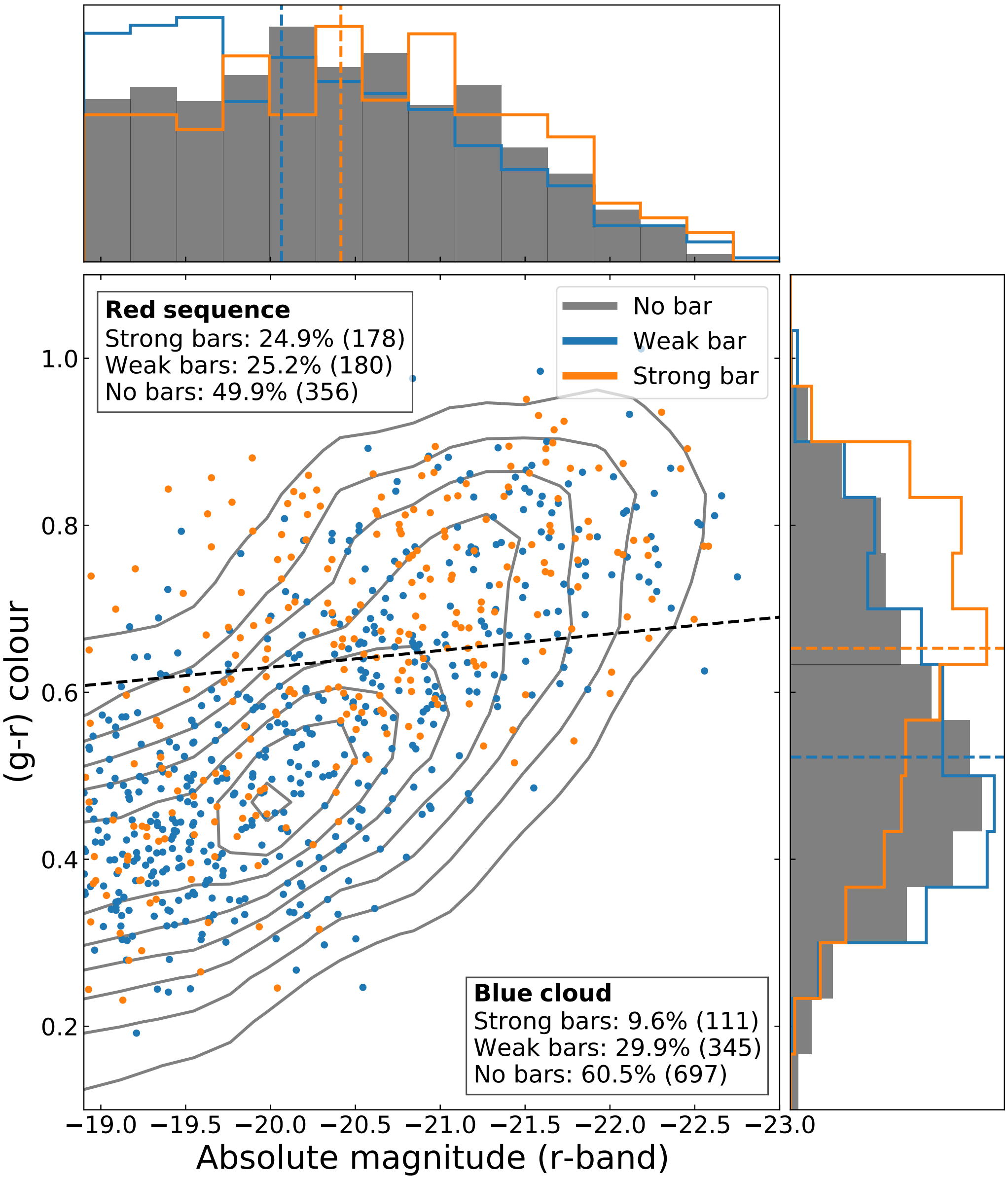

Figure 3.5: The location of all strongly barred (orange) and weakly barred (blue) galaxies in the GZ DECaLS-SDSS sample is shown on the colour-magnitude diagram. The contour plot in the background shows the location of all galaxies without bars in the GZ DECaLS-SDSS sample. The dashed line across the diagram defines the 'blue edge of the red sequence' and effectively divides the sample into the red sequence (above the line) and the blue cloud (underneath the line, as defined in Masters et al. 2010). The histograms on the right side and on top of the main panel are the normalised histograms of the $(g\text{-}r)$ colour and absolute $r$-band magnitude, respectively, for the three different bar types. The galaxies with a strong bar are clustered around the red sequence, while the weakly barred galaxies are distributed equally across the diagram.

unbarred galaxies are also significantly different (p-value$_{\mathrm{KS}}$ = 0.001; 3.2$\sigma_{\mathrm{KS}}$), suggesting a significant population of low-mass galaxies with weak bars, which is consistent with what we saw in the top-right panel of Figure 3.3. In contrast, there seem to be more high-mass galaxies with a strong bar compared to unbarred galaxies (p-value$_{\mathrm{KS}}$ $< 10^{-6}$; $>4.9\sigma_{\mathrm{KS}}$).

Previous studies typically found that bars appear more often in massive, red and quiescent galaxies. These results once again show that this is only true for strong bars. **The fraction of strong bars is much higher among red sequence and quiescent galaxies than among blue cloud and star forming galaxies. Interestingly, the weak bar fraction is similar for these groups.** The weak bar fraction is only slightly higher in blue and low-mass galaxies. However, as noted by Masters et al. (2012), this can be interpreted in multiple ways: is it the strong bar that causes the transition from the SF group to the quiescent group by quenching the galaxy or is it easier to form strong bars in quenched galaxies? This is discussed in the next section.

## 3.4 Bars and quenching

I have shown in Section 3.3 that the fraction of strongly barred galaxies is higher in quiescent galaxies than in SF galaxies, while this is not the case for weakly barred galaxies. However, it is not obvious whether this suggests that it is easier to form strong bars in quenched galaxies or whether strong bars help to quench their host. This issue is addressed by looking at the fibre SFR, which is the SFR in the central 3 arcsec of a galaxy, as the central region of the galaxy is where bars are expected to increase the star formation. The alternative would be to use the global SFRs from MPA-JHU (Brinchmann et al., 2004), however, they are influenced by the colour outside the fibre (see Section 2.1.1 for more details). Kruk et al. (2018) has shown that bars are typically redder than discs, so this could affect our multiple bar types differently. Thus, to address this issue, I decided to work with the fibre SFR based on emission lines rather than the global SFR.

The Kennicutt-Schmidt law (Kennicutt, 1998a,b) suggests a relationship between SFR and gas. In order to probe the differences in gas mass between the different bar types, we use the gas mass measurements from the ALFALFA catalogue of extragalactic HI sources (Giovanelli et al., 2005; Haynes et al., 2011, 2018). However, as discussed in Section 2.1.4, the GZ DECaLS-SDSS sample contains a lot of non-detections in ALFALFA, which have to be correctly accounted for. One method to

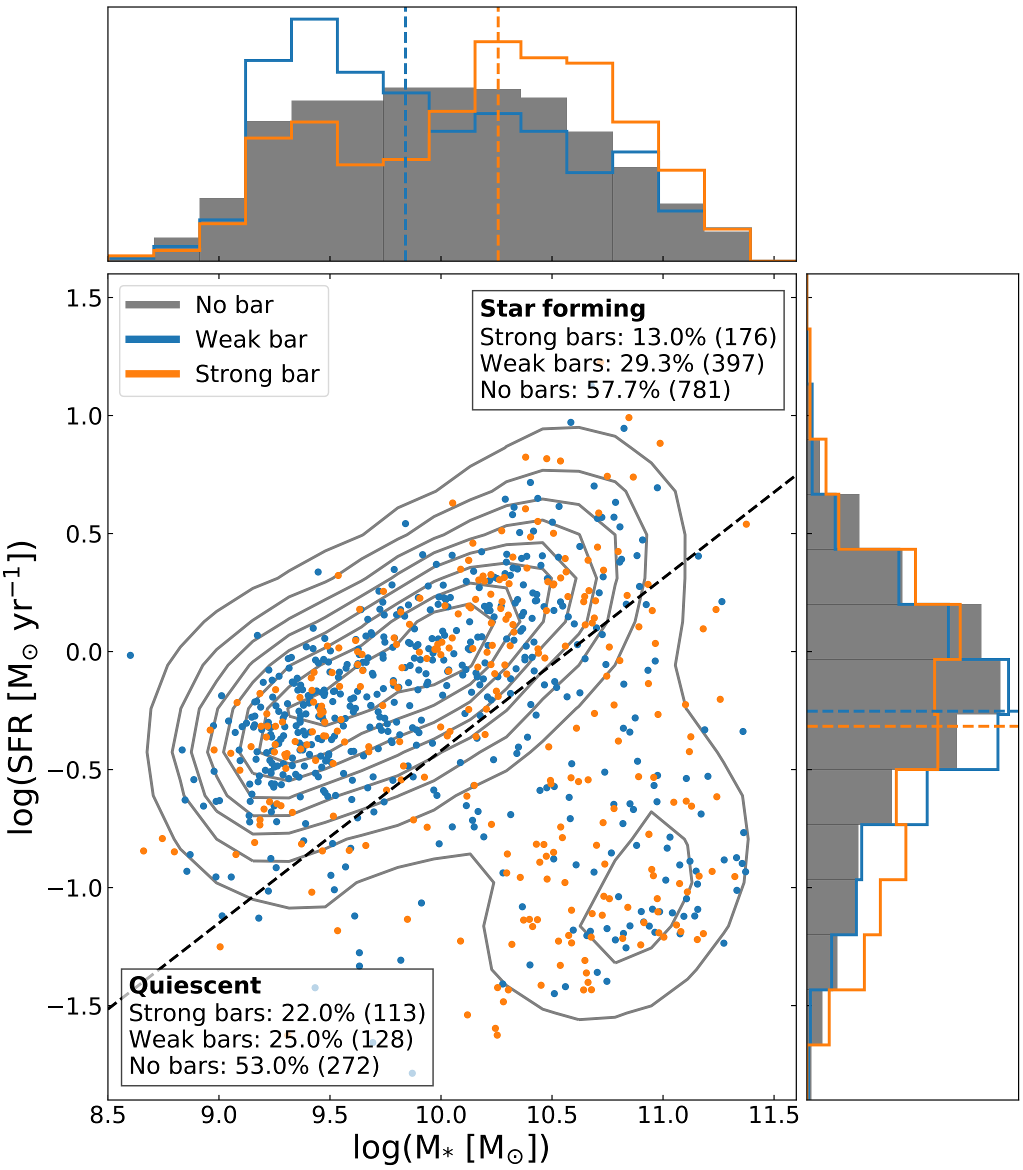

Figure 3.6: The location of all strongly barred (orange) and weakly barred (blue) galaxies is shown on the SFR-stellar mass plane. The contour plot in the background shows the location of all galaxies without bars. The dashed line across the plane divides the sample into a SF region (above the line) and quiescent region (below the line, as defined in Belfiore et al. 2018). The histograms on the right side and on top of the main panel are the normalised histograms of the SFR and stellar mass, respectively, for the three different bar types. The weakly barred galaxies are distributed equally across this plane, while the galaxies with a strong bar seem to concentrate in the quiescent region.

deal with them is called ‘survival analysis’, a statistical technique that is able to compare two populations with left-censored data points (i.e. non-detections) in a parameter by constructing the cumulative density function (CDF) for that parameter. The CDFs for every population can be compared with each other by using the well established Cox’s proportional hazards model and the resultant p-values (p-value$_{\rm CPH}$, Cox, 1972). This is all done in Python using the package `lifelines` (Davidson-Pilon et al., 2020)[1].

I show the CDFs of the fibre SFR and HI gas for all bar types in Figure 3.7. The sample is additionally split up into SF (left column) and quiescent (right column) galaxies, using Equation 3.1. The results for HI gas mass are shown in the top row, which show that SF galaxies with a strong or weak bar have significantly less HI gas than unbarred galaxies (p-value$_{\rm CPH}$ $< 10^{-5}$; $>4.4\sigma_{\rm CPH}$ and p-value$_{\rm CPH}$ $< 10^{-3}$; $>3.3\sigma_{\rm CPH}$, respectively). Galaxies with a strong bar have the least HI gas. The fibre SFR results are shown in the middle row. Interestingly, SF strongly barred galaxies have significantly higher fibre SFR than both weakly and unbarred galaxies (p-value$_{\rm CPH}$ $< 10^{-6}$; $>4.8\sigma_{\rm CPH}$ and p-value$_{\rm CPH}$ $< 10^{-5}$; $>4.4\sigma_{\rm CPH}$, respectively), which do not differ from each other. No differences were observed among the different bar types in quiescent galaxies in terms of HI gas mass or fibre SFR.

Additionally, it is possible to combine the fibre SFR and gas mass measurements together and form the depletion timescale:

$$t_{\rm dep} = \frac{\rm M_{gas}}{\rm fibre\ SFR}\ , \tag{3.3}$$

where $t_{\rm dep}$ is the depletion timescale and $\rm M_{gas}$ is the gas mass. The depletion timescale probes how quickly a galaxy will empty its gas reservoir for a given SFR (Janowiecki et al., 2020). A short depletion timescale suggests that a galaxy will go through its gas reservoir quickly, while the opposite is true for galaxies with a long depletion timescale. However, this is a simplified assumption. As Janowiecki et al. (2020) notes, this assumes a constant SFR and that gas recycling is non-existent, while other work (Kannappan et al., 2013) has shown that refueling can happen in SF galaxies on ∼Gyr timescales. Additionally, ALFALFA provides estimates for HI gas masses, not for the molecular gas which is necessary for star formation (Kennicutt & Evans, 2012; Saintonge et al., 2016; Catinella et al., 2018). However, most of the cool gas mass is typically found as HI gas, so the the HI gas mass accurately represents the complete fuel reservoir of a galaxy that will be used for future star formation (Haynes

---

[1] `lifelines`: `https://lifelines.readthedocs.io/en/latest/#`

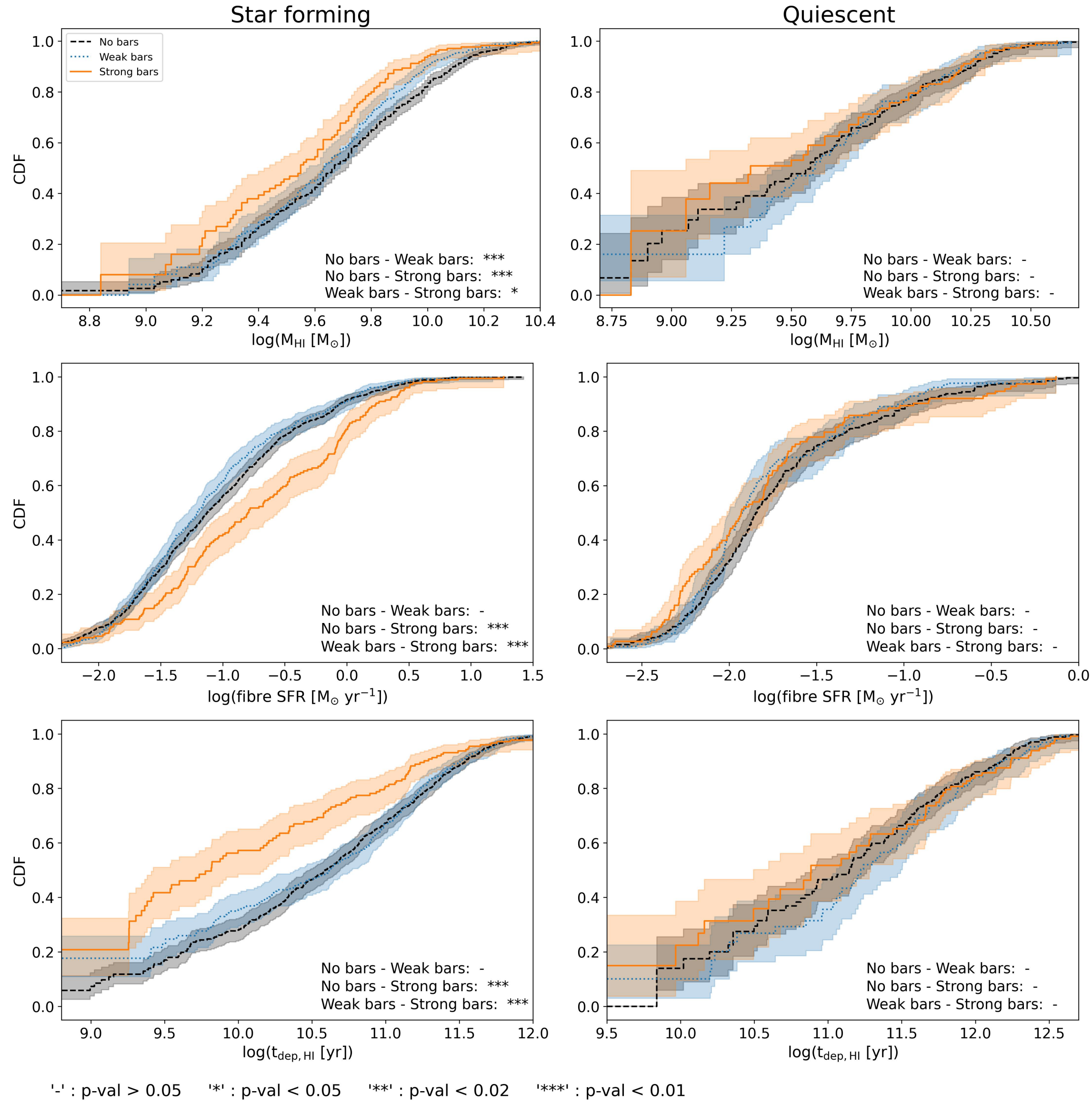

Figure 3.7: The cumulative density functions (CDFs) of HI gas mass (top row), fibre SFR (middle row) and depletion timescale (bottom row) for SF galaxies (left column) and quiescent galaxies (right column) are shown for all our bar types. The CDFs are generated by performing a survival analysis. The results of the Cox's proportional hazards model are displayed in the bottom-right corner of every panel to indicate how significantly different the CDFs are for every population. If the p-value is above 0.05 (i.e. the CDFs are clearly not significantly different), it is denoted with '-'. If the p-value was between 0.02 and 0.05, '*' was used. If it was between 0.01 and 0.02, it is marked with '**'. If the p-value was below 0.01 (i.e. they are significantly different), it is denoted with '***'. SF galaxies with a strong bar seem to be significantly different from weakly barred and unbarred SF galaxies, especially in fibre SFR and depletion timescale. There are no observed differences among the bar types in quiescent galaxies.

et al., 2018). Finally, the SFR in the fibre is used and compared to the global HI gas mass; by doing so it is assumed that there is little to no star formation outside the fibre, which is unlikely. These assumptions will cause the final values calculated here to overestimate the true depletion timescale. Nevertheless, these issues affect our strongly and weakly barred samples the same way, so it is still a useful metric to compare the bar types with.

The CDFs of the depletion timescale for the different bar types is shown in the bottom row of Figure 3.7. I find that SF galaxies with a strong bar have significantly shorter depletion timescales than weakly and unbarred galaxies (p-value$_{\rm CPH} < 10^{-3}$; $>3.2\sigma_{\rm CPH}$ and p-value$_{\rm CPH} < 10^{-5}$; $>4.4\sigma_{\rm CPH}$, respectively). No significant differences are observed between weakly and unbarred SF galaxies and among the different bar types in quiescent galaxies. All these results suggest that SF galaxies with a strong bar are rapidly evolving galaxies that use their gas quickly due to an increase in SFR in the centre of the galaxy.

As mentioned before, the fibre SFR only probes the central 3 arcsec. However, the physical distance corresponding to the central 3 arcsec ($D_{3\ \rm arcsec}$) depends on the redshift of each target; $D_{3\ \rm arcsec}$ is longer for targets at higher redshifts. As shown in Figure 3.4, the different bar types have similar distributions of $D_{3\ \rm arcsec}$, so it is not expected that this will bias the results presented here. To make sure this is not the case, the CDFs of fibre SFR are additionally split up in different bins of $D_{3\ \rm arcsec}$. However, this reduces the sample size in every bin. The results of this are shown in Figure 3.8. As expected, the conclusions remain largely the same. There are little to no significant differences observed among the different bar types in quiescent galaxies. In SF galaxies, strongly barred galaxies have significantly higher fibre SFRs than unbarred galaxies, while weakly barred galaxies do not. This is observed in every $D_{3\ \rm arcsec}$ bin, except in the highest bin (so at the highest redshifts). It is assumed that the effects that the strong bar has on the centre of the galaxy are being diluted by the surrounding areas that, due to the high redshift of these targets, are now placed within the 3 arcsec fibre (the median angular size of the bars in the highest redshift bin is ~5.6 arcsec).

Studies have shown that stellar mass correlates with both gas mass and (fibre) SFR (Brinchmann & Ellis, 2000; Brinchmann et al., 2004; Noeske et al., 2007; Lara-López et al., 2010). As we have observed differences in stellar mass between the bar types (see Figure 3.3), it is important to account for this bias. This is done by generating linear relationships between the different parameters using the Python package `linmix`[2].

---

[2] `linmix`: `http://linmix.readthedocs.org/`

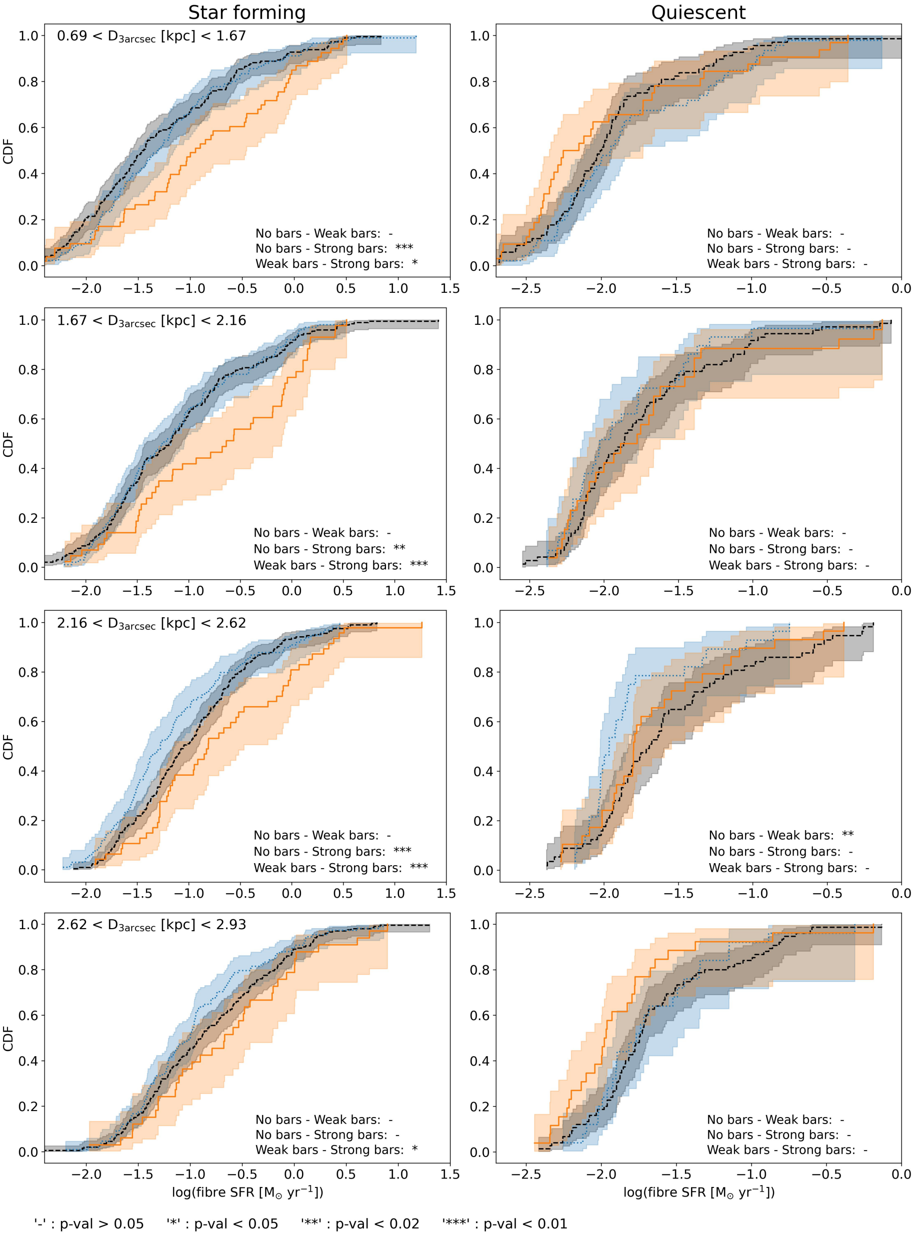

Figure 3.8: The cumulative density functions (CDFs) fibre SFR for SF galaxies (left column) and quiescent galaxies (right column) are shown for all our bar types. The galaxies are additionally split up in four bins of $D_{3\ \mathrm{arcsec}}$ (i.e. physical distance corresponding to the 3 arcsec fibre in kpc), which are shown from lowest $D_{3\ \mathrm{arcsec}}$ bin to highest $D_{3\ \mathrm{arcsec}}$ bin from top to bottom. The CDFs are generated by performing a survival analysis. The results of the Cox's proportional hazards model are displayed in the bottom-right corner of every panel to indicate how significantly different the CDFs are for every population. If the p-value is above 0.05 (i.e. the CDFs are clearly not significantly different), it is denoted with '-'. If the p-value was between 0.02 and 0.05, '*' was used. If it was between 0.01 and 0.02, it is marked with '**'. If the p-value was below 0.01 (i.e. they are significantly different), it is denoted with '***'.

This package is based on the hierarchical Bayesian model described in Kelly (2007) and works by running a Markov chain Monte Carlo (MCMC) algorithm to sample the posterior distributions of the coefficients of the linear relationship between two parameters, while correctly dealing with two-dimensional heteroscedastic uncertainties and non-detections. It is assumed that the distribution of the independent variable ($\xi$, here: stellar mass) can be described as a Gaussian mixture model:

$$p(\xi|\pi, \mu, \tau^2) = \sum_{k=1}^{K} \frac{\pi_k}{\sqrt{2\pi\tau_k^2}} \exp\left(-\frac{1}{2}\frac{(\xi - \mu_k)^2}{\tau_k^2}\right) , \tag{3.4}$$

where $\pi$ is the probability of every Gaussian component, $\mu$ is the mean of every component and $\tau^2$ is the variance of every component. It also assumes that the true independent and dependent ($\eta$, here: gas mass, fibre SFR or depletion timescale) variables are related by:

$$\eta \sim N\left(\alpha + \beta\xi, \sigma^2\right) , \tag{3.5}$$

where $\alpha$ and $\beta$ are the intercept and slope of the linear fit, respectively, and $\sigma^2$ is the Gaussian scatter around the linear fit. The priors on $\alpha$, $\beta$ and $\sigma^2$ are uniform distributions (Kelly, 2007). After running the MCMC algorithm, this technique will provide accurate posterior distributions for $\alpha$ and $\beta$, which are used in Figure 3.9 to estimate the linear relationship between stellar mass and gas mass (top row), fibre SFR (middle row) and depletion timescale (bottom row). The relationship for the unbarred SF targets is shown in the left column, the SF weakly barred galaxies in the middle column and the SF strongly barred galaxies in the rightmost column. The trend for the unbarred galaxies is shown with a dashed line in all subplots to facilitate comparison. Galaxies with a strong bar seem to have lower HI gas masses, especially at higher stellar masses ($10^{9.5} M_\odot > M_*$), compared to unbarred galaxies. The trend for weakly barred galaxies is more similar to the unbarred trend. Additionally, galaxies with weak bars do not have significantly different fibre SFRs, compared to unbarred galaxies, while strongly barred galaxies do, especially at higher stellar masses. Finally, trends for depletion timescale show similar results: especially at higher stellar masses, the depletion timescale is shorter for strongly barred galaxies than for unbarred galaxies, while this is not the case for weakly barred galaxies.

Both the survival analysis shown in Figure 3.7 and the results in Figure 3.9 imply the same result: SF galaxies with a strong bar differ significantly from weakly barred and unbarred SF galaxies. Strongly barred SF galaxies have lower HI gas mass, possibly due to higher fibre SFRs, which leads to shorter depletion timescales,

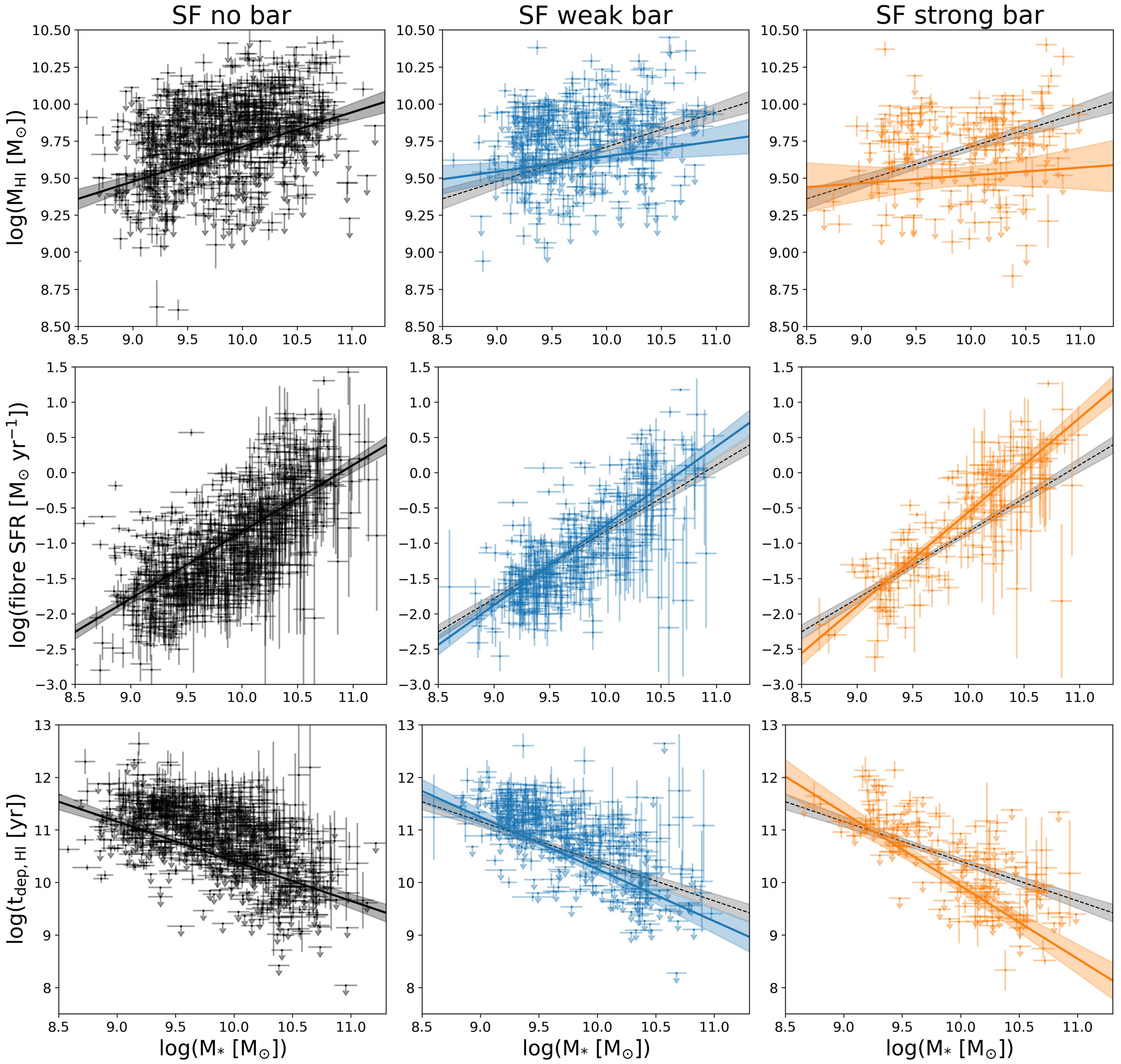

Figure 3.9: The Python package `linmix`, based on the hierarchical Bayesian model of Kelly (2007), was used to create one-dimensional trends between stellar mass and HI gas mass (top row), fibre SFR (middle row) and depletion timescale (bottom row) for the SF galaxies in the sample. The unbarred galaxies are shown in the left column, the weakly barred galaxies in the middle column and the strongly barred galaxies in the right column. The unbarred trends are also shown in the other subplots to facilitate comparison. The shaded region represents the $2\sigma$ errors on the fit. It seems that the trends for the weakly barred SF galaxies are similar to those of the unbarred galaxies. Conversely, trends of the strongly barred SF galaxies seem very different from those of the unbarred galaxies. Strongly barred galaxies have lower HI gas mass, higher fibre SFRs and shorter depletion timescales, except at the lower stellar masses.

compared to unbarred galaxies. In contrast, weakly barred SF galaxies do not differ significantly from unbarred galaxies in terms of fibre SFR and depletion timescale. Therefore, **strongly barred SF galaxies seem to be rapidly evolving galaxies which help to quench their host more efficiently than their unbarred and weakly barred counterparts**.

## 3.5 Bar continuum

The results presented above suggest that strongly barred SF galaxies have higher fibre SFRs than weakly barred and unbarred galaxies. However, do these results still hold when controlling for bar length? In Figure 3.10, the fibre SFR is plotted against the length of the bar for weakly and strongly barred galaxies, which are also divided into SF and quiescent groups. The bar length is given in kpc in the left panel and in relative units (relative to the Petrosian diameter of the galaxy) in the right panel. Interestingly, this figure shows that, after controlling for bar length, galaxies with a strong bar do not have higher fibre SFR than galaxies with a weak bar. It seems that strong and weak bars have similar influences on their host (i.e. they funnel gas to the centre of the galaxy, where it is available to increase SFR) for a given bar length. Additionally, for SF galaxies, the fibre SFR positively correlates with bar length, suggesting that the longest and strongest bars have the higher fibre SFR and will affect their host galaxy the most. This was not observed for the quiescent galaxies. This result leads to a more fundamental question: are strong and weak bars fundamentally distinct physical phenomena and distinct populations, or are they simply two labels given to bars that are on the opposite ends of a continuum of bar types? The results of Figure 3.10 seem to suggest the latter option.

This idea is verified qualitatively in Figure 3.11, where we show DECaLS postage stamps of randomly selected strongly and weakly barred galaxies with an intermediate relative bar length ($0.27 < \mathrm{L_{bar}}/(2\ \mathrm{R}_P) < 0.37$). About 23% (188 out of 814) of our barred galaxies fall within this range. It is not clear at all from visual inspection of these galaxies whether they should be classified as strong or weak. It appears that strongly and weakly barred galaxies in that intermediate relative bar length range are very morphologically similar. This is in stark contrast with the strong and weak bars shown earlier in Figure 2.4 in Section 2.1.6.1, where the differences between weak and strong bars were obvious. All these results suggest that, **after controlling for bar length, strong and weak bars are hard to differentiate**. This supports the idea

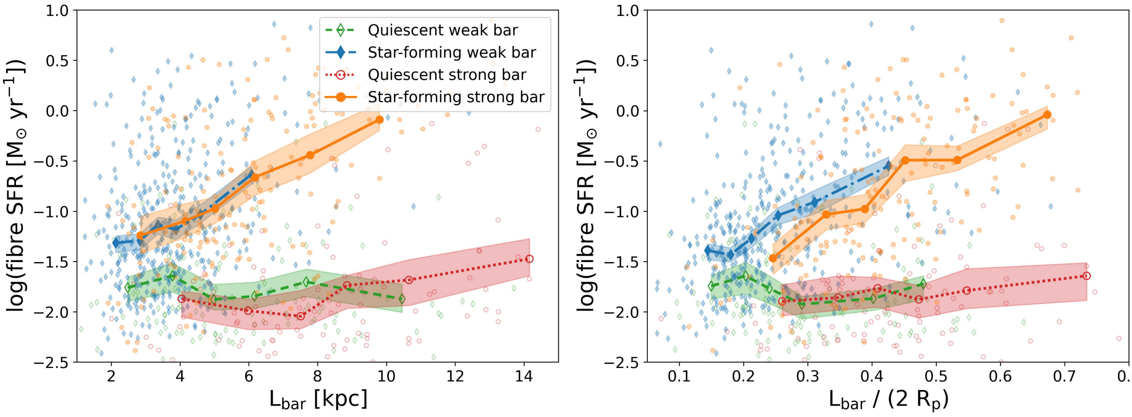

Figure 3.10: The fibre SFR is shown against the absolute bar length (in kpc, left panel) and right relative bar length (the bar length divided by the $r$-band Petrosian diameter) for strongly and weakly barred galaxies. The samples are divided into SF and quiescent as well. This figure suggests that the the fibre SFR for SF galaxies with a strong bar is not higher than the fibre SFR for SF galaxies with a weak bar, after controlling for the length of the bar. The shaded regions represent the $3\sigma$ region after bootstrapping the data 10,000 times and retaining 90% of the data for each iteration.

of a continuum of bar types and suggests that weak and strong bars are not distinct physical phenomena.

## 3.6 Discussion

### 3.6.1 Strong bars are longer than weak bars

Figure 3.1 shows that classifiers (volunteers or experts) are more confident that a bar is strong if it is longer. This is expected, as volunteers are told prior to classification that strong bars '*extend across a large fraction of the galaxy*" while weak bars are "*smaller and fainter relative to the galaxy*". The absolute bar length (in kpc) and the relative bar length (obtained by the dividing the absolute bar length by the $r$-band Petrosian radius) for weak and strong bars are shown in Figure 3.2. The sample was additionally divided into SF and quiescent galaxies. It is clear that strong bars are typically longer than weak bars, using either bar length measurement, as is expected. However, there is still significant overlap in bar length between the two bar types, using either the absolute bar length or the relative bar length.

It is interesting to note that, when looking at the absolute bar length, quiescent galaxies have longer bars than SF galaxies. This observation holds true for both weak and strong bars. Interestingly, the difference between quiescent and SF galaxies disappears when looking at the relative bar length. Weak bars typically cover around

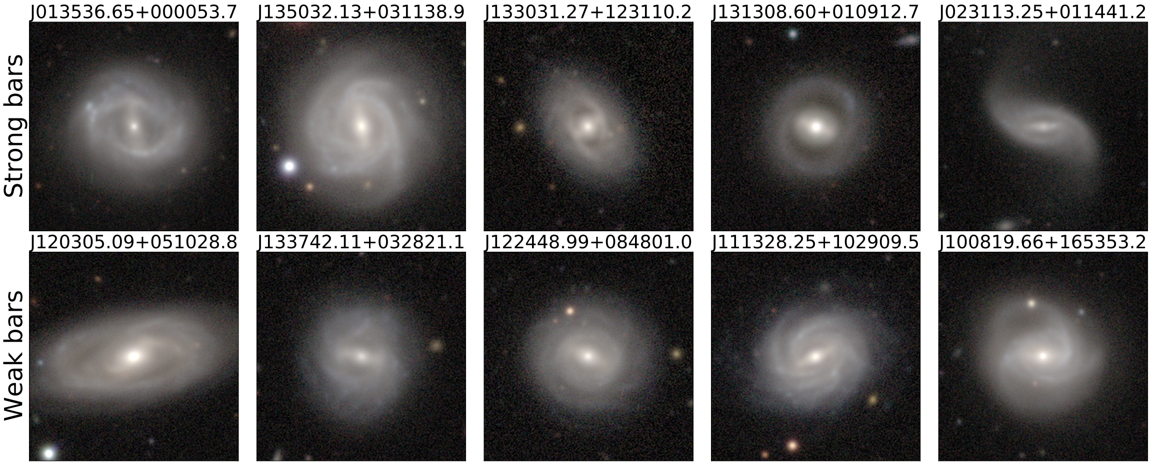

Figure 3.11: DECaLS postage stamps (59x59 arcsec) of galaxies classified by GZ DECaLS as strongly barred (top row) and weakly barred (bottom row). The IAU name of every galaxy is shown on top. All these targets have intermediate relative bar lengths ($0.27 < \mathrm{L}_{\mathrm{bar}}/(2\ \mathrm{R}_P) < 0.37$) and redshifts between $0.027 < z < 0.035$. It is much more difficult to discern between weak and strong bars in this intermediate bar length range, especially considering the obvious morphological differences shown in Figure 2.4 in Section 2.1.6.1. Around 23% of the bars in the GZ DECaLS-SDSS sample are in this intermediate relative bar length range.

20-30% of their host, regardless of whether the host is SF or quiescent. Strong bars cover around 30-45% of the Petrosian diameter of their host. This suggests that bars do not grow independently from their host and that their evolution is tightly connected.

### 3.6.2 Strong bars are more common in quiescent galaxies

Figure 3.3 shows that the strong bar fraction increases monotonically with ($g$-$r$) colour and stellar mass. The strong bar fraction reaches a maximum at lower SFR bins, but there is still a significant population of strong bars at higher (fibre) SFRs. This is in agreement with many other studies, who have found that bars are more common among galaxies with high stellar mass, redder colours and low SFRs (Nair & Abraham, 2010b; Masters et al., 2012; Vera et al., 2016; Cervantes Sodi, 2017). However, we see this for strong bars, not weak bars. In fact, the weak bar fraction decreases with increasing ($g$-$r$) colour and stellar mass. Thus, these results show that the trends observed by previous studies only apply for strong bars, not weak bars.

The strong bar fraction is higher in red sequence and in quiescent galaxies (24.9% and 22.0%, respectively) than in the blue cloud and in SF galaxies (9.6% and 13.0%, respectively), as shown in Figures 3.5 and 3.6. Conversely, the fraction of galaxies with a weak bar is roughly similar in red sequence and in quiescent galaxies (25.2% and 25.0%, respectively) when compared to the blue cloud and in SF galaxies (29.9% and 29.3%, respectively). As suggested by Masters et al. (2012), this means that either strong bars help to quench the galaxy, or that it is easier to form strong bars in quenched galaxies. This is discussed in more detail in Section 3.6.3.

Erwin (2018) have found that the bar fraction remains constant over a range of ($g$-$r$) colours and gas fractions in a sample drawn from the Spitzer Survey of Stellar Structure in Galaxies (S4G). Additionally, their bar fraction decreases for stellar masses higher than $\sim 10^{9.7} M_{\odot}$. This is in contrast with many SDSS-based studies (Masters et al., 2011, 2012; Vera et al., 2016; Cervantes Sodi, 2017; Kruk et al., 2018). According to Erwin (2018), this apparent contradiction can be resolved if bars in low-mass blue galaxies are missed by SDSS-based studies. Figures 2.5 and 3.3 showed that most of the newly detected bars in GZ DECaLS (compared to GZ2) are weak bars in low-mass blue galaxies. Nevertheless, the addition of these weak bars is insufficient to resolve the apparent contradiction with Erwin (2018). It seems more likely that the disagreement stems from a very different sample selection between S4G and SDSS. The sample in Erwin (2018) has a median stellar mass of $\sim 10^{9.6} M_{\odot}$ (based on their Figure 4 and the bins in the top-left panel of their Figure 5), while our median stellar mass is $10^{10.6} M_{\odot}$. This can have major consequences, as stellar mass is correlated with many parameters (Brinchmann & Ellis, 2000; Brinchmann et al., 2004; Noeske et al., 2007; Lara-López et al., 2010), including bar length (Erwin, 2019; Kim et al., 2021). Erwin (2018) also notes the differences in resolution. DECaLS has an $r$-band full width at half maximum (FWHM) of 1.18 arcsec (Dey et al., 2019), which suggests that the mean linear resolution of our sample is equal to ~834 pc, as the mean redshift is equal to 0.036. This is significantly higher than the resolution quoted in Erwin (2018), which is 165 pc. This also explains why no sub-kpc bars are found in the GZ DECaLS-SDSS sample, while they are found in Erwin (2018). Because of these differences in resolution and stellar mass, the final conclusions of Erwin (2018) are not directly comparable to those presented here.

### 3.6.3 Strong bars in star forming galaxies facilitate quenching

I show in Figures 3.7 and 3.9 that SF galaxies with a strong bar typically have higher fibre SFRs, lower gas masses and shorter depletion timescales, when compared to SF unbarred galaxies. This implies that, on average, strongly barred SF galaxies are rapidly evolving galaxies, compared to unbarred galaxies, and are more efficient with their star formation. This suggests that the presence of a strong bar in a SF galaxy will facilitate the quenching process. In contrast, weakly barred SF galaxies are more similar to unbarred galaxies and no differences were observed among quiescent galaxies of any bar type.

Many other studies have suggested before that bars can affect and potentially quench their host through ‘secular evolution’ (Kormendy & Kennicutt, 2004; Sheth et al., 2005; Athanassoula, 2007; Masters et al., 2011; Cheung et al., 2013; Kruk et al., 2018; Efthymiopoulos et al., 2019). Bars funnel gas inwards (Athanassoula, 1992b; Athanassoula et al., 2013; Villa-Vargas et al., 2010) and after the gas is concentrated in the centre, it is consumed to enhance SFR. This speeds up the rate of gas consumption and facilitates the transition of the host from being star forming to quenched. Studies have found an increase in SFR in barred galaxies before (Alonso-Herrero & Knapen, 2001; Hunt et al., 2008; Ellison et al., 2011; Coelho & Gadotti, 2011; Hirota et al., 2014; Janowiecki et al., 2020; Magaña-Serrano et al., 2020; Lin et al., 2020). However, based on the results in this chapter, it can be concluded that evidence for quenching through secular evolution has only been observed in strong bars in SF galaxies, whereas weak bars do not seem to have this effect.

Interestingly, multiple studies find that bars do not result in an increase of SFR or star formation efficiency (SFE). For example, Sheth et al. (2000) found that the region between the centre of the galaxy and bar ends in NGC 5383 has lower SFR. Additionally, Watanabe et al. (2011) used observations to find that the SFE within the bar radius is similar to the disc region in NGC 3627. Khoperskov et al. (2018) have used N-body/hydrodynamical simulations of gas-rich barred galaxies and found lower SFR after bar formation. These lower SFRs/SFEs in barred regions have been explained by fast cloud-cloud collisions (Fujimoto et al., 2014; Maeda et al., 2018; Fujimoto et al., 2020; Maeda et al., 2021) or strong gas flows and/or shear effects caused by the bar potential (Athanassoula, 1992b; Reynaud & Downes, 1998; Sheth et al., 2000; Sorai et al., 2012; Meidt et al., 2013; Momose et al., 2010; Nimori et al., 2013; Krishnarao et al., 2020). However, the results presented here suggest an increase of SFR in the 3 arcsec fibre for strongly barred galaxies. In our sample, this corresponds to the central 0.69 - 2.93 kpc. The strong bars in our sample are usually larger than that, as shown in Figure 3.2, which implies that only the centre of the bar is covered by the fibre. Therefore, the increase in SFR shown here is only valid for the centre of the bar, and not over the entire bar and bar-end region, which is the area where the studies above look at. This issue can be clarified by using integral field spectroscopic surveys, such as MaNGA (Bundy et al., 2015), which is used to tackle this question in Chapter 5. Furthermore, many of these studies do not distinguish between strong and weak bars, which also could explain the discrepancy, as the results present here only show an increase in fibre SFR among strongly barred SF galaxies.

Finding more bars in quiescent galaxies is typically explained by either assuming that bars help to quench their host, or that it is easier to form bars in quenched galaxies. Multiple studies have found evidence for the latter statement (Sheth et al., 2008; Villa-Vargas et al., 2010; Cervantes Sodi, 2017). For example, the simulations performed by Athanassoula et al. (2013) show that a bar starts forming later and forms more slowly when the gas fraction is high. Additionally, they found that the bar is much weaker in gas-rich galaxies. In contrast, the results presented here suggest that strong bars in SF galaxies help to quench their host through secular evolution. However, it is important to note that these two statements are not mutually exclusive and both can be correct at the same time.

### 3.6.4 Bar continuum

It is shown in Figure 3.10 that the differences observed between weak and strong bars in SF galaxies in terms of fibre SFR disappear after controlling for bar length. In other words, at a fixed bar length, weak and strong bars are indistinguishable in terms of fibre SFR. After looking at images of weak and strong bars in galaxies with intermediate bar length (defined as $0.27 < \mathrm{L_{bar}}/(2\ \mathrm{L}_p) < 0.37$) in Figure 3.11, it must be concluded that they look very much alike. As all observed differences disappear when controlling for bar length, I concluded that weak and strong bars are not distinct physical phenomena. Rather, the evidence supports the idea of an continuum of bar types.

The idea of a bar continuum is also supported by Figure 3.1, shown earlier in Section 3.1, where the bar vote fraction is plotted against the bar length. It was shown that there is no distinctive bar length threshold after which a bar is always classified as strong. This is consistent with the idea of the continuous nature of bar types, rather than weak and strong bars being distinct categories. This is also supported by Figure 3.2 in Section 3.1, where it is shown that there is significant overlap in bar length between weak and strong bars. As mentioned above, there are very few long weak bars and short strong bars. Only $\sim 12\%$ of weak bars have a relative bar length longer than the median of the strong bars. Similarly, only $\sim 7\%$ of strong bars have a relative bar length shorter than the median of the weak bars.

The proposed bar continuum is visualised in Figure 3.12 with example galaxies taken from DECaLS. The targets are ordered from having weaker bars (left) to

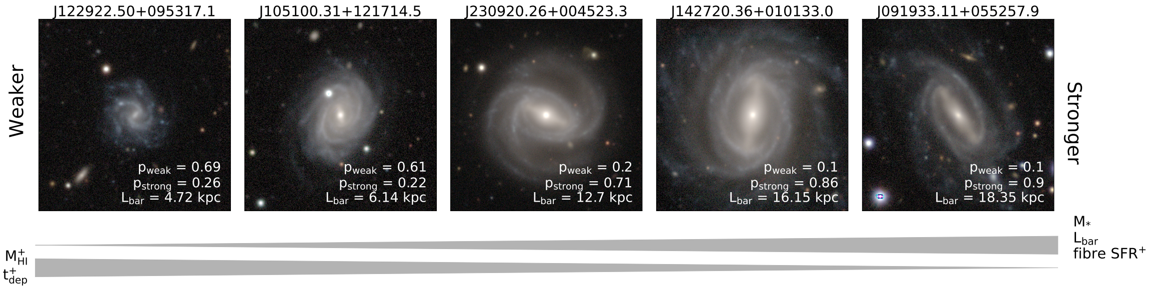

Figure 3.12: The proposed bar continuum is visualised above using DECaLS postage stamps (93x93 arcsec). The IAU name of every galaxy is shown on top. The continuum goes from weaker bars (left) to stronger bars (right). I found that multiple parameters scale with this continuum, such as bar length, strong bar vote fraction from GZ DECaLS ($p_{strong}$), stellar mass and fibre SFR. Additionally, the weak bar vote fraction from GZ DECaLS ($p_{weak}$), Hɪ gas mass and the depletion timescale are inversely proportional to this continuum. These parameters are shown on the bottom of these plots. Please note that the parameters indicated with '+' (depletion timescale, Hɪ gas mass and fibre SFR) are found to only scale in SF galaxies.

stronger bars (right). The continuum is shown here based on the absolute bar length (in kpc). However, I want to explicitly state that it is also possible to imagine the bar continuum based on other parameters, such as the relative bar length or a combination of $p_{weak}$ and $p_{strong}$ and that a combination of these parameters make a bar weaker or stronger. Within the context of this continuum, instead of referring to bars as 'strong' and 'weak', it is more accurate to talk about 'stronger' and 'weaker' bars. The results in this chapter suggest that multiple parameters scale with this bar continuum, such as bar length, strong bar vote fraction from GZ DECaLS ($p_{strong}$) and stellar mass. More specifically, stronger bars in SF galaxies have higher fibre SFRs, lower Hɪ gas masses and shorter depletion timescales. This is not found for weaker bars, which highlights how the position of a bar on this continuum has important consequences for the host galaxy.

However, as the extremes of the bar continuum do have varying effects on their host (e.g. fibre SFR, gas mass and depletion timescale), it is still worthwhile to differentiate between the ends of the continuum. This can be done by splitting the bar population into different categories, such as weak and strong. One must only exercise caution when selecting a threshold to differentiate between weak and strong, as well as keep the continuous nature of bar types in mind when interpreting the results.

Multiple studies have found that bars can grow stronger and longer over time (Athanassoula, 2003; Kim et al., 2015, 2016; Díaz-García et al., 2016; Algorry et al., 2017). This suggests that bars can change their position on the bar continuum over time.

Multiple other studies have shown that there are differences in the surface brightness profile between strong and weak bars. Weaker bars have exponential profiles, while stronger bars tend to have flatter profiles (Elmegreen & Elmegreen, 1985; Elmegreen et al., 1996; Kruk et al., 2018). Kim et al. (2015) suggest that bars initially start with an exponential profile. After trapping more stars into bar orbits, bars will evolve to have a flatter profile. This allows for the existence of many surface brightness profiles in between exponential and flat. This is consistent with the hypothesis of the continuous nature of bar types and suggests that the surface brightness of profile of the bar scales according to the bar continuum as well.

## 3.7 Conclusions

In this chapter, I used the GZ DECaLS-SDSS sample to investigate differences and similarities between weak and strong bars, with a focus on quenching. The large sample size of the GZ DECaLS-SDSS sample, which contains 1,867 galaxies (289 strongly barred, 525 weakly barred and 1,053 unbarred galaxies) is unique in having such a large number of weakly barred galaxies. This is important, as weak bars have typically been underrepresented in previous research. The weak bars in this sample could be identified because of a combination of deep imaging and the detailed decision tree employed in GZ DECaLS during classification. GZ DECaLS was combined with MPA-JHU (Kauffmann et al., 2003; Brinchmann et al., 2004; Tremonti et al., 2004) to obtain SFR and stellar mass measurements, as well as with ALFALFA (Giovanelli et al., 2005; Haynes et al., 2011, 2018) for gas mass estimates. The results presented in this chapter show that:

1. ***Stronger bars are longer than weaker bars.***
    - I found that volunteers (and expert classifiers) are collectively more confident that a bar is strong if it is longer, as is expected.
    - However, there is still a big overlap in terms of bar length between the two bar types, i.e. there is no distinct bar length threshold above which all bars are strong.

- When measuring bar length in kpc, I found that bars in quiescent galaxies are typically longer than bars in SF galaxies, for both bar types. Interestingly, this difference disappears when measuring bar length relatively to the Petrosian diameter.

2. ***The strongest bars facilitate quenching in SF galaxies.***
    - The weak bar fraction is roughly similar in both the red sequence and quiescent galaxies (25.2% and 25.0%, respectively) compared to the blue cloud and SF galaxies (29.9% and 29.3%, respectively). However, the strong bar fraction is significantly higher in the red sequence and in quiescent galaxies (24.9% and 22.0%, respectively) than in the blue cloud and in SF galaxies (9.6% and 13.0%, respectively).
    - SF galaxies with a stronger bar have, on average, significantly higher fibre SFRs, lower gas masses and shorter depletion timescales than unbarred SF galaxies, especially at higher stellar masses. This suggests that SF galaxies with a stronger bar are typically rapidly evolving galaxies and that the quenching process in these galaxies is facilitated by the presence of a strong bar. These differences were not observed between galaxies with a weaker bar and unbarred galaxies.
    - No differences were observed among the different bar types in quiescent galaxies in terms of fibre SFR, gas mass and depletion timescale.

3. ***Weak and strong bars are part of a continuum of bar types.***
    - The differences between weak and strong bars disappears when controlling for bar length. This suggests that weak and strong bars are not fundamentally distinct physical phenomena, but rather are part of a continuum of bar types.
    - Instead of referring to bars as 'strong' and 'weak', it is more accurate to use 'stronger' and 'weaker', within the context of this continuum.
    - The position of the a bar on this continuum will dictate how much of an effect the bar has on its host. Stronger bars have more of an effect, especially in terms of fibre SFR, gas mass and depletion timescale.

The results in this chapter reveal a lot about the nature of weak and strong bars. However, the kinematics of weak and strong bars has not yet been considered, which I will do in the next chapter.

# Chapter 4

# Tremaine-Weinberg Method: Kinematics of strongly and weakly barred galaxies

*The contents of this chapter have been published in Géron et al. (2023).*

The pattern speed of the bar, also known as the rotational frequency of the bar, is an important dynamical parameter, as it is tightly linked to its evolution. Simulations have shown that the pattern speed decreases as the bar grows and exchanges angular momentum with its host (Debattista & Sellwood, 2000; Athanassoula, 2003; Martinez-Valpuesta et al., 2006; Okamoto et al., 2015). This implies that bars with lower pattern speeds are more evolved and older structures than bars with higher pattern speeds. If the stellar kinematics of the galaxy are known, the pattern speed can be used to determine the corotation radius (for more details, please refer to Section 2.2.4.4). The dimensionless ratio of the corotation radius to the bar radius, $\mathcal{R}$, is used to classify bars based on their kinematic properties. Bars with $\mathcal{R} > 1.4$ are called 'slow' bars, while bars that have $1.0 < \mathcal{R} < 1.4$ are 'fast' bars and bars with $\mathcal{R} < 1.0$ are called 'ultrafast' bars. The ratio $\mathcal{R}$ has also been linked to the formation processes of the bar. Bars triggered by global bar instabilities typically have lower values for $\mathcal{R}$ than bars formed by tidal interactions (Sellwood, 1981; Miwa & Noguchi, 1998; Martinez-Valpuesta et al., 2016; Gajda et al., 2017; Martinez-Valpuesta et al., 2017). As the pattern speed and $\mathcal{R}$ are linked to the formation and evolution of bars, they have been the focus of many observational studies (Rautiainen et al., 2008; Aguerri et al., 2015; Font et al., 2017; Cuomo et al., 2019; Guo et al., 2019; Garma-Oehmichen et al., 2020, 2022). However, the sample sizes of these studies are typically limited, especially for weak bars. Most studies do not mention weak bars at all. Cuomo et al.

(2019) measure the pattern speed for 16 weak bars, while Font et al. (2017) have 42 weak bars in their sample, although they have used a different method to calculate the bar pattern speed (this is discussed in more detail in Section 4.5).

As noted in Section 1.3.3, the dimensionless ratio $\mathcal{R}$ is studied for a few additional reasons. Firstly, it is thought that bars can only grow up until their corotation radius, which implies that ultrafast bars (bars with $\mathcal{R} < 1.0$) should not exist. (Contopoulos, 1980, 1981; Athanassoula, 1992b). However, they are repeatedly observed. The fraction of ultrafast bars in observations has been found to range from 11-16% (Rautiainen et al., 2008; Garma-Oehmichen et al., 2022) to roughly half of all barred galaxies (Aguerri et al., 2015; Cuomo et al., 2019) and their existence remains an open question. Simulations also predict that bars should slow down due to dynamical friction with their dark matter (DM) halo, which increases $\mathcal{R}$. However, observations consistently find lower values for $\mathcal{R}$ than simulations, which has been raised as a tension for ΛCDM (Algorry et al., 2017; Peschken & Łokas, 2019; Fragkoudi et al., 2021; Roshan et al., 2021a,b; Frankel et al., 2022).

In this chapter, I present the results of measuring the bar pattern speed, corotation radius and $\mathcal{R}$ for a large sample of strongly and weakly barred galaxies using the Tremaine-Weinberg (TW) method (see Section 2.2.4). In order to apply the TW method, I used the stellar velocity and flux obtained from MaNGA (see Section 2.1.2). I have calculated reliable pattern speed estimates for the entire TW sample, which contains 225 galaxies (122 strong bars and 103 weak bars). This is the largest sample of barred galaxies that the TW method has been applied to so far. For a detailed description on how the TW sample was constructed, please refer to Section 2.2.4.5. I used classifications from Galaxy Zoo DESI (see Section 2.1.6.1) to classify galaxies into strongly barred or weakly barred. I will test whether strong and weak bars have similar distributions in these kinematic parameters, which will allow me to probe whether the formation and evolution of weak and strong bars is significantly different. Additionally, I will see if a significant number of ultrafast bars are observed and whether the tension with ΛCDM still persists with a large sample of both strong and weak bars.

In Section 4.1, I describe the effect that the slit width has on the pattern speed estimates. The final distributions of the bar pattern speed, corotation radius and $\mathcal{R}$ for strongly and weakly barred galaxies are shown and compared to each other in Section 4.2. The relationship between these dynamical parameters is studied in Section 4.3, where I also investigate their dependence on bar length and stellar mass. In Section 4.4, I look at the differences in the distributions of these dynamical parameters between SF and quenching galaxies. The estimates of bar pattern speed, corotation radius and $\mathcal{R}$ calculated here are compared to values obtained from the literature in Section 4.5. Finally, the results are discussed in Section 4.6 and the conclusions are summarised in Section 4.7.

## 4.1 Effect of slit width

In order to calculate the pattern speed using the TW method, a number of pseudo-slits are placed along the major axis of the galaxy (see Section 2.2.4 for more details). Most studies use a slit width of 1 arcsec (e.g. Aguerri et al., 2015; Cuomo et al., 2019), while I use a slit width of 0.5 arcsec. This is because a minimum of three slits need to be placed in order to reliably determine the pattern speed and more slits can be placed when using a smaller slit width. This is especially important in this work, as I want to determine the pattern speed for weak bars, which tend to be significantly shorter than strong bars (see Section 3.1). The average bar length for a weak bar in the GZ DESI-MaNGA sample, which is the parent sample of the TW sample, is 5.8 arcsec. Guo et al. (2019) also used a slit width of 0.5 arcsec and were successful in determining pattern speeds and found that using a slit width of 1 arcsec did not have a significant impact on their final measurements. Zou et al. (2019) also found that different slit width did not change the final pattern speed measurements significantly.

However, to make sure this decision does not affect the measurements, the pattern speeds of all the galaxies in the TW sample are calculated again using slit widths of 1 and 2 arcsec. The pattern speeds are compared to each other in Figure 4.1. Out of the 225 galaxies in the TW sample, it was possible to reliably estimate the pattern speed for 167 galaxies using a slit width of 1 arcsec and for 81 galaxies using a slit with of 2 arcsec. The remaining targets did not pass the quality thresholds imposed to ensure reliable estimates (see Section 2.2.4). The most common problem was that it was not possible to place a minimum of three slits with wider widths on the shorter bars (which were usually weak bars).

Figure 4.1 shows that there is a very good correlation between the results using the different slit widths. All pattern speeds determined with a slit width of 0.5 and 1 arcsec fall within the $1\sigma$ error limits of each other, whereas this holds for 98.8% (or 80 out of 81 targets) of the pattern speeds determined with a slit width of 0.5 and 2 arcsec. The median value of the pattern speed across all comparisons is 15.2 km $\mathrm{s}^{-1}$ $\mathrm{arcsec}^{-1}$. The median of the absolute value of the difference between the pattern

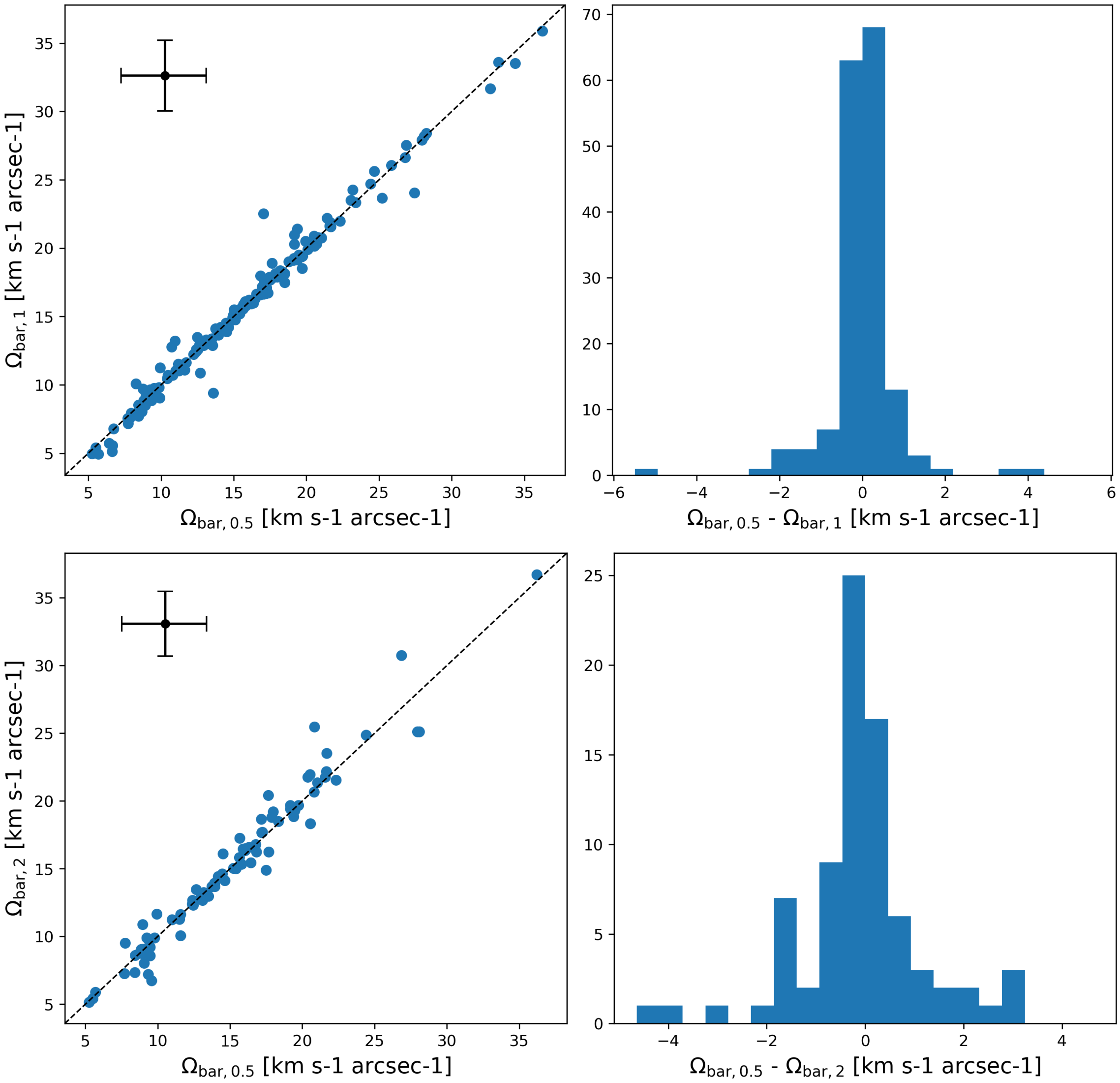

Figure 4.1: This figure shows how the final pattern speed estimates change depending on slit width. The top row compares pattern speeds determined with a slit width of 0.5 arcsec and 1 arcsec, while the bottom row compares 0.5 arcsec with 2 arcsec. The left column shows a direct comparison with the two slit widths. The median error in the x and y axes is visualised in the top-left corner of each panel. The panels in the right column show the difference between the two estimates. A total of 167 galaxies in the TW sample have pattern speed estimates using a slit width of 1 arcsec, while only 81 targets have pattern speeds when using a slit width of 2 arcsec. There is a clear correlation between the measurements, which implies that using a different slit width does not affect individual pattern speed measurements. Note that the median pattern speed across all comparisons is 15.2 km $s^{-1}$ $arcsec^{-1}$ and that the median of the absolute value of the difference in the top comparison is 0.21 km $s^{-1}$ $arcsec^{-1}$ and 0.46 km $s^{-1}$ $arcsec^{-1}$ in the bottom comparison.

speed estimates using a slit width of 0.5 and 1 arcsec is 0.21 km s$^{-1}$ arcsec$^{-1}$, while it is 0.46 km s$^{-1}$ arcsec$^{-1}$ when using a slit width of 0.5 and 2 arcsec.

Thus, I find that **using a different slit width does not affect individual pattern speed measurements** in a significant way. However, more slits can be placed on shorter bars when using a smaller slit width and consequently results in more weak bars in the final sample. A slit width of 0.5 arcsec is therefore ideal for the purposes of this work. However, even though a slit width of 0.5 arcsec allows me to measure the pattern speed of more weak bars, it is still not possible to do this for the weakest and shortest of bars. This should be kept in mind while interpreting the results. Additionally, the pattern speed is better constrained when more pseudo-slits are used, which implies that the errors on the pattern speed tend to be larger for weak bars than for strong bars (6.83 km s$^{-1}$ kpc$^{-1}$ and 4.89 km s$^{-1}$ kpc$^{-1}$, respectively).

## 4.2 Bar pattern speeds, corotation radii and $\mathcal{R}$

The bar pattern speed ($\Omega_{\rm b}$) estimates for all the weakly and strongly barred galaxies in the TW sample are shown in Figure 4.2. The final values of the pattern speed for each individual target were estimated after performing 1,000 MC iterations, where the inclination, position angle of the disc, bar length and position angle of the bar was varied in every iteration. The median of the posterior distribution was taken as the final value, while the 16th and 84th percentiles of the distribution are taken as the $1\sigma$ errors. More details on this process can be found in Section 2.2.4.2. The top row of Figure 4.2 shows $\Omega_{\rm b} \sin{(i)}$, while the bottom row shows $\Omega_{\rm b}$. The pattern speed shown in the left column is measured in observational units (km s$^{-1}$ arcsec$^{-1}$), which are converted to physical units (km s$^{-1}$ kpc$^{-1}$) in the right column. The results in physical units are the ones that are physically meaningful, however, the results in observational units are also shown to facilitate comparison with other work.

There is a large overlap in the bar pattern speed distributions of weakly and strongly barred galaxies, although the median of the sample of the strongly barred galaxies is always lower than the median of the weakly barred galaxies. An Anderson-Darling test shows that both distributions are significantly different: the p-value for the distributions using observational units are 0.003 (which corresponds to $3.0\sigma$) and 0.013 ($2.5\sigma$) for $\Omega_{\rm b} \sin{(i)}$ and $\Omega_{\rm b}$, respectively. The p-value for the distributions using physical units are <0.001 (>$3.3\sigma$) and 0.002 ($3.1\sigma$) for $\Omega_{\rm b} \sin{(i)}$ and $\Omega_{\rm b}$, respectively.

This shows that strongly barred galaxies have significantly lower bar pattern speeds than weakly barred galaxies. The median along with the 16th and 84th per-

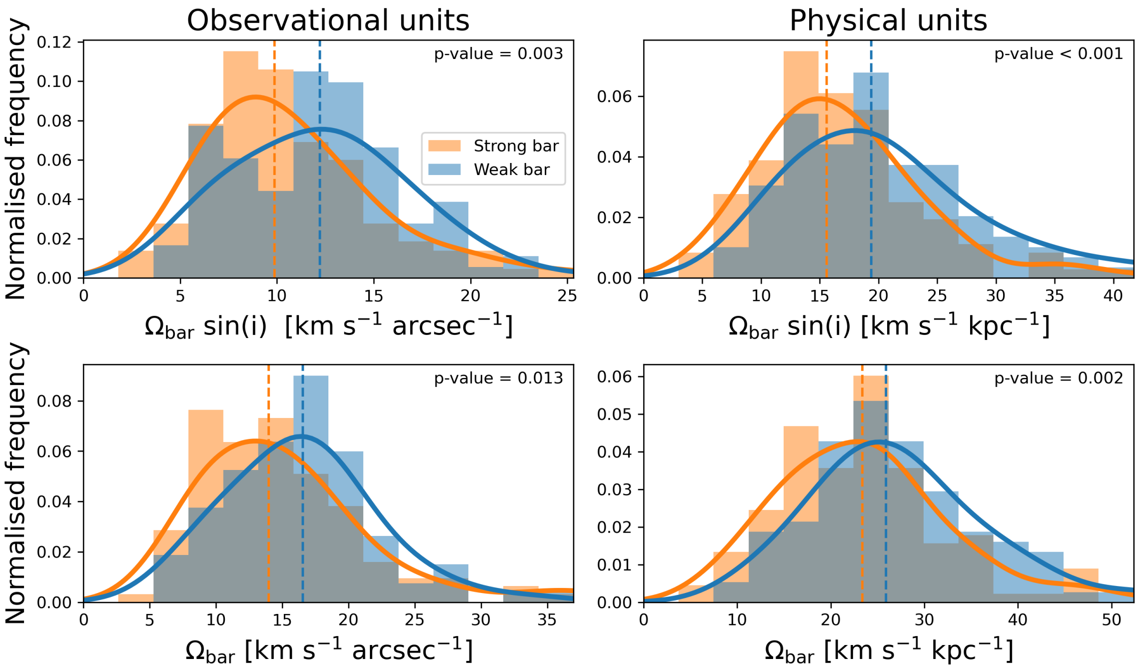

Figure 4.2: The final median values for $\Omega_{\rm b} \sin(i)$ (top row) and $\Omega_{\rm b}$ (bottom row) for every galaxy, after doing a Monte Carlo simulation of 1,000 iterations. The sample is divided into strongly barred (orange) and weakly barred (blue). The MC is done over observational units (which include arcsec), which are afterwards converted to kpc. The left column shows the results for the observational units, while the right column shows the results for the physical units. The vertical dashed lines show the median values for every histogram. The full lines are kernel density estimates of these histograms, using a Gaussian kernel. The p-value of a two-sample Anderson-Darling test is shown inside each subplot, with the null hypothesis being that the two samples are drawn from the same population. We see that, on average, strongly barred galaxies have significantly lower bar pattern speeds, despite there being significant overlap between the two populations. The p-value of the comparisons in physical units is <0.001-0.002 (which corresponds to 3.1-3.3$\sigma$).

centiles is $\Omega_{\rm b} = 23.36^{+9.25}_{-8.1}$ km s$^{-1}$ kpc$^{-1}$ for strongly barred galaxies and $\Omega_{\rm b} = 25.91^{+10.42}_{-7.26}$ km s$^{-1}$ kpc$^{-1}$ for weakly barred galaxies.

Figure 4.3 shows the distribution of the corotation radii of the strongly and weakly barred galaxies. A two-sample Anderson-Darling test reveals that the distributions are not significantly different, as the significance is below 3$\sigma$. The p-values are 0.06 (1.9$\sigma$) and 0.012 (2.5$\sigma$) for comparisons in observational and physical units, respectively. The median of the corotation radius distribution of the strongly barred galaxies is $\rm R_{CR} = 8.33^{+4.57}_{-3.31}$ kpc, while it is $\rm R_{CR} = 7.19^{+3.82}_{-2.96}$ for the weakly barred galaxies

The distributions of $\mathcal{R}$ for strong and weak bars overlap significantly, as shown in Figure 4.4. Nevertheless, the p-value of an Anderson-Darling test is 0.001, which

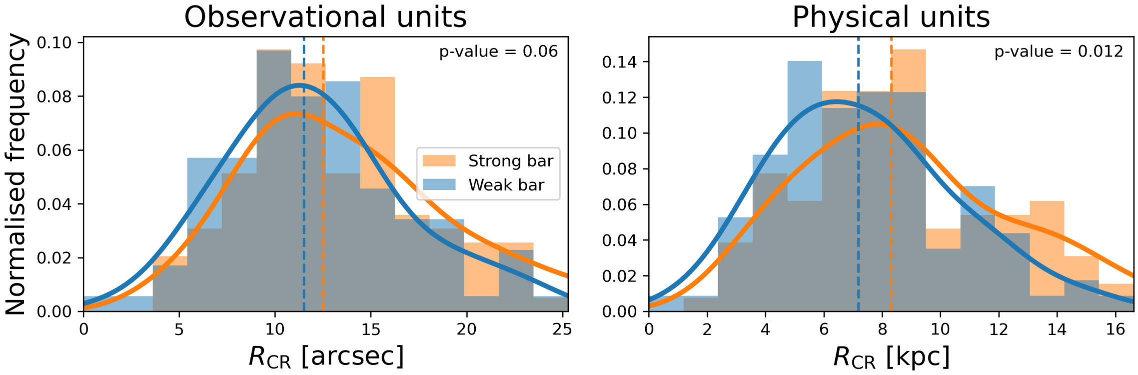

Figure 4.3: The final median values for $R_{\rm CR}$ for every galaxy, after doing a Monte Carlo simulation of 1,000 iterations. The sample is divided into strongly barred (orange) and weakly barred (blue). The MC is done over observational units (which is in arcsec), which are afterwards converted to kpc. The left column shows the results for the observational units, while the right column shows the results for the physical units. The vertical dashed lines show the median values for every histogram. The full lines are kernel density estimates of these histograms, using a Gaussian kernel. The p-value of a two-sample Anderson-Darling test is shown inside each subplot, with the null hypothesis being that the two samples are drawn from the same population. As the p-value of the comparison in physical units is 0.012 (which corresponds to $2.5\sigma$), we conclude that we see no significant difference between weak and strong bars in terms of their corotation radii.

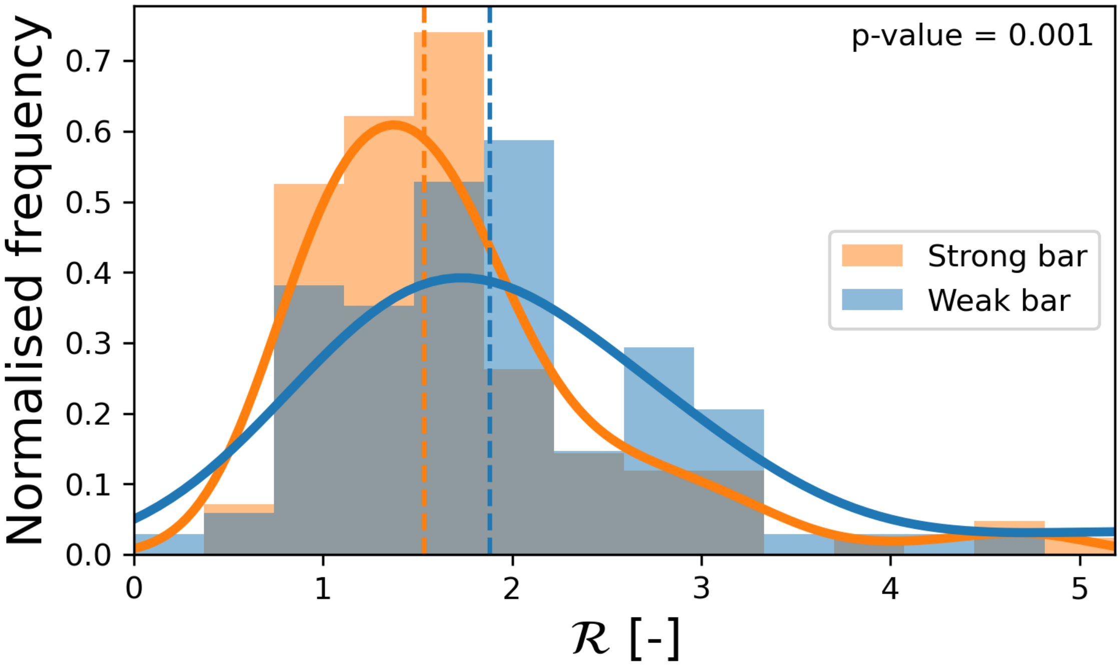

Figure 4.4: The final median values for $\mathcal{R}$ for every galaxy, after doing a Monte Carlo simulation of 1,000 iterations. The sample is divided into strongly barred (orange) and weakly barred (blue). The vertical dashed lines show the median values for every histogram. The full lines are kernel density estimates of these histograms, using a Gaussian kernel. The p-value of a two-sample Anderson-Darling test is shown inside each subplot, with the null hypothesis being that the two samples are drawn from the same population. We see that strong bars have significantly lower values of $\mathcal{R}$ than weak bars, despite the big overlap (p-value = 0.001; $3.3\sigma$).

corresponds to $3.3\sigma$. This suggests that strong bars have significantly lower values for $\mathcal{R}$ than weak bars. The median value for strongly barred galaxies is $\mathcal{R} = 1.53^{+0.74}_{-0.53}$ and $\mathcal{R} = 1.88^{+1.08}_{-0.75}$ for weakly barred galaxies. As explained in Section 2.2.4.4, the bar-ends of bars with $\mathcal{R} = 1$ rotate at the same speed as stars in the disc at that radius. This result therefore suggests that the difference in velocity between the stars in the disc and the bar-ends of a typical strong bar is lower than the difference in velocity between the stars in the disc and the bar-ends of a typical weak bar. This result also implies that strong bars tend to end closer to their corotation radius than weak bars. As mentioned before, $\mathcal{R}$ is commonly used to classify bars as slow ($\mathcal{R} > 1.4$), fast ($1.0 < \mathcal{R} < 1.4$) or ultrafast ($\mathcal{R} < 1.0$). I find that the majority of bars in the TW sample are slow bars (62% of our sample). Around 27% of bars in the TW sample are fast bars, while only 11% of bars are ultrafast. This is lower than what other observational studies typically find, which is discussed in more detail in Section 4.6.3.

In summary, I find that **strongly barred galaxies have significantly lower bar pattern speeds and lower estimates for $\mathcal{R}$ than weakly barred galaxies, while having similar corotation radii**. However, there is still a significant overlap in all distributions and I did not find any threshold in pattern speed or $\mathcal{R}$ that separates strong and weak bars. The implications for the evolution and formation of strong and weak bars are discussed in Sections 4.6.1 and 4.6.2, respectively.

## 4.3 Relationship between the parameters

In this section, I will delve more deeply into the relationship between the dynamical parameters calculated above. As stated in Section 2.2.4.4, the corotation radius is determined by finding the intersection of the rotation curve of the galaxy with the curve describing absolute speed of the bar at any radius (see Figure 2.15 for a visualisation). In theory, a higher pattern speed will have a steeper gradient of that line, which results in a shorter corotation radius. The inversely proportional relationship is clearly visible in Figure 4.5, where the pattern speed is plotted against the corotation radius.

Additionally, as $\mathcal{R}$ is defined as the ratio of the corotation radius to the bar radius, it follows that $\mathcal{R}$ is proportional to the corotation radius. This implies that $\mathcal{R}$ is, in turn, inversely proportional to the pattern speed. This is observed in Figure 4.5: galaxies that have the highest values for $\mathcal{R}$ (identified by the colour of each point) tend to have lower values for the pattern speed, while galaxies with lower $\mathcal{R}$ have shorter corotation radii. The residual scatter that is observed is due to the different bar lengths and rotation curves of the individual targets, as these are the only other variables not accounted for in this figure.

The corotation radius is plotted against the bar radius in Figure 4.6. As $\mathcal{R} = R_{\mathrm{CR}}/R_{\mathrm{bar}}$, lines of constant $\mathcal{R}$ are found diagonally in this figure. This means that this plot is divided into three separate regions: the region with slow bars ($\mathcal{R} > 1.4$), the region with fast bars ($1 < \mathcal{R} < 1.4$) and the region with ultrafast bars ($\mathcal{R} < 1$). As expected, the galaxies with the fastest pattern speeds (shown by the colour of the points) usually have low values for the corotation radius, shorter bar radii and higher values for $\mathcal{R}$. This figure also shows that very few bars in our sample are ultrafast, as mentioned above, and the bars that are ultrafast are mostly very close to the $\mathcal{R} = 1$ line.

Figure 4.7 shows the bar radius plotted against the pattern speed, corotation radius and $\mathcal{R}$. There is a clear downward trend of the pattern speed with radius,

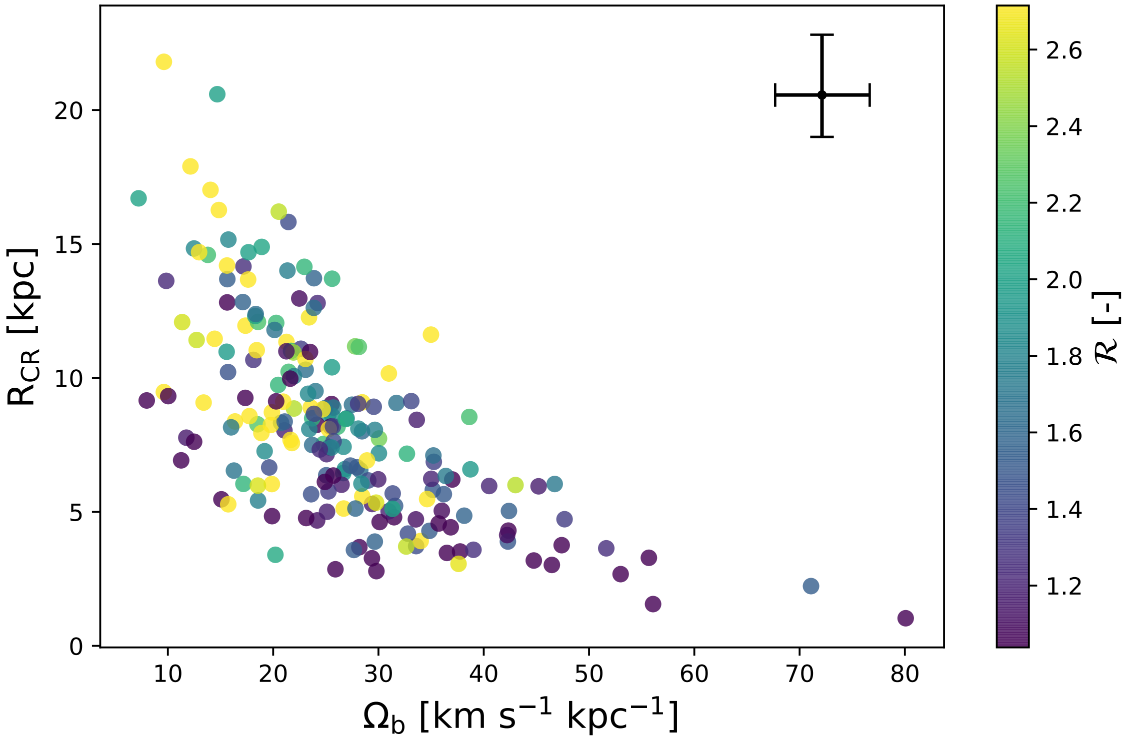

Figure 4.5: The bar pattern speed ($\Omega_b$) of all our targets plotted against the corotation radius ($R_{CR}$). The colour of the data points is determined by $\mathcal{R}$. The median error on the x and y axes is shown in the top-right corner. We can see that $\Omega_b$ and $R_{CR}$ are clearly inversely proportional, as expected. Additionally, we see that low $\mathcal{R}$ values cluster at lower values for $R_{CR}$, while the targets with the highest values for $\mathcal{R}$ typically have lower values for $\Omega_b$. To aid visualisation, the colors used to indicate $\mathcal{R}$ were capped at the 16th and 84th percentile.

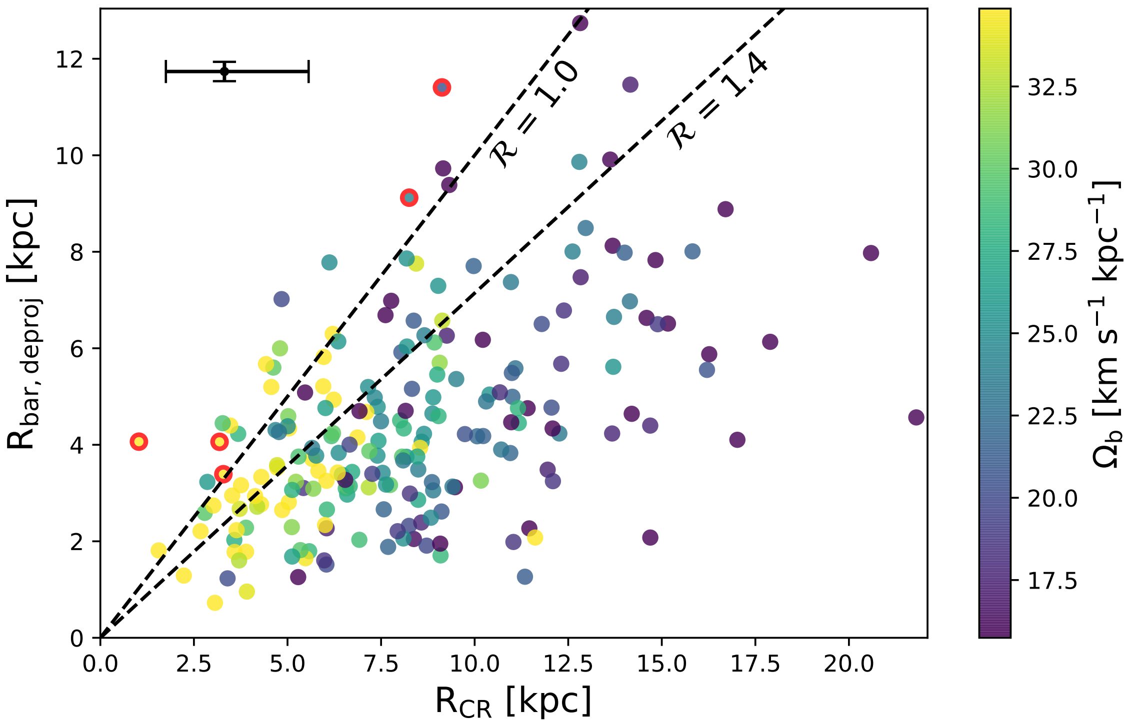

Figure 4.6: The corotation radius is plotted against the deprojected bar length. As $\mathcal{R} = R_{\mathrm{CR}}/R_{\mathrm{bar}}$, this figure is divided into three regions: the region with slow bars ($\mathcal{R} > 1.4$), the region with fast bars ($1 < \mathcal{R} < 1.4$) and the region with ultrafast bars ($\mathcal{R} < 1$). The colour indicates the bar pattern speed. Targets that have a $1\sigma$ upper limit with $\mathcal{R} < 1$ are additionally outlined in red. The median error on the x and y axes is shown in the top-left corner. To aid visualisation, the colors used to indicate the bar pattern speed were capped at the 16th and 84th percentile.

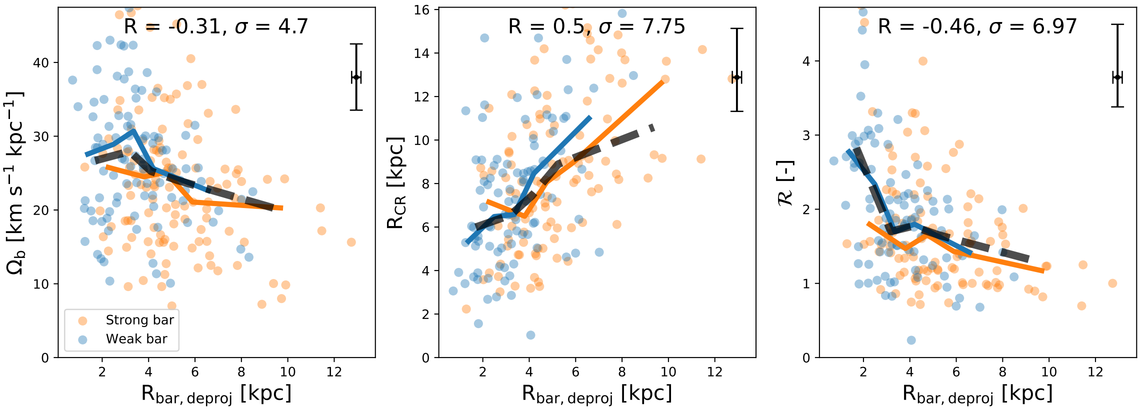

Figure 4.7: The bar pattern speed (left panel), corotation radius (middle panel) and $\mathcal{R}$ (right panel) against the bar radius. All strongly barred galaxies are coloured orange, while all weakly barred galaxies are coloured blue. The median trend for the weakly and strongly barred galaxies is shown with the blue and orange full lines, respectively. Additionally, the general median trend of all barred galaxies is shown in the dashed black line. The Spearman correlation coefficient, R, and its significance, $\sigma$, are shown in every subplot. The median error on the x and y axes is shown in the top-right corner. We see that the pattern speed and $\mathcal{R}$ decrease with bar length, while the corotation radius increases.

which is consistent with what was found in the previous section (see Figure 4.2), as stronger bars are typically longer. Even though the Spearman correlation index is quite small (R = -0.31), most likely due to the high amounts of scatter, the associated significance stays high ($4.7\sigma$), suggesting that the pattern speed and bar radius are correlated. Bars with higher pattern speeds tend to be shorter, while the largest bars all have lower pattern speeds. The middle panel of Figure 4.7 shows that the corotation radius is positively correlated with the bar radius (R = 0.5; $7.75\sigma$). This is expected, as the bar can theoretically only grow as large as its corotation radius, which necessitates that larger bars have larger corotation radii. $\mathcal{R}$ is shown to decrease with bar radius (R = -0.46; $6.97\sigma$) in the right panel of Figure 4.7, consistent with the previous conclusion that strong bars have lower values of $\mathcal{R}$. This anti-correlation is expected, as $\mathcal{R} = R_{\rm CR}/R_{\rm bar}$. Finally, it is also interesting to note that the median trends for weakly barred galaxies and strongly barred galaxies are very alike.

As shown in Chapter 3, stronger bars are more common among high mass galaxies. Observations have also shown that many properties scale with stellar mass (Brinchmann & Ellis, 2000; Brinchmann et al., 2004; Noeske et al., 2007; Lara-López et al., 2010). The stellar mass is therefore plotted in Figure 4.8 against bar pattern speed, corotation radius and $\mathcal{R}$, to see whether any of these kinematic parameters scale with

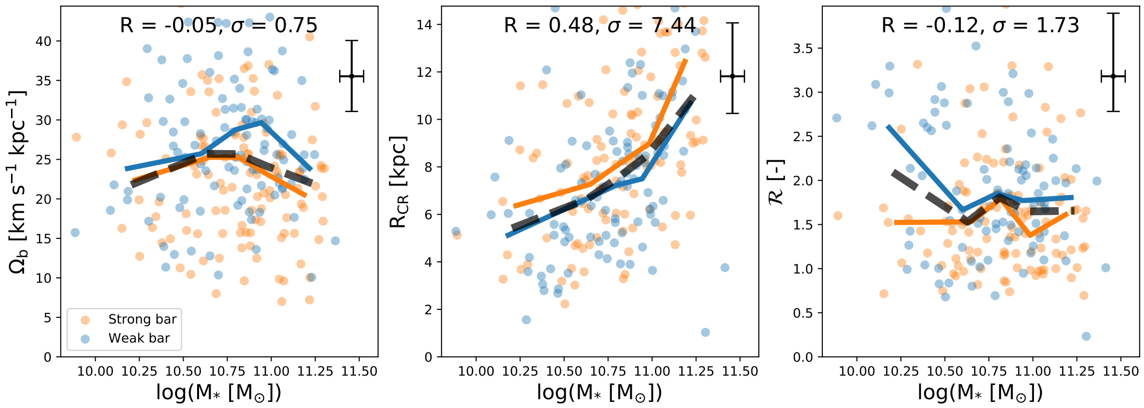

Figure 4.8: The bar pattern speed (left panel), corotation radius (middle panel) and $\mathcal{R}$ (right panel) against the stellar mass. All strongly barred galaxies are coloured orange, while all weakly barred galaxies are coloured blue. The median trend for the weakly and strongly barred galaxies is shown with the blue and orange full lines, respectively. Additionally, the general median trend of all barred galaxies is shown in the dashed black line. The Spearman correlation coefficient, R, and its significance, $\sigma$, are shown in every subplot. The median error on the x and y axes is shown in the top-right corner. We see that the pattern speed and $\mathcal{R}$ do not show a significant trend with stellar mass, while the corotation radius increases with stellar mass.

stellar mass. The left and right panel show that the pattern speed and $\mathcal{R}$ are not correlated with stellar mass (R = -0.05; 0.75$\sigma$ and R = -0.12; 1.73$\sigma$, respectively). This confirms that the previously obtained results that strong bars have significantly lower values for the pattern speed and $\mathcal{R}$ (see Section 4.2) are not caused by differences in stellar mass between weakly and strongly barred galaxies. However, the middle panel of Figure 4.8 shows that stellar mass is positively correlated with the corotation radius (R = 0.48; 7.44$\sigma$). This is presumably because the strong bar fraction increases with stellar mass (see Section 3.6.2). As strong bars tend to be longer (see Section 3.6.1) and bar length is shown to be correlated with corotation radius in Figure 4.7, a positive correlation between stellar mass and corotation radius should be expected.

## 4.4 Quenching

So far, I have shown that there is a relationship between pattern speed, corotation radius, $\mathcal{R}$, bar length and bar strength. Additionally, as shown in Section 3.3, the fraction of strongly barred galaxies is higher among quiescent galaxies than in SF galaxies. Chapter 3 also shows that strong bars in SF galaxies facilitate quenching. Can the kinematic properties of the bar tell us something more about the mechanisms

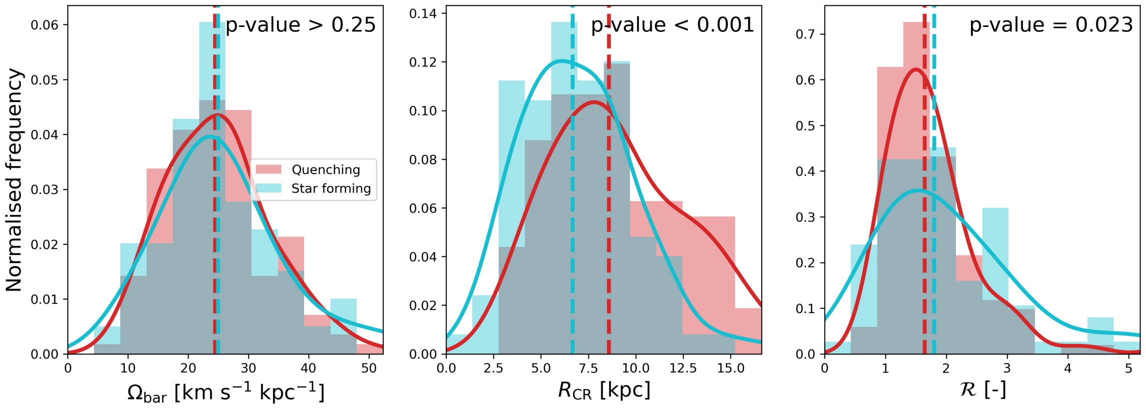

Figure 4.9: The final median values for bar pattern speed (left panel), corotation radius (middle panel) and $\mathcal{R}$ (right panel) after doing a Monte Carlo simulation of 1,000 iterations. The sample is divided into quenching galaxies (red) and star forming galaxies (blue). The vertical dashed lines show the median values for every histogram, while the full lines are kernel density estimates of these histograms, using a Gaussian kernel. The p-value of a two-sample Anderson-Darling test is shown in the top-right corner of every subplot. The null hypothesis is that the two samples in each subplot are drawn from the same population. We can see that the quenching and star forming subsamples are not significantly different in terms of pattern speed and $\mathcal{R}$, but are in terms of corotation radius.

by which a bar facilitates quenching? To test this, I have plotted the distribution of pattern speed, corotation radius and $\mathcal{R}$ between quenching and SF galaxies in Figure 4.9. Galaxies are classified as SF or quenching based on Equation 3.1 in Section 3.1; I find that 43% of the TW sample is SF, while 57% are quenching. Figure 4.9 shows that the pattern speed and $\mathcal{R}$ are not significantly different between SF and quenching galaxies (both comparisons have $<3\sigma$ in an Anderson-Darling test), which suggests that how rapidly bars rotate does not influence quenching. Interestingly, the corotation radius is significantly different (p-value $< 0.001$; $>3.3\sigma$), with **quenching galaxies having significantly larger corotation radii than SF galaxies**. As bars can grow up until their corotation radius (Contopoulos, 1980, 1981; Athanassoula, 1992b), this result suggests that longer bars are more efficient at quenching, which is in agreement with the results from Chapter 3. These results are discussed in more detail in Section 4.6.5.

## 4.5 Comparison with other work

Other studies have also measured pattern speeds, corotation radii and $\mathcal{R}$ for barred galaxies. For example, Rautiainen et al. (2008) used data from the Ohio State University Bright Spiral Galaxy Survey (Eskridge et al., 2002) to look at a sample of 38 galaxies. The Calar Alto Legacy Integral Field Area (CALIFA, Sánchez et al. 2012) survey was used in Aguerri et al. (2015) to determine the pattern speeds, corotation radii and $\mathcal{R}$ for 15 galaxies. Font et al. (2017) used previously determined corotation radii in combination with Spitzer images to estimate $\mathcal{R}$ for 68 barred galaxies. Cuomo et al. (2019) used data from CALIFA to look at 16 weakly barred galaxies. Additionally, Guo et al. (2019) used MaNGA data to study a sample of 53 barred galaxies. Garma-Oehmichen et al. (2020) used both CALIFA and MaNGA to obtain estimates for pattern speeds, corotation radii and $\mathcal{R}$ for 18 galaxies, while characterising the most common sources of error. Finally, Garma-Oehmichen et al. (2022) also used MaNGA to study a large sample of 97 barred Milky Way analogues.

The results presented here are compared to these studies in Figure 4.10. The bar pattern speed estimates calculated here agree well with that of other studies, especially the ones with larger sample sizes (n $>$ 50). The corotation radii calculated here also agree relatively well with the other studies with larger sample sizes, except with Font et al. (2017). The corotation radii in Font et al. (2017) were calculated using the Font-Beckman method (Font et al., 2011, 2014) rather than the TW method, which is used in all the other studies. The Font-Beckman method uses phase-reversals of the streaming motions based on H$\alpha$ velocity field to estimate the corotation radius. The values for $\mathcal{R}$ calculated in this thesis are slightly higher and more spread out than what other studies tend to find.

Interestingly, the median value of $\mathcal{R}$ seems to be moving upwards as the sample sizes increase. This is possibly due increased representation in larger samples of the huge variety of galaxy and bar types. The sample used here is the largest sample on which the TW method has been applied to so far and includes both weak and strong bars from a volume-limited sample and a wide range of magnitudes. This increase in sample size and representation will cause the observed distribution of $\mathcal{R}$ to more closely approximate the real distribution. For example, previous studies have typically focussed on strong bars. However, Figure 4.4 has shown that strong bars have significantly lower values for $\mathcal{R}$ than weak bars. The observed distribution of $\mathcal{R}$ in studies of mostly strongly barred galaxies will therefore underestimate the true distribution of $\mathcal{R}$. This has consequences for the high observed fraction of ultrafast bars in other studies and the tension with $\Lambda$CDM, which can both be relieved by finding a higher overall distribution of $\mathcal{R}$. This is discussed in more detail in Section 4.6.3.

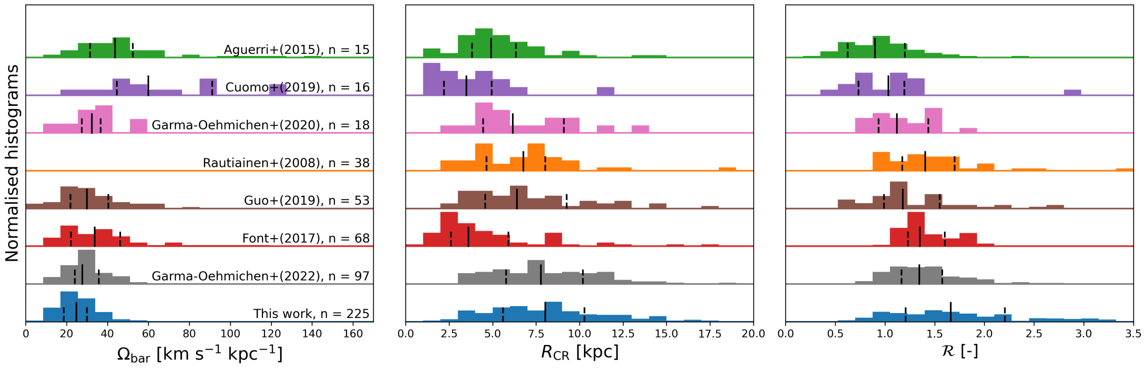

Figure 4.10: A comparison to estimates of the bar pattern speeds (left), corotation radii (middle) and $\mathcal{R}$ (right) found in other work. All the histograms are normalised and offset from each other vertically to facilitate comparison. The median, 25th and 75th percentile for every distribution are indicated by the short full and dashed lines. The studies are ordered by sample size, which is also shown in the left panel. The values from Rautiainen et al. (2008) and Aguerri et al. (2015) were converted from the observational units cited in their papers to physical units using redshifts obtained from the NASA/IPAC Extragalactic Database (NED). The values obtained from Guo et al. (2019) were converted using their own cited redshifts. Similarly, the values from Font et al. (2017) were converted using the distances cited. The values for the bar pattern speeds from Rautiainen et al. (2008) are not publicly available, hence the empty histogram. The distributions of pattern speed and corotation radius calculated here generally agrees well with that of other studies, especially those with larger sample sizes. The distribution of $\mathcal{R}$ calculated here is higher and more spread out than what the literature typically finds.

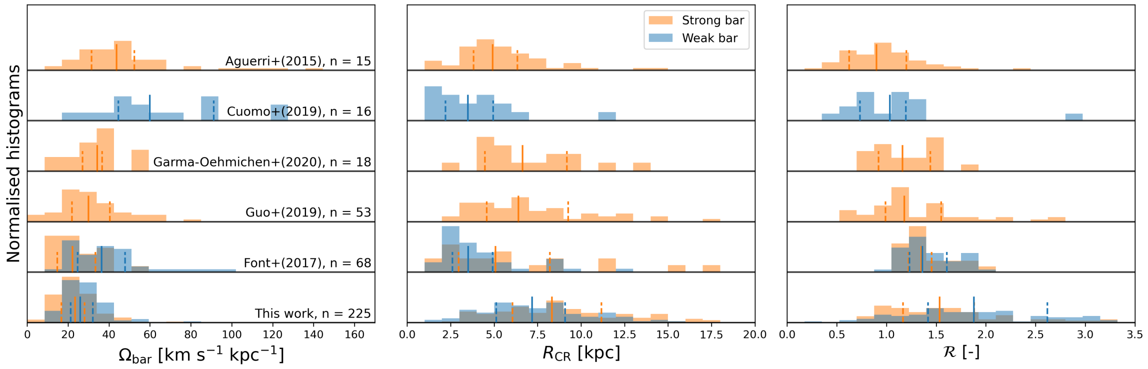

Figure 4.11: A comparison to estimates of the bar pattern speeds (left), corotation radii (middle) and $\mathcal{R}$ (right) found in other work. The data is split between weakly barred galaxies (blue) and strongly barred galaxies (orange). Font et al. (2017) have both weak and strong bars, whereas the other studies focus only on either weak or strong bars. All the histograms are normalised and offset from each other vertically to facilitate comparison. The median, 25th and 75th percentile for every distribution are indicated by the short full and dashed lines. The studies are ordered by sample size, which is also shown in the left panel. The values from Aguerri et al. (2015) were converted from the observational units cited in the papers to physical units using redshifts obtained from the NASA/IPAC Extragalactic Database (NED). The values obtained from Guo et al. (2019) were converted using their own cited redshifts. Similarly, the values from Font et al. (2017) were converted using the distances cited in the paper.

Figure 4.11 shows a similar comparison, but this time the distributions are split into strongly or weakly barred galaxies, if this was clearly specified in the comparison studies. The left panel reveals that the pattern speed of weakly barred galaxies in other studies tends to be higher than that of strongly barred galaxies, in agreement with the findings presented here. However, the middle panel of Figure 4.11 shows that the corotation radius of weakly barred galaxies in other studies tends to be shorter than the corotation radius of strongly barred galaxies, which is not observed here. However, many of those studies (Aguerri et al., 2015; Cuomo et al., 2019; Guo et al., 2019) assume that the corotation radius lies in the region where the rotation curve has flattened. This is not always the case and can bias the final corotation estimates (see Section 2.2.4.4 for more details). Finally, I find that weakly barred galaxies have higher values for $\mathcal{R}$ than strongly barred galaxies, although this is not typically observed in other studies. This is discussed in more detail in Section 4.6.2.

## 4.6 Discussion

### 4.6.1 Are strong bars older than weak bars?

Simulations have shown that the pattern speed slows down and the bar grows larger as the bar exchanges angular momentum with its host, which suggests that bars with lower pattern speeds are older and more evolved than bars with higher pattern speeds (Debattista & Sellwood, 2000; Athanassoula, 2003; Martinez-Valpuesta et al., 2006; Okamoto et al., 2015). The pattern speed has been correlated with bar strength and length before. For example, Font et al. (2017) found that bars with the largest pattern speeds are small, while the largest bars tend to have the lowest pattern speeds. Cuomo et al. (2020) found, using the CALIFA and MaNGA surveys, that stronger bars tend to have lower bar pattern speeds as well. Lee et al. (2022) used CALIFA, MaNGA and Pan-STARRS DR1 (PS1) and found that the bar pattern speed is negatively correlated to bar length and strength. However, their sample size, especially of weakly barred galaxies, is limited.

Figure 4.2 shows that strongly barred galaxies in the sample used here have significantly lower bar pattern speeds than weakly barred galaxies (p-value = 0.002; $3.1\sigma$), despite a large overlap in both distributions. Figure 4.8 shows that this observed difference is not due to differences in stellar mass between weak and strong bars, as the pattern speed does not change with stellar mass. The pattern speed is also found to be negatively correlated with bar length in Figure 4.7. Therefore, our results imply that strong bars are more evolved and older structures compared to weak bars. However, it must be noted that it is also possible that strong bars are simply more efficient at redistributing angular momentum, as this depends on multiple parameters, such as the velocity dispersion and mass distribution of the emitting and absorbing components (Athanassoula, 2003).

### 4.6.2 How are strong and weak bars triggered?

The formation mechanism of the bar has an influence on $\mathcal{R}$, as demonstrated by simulations. Bars formed by global bar instabilities tend to have lower values for $\mathcal{R}$ than bars triggered by tidal interactions, which stay in the slow regime for a longer time (Sellwood, 1981; Miwa & Noguchi, 1998; Martinez-Valpuesta et al., 2016; Gajda et al., 2017; Martinez-Valpuesta et al., 2017). Interestingly, Guo et al. (2019) and Cuomo et al. (2020) find no relationship between bar strength and $\mathcal{R}$. However, both studies have a lower sample size, especially for weak bars. Guo et al. (2019) only have strong bars in their sample, whereas Cuomo et al. (2020) only have 16 weakly barred galaxies.

I find that strongly barred galaxies have statistically significantly lower values for $\mathcal{R}$ than weakly barred galaxies (p-value = 0.001; $3.3\sigma$), as shown in Figure 4.4. However, note that there is still a large overlap between the two distributions. Figure 4.8 shows that this difference is not caused by differences in stellar mass. Additionally, I show in Figure 4.7 that bar length is negatively correlated with $\mathcal{R}$. The results presented here therefore suggest that weak bars are more likely to be formed by tidal interactions, whereas strong bars are more likely to be triggered by global bar instabilities. This result can be verified observationally by looking at the environment of a large mass-matched sample of strongly and weakly barred galaxies in a future study. However, $\mathcal{R}$ depends heavily on the bar length and inclination estimates (Cuomo et al., 2021; Roshan et al., 2021a), so this trend could be biased by differences in bar length between strong and weak bars. Comparing different bar length metrics with each other could help to clarify this issue.

### 4.6.3 Tension with ΛCDM and ultrafast bars

The prevalence of ultrafast and fast bars in observations has been raised as a tension for the ΛCDM paradigm, since cosmological simulations predict that bars should slow down significantly (Algorry et al., 2017; Peschken & Łokas, 2019; Fragkoudi et al., 2021; Roshan et al., 2021a,b; Frankel et al., 2022). This slow down is usually attributed to dynamical friction caused by the DM halo on the bar (Debattista & Sellwood, 1998, 2000; Fragkoudi et al., 2021). This has been the subject of many recent studies, which have tried to relieve this tension. For example, Fragkoudi et al. (2021) show with their cosmological simulations that they actually do find fast bars in baryon-dominated discs, and suggest that the DM fraction is too high in other studies. Reducing the DM fraction lowers the dynamical friction, which allows the existence of fast bars. Additionally, Frankel et al. (2022) have suggested that simulations get higher values of $\mathcal{R}$ as simulations predict shorter bars, rather than bars that rotate slower. Finally, the gas phase of the disc can help to stabilise the bar pattern speed and prevent it from slowing down, as shown by Beane et al. (2022). Nevertheless, this tension remains and measuring $\mathcal{R}$ for larger samples of barred galaxies will help to better address this issue.

A related problem is that ultrafast bars, which have $\mathcal{R} < 1$, should theoretically not exist. $\mathcal{R}$ is defined as $\mathcal{R} = R_{\mathrm{CR}}/R_{\mathrm{bar}}$, and it is believed that a bar cannot extend beyond its corotation radius as the stellar orbits that make up the bar become unstable

Table 4.1: Summary of how many ultrafast bars ($\mathcal{R} < 1$), fast bars ($1 < \mathcal{R} < 1.4$) and slow bars ($\mathcal{R} > 1.4$) are found in other work. Note that Aguerri et al. (2015) and Guo et al. (2019) have multiple different samples, hence the range.

| | Sample size | % Ultrafast | % Fast | % Slow |
|---|---|---|---|---|
| Rautiainen et al. (2008) | 38 | 16 | 34 | 50 |
| Aguerri et al. (2015) | 15 | 46-67 | 20-40 | 7-13 |
| Font et al. (2017) | 68 | 1 | 59 | 40 |
| Cuomo et al. (2019) | 16 | 44 | 50 | 6 |
| Guo et al. (2019) | 53 | 26-47 | 13-34 | 38-43 |
| Garma-Oehmichen et al. (2020) | 18 | 39 | 22 | 39 |
| Garma-Oehmichen et al. (2022) | 97 | 11 | 43 | 45 |
| This work | 225 | 11 | 27 | 62 |

at radii larger than the corotation radius (Contopoulos, 1980, 1981; Athanassoula, 1992b). However, galaxies with these ultrafast bars are repeatedly observed. The fraction of ultrafast bars found in other work varies significantly. Some studies find relatively few ultrafast bars (11-16% of their sample, Rautiainen et al., 2008; Garma-Oehmichen et al., 2022), while others find that roughly half of all barred galaxies are ultrafast (44 - 67%, Aguerri et al., 2015; Cuomo et al., 2019). The fraction of ultrafast bars in multiple other studies is summarised in Table 4.1.

I find that 11% of the galaxies in the TW sample have an ultrafast bar, while only 2% have a $1\sigma$ upper limit that has $\mathcal{R} < 1$. This means that only 2% of the entire sample is confidently within the ultrafast regime, which is significantly lower that what other studies typically find. Additionally, as shown in Figure 4.4, strong bars have significantly lower values for $\mathcal{R}$ than weak bars, which implies that there are more ultrafast bars among strong bars than weak bars (13.9% and 7.8%, respectively). This can partially explain why many previous studies find higher fractions of ultrafast bars, as they have mostly focussed on strongly barred galaxies. Similarly, most studies find that around 6 - 50% of their sample have a slow bar (a more detailed breakdown is shown in Table 4.1), while I find that 62% of the bars are slow. However, only 35% of the targets in the TW sample have a $1\sigma$ lower limit that has $\mathcal{R} > 1.4$. In other words, the values of $\mathcal{R}$ calculated here tend to be higher than what is found in most other studies. This is confirmed in Figure 4.10, where it is shown that the overall distribution of $\mathcal{R}$ is higher in this sample than what is typically found elsewhere.

The higher overall values for $\mathcal{R}$ in the TW sample reduces the tension with ΛCDM. However, the median value of $\mathcal{R}$ found here ($\mathcal{R} = 1.66^{+1.05}_{-0.62}$) is still significantly lower than what is typically found in simulations, whose average values at z$\sim$0 are $\mathcal{R} > 2.5$

(Algorry et al., 2017; Peschken & Łokas, 2019; Roshan et al., 2021b), which suggests that the tension is not completely relieved.

While the estimates of $\mathcal{R}$ calculated here are more consistent with theory and simulations than the other studies discussed above, it is crucial to understand the different biases that might affect $\mathcal{R}$, as it is a difficult parameter to correctly estimate. It is directly dependent on the corotation radius and the bar radius, which suggests that it is important to correctly estimate them in order to evaluate $\mathcal{R}$. However, neither is straight-forward. Measuring the bar length can be difficult, as bars are often associated with rings and spiral arms (Hilmi et al., 2020; Cuomo et al., 2021; Roshan et al., 2021a), although deeper imaging helps to separate the bar from other structures and to measure the bar length as accurately as possible. Different studies will employ different methods to measure the bar length, which affects the final distribution of $\mathcal{R}$ (see Section 2.2.2 for more details on the bar length measurement used here and the precautions used to make it as reliable as possible). The corotation radius is dependent on an accurate estimate of the pattern speed and a correctly modelled rotation curve (for more details, see Section 2.2.4.4). A strong bar can influence the inclination measurement that will cause biases in the line of sight velocity corrections. This will, in turn, affect the rotation curve and the estimate for the corotation radius. Correctly identifying and dealing with these biases, while appropriately propagating the associated errors is crucial to accurately measure $\mathcal{R}$.

Additionally, Guo et al. (2019) have shown that the pattern speed estimate will be systematically lower when using kinematic position angles instead of photometric position angles. The kinematic position angle is calculated by minimising asymmetry in the velocity field (see Section 2.2.1 for more details). However, this reduces the value of the kinematic integral (see Equation 2.11 in Chapter 2). This will lower the estimate of the pattern speed, which will increase the final estimate for $\mathcal{R}$. Kinematic position angles are used in this work, as they tend to be more robust and accurate than photometric position angles, especially in barred galaxies (see Figure 2.8 in Section 2.2.1). This could explain the higher values for $\mathcal{R}$ observed here, compared to other work that uses photometric position angles.

Finally, Figure 4.4 shows that the value of $\mathcal{R}$ is significantly lower for strong bars than for weak bars in the TW sample. This suggests that there are differences in the DM fractions of strongly and weakly barred galaxies, as $\mathcal{R}$ is thought to increase due to interactions with the DM halo (Debattista & Sellwood, 1998, 2000; Fragkoudi et al., 2021). The DM fraction can be estimated by creating Jeans Anisotropic Models (JAM) of these galaxies (Cappellari, 2008), which will allow me to study the relationship between the DM fraction, bar strength and $\mathcal{R}$ in greater detail in a future study and provide possible new insights to address the tension with ΛCDM mentioned above.

### 4.6.4 Strong and weak: part of a continuum

While strong bars have lower bar pattern speeds and lower values for $\mathcal{R}$ than weak bars, their distributions still overlap significantly, as seen in Figures 4.2 and 4.4. There is no distinct threshold in the bar pattern speed or $\mathcal{R}$ that can be used to perfectly separate weak and strong bars. Furthermore, when plotting these parameters against bar radius in Figure 4.7, I find that the differences in pattern speed and $\mathcal{R}$ are driven by the smallest and largest bars in the sample, as these trends are almost identical for weakly barred and strongly barred galaxies at intermediate bar lengths. I also find that weakly and strongly barred galaxies do not have statistically significantly different corotation radii. This result implies that weak bars still have the potential to grow to be as large as strong bars, as bars are able to grow up until their corotation radius (Contopoulos, 1980, 1981; Athanassoula, 1992b).

These findings are consistent with the bar continuum proposed in Section 3.6.4, where I show that weak and strong bars are not distinct physical phenomena. Instead, bar types are continuous and vary from ‘weakest’ to ‘strongest’. The kinematics of bars studied in this chapter support this conclusion as well.

### 4.6.5 Effect on quenching

Observations have shown that strong bars are more often found in red sequence galaxies (Masters et al., 2012; Vera et al., 2016; Cervantes Sodi, 2017; Fraser-McKelvie et al., 2020b). Additionally, I have shown in Chapter 3 that stronger bars can facilitate quenching, whereas weaker bars cannot. The effect that pattern speed, corotation radius and $\mathcal{R}$ have on quenching is probed in Figure 4.9. It is shown that the pattern speed and $\mathcal{R}$ are not significantly different between SF and quenching galaxies, which implies that how rapidly bars rotate does not have a measurable effect on quenching. This can be explained by looking at the timescales that are involved. A bar that has a pattern speed of $\sim$25 km s$^{-1}$ kpc$^{-1}$, which is the median pattern speed of the entire TW sample, will make one full rotation every $\sim$250 Myr. Secular quenching usually occurs on $\sim$Gyr timescales (Schawinski et al., 2014; Smethurst et al., 2015), which suggests that a typical bar will have made multiple full rotations before the galaxy is fully quenched. This suggests that an average bar (with an average pattern speed) has had ample opportunity to sweep up gas within the timescale where secular quenching typically happens, regardless of how rapidly it rotates.

It is interesting to see in Figure 4.9 that the corotation radius is significantly higher in quenching galaxies than in SF galaxies. The corotation radius is proportional to bar length (see Figure 4.7) and bars are able to grow up until their corotation radius (Contopoulos, 1980, 1981; Athanassoula, 1992b), which means that this result could be a consequence of longer and stronger bars having a bigger effect on quenching, in agreement with the results of Chapter 3. Nevertheless, a more detailed study on the relationship between these dynamical parameters, bar strength and quenching will be beneficial to better understand how bar kinematics affect quenching. In Chapter 5 I will look at several resolved SF indicators for slow and fast bars to help clarify these issues.

## 4.7 Conclusions

In this chapter, I have calculated the bar pattern speed for a large sample of 122 strongly and 103 weakly barred galaxies using the TW method on data obtained from MaNGA, which is the largest sample this method has been applied to so far. The bar pattern speed is used to estimate the corotation radius and $\mathcal{R}$, which is the ratio of the corotation radius and the bar radius. Classifications from Galaxy Zoo DESI were used to discern between weakly and strongly barred galaxies. I have found that:

- The bar pattern speed of strongly barred galaxies is significantly lower than weakly barred galaxies (p-value = 0.001-0.002; 3.1-3.3$\sigma$). The median bar pattern speed, together with the 16th and 84th percentiles, is $23.36^{+9.25}_{-8.1}$ km s$^{-1}$ kpc$^{-1}$ for the strongly barred galaxies and $25.91^{+10.42}_{-7.26}$ km s$^{-1}$ kpc$^{-1}$ for the weakly barred galaxies. However, it must be noted that there is still a significant overlap between the pattern speed distributions of weak and strong bars. I also show that this difference is not due to variability in stellar mass between weakly and strongly barred galaxies. Additionally, I find that the pattern speed is inversely proportional to bar length. These findings imply that strong bars are more evolved and older structures than weak bars, as simulations suggest that the pattern speed goes down as the bar evolves and exchanges angular momentum.

- I could find no evidence that the corotation radius between strongly barred galaxies ($R_{CR} = 8.33^{+4.57}_{-3.31}$ kpc) and weakly barred galaxies ($R_{CR} = 7.19^{+3.82}_{-2.96}$ kpc) is significantly different (p-value = 0.012; 2.5$\sigma$). This result suggests that weak bars can still grow to be as long as strong bars, as bars are able to grow up until their corotation radius.

- Although there is significant overlap in the distributions, I find that $\mathcal{R}$ is statistically significantly different between strongly and weakly barred galaxies (p-value = 0.001; 3.3$\sigma$). The median value for strong bars is $1.53^{+0.74}_{-0.53}$, while the median value for weak bars is $1.88^{+1.08}_{-0.75}$. This difference was shown not to be due to differences in stellar mass. Additionally, I find that $\mathcal{R}$ is inversely proportional to bar length. Simulations suggest that $\mathcal{R}$ depends on the formation mechanism of the bar. These results therefore suggest that strong bars are more likely to be formed by global bar instabilities, whereas weak bars are more likely to be triggered by tidal interactions.

- Even though significant differences are found in terms of pattern speed and $\mathcal{R}$ between weakly and strongly barred galaxies, no distinct threshold was found that separates them from each other. These results are consistent with the bar continuum proposed in Section 3.6.4.

- I find that 11% of the sample host ultrafast bars, however only ~2% have a 1$\sigma$ upper limit that has $\mathcal{R} < 1$ (i.e. only 2% of the entire sample is confidently within the ultrafast regime). This is lower than what other studies typically find. A total of 27% of the bars in the sample are fast, while 62% are slow. The lower fraction of ultrafast and fast bars decreases the recently claimed tension with $\Lambda$CDM. However, the value of $\mathcal{R}$ that is typically predicted from simulations is still significantly higher than what is estimated here.

- I find that SF and quenching galaxies do not have significantly different values for the pattern speed and $\mathcal{R}$. This suggests that the speed at which bars rotate does not have a significant effect on quenching. Interestingly, the corotation radius is significantly higher for quenching galaxies than for SF galaxies (p-value < 0.001; >3.3$\sigma$). As the corotation radius is proportional to bar length, this result confirms that longer bars are more efficient at quenching their hosts.

# Chapter 5

# Radius profiles: Slow and strong bars affect their hosts the most

I showed in Chapter 3 that strongly barred star forming galaxies have higher star formation rates (SFRs) in their central 3 arcsec, compared to weakly barred and unbarred galaxies. However, it is not clear what happens in other regions, such as the arms of the bar or the bar-ends[1]. Can strong bars affect other regions of their hosts, besides the centre, and how does this compare to the behaviour of weak bars? It is also unclear how the kinematics of bars affect galaxy evolution and quenching. In Chapter 4, I identified and discussed the properties of fast ($1.0 < \mathcal{R} < 1.4$) and slow ($\mathcal{R} > 1.4$) bars. However, do fast and slow bars affect star formation in the same way? Finally, do the kinematics of a bar influence the effect that strong or weak bars have on their host: do slow strong bars and fast strong bars affect their hosts in the same way? These topics are studied in this chapter. This is only possible to do with resolved star formation indicators measured by IFUs surveys, such as MaNGA (see Section 2.1.2).

In order to probe what effect bars have on their host, I look at the Gaussian-fitted equivalent width measurement of H$\alpha$, EW[H$\alpha$], from MaNGA. H$\alpha$ emission is found at a rest-frame wavelength of 6564 Å and comes from HII regions that are excited by the ionizing radiation of OB type stars, which are present in young stellar populations (Argence & Lamareille, 2009; Spindler et al., 2018; Smethurst et al., 2019). The amount of H$\alpha$ radiation is proportional to the number of OB stars, and thus the amount of star formation (Kennicutt, 1998a). The equivalent width is defined as the width of a rectangle with an area identical to the flux of the line in rest-frame and height equal to the continuum of the spectrum ($F_l = EW \times C_l$, Westfall et al., 2019).

---

[1] These different regions were defined in Figure 1.5 of Chapter 1.

Because of this normalisation to the continuum (which is a proxy for stellar mass), EW[H$\alpha$] traces specific SFR, rather than SFR.

I also look at the strength of the 4000 Å break, which is caused by a combination of absorption of radiation around 4000 Å by older stellar populations with higher metallicities and the lack of emission from young, blue OB type stars. This implies that $D_n4000$ traces the age of the stellar population (Kauffmann et al., 2003; Smethurst et al., 2019; Paulino-Afonso et al., 2020). I use the definition of the 4000 Å break from Balogh et al. (1999), $D_n4000$, which is an update to the definition of Bruzual A. (1983). $D_n4000$ is a dimensionless ratio of the flux between 4000-4100 Å and 3850-3950 Å, which is measured by the MaNGA data analysis pipeline (DAP, Westfall et al., 2019). If $D_n4000$ is low, there has been recent star formation and the average stellar population is relatively young. In contrast, an older stellar population is present if $D_n4000$ is high (Kauffmann et al., 2003; Smethurst et al., 2019; Paulino-Afonso et al., 2020). This also means that $D_n4000$ is a useful probe to test whether a quenching mechanism (e.g. a strong bar) has had a long-lasting effect on the galaxy, which helps to probe the timescales of that mechanism. For example, while there is a dependence on stellar metallicity to keep in mind, a value of 1.0 for $D_n4000$ suggests a relatively young mean age of the underlying stellar population ($\sim$10 Myr), while a value of 1.5 corresponds to an older mean age of $\sim$1 Gyr (Kauffmann et al., 2003; Paulino-Afonso et al., 2020).

In this chapter, I make use of spatially resolved data from MaNGA (more specifically: EW[H$\alpha$] and $D_n4000$), which allows me to study different regions in barred galaxies. This chapter is divided in two main parts. In Section 5.1, I generate radius profiles of EW[H$\alpha$] and $D_n4000$ of the entire GZ DESI-MaNGA sample to assess differences in star formation between strong and weak bars. A similar analysis is done for fast and slow bars in Section 5.2 for the galaxies in the TW sample (which is a subset of the GZ DESI-MaNGA sample). Lastly, the conclusions of both parts are summarised in Section 5.3.

## 5.1 Strong and weak bars

Observations have shown that barred galaxies have higher star formation in their centre (Alonso-Herrero & Knapen, 2001; Hunt et al., 2008; Ellison et al., 2011; Coelho & Gadotti, 2011; Lin et al., 2020) and bar-end region (Reynaud & Downes, 1998; Verley et al., 2007; Díaz-García et al., 2020; Fraser-McKelvie et al., 2020a; Maeda et al., 2020a), while suppressing star formation along the arms of the bar (Reynaud

& Downes, 1998; Zurita et al., 2004; Watanabe et al., 2011; Haywood et al., 2016), suggesting that bars can significantly influence the evolution of their host. However, it is unclear whether this is true for both weak and strong bars. This was first investigated in Chapter 3, where I found in an increase of central star formation for strongly barred galaxies, but not for weakly barred galaxies. However, differences in star formation in the arms of the bar and the bar-end region of weak and strong bars have not yet been studied in this thesis. This is the topic of the first part of this Chapter, in which I make use of resolved star formation indicators measured by the MaNGA pipeline. The results are presented from Section 5.1.1 to Section 5.1.4 and discussed in Section 5.1.5.

### 5.1.1 EW[H$\alpha$] along strong and weak bars

In order to probe the effect that a bar has on different regions of a galaxy, I create radius profiles of EW[H$\alpha$] and $\mathrm{D_n}4000$, which are obtained from MaNGA. More details on how these radius profiles are constructed can be found in Section 2.2.5. These radius profiles are constructed for all the galaxies in the GZ DESI-MaNGA sample. In Figure 5.1, the radius profiles of the Gaussian-fitted equivalent width measurement of H$\alpha$ (EW[H$\alpha$]) from MaNGA are shown for every bar type: strong, weak and unbarred. The galaxies are split into star forming (SF) or quenching based on Equation 3.1 in Section 3.1. This threshold is also shown in Figure 3.6. The top row shows the profiles for SF galaxies, while the bottom row shows the profiles for quenching galaxies. The profiles are shown in terms of distance to the centre of the galaxy (in arcsec, left column), as well as relative to the bar radius (right column). However, it is useful to keep in mind that strong bars are longer than weak bars (see Section 3.1), which implies that a distance of e.g. $2R_{\mathrm{bar}}$ is farther out in the disc of the galaxy for a strong bar than for a weak bar. The bottom part of every panel shows the difference between the radius profiles of two samples. The significance of the difference in every bin is shown by the size of the point; the largest sizes represent a significant difference greater than $3\sigma$ after comparing the two populations with an Anderson-Darling test, while the smallest sizes represent $<1\sigma$. The bins with a significant difference of $>3\sigma$ are also outlined in black.

The radius profile of strongly barred SF galaxies (orange, top row of Figure 5.1) has an interesting shape. The EW[H$\alpha$] is highest in the central bins, after which it reaches a minimum in the arms of the bar. Interestingly, the profile increases again and reaches another peak beyond the bar-end region (at $R \approx 1.2 - 1.5R_{\mathrm{bar}}$) before declining at higher radii. This profile suggests the SFR is higher in the centre and

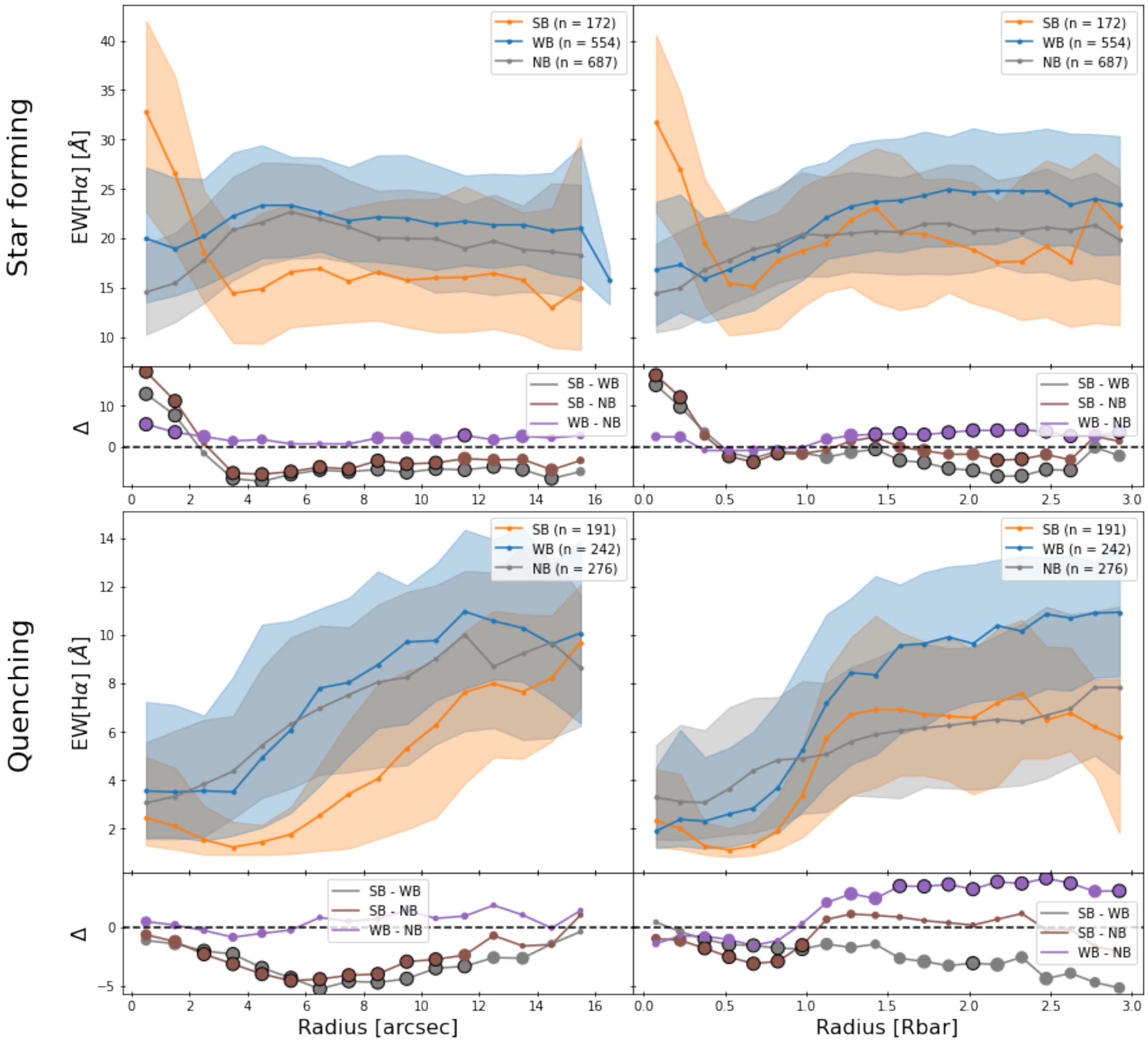

Figure 5.1: The radius profiles of EW[H$\alpha$] are shown for SF galaxies (top row) and quenching galaxies (bottom row) for strongly barred (orange), weakly barred (blue) and unbarred galaxies (grey). The radius profiles are shown in arcsec (left column) and normalised against the bar radius (right column). The profiles for unbarred galaxies are normalised to the bar radius by assigning a random bar radius to every unbarred galaxy, which is drawn from a log-normal distribution fitted to all the barred galaxies in the sample. The sample size, n, for every sample is indicated in the legend. The solid line is the median in every bin, while the shaded regions bound the 33$^{\mathrm{rd}}$ and 66$^{\mathrm{th}}$ percentiles. The width of the bins in the left column is 1 arcsec and 0.15 $R_{\mathrm{bar}}$ in the right column. The bottom part of each panel shows the difference between each radius profile in every bin, where the size of the point represents the significance of the difference after comparing the two populations with an Anderson-Darling test. The smallest sizes represent a significant difference of less than $1\sigma$, while the largest sizes represent $>3\sigma$ and are additionally outlined in black. Strongly barred SF galaxies have higher values for EW[H$\alpha$] in the centre and bar-end, while having less EW[H$\alpha$] in the arms of the bar. The profiles of weak and unbarred SF galaxies are very similar to each other.

bar-end, as EW[H$\alpha$] is a proxy for SFR, while it is suppressed in the arms of the bar. This is consistent with the results presented in Section 3.4, where I found increased SFR in the central 3 arcsec fibre for strongly barred SF galaxies. The EW[H$\alpha$] profiles of weakly barred SF galaxies and unbarred SF galaxies are very similar to each other; both are flat in the outskirts (at R $\gtrsim$ 10 arcsec or $\gtrsim$ 1.5 $R_{\mathrm{bar}}$) and have lower median values for EW[H$\alpha$] closer to the centre. This is also consistent with the results shown in Section 3.4, where no differences in SFR were found between weakly barred and unbarred SF galaxies. It is also interesting to note that in the outskirts of the galaxy, the EW[H$\alpha$] is lower for strongly barred SF galaxies than for weakly barred and unbarred SF galaxies.

The bottom half of Figure 5.1 shows the radius profiles for strongly barred, weakly barred and unbarred galaxies that are quenching. Strongly barred quenching galaxies have lower values for EW[H$\alpha$] overall, while weakly and unbarred galaxies have roughly similar values to each other. All profiles have higher values for EW[H$\alpha$] in the outskirts, which decrease towards the centre of the galaxy. However, interestingly, for both weak and strong bars, this decrease starts to happen around the bar-end ($R \approx 1.0 - 1.2R_{\mathrm{bar}}$), although it is more sudden for strong bars. This decrease at at bar-end region is not observed for the unbarred galaxies normalised to the bar radius. However, it is worth keeping in mind that the unbarred profiles normalised to the bar radius are not physical; they are constructed by assigning a random bar radius to every unbarred galaxy, which is drawn from a log-normal distribution fitted to all the barred galaxies in the sample (see Section 2.2.5 for more details).

### 5.1.2 D$_{\mathrm{n}}$4000 along strong and weak bars

Figure 5.2 shows the radius profiles for D$_{\mathrm{n}}$4000. The average profile for strongly barred SF galaxies is low in the centre, rises to a maximum in the middle of the arms of the bar ($R \approx 0.5R_{\mathrm{bar}}$), after which it goes back down and flattens beyond the bar-end region ($R \approx 1.2 - 1.5R_{\mathrm{bar}}$). This is very different from the profile observed in weakly barred and unbarred galaxies, where D$_{\mathrm{n}}$4000 is highest in the centre and monotonically decreases with radius. On average, strongly barred galaxies have the highest values for D$_{\mathrm{n}}$4000 and therefore have the oldest stellar populations, followed by weakly barred and unbarred SF galaxies, which have very similar values to each other. These results show that strongly barred SF galaxies have younger stellar population in their centre. Additionally, the stellar population is oldest in the arms of the bar of strongly barred SF galaxies. These results are consistent with the results obtained from the EW[H$\alpha$] radius profiles and with the results presented in Section 3.4, where

I found higher values of fibre SFR for strongly barred SF galaxies compared to weakly barred and unbarred SF galaxies, whose fibre SFRs are similar to each other.

These results confirm that strong bars can affect stellar populations, which suggests that strong bars are a long-lived phenomena. This is not the case for weakly barred galaxies, whose $\mathrm{D_n}4000$ profiles are very similar to those of unbarred galaxies. This is consistent with the results shown in Section 4.6.1, where I found that strong bars are older and more evolved structures than weak bars based on their pattern speeds. These results are discussed in more detail in Section 5.1.5.4.

Among quenching galaxies (bottom row of Figure 5.2), the trends of the profiles of the three samples are similar: highest in the centre, and decreasing monotonically with radius. However, for strongly barred galaxies, this decrease happens around the bar-end region, while it is much more gradual for weakly barred and unbarred galaxies. The value for $\mathrm{D_n}4000$ is similar for all three samples in the outskirts of the galaxy. Strongly barred quenching galaxies have higher values for $\mathrm{D_n}4000$ overall, while weakly and unbarred galaxies have similar values to each other.

In summary, **strongly barred SF galaxies have increased star formation in the centre and bar-end region, while suppressing star formation in the arms of the bar. In contrast, the profiles of weakly barred and unbarred galaxies are very similar to each other**. Weakly and unbarred galaxies have lower star formation in the centre, which increases with radius. These results are discussed in more detail and compared to the literature in Section 5.1.5.1.

### 5.1.3 Effect of stellar mass

In Chapter 3, I found that the strong bar fraction increases with stellar mass, while the weak bar fraction decreases with stellar mass. To make sure stellar mass did not affect the conclusions above, I also constructed the radius profiles for all SF galaxies in three different mass bins: low mass ($M_* < 10^{10.18} M_\odot$), intermediate mass ($10^{10.18} M_\odot < M_* < 10^{10.58} M_\odot$) and high mass ($M_* > 10^{10.58} M_\odot$). These thresholds were chosen so that an equal number of galaxies are in each bin (471 galaxies in each bin).

The radius profiles of EW[H$\alpha$] for the three mass bins are found in Figure 5.3, where I show that the central EW[H$\alpha$] peak for strongly barred SF galaxies is found in all mass bins. However, interestingly, the suppression of EW[H$\alpha$] and the subsequent second peak beyond the bar-end region ($R \approx 1.2 - 1.5 R_{\mathrm{bar}}$) among strongly barred SF galaxies are only observed in the intermediate and high mass bins, not in the low mass bin. The profiles of the weakly barred SF galaxies and unbarred SF galaxies are

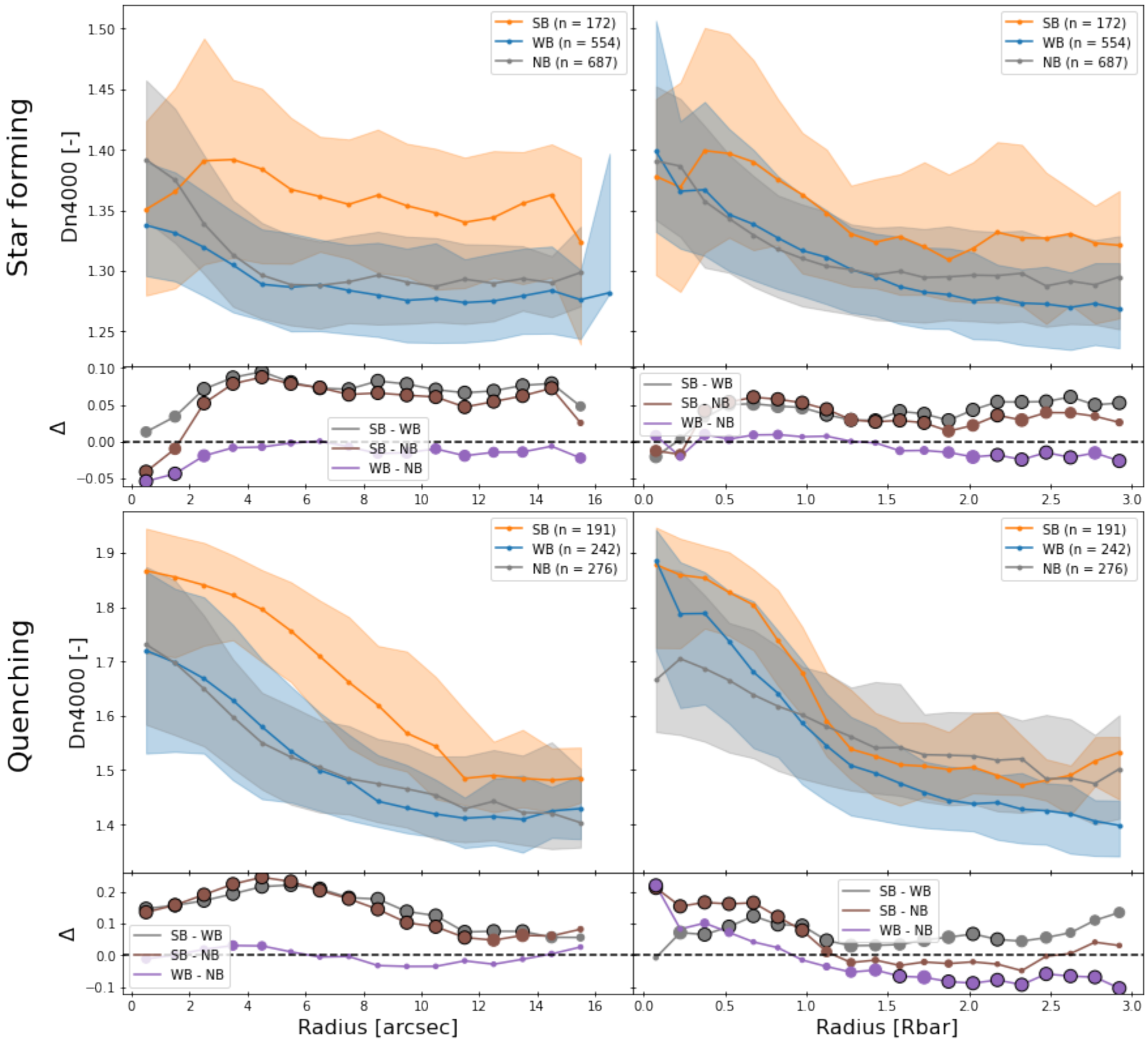

Figure 5.2: The radius profiles of $D_n4000$ are shown for SF galaxies (top row) and quenching galaxies (bottom row) for strongly barred (orange), weakly barred (blue) and unbarred galaxies (grey). The radius profiles are shown in arcsec (left column) and normalised against the bar radius (right column). The profiles for unbarred galaxies are normalised to the bar radius by assigning a random bar radius to every unbarred galaxy, which is drawn from a log-normal distribution fitted to all the barred galaxies in the sample. The sample size, n, for every sample is indicated in the legend. The solid line is the median in every bin, while the shaded regions bound the 33rd and 66th percentiles. The width of the bins in the left column is 1 arcsec and 0.15 $R_{\mathrm{bar}}$ in the right column. The bottom part of each panel shows the difference between each radius profile in every bin, where the size of the point represents the significance of the difference after comparing the two populations with an Anderson-Darling test. The smallest sizes represent a significant difference of less than $1\sigma$, while the largest sizes represent $>3\sigma$ and are additionally outlined in black. Strongly barred SF galaxies have lower values for $D_n4000$ in the centre, while having higher values for $D_n4000$ in the arms of the bar. The profiles of weak and unbarred SF galaxies are very similar to each other.

similar across all mass bins. A similar result is shown in Figure 5.4, where the radius profiles of $D_n4000$ for the different mass bins are shown for SF galaxies. The increase of $D_n4000$ in the arms of strong bars is much more pronounced in the intermediate mass and high mass bins, compared to the low mass bin. Again, the profiles of weakly barred and unbarred SF galaxies look similar in every mass bin.

These results show that **the conclusions from the previous section are valid for intermediate mass and high mass galaxies, but not for low mass galaxies**. This is consistent with the results shown in Section 3.4, where differences in fibre SFR, HI gas and depletion timescale between strongly barred SF galaxies and unbarred SF galaxies were found to increase with stellar mass. This is discussed in more detail in Section 5.1.5.2.

### 5.1.4 Focus on bar-end region

The bar-end region seems of particular interest. It is here that a local peak of EW[H$\alpha$] is found for strongly barred SF galaxies, but not for weakly barred SF galaxies. Additionally, the bar-end region seems to be a turn-over point in the EW[H$\alpha$] and $D_n4000$ profiles for strongly barred galaxies. To investigate this region in more detail, I create radius profiles with the aperture placed parallel and perpendicular to the bar (the rest of the procedure remains identical, see Section 2.2.5 for more details). The profiles generated with the aperture placed parallel to the bar (as in the figures above) will give information specifically about the barred region. In contrast, the profiles generated with the aperture placed perpendicular to the bar will help to probe the off-bar regions. Comparing the profiles generated with these two apertures will help show what the effect of the bar is (e.g. in the bar-end region) with respect to the rest of the galaxy. However, do note that the central region of the profiles should be similar, as the parallel and perpendicular apertures overlap in the 3 arcsec centre.

This is done in Figure 5.5 for all strongly barred SF galaxies (top row) and weakly barred SF galaxies (bottom row) for both EW[H$\alpha$] (left column) and $D_n4000$ (right column). The difference in EW[H$\alpha$] beyond the bar-end region ($R \approx 1.2 - 1.5R_{\rm bar}$) for strongly barred SF galaxies is ~10 Å, while this is only ~4 Å for weakly barred star forming galaxies. Additionally, the peak beyond the bar-end region is clearly visible in the profile with the aperture aligned with the bar, while it is not there in the profile with the aperture perpendicular to the bar. The difference in $D_n4000$ at the bar-end region is ~0.05 for strongly barred SF galaxies, while it is only ~0.01 for weakly barred SF galaxies.

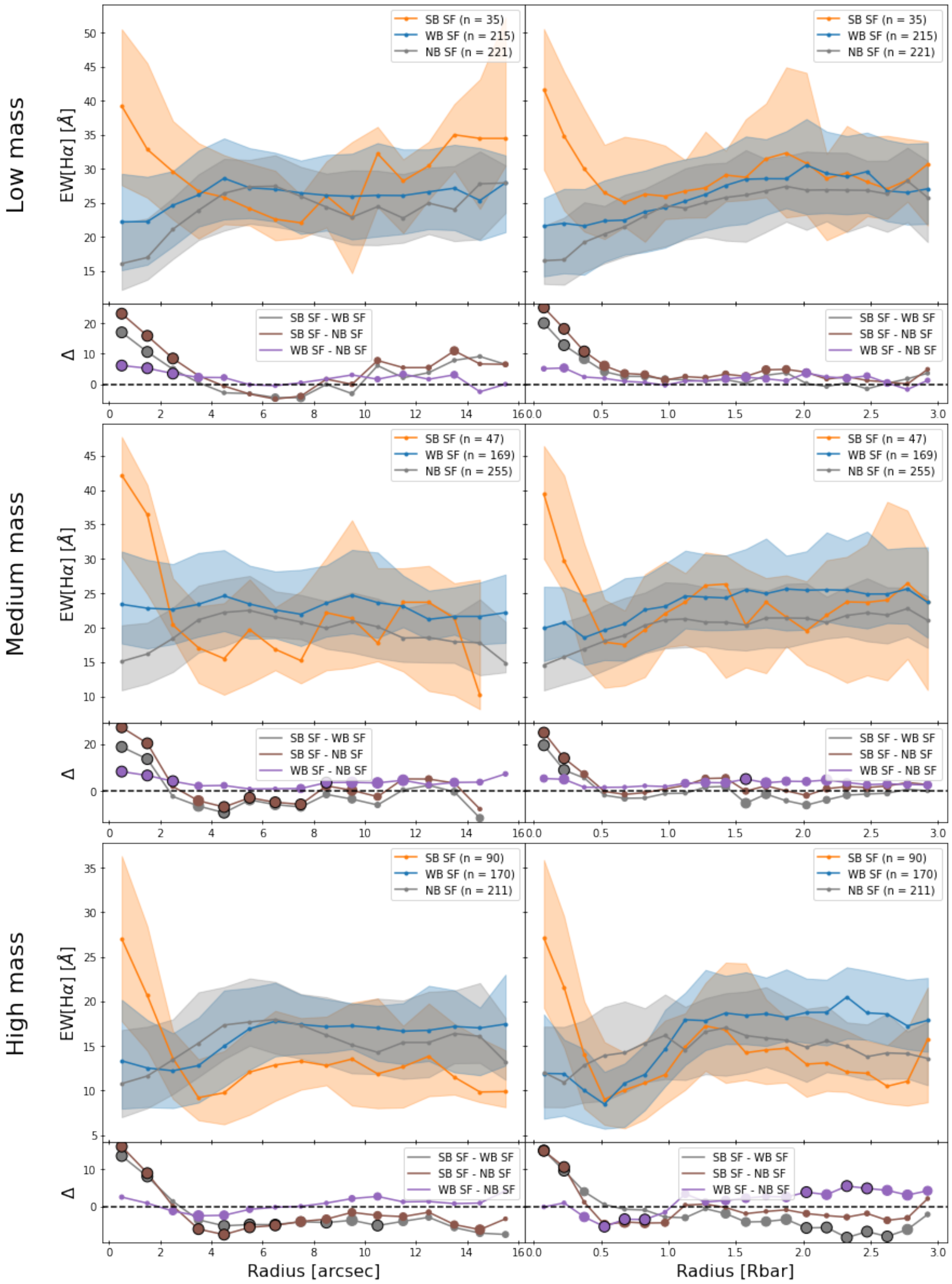

Figure 5.3: The radius profiles of EW[H$\alpha$] are shown for SF galaxies for strongly barred (orange), weakly barred (blue) and unbarred galaxies (grey), which are constructed similarly to those in Figure 5.1. However, the profiles here are shown in three different mass bins: low mass ($M_* < 10^{10.18} M_\odot$, top row), intermediate mass ($10^{10.18} M_\odot < M_* < 10^{10.58} M_\odot$, middle row) and high mass ($M_* > 10^{10.58} M_\odot$ bottom row). The profiles for intermediate and high mass galaxies are similar to those found in Figure 5.1. This is not true for the low mass galaxies.

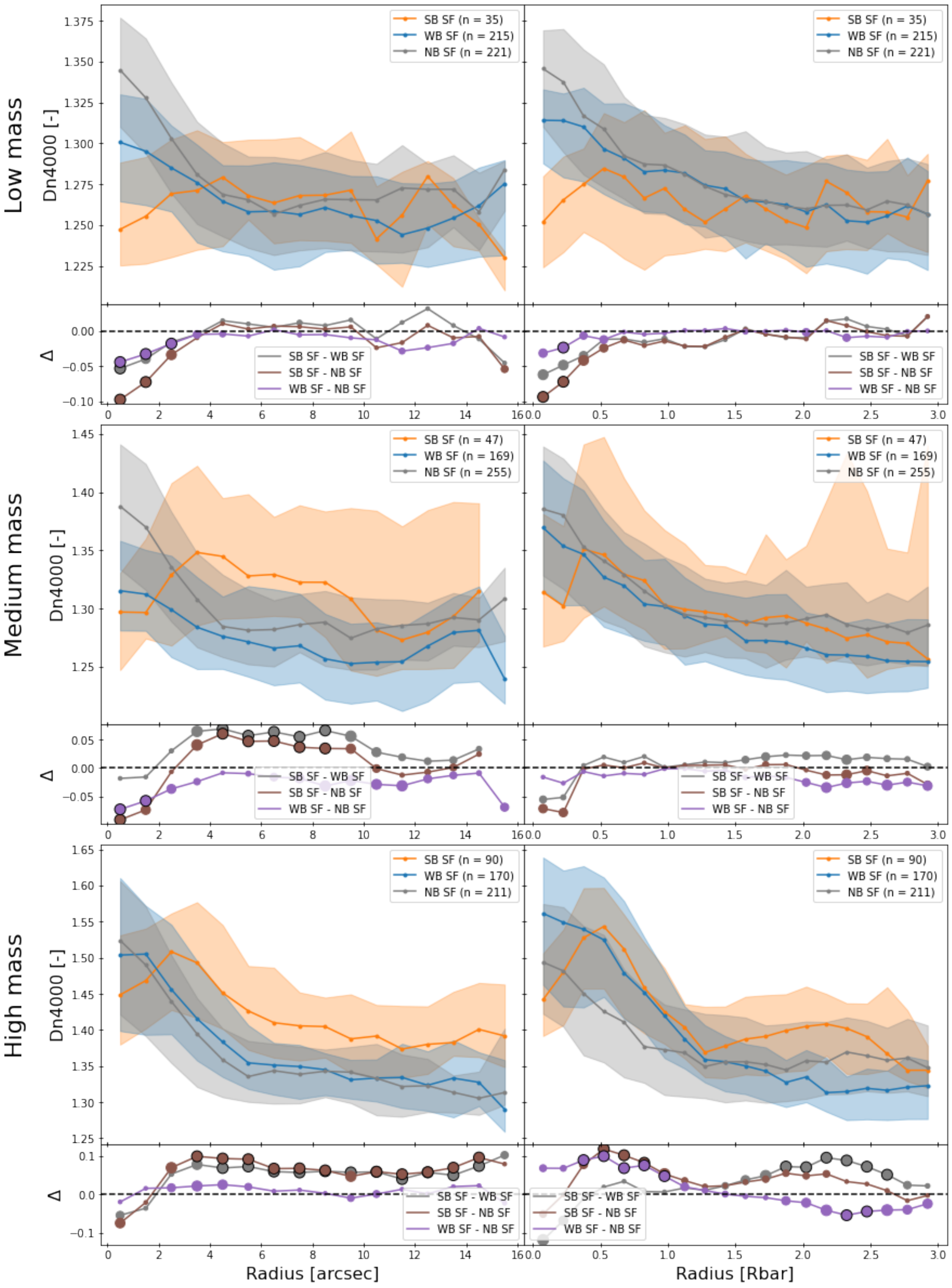

Figure 5.4: The radius profiles of $D_n4000$ are shown for SF galaxies for strongly barred (orange), weakly barred (blue) and unbarred galaxies (grey), which are constructed similarly to those in Figure 5.2. However, the profiles here are shown in three different mass bins: low mass ($M_* < 10^{10.18} M_\odot$, top row), intermediate mass ($10^{10.18} M_\odot < M_* < 10^{10.58} M_\odot$, middle row) and high mass ($M_* > 10^{10.58} M_\odot$ bottom row). The profiles for intermediate and high mass galaxies are similar to those found in Figure 5.2. This is not true for the low mass galaxies.

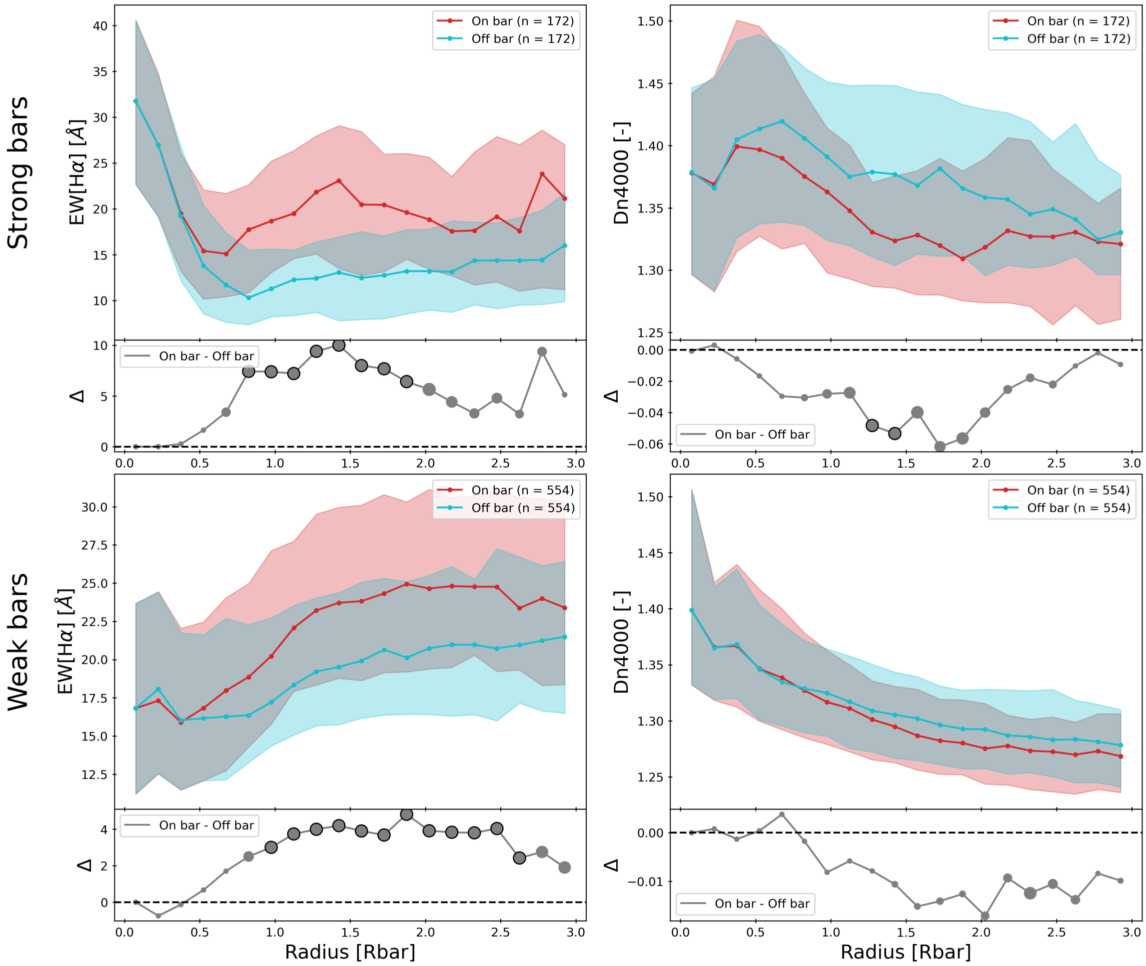

Figure 5.5: The effect of the bar-end region is probed in more detail in SF galaxies by creating radius profiles with apertures placed on the bar (parallel to the PA of the bar, shown in red) and off the bar (perpendicular to the PA of the bar, shown in light blue). This is done for the EW[H$\alpha$] profiles (left column) and the $D_n4000$ profiles (right column). The width of the bins is 0.15 $R_{\rm bar}$. The difference is much greater for strongly barred SF galaxies (top row) than for weakly barred SF galaxies (bottom row). The difference in EW[H$\alpha$] and $D_n4000$ in the bar-end is bigger for strongly barred galaxies than weakly barred SF galaxies.

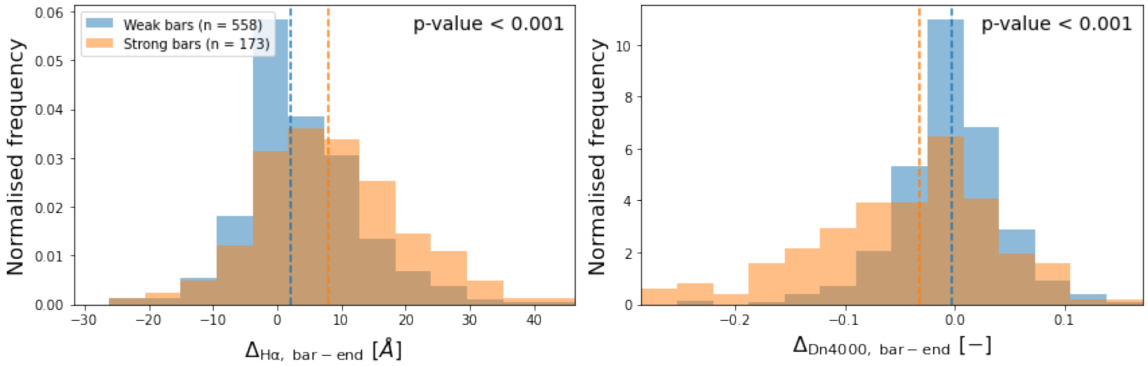

Figure 5.6: The difference between the EW[H$\alpha$] and D$_{\rm n}$4000 between the radius profile with the slit parallel and perpendicular to the bar is calculated for all SF galaxies. The median value of this difference between $1.2 - 1.5R_{\rm bar}$ is shown here for EW[H$\alpha$] (left panel) and D$_{\rm n}$4000 (right panel). While there is great overlap between strongly barred (orange) and weakly barred (blue) SF galaxies, it is clear that the difference is bigger for strongly barred SF galaxies.

The difference in EW[H$\alpha$] and D$_{\rm n}$4000 between the radius profile with the slit parallel and perpendicular to the bar is calculated for every galaxy and the median value of the difference between $1.2 - 1.5R_{\rm bar}$ was found ($\Delta_{\rm H\alpha,\ bar-end}$ and $\Delta_{\rm Dn4000,\ bar-end}$, respectively). These are shown in Figure 5.6 for all weakly and strongly barred SF galaxies. While there is great overlap, I find that $\Delta_{\rm H\alpha,\ bar-end}$ is statistically significantly higher and $\Delta_{\rm Dn4000,\ bar-end}$ is statistically significantly lower for strongly barred SF galaxies than for weakly barred SF galaxies, which is in agreement with the radius profiles shown in Figure 5.5. This suggests that there is **more star formation in the bar-end region of a strongly barred SF galaxy compared to the bar-end region of a weakly barred SF galaxy**.

### 5.1.5 Discussion: Strong and weak bars

#### 5.1.5.1 Star formation in different regions of strong and weak bars

The results from Chapter 3 suggest that strong bars in SF galaxies increase the central star formation of their hosts, while weak bars do not. However, the effect that strong bars have in other regions, and whether weak bars behave similarly, was unclear. This was studied in Figures 5.1 and 5.2 using EW[H$\alpha$] and D$_{\rm n}$4000, respectively. These figures show that strongly barred SF galaxies have higher star formation in the centre of their galaxy, compared to weakly barred and unbarred SF galaxies, in agreement with the results from Chapter 3. There are many examples in the literature of barred galaxies increasing the SFR in their host (Alonso-Herrero & Knapen, 2001;

Hunt et al., 2008; Ellison et al., 2011; Coelho & Gadotti, 2011; Hirota et al., 2014; Janowiecki et al., 2020; Magaña-Serrano et al., 2020; Lin et al., 2020). As discussed in Section 3.6.3, the increase in central star formation in strongly barred galaxies can be attributed to the inflow of gas from the outskirts to the centre caused by the bar (Athanassoula, 1992b; Athanassoula et al., 2013; Villa-Vargas et al., 2010), where the gas is available to increase star formation. However, this is only found for strongly barred SF galaxies, not for weakly barred SF galaxies or all quenching galaxies.

It was also shown in Figures 5.1 and 5.2 that the arms of a strong bar on average suppress star formation, as shown by low values for EW[H$\alpha$] and high values for $\mathrm{D_n}4000$ around $R \approx 0.5 R_{\mathrm{bar}}$. This is consistent with other studies that have found evidence for lower star formation efficiency (SFE) and SFR in the arms of the bar (Reynaud & Downes, 1998; Sheth et al., 2000; Watanabe et al., 2011; Khoperskov et al., 2018), which is explained by high velocity dispersion or shear caused by the bar potential (Athanassoula, 1992b; Reynaud & Downes, 1998; Sheth et al., 2000; Zurita et al., 2004; Haywood et al., 2016; Khoperskov et al., 2018) or by fast cloud-cloud collisions (Fujimoto et al., 2014; Maeda et al., 2018; Fujimoto et al., 2020; Maeda et al., 2021). Regardless of the physical process at work, these results imply heavy gas flows along the arms of a strong bar. These findings are also consistent with the 'star formation desert' described by James & Percival (2018) as well as the gas-depleted regions found in observations of barred galaxies by George et al. (2019) and Newnham et al. (2020). The EW[H$\alpha$] and $\mathrm{D_n}4000$ profiles of weakly barred galaxies are typically very similar to the profiles of unbarred galaxies in the arms of the bar of SF galaxies. This suggests that the suppression of star formation and evidence for gas flows are not found for weak bars in SF galaxies and that such bars are not as efficient in transporting gas to the centre of the galaxy. This is also in agreement with my previous result: lower rates of star formation in the centre of weakly barred galaxies. Interestingly, the EW[H$\alpha$] profile of weakly barred quenching galaxies also drops at $R \approx 1 R_{\mathrm{bar}}$, although not as suddenly as strongly barred quenching galaxies. Nevertheless, this suggests that the arms of a weak bar in a quenching galaxy are able to suppress some star formation, possibly due to increased velocity dispersion in the barred region of galaxies with lower concentrations of gas.

There is a second peak of EW[H$\alpha$] found just beyond the bar-end ($R \approx 1.2 - 1.5 R_{\mathrm{bar}}$) in strongly barred SF galaxies, shown in Figure 5.1. This was examined in more detail in Figures 5.5 and 5.6, where I found that the bar-end region of strongly barred SF galaxies has significantly higher EW[H$\alpha$] and lower $\mathrm{D_n}4000$ compared to weakly barred SF galaxies, which shows that the bar-end region is of great importance for strong bars. This is in agreement with other studies that have found increased star formation in the bar-end region (Reynaud & Downes, 1998; Verley et al., 2007; Emsellem et al., 2015; Díaz-García et al., 2020). For example, Maeda et al. (2020a) found higher SFEs in the bar-end region than in the arms of the bar. Fraser-McKelvie et al. (2020a) also found increased H$\alpha$ in the bar-ends of 18% of barred galaxies, most of which have high stellar masses ($M_* > 10^{10} M_\odot$). They also find that an additional 21% of their sample have increased H$\alpha$ in a ring around the bar, including at the bar-end. This brings the total up to a 38% of galaxies in Fraser-McKelvie et al. (2020a) with increased H$\alpha$ emission at the bar-end. However, I only observe increased H$\alpha$ emission in SF galaxies, while Fraser-McKelvie et al. (2020a) do not distinguish between quenching and SF galaxies. This suggests that the fraction of galaxies where this is observed in Fraser-McKelvie et al. (2020a) will be even higher if only SF galaxies were considered. These increases in star formation at the bar-end can be attributed to an increased probability of cloud-cloud collisions due to orbital crowding and high gas density, and low amounts of shear in the bar-end region (Renaud et al., 2015; Emsellem et al., 2015; Fraser-McKelvie et al., 2020a). However, an increase in star formation in the bar-end is only observed in this work for strongly barred SF galaxies, not for weakly barred SF galaxies. This suggests that a weak bar is not able to induce or support the effects described above.

Figures 5.1 and 5.2 show that strongly barred SF galaxies have significantly lower EW[H$\alpha$] and higher $\mathrm{D_n}4000$, and thus lower star formation, in the outskirts of the galaxy, compared to weakly barred and unbarred SF galaxies. This result is consistent with the hypothesis that strong bars cause inflow of gas from the outskirts to the centre of the galaxy, where it is available to increase star formation (Athanassoula, 1992b; Athanassoula et al., 2013). However, this result is more prominent in the radius profiles expressed in absolute units, and less in the ones normalised to the length of the bar. This can be explained by the normalisation that is used: a distance of $2R_{\mathrm{bar}}$ is much farther out in the disc of the galaxy for a strong bar than for a weak bar, as strong bars are longer than weak bars (see Section 3.1).

In conclusion, these results show that strong bars have more star formation in their centre and beyond the bar-end, while suppressing star formation in the arms of the bar, which is consistent with much of the literature. This is indicative of heavy gas flows along the arms of a strong bar to the centre and confirms that strong bars have a significant influence on their host and can facilitate the quenching process, which is in agreement with the results from Chapter 3. However, it is interesting to note that these observations are not found for weakly barred galaxies, which suggest that they do not affect their host in a significant way. This highlights the importance of bar strength on galaxy evolution and quenching.

#### 5.1.5.2 Effect of stellar mass

The radius profiles are shown in Figures 5.3 and 5.4 in three different mass bins, in order to assess the effect of stellar mass on these radius profiles. I found that the results described above are valid for intermediate mass ($10^{10.18} M_{\odot} < M_{*} < 10^{10.58} M_{\odot}$) and high mass ($M_{*} > 10^{10.58} M_{\odot}$). However, interestingly, the radius profiles of strongly barred low mass ($M_{*} < 10^{10.18} M_{\odot}$) galaxies are slightly different. The increase in central star formation is still found, but the suppression in the arms of the bar, as well as the increase of star formation beyond the bar-end, are not. This is in agreement with the results found in Chapter 3, where I also found that strong bars were most efficient at facilitating quenching at higher stellar masses.

Other studies have found that more massive galaxies have longer and stronger bars (Aguerri et al., 2009; Erwin, 2019; Fraser-McKelvie et al., 2020a; Kim et al., 2021). This suggests that the strongest bars, which would have the most effect on their host, are in the highest mass bin. This could be tested quantitatively in future work by weighting the bins in the profiles by a continuous measure of the strength of the bar, such as the strong bar vote fraction ($p_{\mathrm{strong}}$) from Galaxy Zoo DESI.

#### 5.1.5.3 Contamination by AGN

H$\alpha$ emission can be contaminated by other sources, such as AGN, which can bias the results presented here. However, the results from Chapter 3 show an increase of central SFR using estimates from MPA-JHU, where the SFRs are corrected for AGN (see Section 2.1.1 in Chapter 2 for more details), which suggests that the increase in central EW[H$\alpha$] in the centre of strongly barred galaxies found in this chapter is due to increased central star formation, not due to contamination by AGN. However, to make sure the results presented in this chapter are not biased by AGN, I cross-matched the galaxies in the GZ DESI-MaNGA catalogue to the MaNGA AGN value added catalogue (Comerford et al., 2020).

The MaNGA AGN catalogue identified AGN in MaNGA galaxies using four different methods. The first method involves the use of the Wide-field Infrared Survey Explorer (WISE) colours (Wright et al., 2010), based on the $W1$ and $W2$ bands, which correspond to 3.5 $\mu$m and 4.6 $\mu$m, respectively (Assef et al., 2018). Here, the MaNGA AGN catalogue applied the 75% reliability criteria: $W1 - W2 > 0.486 \exp[0.092(W2 - 13.07)^2]$ and $W2 > 13.07$, or $W1 - W2 > 0.486$ and $W2 \leq$

13.07 (Assef et al., 2018; Comerford et al., 2020). The second method is based on X-ray sources from the Swift observatory's Burst Alert Telescope (BAT) all-sky survey. The BAT catalogue has identified AGN and cross-matched them with SDSS (Oh et al., 2018), which are included in the MaNGA AGN catalogue (Comerford et al., 2020). The third method uses radio observations. Best & Heckman (2012) have created an AGN catalogue based on the NRAO Very Large Array Sky Survey (NVSS, Condon et al., 1998) and the Faint Images of the Radio Sky at Twenty centimeters survey (FIRST, Becker et al., 1995), which was cross-matched against MaNGA and added in the MaNGA AGN catalogue (Comerford et al., 2020). Finally, AGN were also identified in the MaNGA AGN catalogue using broad H$\alpha$ emission lines in spectra obtained from SDSS (Oh et al., 2015). They identified AGN based on a few thresholds. Firstly, the full-width at half-maximum (FWHM) of the broad H$\alpha$ component has to be higher than 800 km s$^{-1}$ and the amplitude over noise (A/N) ratio of the broad H$\alpha$ component must be larger than 3. Finally, the ratio of the area of the broad H$\alpha$ component to the noise level of the continuum (more specifically: the measurement uncertainty around [Nii] $\lambda$6584) must be greater than 2 (Oh et al., 2015).

It is expected that the AGN identified with the broad emission lines will affect the results presented here the most, as they will interfere with the H$\alpha$ measurement. This method identified 14 out of 2,125 galaxies (0.7%) in the GZ DESI-MaNGA sample as an AGN. A total of 106 galaxies in the GZ DESI-MaNGA sample are identified as an AGN in the MaNGA AGN catalogue by any of the methods mentioned above, implying a total AGN fraction of 5.0%. However, the MaNGA AGN catalogue only surveyed 6,261 of the 11,273 MaNGA targets (Comerford et al., 2020). If a similar AGN fraction is assumed for the remaining galaxies, then the estimated AGN fraction of the GZ DESI-MaNGA sample is 1.2% when only considering AGN identified by the broad emission lines, or 9.0% when including AGN identified by any of the methods described above. In order to be overly cautious and make sure the presence of AGN did not bias the results presented here, I removed the 106 galaxies that the MaNGA AGN catalogue identified as AGN using any method from the sample and I found that all the results presented here remained qualitatively the same. Thus, I conclude that the results in this chapter are not significantly biased by the presence of AGN.

#### 5.1.5.4 Strong bars are long-lived

As shown in Figure 5.2, the shape of the $\mathrm{D_n}$4000 profiles of strongly barred galaxies are very different to those of weakly and unbarred galaxies. This suggests that strong bars are long-lived structures, as they have been able to able to influence the average age of the stellar populations. This is especially visible in the arms of the bar. The median value of $D_n4000$ for strongly barred SF in the arms of the bar is ~1.4 (which goes up to ~1.55 in the highest mass bins), which implies that the mean age of the stellar population in the arms of the bar is ~1 Gyr (Kauffmann et al., 2003; Paulino-Afonso et al., 2020). This is in agreement with the results presented in Section 4.6.1 as well as other studies that show that bars are robust and have a long lifetime (Jogee et al., 2004; Shen & Sellwood, 2004; Debattista et al., 2006; Kraljic et al., 2012; Athanassoula et al., 2013).

However, this was not found for weakly barred galaxies, whose $D_n4000$ profiles are very similar to that of unbarred galaxies. This could mean that weak bars are short-lived structures that do not have the time to affect the stellar populations of their host. The simulations of Bournaud & Combes (2002) and Bournaud et al. (2005) found that bars are short-lived and significantly weaken before they are destroyed. The results presented here suggest that this might be true for weak bars, but not for strong bars. An alternative explanation is that weak bars are simply recently formed structures, or that they do not have the ability to influence the stellar population of their host in a significant way, even if they were long-lived.

#### 5.1.5.5 Implications for bar continuum

The bar continuum was introduced in Section 3.6.4, which showed that weak and strong bars are part of a continuum of bar types and that differences between weak and strong bars disappeared when correcting for bar length. The results in this chapter show that the median radius profiles of weak and strong bars are very different. The bar continuum implies that the radius profile of a weak bar would change gradually to the profile of a strong bar when considering bars of increasing bar strength along continuum. For example, the increase of EW[H$\alpha$] in the centre and the suppression of EW[H$\alpha$] in the arms of the bar should become increasingly more pronounced as the bar becomes stronger. This suggests that there are many intermediate radius profiles between the typical weak and strong profiles observed here. This is the case, as the shaded regions in the radius profiles indicate that there is a large amount of variability and scatter in the profiles. An alternative possibility is that the probability of finding these features (i.e. the peak of EW[H$\alpha$] in the centre and its suppression in the arms of the bar) becomes larger if a bar is stronger. It is possible to test either scenario in future work by characterising the diversity of the radius profiles of galaxies of different bar types.

## 5.2 Fast and slow bars

It is important to look at kinematics as well as morphology to get a complete understanding of galaxy evolution. In the second part of this chapter, I investigate whether the kinematics of bars have a measurable impact on the star formation of their hosts. Bars are kinematically classified as fast or slow based on $\mathcal{R}$, the ratio of the corotation radius to the bar radius; slow bars have $\mathcal{R} > 1.4$, while fast bars have $1.0 < \mathcal{R} < 1.4$. Bars with $\mathcal{R} < 1.0$, which are called ultrafast bars, should theoretically not exist (Contopoulos, 1980, 1981; Athanassoula, 1992b), but are nevertheless repeatedly observed (Buta & Zhang, 2009; Aguerri et al., 2015; Cuomo et al., 2019; Guo et al., 2019; Garma-Oehmichen et al., 2020). The Tremaine-Weinberg (TW) method, which is described in detail in Section 2.2.4 of Chapter 2, was used to calculate $\mathcal{R}$ for all galaxies in the TW sample and the first results were discussed in detail in Chapter 4. As I find very few ultrafast bars (11% of the sample, with only 2% confidently within the ultrafast regime), they are grouped together with fast bars in this analysis. In this section, I will investigate whether there are significant differences between fast and slow bars in terms of their EW[H$\alpha$] and $\mathrm{D_n}4000$ profiles, in order to probe whether the kinematics of the bar has an effect on galaxy quenching, which has not been studied before. Additionally, I will study whether the kinematics of the bar are influenced by the bar strength, i.e. whether fast strong bars have different effects on their hosts compared to slow strong bars. These results are presented from Sections 5.2.1 to 5.2.4 and discussed in Section 5.2.5.

### 5.2.1 EW[H$\alpha$] and $\mathrm{D_n}4000$ along fast and slow bars

The radius profiles of EW[H$\alpha$] for fast and slow bars in SF and quenching galaxies are shown in Figure 5.7. The profiles are shown in terms of distance to the centre of the galaxy (in arcsec, left column), as well as normalised to the bar radius (right column). The galaxies are additionally split into SF or quenching based on Equation 3.1 in Section 3.1. This threshold is also shown in Figure 3.6. The profiles for SF galaxies are shown in the top row, while the profiles for quenching galaxies are shown in the bottom row. The difference between the radius profiles of two samples is shown in the bottom of every panel. Here, the significance of the difference in every bin is shown by the size of the point. The smallest size represent a significant difference of less than $1\sigma$ after comparing the two populations with an Anderson-Darling test, while the largest sizes represent a significant difference of more than $3\sigma$, which are also additionally outlined in black.

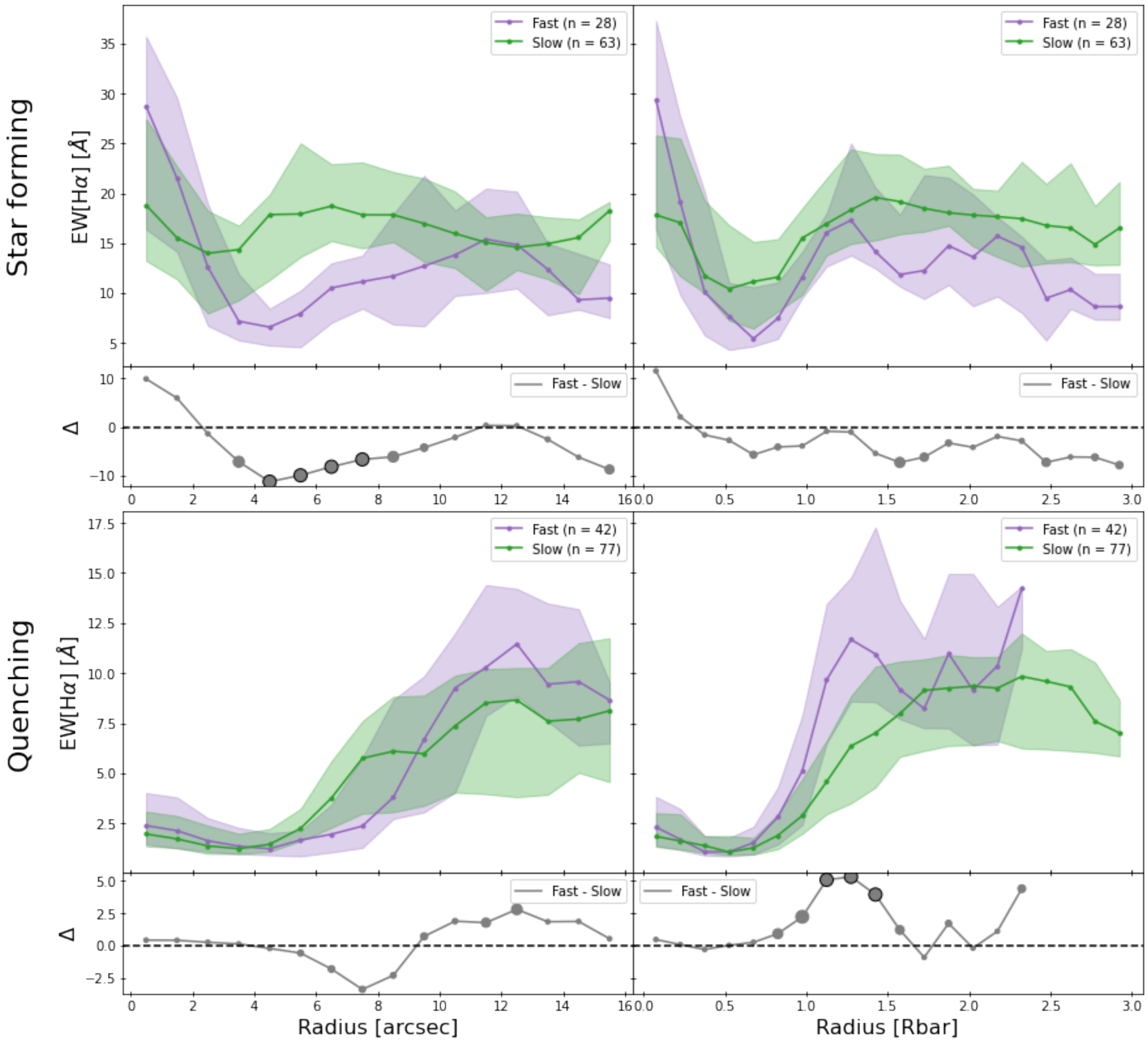

Figure 5.7: The radius profiles of EW[H$\alpha$] are shown for SF galaxies (top row) and quenching galaxies (bottom row) for fast bars (purple) and slow bars (green). The radius profiles are shown in arcsec (left column) and normalised against the bar radius (right column). The sample size, n, for every sample is indicated in the legend. The solid line is the median in every bin, while the shaded regions bound the 33$^{\text{rd}}$ and 66$^{\text{th}}$ percentiles. The width of the bins in the left column is 1 arcsec and 0.15 $R_{\text{bar}}$ in the right column. The bottom part of each panel shows the difference between each radius profile in every bin, where the size of the point represents the significance of the difference after comparing the two populations with an Anderson-Darling test. The smallest sizes represent a significant difference of less than $1\sigma$, while the largest sizes represent $>3\sigma$ and are additionally outlined in black. Slow bars in SF galaxies have higher values for EW[H$\alpha$] in the middle of the galaxy than fast bars.

The top-left panel clearly shows that the EW[H$\alpha$] is higher for slow bars than for fast bars in SF galaxies, especially in the middle of the galaxy (~4-8 arcsec), where the difference is more than $3\sigma$. The top-right panel shows that the median profile is higher for slow bars than for fast bars in SF galaxies, however the difference is always less than $3\sigma$. Both slow and fast bars have higher EW[H$\alpha$] in the centre and bar-end than in the arms of the bar. The profiles for quenching galaxies are relatively similar for slow and fast bars, except around the bar-end, where fast bars have significantly ($>3\sigma$) higher EW[H$\alpha$]. The rest of the EW[H$\alpha$] profile rises slowly with increasing distance from the galaxy.

Similar conclusions can be drawn for $D_n4000$, the radius profiles for which are shown in Figure 5.8. Slow bars in SF galaxies have significantly lower values for $D_n4000$ in the middle of the galaxy (~5-9 arcsec) than fast bars. The average profile for slow bars in SF galaxies decreases monotonically with radius, while the profile for fast bars shows a bump in the arms of the bar. Again, the profiles of slow and fast bars are relatively similar among quenching galaxies, except at the bar-end region.

Based on higher values for EW[H$\alpha$] and lower values for $D_n4000$, these results suggest that **there is more star formation along slow bars, compared to fast bars**. Interestingly, this is found for SF galaxies, but not for quenching galaxies.

### 5.2.2 Effect of bar strength

The previous section showed that there is more star formation along slow bars than fast bars in SF galaxies, while the results from Section 5.1 suggest that there is more star formation in strongly barred galaxies than weakly barred galaxies. In this section, I will address whether there is a synergistic effect between these two independent results.

The effect of bar strength on the profiles of fast and slow bars is probed in Figure 5.9, which shows the radius profiles for EW[H$\alpha$] (left column) and $D_n4000$ (right column) for strongly barred SF galaxies (top row) and weakly barred SF galaxies (bottom row). The top-left panel shows that the median profile of EW[H$\alpha$] for slow strong bars is always higher than that of fast strong bars, however the significance of the difference is always $<3\sigma$. These profiles are reminiscent of the profiles shown in Figure 5.1 for strong bars: EW[H$\alpha$] is high in the centre, lower in the arm of the bar and a second peak beyond the bar-end. However, the increase of EW[H$\alpha$] beyond the bar-end region is much more pronounced in slow strong bars than in fast strong bars and the median EW[H$\alpha$] is also higher in the arms of slow strong bars than in the arms of fast strong bars. The EW[H$\alpha$] profiles for slow weak bars and fast weak bars,

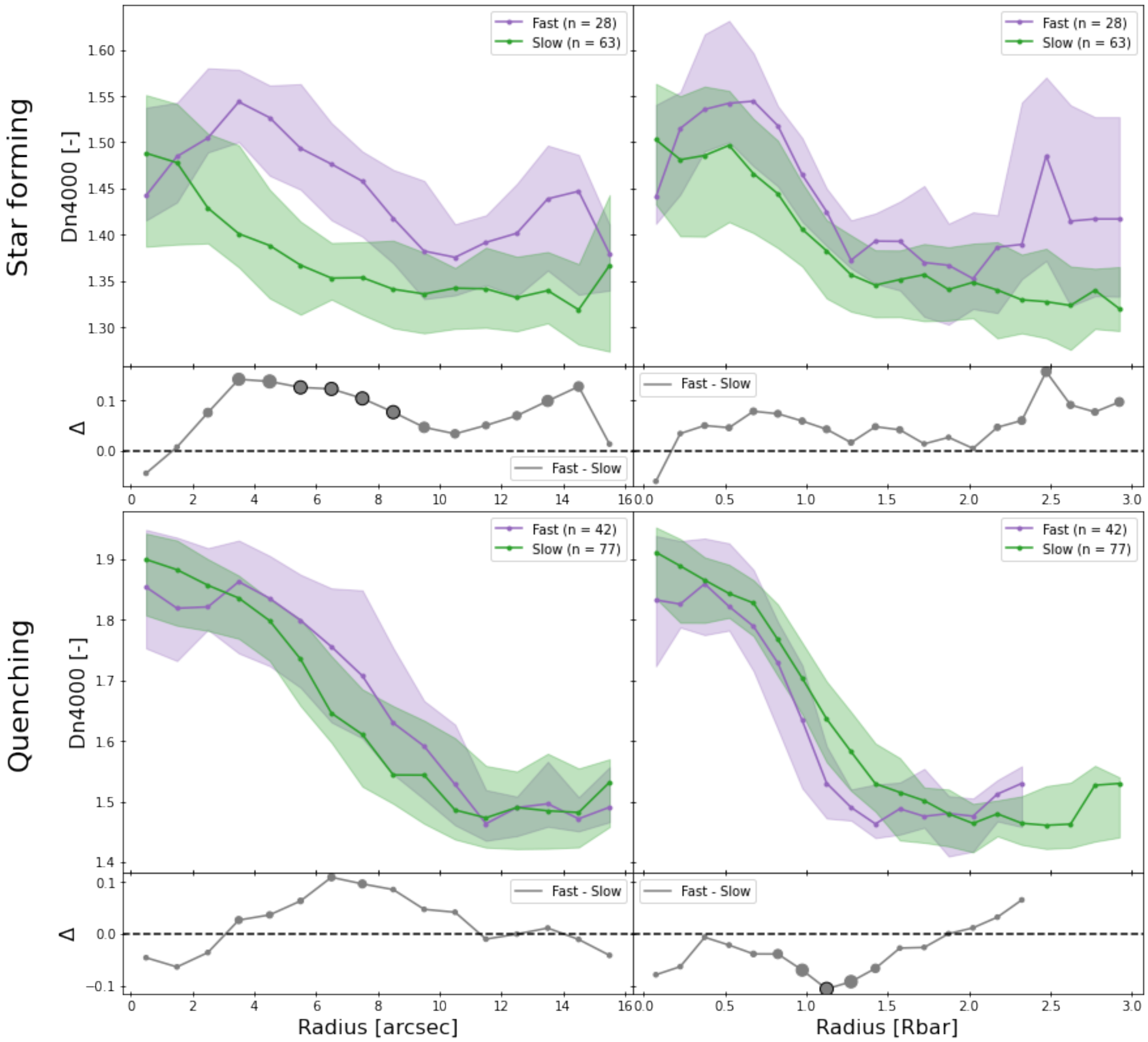

Figure 5.8: The radius profiles of $D_n$4000 are shown for SF galaxies (top row) and quenching galaxies (bottom row) for fast bars (purple) and slow bars (green). The radius profiles are shown in arcsec (left column) and normalised against the bar radius (right column). The sample size, n, for every sample is indicated in the legend. The solid line is the median in every bin, while the shaded regions bound the 33rd and 66th percentiles. The width of the bins in the left column is 1 arcsec and 0.15 $R_{\mathrm{bar}}$ in the right column. The bottom part of each panel shows the difference between each radius profile in every bin, where the size of the point represents the significance of the difference after comparing the two populations with an Anderson-Darling test. The smallest sizes represent a significant difference of less than $1\sigma$, while the largest sizes represent $>3\sigma$ and are additionally outlined in black. Slow bars in SF galaxies have lower values for $D_n$4000 in the middle of the galaxy than fast bars.

shown in the bottom-left panel, are similar to each other ($<1\sigma$ at all radii smaller than $2R_{\rm bar}$).

The top-right panel shows that the median values for $\mathrm{D_n}4000$ are always lower for slow strong bars than for fast strong bars, which is consistent with the EW[H$\alpha$] profiles. Fast strong bars have a very pronounced peak of $\mathrm{D_n}4000$ in the arms of the bar, which is not as apparent in slow strong bars, suggesting that the latter might have younger stellar populations in the arms of the bar due to more recent star formation, presumably triggered by the presence of the slow strong bar. However, these differences are again not significantly different ($<3\sigma$), perhaps due to the very low sample size. The $\mathrm{D_n}4000$ profiles for fast weak and slow weak bars are very similar to each other ($<1\sigma$ at all radii smaller than $2R_{\rm bar}$), as shown in the bottom-right panel.

Although the sample sizes used here are small, these results hint that bar strength has an effect on the profiles observed in fast and slow bars. While not statistically significant ($<3\sigma$), **the profiles of fast and slow strong bars suggest more star formation at all radii in the latter. The profiles of fast and slow weak bars are very similar to each other**. Increasing the sample size in future studies will help to clarify these issues. This is discussed in more detail in Section 5.2.5.2. The physical interpretation of this observation will be the topic of the next two sections.

### 5.2.3 Global or local effect?

So far, I have shown that slow bars have higher EW[H$\alpha$] than fast bars in SF galaxies, which implies more star formation in slow bars than fast bars. Interestingly, Figure 5.10 shows that the global SFR (obtained from Pipe3D) is not significantly different between SF galaxies with fast and slow bars. This was tested with an Anderson-Darling test between fast and slow bars for strong bars, weak bars and all bars, and the p-value was >0.25 for all comparisons. These statements seem contradictory to each other. However, the radius profiles are constructed using a aperture with a width of 3 arcsec oriented along the position angle (PA) of the bar. These results suggest that the increase in EW[H$\alpha$] observed in slow bars only affects the bar region locally, but not the galaxy globally.

This can be tested by constructing radius profiles of EW[H$\alpha$] with apertures parallel and perpendicular to the bar and comparing the differences. This is done for all SF galaxies in Figure 5.11, where the barred galaxies are divided into four subsamples: galaxies with slow strong bars, fast strong bars, slow weak bars and fast weak bars. The biggest difference between the parallel and perpendicular apertures was

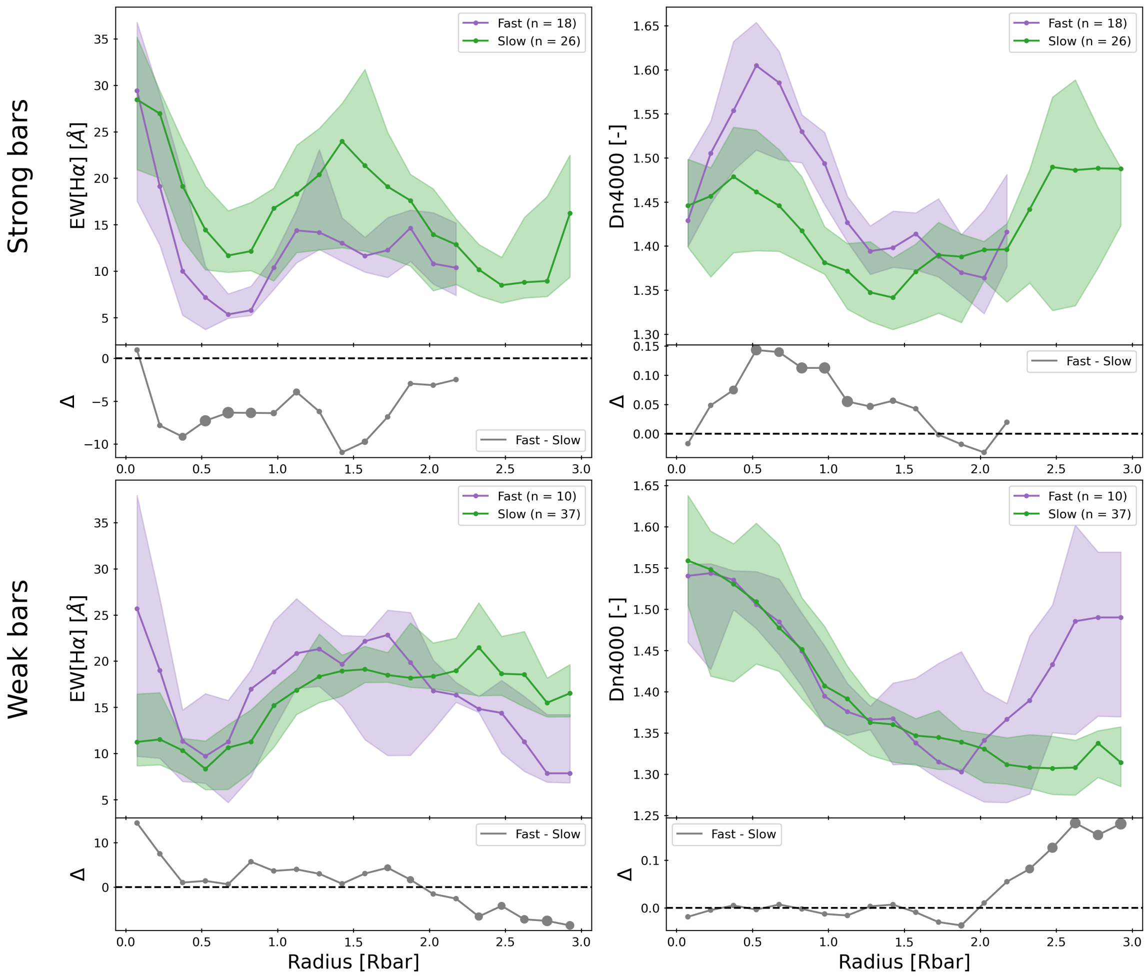

Figure 5.9: The radius profiles of EW[H$\alpha$] (left column) and $\mathrm{D_n}4000$ (right column) are shown for strongly barred SF galaxies (top row) and weakly barred SF galaxies galaxies (bottom row). The sample is additionally divided into fast bars (purple) and slow bars (green). The radius profiles are shown normalised against the bar radius (right column). The sample size, n, for every sample is indicated in the legend. The solid line is the median in every bin, while the shaded regions bound the 33rd and 66th percentiles. The width of the bins in is 0.15 $R_{\mathrm{bar}}$. The bottom part of each panel shows the difference between each radius profile in every bin, where the size of the point represents the significance of the difference after comparing the two populations with an Anderson-Darling test. The smallest sizes represent a significant difference of less than 1$\sigma$, while the largest sizes represent >3$\sigma$ and are additionally outlined in black. It is clear that a slow bar will affect its host more if it is also strong. The profiles of fast and slow weak bars are very similar to each other.

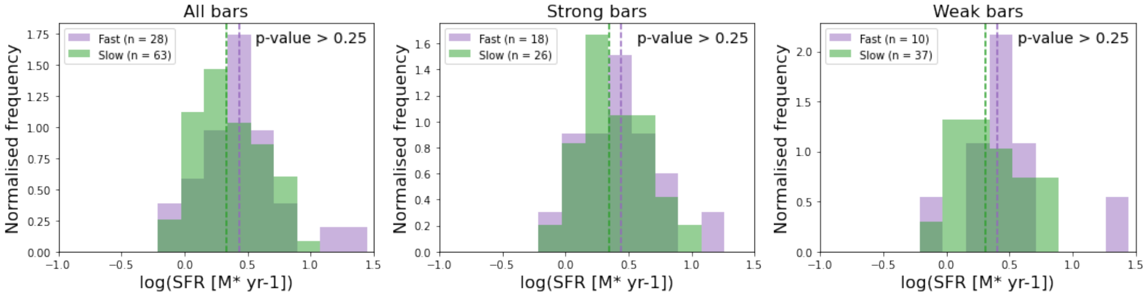

Figure 5.10: The difference in global star formation rate (obtained from Pipe3D) between fast bars in SF galaxies (purple) and slow bars in SF galaxies (green). This difference is tested for all bars (left panel), only strong bars (middle panel) and only weak bars (right panel). The p-value of a two-sample Anderson-Darling test is shown inside each subplot, with the null hypothesis being that the two samples are drawn from the same population. The global star formation rate is not significantly different between fast and slow bars.

observed among slow strong bars, where the parallel aperture has significantly ($>3\sigma$) higher values for EW[H$\alpha$] between ~1.2 - 1.8 $R_{\rm bar}$ than the perpendicular aperture. There is no significant difference observed in the apertures placed on fast strong bars, fast weak or slow weak bars. This confirms that **a slow bar will increase star formation along the position angle of the bar, but not in the entire galaxy.** This result is discussed in more detail in Section 5.2.5.3. This was only observed for slow strong bars, which suggests that a slow bar will have more of an effect on its host if it is also a strong bar.

### 5.2.4 Differences in velocity at bar-end

The results in the past few sections suggest that slow bars induce more star formation along the PA of the bar than fast bars in SF galaxies. However, it is still unclear what the physical cause is of this increase in star formation. As mentioned before, the distinction between fast and slow bars depends on $\mathcal{R}$, which is based on the kinematics of the galaxy. Fast bars tend to end near the corotation radius, whereas slow bars have bar radii that are shorter than the corotation radius, as $\mathcal{R} = R_{\rm CR}/R_{\rm bar}$ (see Section 2.2.4.4 for more information on how $\mathcal{R}$ is calculated). This means that the bar-end region of fast bars moves with a velocity similar to stars in the disc, whereas the bar-ends of slow bars should rotate much slower. This is shown in the left panel of Figure 5.12, where the difference between the velocity of the stars ($V_*$) at $R_{\rm bar}$, based on the stellar rotation curve, and the velocity of the bar-end ($V_{\rm bar-end}$) is calculated for all SF galaxies. Bars with $\mathcal{R} > 1$ will have $V_* > V_{\rm bar-end}$, whereas bars

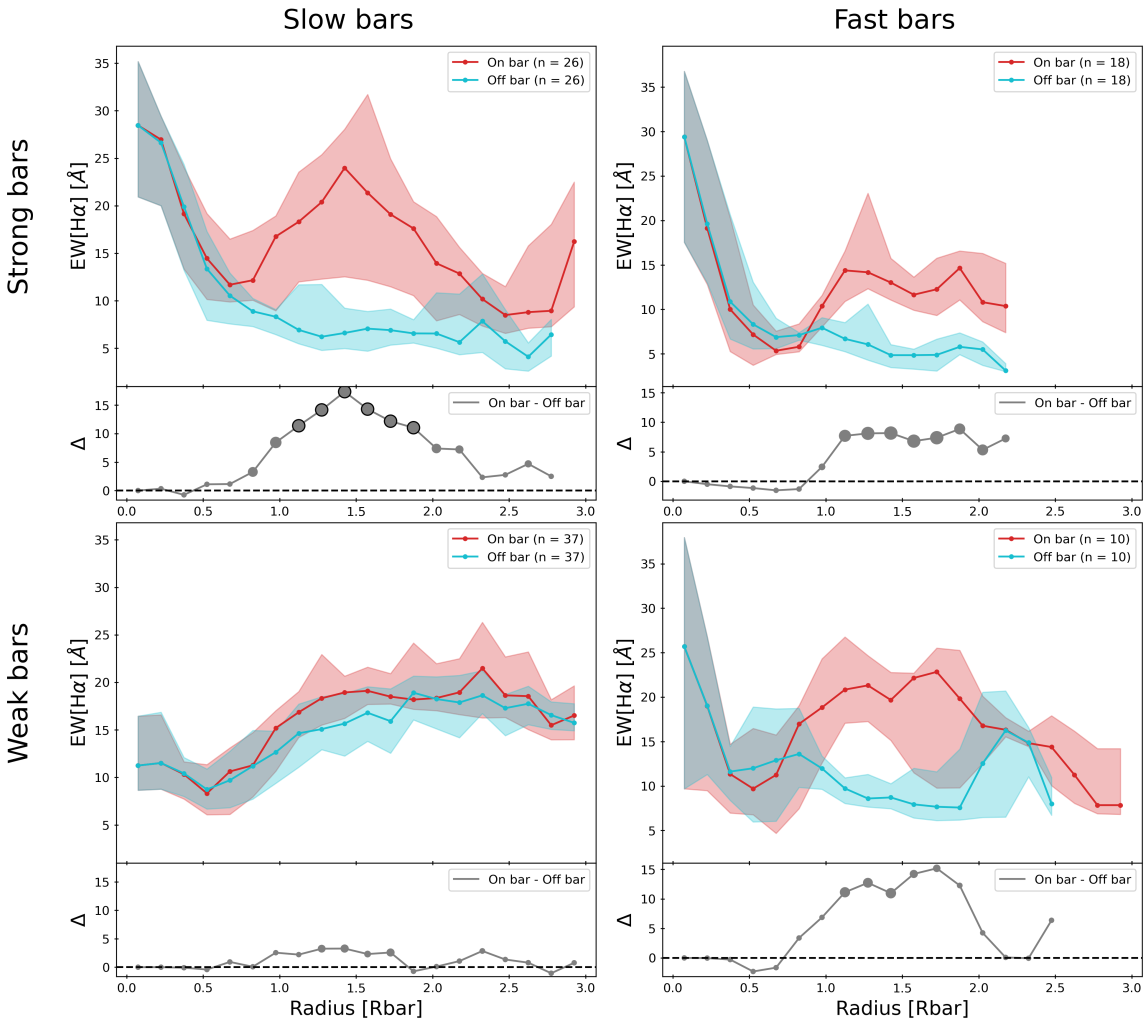

Figure 5.11: The radius profiles of EW[H$\alpha$] are shown for strongly barred SF galaxies (top row) and weakly barred SF galaxies (bottom row) for slow bars (left column) and fast bars (right column). A radius profile was calculated for every target with the aperture positioned along the bar (red) and perpendicular to the bar (light blue). The radius profiles are shown normalised against the bar radius. The sample size, n, for every sample is indicated in the legend. The solid line is the median in every bin, while the shaded regions bound the 33$^{\text{rd}}$ and 66$^{\text{th}}$ percentiles. The width of the bins is 0.15 $R_{\text{bar}}$. The bottom part of each panel shows the difference between each radius profile in every bin, where the size of the point represents the significance of the difference after comparing the two populations with an Anderson-Darling test. The smallest sizes represent a significant difference of less than 1$\sigma$, while the largest sizes represent $>3\sigma$ and are additionally outlined in black. This figure shows that a slow strong bar, will increase star formation along the PA of the bar, but not in the entire galaxy.

with $\mathcal{R} < 1$ (i.e. ultrafast bars) will have $V_* < V_{\mathrm{bar-end}}$. Finally, the velocities will be equal to each other for bars with $\mathcal{R} = 1$, as $R_{\mathrm{CR}} = R_{\mathrm{bar}}$. It is clear that the difference in velocity is significantly bigger for slow bars in SF galaxies than for fast bars in SF galaxies, as indicated by an Anderson-Darling test (p-value $< 0.001$; $>3.3\sigma_{\mathrm{AD}}$). The median difference in velocity is 4.2 km $\mathrm{s}^{-1}$ for fast bars and 49.6 km $\mathrm{s}^{-1}$ for slow bars.

The difference between the velocity of the gas ($V_{\mathrm{gas}}$) at $R_{\mathrm{bar}}$, based on the gas rotation curve, and the velocity of the bar-end ($V_{\mathrm{bar-end}}$) is shown in the right panel of Figure 5.12. The gas rotation curves are constructed similarly to the stellar rotation curves, which is described in Section 2.2.4.4 in Chapter 2. However, instead of using the stellar velocity maps from MaNGA, the velocity derived from a Gaussian fit to the H$\alpha$ emission line is used. The difference between $V_{\mathrm{gas}}$ and $V_{\mathrm{bar-end}}$ is found to be significantly higher for slow bars in SF galaxies (the median value is 59.0 km $\mathrm{s}^{-1}$) than for fast bars (12.7 km $\mathrm{s}^{-1}$) in SF galaxies.

These results confirm that **the bar-ends of slow bars have a large difference in velocity from the stars and gas in the disc, while this is not observed for fast bars**. These differences in velocity at the bar-end between slow and fast bars imply that slow bars come into contact with much more gas than fast bars, which could explain the observed differences in local star formation. The implications of this are discussed in more detail in Section 5.2.5.4.

## 5.2.5 Discussion: Fast and slow bars

### 5.2.5.1 Star formation in different regions of fast and slow bars

In the second part of this chapter, I investigated the effects that bar kinematics have on their host in terms of star formation. This was studied in Figures 5.7 and 5.8 using EW[H$\alpha$] and $\mathrm{D_n}4000$. Figure 5.7 shows that slow bars in SF galaxies have significantly higher values for EW[H$\alpha$] in the middle of the galaxy (~4-8 arcsec) than fast bars in SF galaxies. This is consistent with the results found in Figure 5.8, where significantly higher values for $\mathrm{D_n}4000$ were found in the middle of SF galaxies with slow bars, compared to fast bars in SF galaxies. This implies the presence of younger stellar populations, due to more recent star formation and suggests that slow bars in SF galaxies have significantly more star formation than fast bars along the PA of the bar. Interestingly, the radius profiles for fast and slow bars in quenching galaxies have similar trends: EW[H$\alpha$] increases with radius, while $\mathrm{D_n}4000$ decreases monotonically with radius.

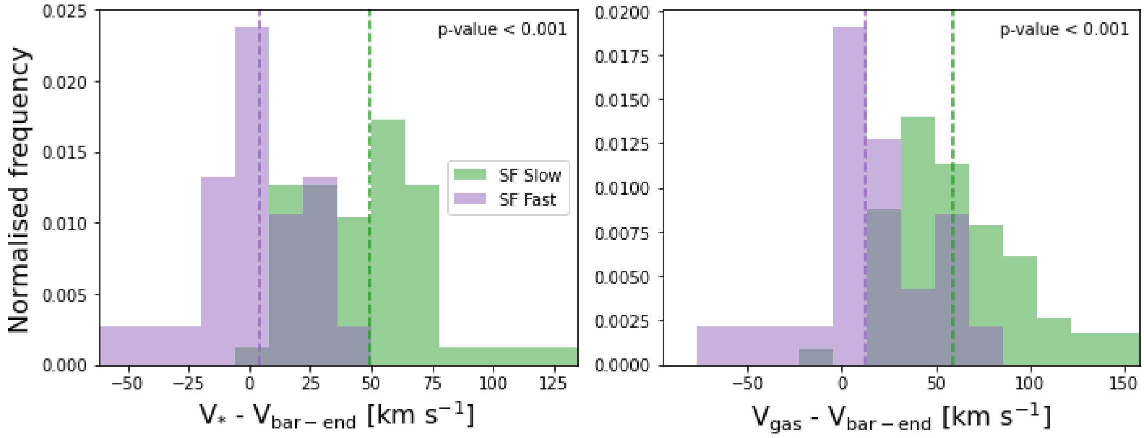

Figure 5.12: The difference between the velocity of the bar-end region ($V_{\rm bar-end}$) and the velocity of the stars ($V_*$) at $R_{\rm bar}$ is shown in the left panel, while the difference between $V_{\rm bar-end}$ and the velocity of the gas ($V_{\rm gas}$) at $R_{\rm bar}$ is shown in the right panel for all slow (green) and fast (purple) SF galaxies. The dashed vertical lines represent the median value of each distribution. The p-value of a two-sample Anderson-Darling test is shown inside each subplot, with the null hypothesis being that the two samples are drawn from the same population. It is clear that the velocity difference is significantly bigger for slow bars than for fast bars.

This effect is observed for SF galaxies, but not for quenching galaxies. This is reminiscent of the results from Chapter 3, where I found that strong bars increase the central star formation in SF galaxies, but not in quenching galaxies. This is presumably because the underlying physical processes that cause the observed differences in star formation are related to the gas distribution of the galaxy. If a structure (e.g. a slow bar) affects the gas in a galaxy, and SF galaxies have more gas than quenching galaxies (Baldry et al., 2006; Dekel & Birnboim, 2006), it makes sense that it would affect SF galaxies more than quenching galaxies.

### 5.2.5.2 Effect of bar strength

The effect of bar strength on the results presented above was explored in Figures 5.9 and 5.11 for EW[H$\alpha$] and $\rm D_n4000$ for SF galaxies. I found that the median value for EW[H$\alpha$] was always higher in slow strong bars than in fast strong bars. The increase of EW[H$\alpha$] beyond the bar-end region, which is typical for strong bars, was much more pronounced in slow strong bars than in fast strong bars, suggesting that the latter have more star formation there than the former. Similarly, the median EW[H$\alpha$] was also higher in the arms of a slow strong bar than in the arms of a fast strong bar.

The median value for $\rm D_n4000$ was also always lower along slow strong bars than in fast strong bars. The value for $D_n4000$ was especially high in the arms of fast strong bars, suggesting that the arms of fast strong bars suppress star formation more than those of slow strong bars. Nevertheless, an Anderson-Darling test reveals that these profiles are not significantly different. The profiles for fast weak and slow weak bars are very similar to each other and are not significantly different.

At the moment, the biggest limiting factor of this analysis is the sample size. These results hint that a slow bar will increase star formation more if it is also strong, while the profiles of fast weak and slow weak bars are difficult to distinguish from each other. However, a bigger sample size is needed to see whether these effects are statistically significant. The sample size is relatively low because of the need for very robust data to perform the TW method. Though this is the largest sample the TW method has been applied to so far, there are only 210 galaxies with reliable measurements of $\mathcal{R}$ (see Section 2.2.4 for more details). Further dividing the sample into multiple subsamples (SF or quenching, weak or strong, fast or slow) reduces the sample size in the final comparisons. Increasing the total sample size would greatly help to clarify the effect that bar strength has on the profiles of fast and slow bars.

I found in Section 5.1.5.2 that the effects induced by strong bars are most prevalent in high mass galaxies. As bar strength was shown to influence the profiles of fast and slow bars, it is possible that stellar mass has an influence as well. However, this is difficult to test with the current small sample size, which highlights the importance of studying the kinematics of a larger sample of barred galaxies.

#### 5.2.5.3 Local, but not global effect

Even though I have shown that slow bars in SF galaxies have higher EW[H$\alpha$] along the PA of the bar, Figure 5.10 shows that the global SFR is not significantly different in SF galaxies with slow or fast bars. This apparent contradiction is explained in Figure 5.11. Here, radius profiles are constructed with apertures placed parallel and perpendicular to the PA of the bar. I found that the difference in EW[H$\alpha$] between the parallel and perpendicular profiles is only significantly different for slow strong bars in SF galaxies, especially in the region beyond the bar-end (1.2-1.5 $R_{\rm bar}$). Note that this is also the region where the second peak of EW[H$\alpha$] was typically found in strongly barred SF galaxies in Figure 5.1, suggesting that this peak is most prevalent among slow strong bars in SF galaxies. The median value of EW[H$\alpha$] for the profile with the parallel aperture is higher than the profile with the perpendicular aperture in the region beyond the bar-end of fast strong and fast weak bars as well, but it was not statistically significantly different. The profiles for the parallel and perpendicular slits for weak strong bars in SF galaxies were also not significantly different. This suggests that the distribution of star formation along the PA of the bar is significantly shaped by whether the bar is fast or slow, even though both fast and slow bars have similar effects on their host in terms of global SFR. This implies that a slow bar concentrates all star formation along its bar more than a fast bar does. However, as the global SFR stays the same, this also suggests that a slow bar does not change the overall rate of gas consumption of its host. Rather, a slow bar will influence its host by altering where gas consumption and star formation occurs.

As a side note, these results also highlight the importance of using IFUs to understand galaxy evolution, as this crucial kinematic distinction between fast and slow bars could not have been found using only global properties and photometry. This is also the case for the work done in Cappellari et al. (2011b), who looked at the stellar kinematics of early-type galaxies and found that there are clear distinct categories (fast and slow rotators), even though they look similar when only using photometry.

#### 5.2.5.4 Effect of velocity

Figure 5.12 helps to delve deeper into a possible physical explanation for why slow bars have more star formation along their bars. A bar is classified as slow or fast based on its kinematics. Fast bars end near the corotation radius, whereas slow bars are shorter than their corotation radius. This implies that the bar-end region of fast bars should move with a similar velocity to the stars in the disc. In contrast, the difference in velocity between the bar-end region of slow bars and the stars in the disc should be relatively large. This is confirmed in the left panel of Figure 5.12. The right panel shows that this is also the case for gas: the difference in velocity between the bar-end and gas in the disc is much higher for slow bars than for fast bars. This suggests that, as a bar evolves, a slow bar will come into contact with much more of the gas of its host than a fast bar. This gas could become trapped in the bar, where it is available for star formation. In other words, this work implies that slow bars are more efficient at sweeping up and concentrating gas in the bar than fast bars, because of the greater difference in velocity between the bar and the gas in the disc, and are possibly more efficient at creating gas-depleted regions, such as the ones observed by Gavazzi et al. (2015); James & Percival (2018); George et al. (2019); Newnham et al. (2020).

Gas-depleted regions are also found in simulations. For example, the high-resolution cosmological ‘zoom-in’ simulation of Spinoso et al. (2017) shows a very clear gas-depleted region in a barred galaxy. The bar has a radius of $\sim$1.5 kpc at z = 0.02, at which point the corotation radius is ∼3.5 kpc. This implies that $\mathcal{R} \approx 2.3$, which makes the bar that caused the obvious gas-depleted region a very slow bar. Similar conclusions can be drawn from the self-consistent simulations of Milky Way-sized isolated disc galaxies in Seo et al. (2019), where clear gas-depleted regions are also found. The bars all start out as fast, but quickly become slow. However, as explained in Chapter 4, simulations tend to overestimate the observed values for $\mathcal{R}$, which suggests that studying the effect that slow and fast bars have on the gas-depleted regions using simulations might not be reliable. Instead, it would be better to study this observationally. This could be done with resolved gas observations of multiple slow and fast bars in galaxies, verifying whether the gas-depleted region is more pronounced in slow bars than in fast bars.

However, as noted in the previous section and shown in Figures 5.10 and 5.11, the global SFRs of slow and fast bars are similar, despite the differences observed along the bar. This implies that the total star formation efficiency of the galaxies remains the same. So even though a slow bar is likely to be more efficient at sweeping up and concentrating gas in the bar than fast bars, another element must be acting to counteract the increase in star formation efficiency that a higher gas concentration implies. A probable candidate is the increased velocity dispersion or shear that is commonly associated with strong gas flows in the arms of the bar (Athanassoula, 1992b; Reynaud & Downes, 1998; Sheth et al., 2000; Zurita et al., 2004; Haywood et al., 2016; Khoperskov et al., 2018), as the arms of the bar is where the most significant difference is observed between fast and slow bars, especially for strong bars (see Figure 5.9). Thus, slow bars increase the concentration of gas in the bar, however, the global SFR does not increase due to the high amounts of shear in the arms of the bar. These counteracting effects result in a global SFR in slow bars that is similar to that of fast bars.

#### 5.2.5.5 A ‘kinematic’ bar continuum

Conceptually, the idea of fast and slow bars works well with the continuous nature of bar types, as $\mathcal{R}$, which is used to classify bars into fast or slow, is a continuous variable. Additionally, $\mathcal{R}$ is defined as the ratio of the corotation radius to the bar radius, which are both known to change over time. This implies that $\mathcal{R}$ can change over time and that bars can become ‘faster’ or ‘slower’. This is reminiscent of the categorisation of bars into strong and weak, based on $p_{\mathrm{strong}}$, which can also change over time so that bars can become stronger or weaker. However, the classification of bars into weak or strong, and the bar continuum presented in Section 3.6.4, are based

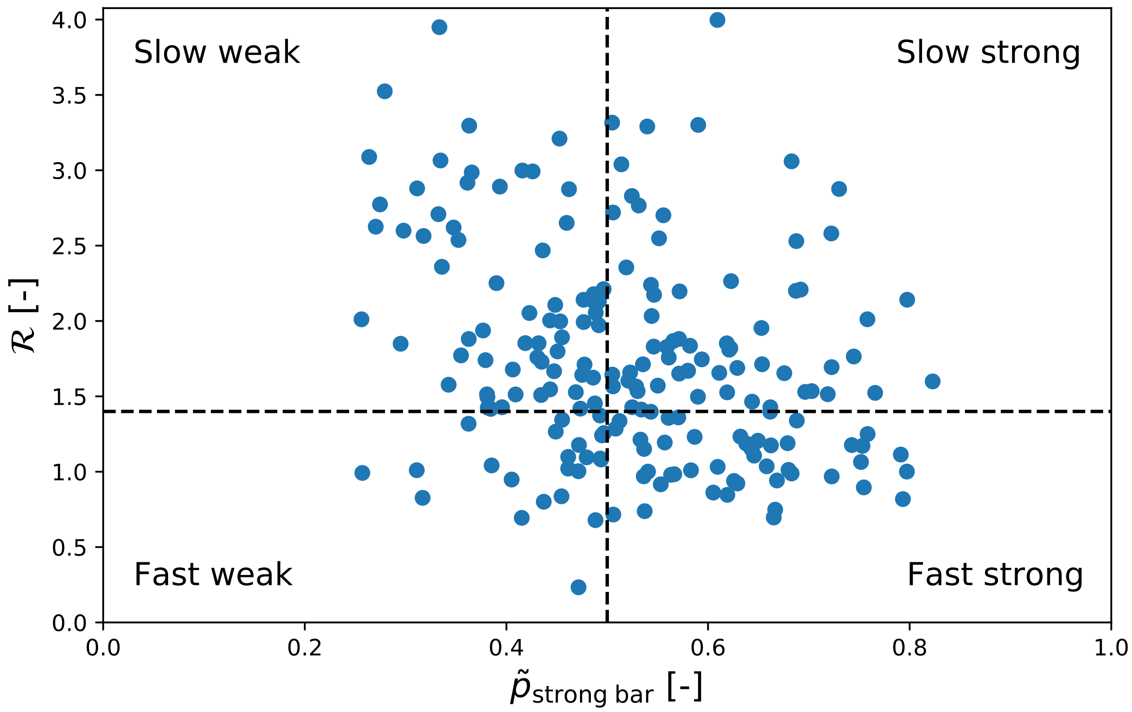

Figure 5.13: Visualisation of how the targets in the TW sample would lie on a two-dimensional bar continuum, with one axis based on morphological arguments (horizontal axis, $\tilde{p}_{\text{strong bar}}$) and one axis based on kinematic arguments (vertical axis, $\mathcal{R}$). The dashed vertical line separates strong and weak bars, while the dashed horizontal line separates (ultra)fast and slow bars. This means that there are four distinct quadrants in this plot for the different bar types: slow weak bars, fast weak bars, fast strong bars and slow strong bars. The Spearman correlation coefficient equals -0.31, and its significance is $4.63\sigma$.

on visual morphology. In contrast, the division of bars as fast and slow is based on the kinematics of the bar. This suggests that a possible second - kinematic - axis should be added to the bar continuum, which would accurately reflect that the kinematics of the bar has an important role in galaxy evolution as well.

A visualisation of how the galaxies in the TW sample are distributed on such a two-dimensional plane is shown in Figure 5.13, where $\mathcal{R}$ is plotted against the normalised strong bar vote fraction ($\tilde{p}_{\text{strong bar}}$) from GZ DESI. The normalised strong bar vote fraction is defined as follows:

$$\tilde{p}_{\text{strong bar}} = \frac{p_{\text{strong bar}}}{p_{\text{weak bar}} + p_{\text{strong bar}}} , \tag{5.1}$$

where $p_{\text{strong bar}}$ is the strong bar vote fraction from GZ DESI and $p_{\text{weak bar}}$ the weak bar fraction fraction from GZ DESI (please see Section 2.1.5 for more detailed information about Galaxy Zoo and vote fractions in general). This is done so that the dependence of the unbarred vote fraction ($p_{\text{no bar}}$) is factored out, and implies that all strong bars have $\tilde{p}_{\text{strong bar}} > 0.5$ and all weak bars have $\tilde{p}_{\text{strong bar}} < 0.5$. There are four separate quadrants in this plane: one for galaxies with slow weak bars, fast weak bars, fast strong bars and slow strong bars. The Spearman correlation coefficient and the significance are -0.31 and 4.63, respectively. This is consistent with the results from Chapter 4, where I show that strong bars have significantly lower values for $\mathcal{R}$ than weak bars. However, it is also clear from this figure that there are barred galaxies in every quadrant. This means that a classification based on bar strength does not preclude any classification based on kinematics, i.e. a strong bar can still be either fast or slow. This also implies that both the kinematics and photometry are needed in order to fully characterise a barred galaxy.

The results in this chapter suggest that barred galaxies on the right side of the plot (strong bars, $\tilde{p}_{\text{strong bar}} > 0.5$) will increase the total star formation in their host, especially in the centre and the region beyond the bar-end, which facilitates the quenching process, compared to barred galaxies on the left side of the plot (weak bars). In contrast, barred galaxies in the upper half of the plot (slow bars, $\mathcal{R} > 1.4$) will have their star formation more concentrated in their bars and sweep up gas more efficiently, compared to barred galaxies in the bottom half of this plot (fast bars). Thus, bars in the upper-right quadrant of Figure 5.13, i.e. slow strong bars, will affect their hosts the most.

However, it must be noted that the relation between the bar continuum, bar strength and bar kinematics should be studied in more detail and, as mentioned in Section 5.2.5.2, a larger sample size is needed to do this properly.

## 5.3 Conclusions

In Chapter 3, I showed that strong bars increase central star formation in SF galaxies, compared to weak bars. However, in that chapter, I did not discuss what happened in different regions of the bar, such as the arms of the bar and the bar-end regions. In Chapter 4, I looked at the kinematics of barred galaxies and identified slow ($\mathcal{R} > 1.4$), fast ($1.0 < \mathcal{R} < 1.4$) and ultrafast bars ($\mathcal{R} < 1.0$). However, it was still unclear whether fast and slow bars affect their host differently in terms of star formation and galaxy quenching.

In this chapter, I have created radius profiles of EW[H$\alpha$] and $\mathrm{D_n}4000$ for all the strongly, weakly and unbarred galaxies in the GZ DESI-MaNGA sample in Section

5.1 and for all the fast and slow bars in the TW sample in Section 5.2 using IFU data from MaNGA. I did this to investigate how strong and weak bars, as well as fast and slow bars, affect star formation in different regions of the galaxy.

1. ***Strong and weak bars:***

    - I showed that there is more star formation in the centre and beyond the bar-end region of strongly barred SF galaxies, compared to weakly barred and unbarred SF galaxies. In contrast, there is less star formation in the arms of the bar and the outskirts of the galaxy in strongly barred SF galaxies. These observations can be explained by heavy gas flows induced by the bar, which flow along the arms of the bar to the centre of the galaxy, where the gas is available for star formation. This suggests that strong bars can significantly affect the evolution of galaxies.
    - In contrast, the EW[H$\alpha$] and $D_n4000$ profiles of weakly barred SF galaxies was largely similar to those of unbarred SF galaxies, suggesting that weak bars do not induce significant gas flows and do not have the ability to significantly affect their host.
    - These results remained valid in intermediate and high mass galaxies. However, the suppression of star formation in the arms of the bar and the increase of star formation in the bar-end for strongly barred SF galaxies were no longer observed among low mass galaxies, suggesting that stellar mass plays an important role in galaxy quenching. However, the increase in central star formation in strongly barred SF galaxies was still observed in low mass galaxies.
    - Strong bars are long-lived structures, as they can influence the age of the stellar population, as shown by the $D_n4000$ profiles. This was not found for weak bars, whose $D_n4000$ profiles are similar to those of unbarred galaxies.
    - These results confirm the conclusion of Chapter 3: that strong bars have a big effect on their host and facilitate quenching, while weak bars do not.
    - The median radius profiles of weakly and strongly barred galaxies are found to be very different. However, the shaded regions around these median profiles indicate that there is still large amount of variability, which suggests that there are many intermediate profiles. This is consistent with the idea of the bar continuum that was introduced in Chapter 3.

2. ***Fast and slow bars:***

    - Slow bars have significantly higher star formation along the bar than fast bars in SF galaxies, indicated by the EW[H$\alpha$] and $D_n4000$ profiles.
    - However, I found that the global star formation rate is similar between fast and slow bars, which implies that the rate of gas consumption in fast and slow bars is still similar. Nevertheless, this shows that slow bars increase star formation locally along the bar and that the kinematics of the bar dictate where star formation occurs.
    - This increase in star formation along slow bars is most likely caused by larger differences in velocity between the bar-end and the gas in the disc observed in slow bars, compared to fast bars. This implies that slow bars are likely more efficient at sweeping up and concentrating gas in the bar and creating gas-depleted regions.
    - The work presented in this section suggests that the distinction between fast and slow bars is physically meaningful and that they affect their host in different ways.

3. ***Combining bar strength with bar kinematics:***

    - The results presented in this chapter suggest that there is a synergistic effect between bar strength and bar kinematics: a bar will affect its host the most, in terms of star formation, if it is both strong and slow.
    - As $\mathcal{R}$ is a continuous variable, bars can become ‘faster’ and ‘slower’. This is consistent with the continuous nature of bar types from ‘weakest’ to ‘strongest’. However, the bar continuum presented in Chapter 3 was based on visual morphology, whereas the distinction between fast and slow is based on kinematics. Furthermore, a strong (or weak) bar can be either fast or slow. These results suggest that a possible second axis could be added to the bar continuum, so that it has one morphological axis and one kinematic axis.

In this chapter, I have demonstrated the importance of considering both the kinematics and morphology of bars in galaxy evolution, as both separately have a significant effect on how the bar influences its host. However, a larger sample size will greatly improve our understanding of the combined effects of kinematics and bar strength, as the current sample size is still too small to make definitive statements.

# Chapter 6

# Conclusions and future perspectives

In this thesis, I have investigated the impact that strong and weak bars have on their hosts, considering especially galaxy evolution and quenching. Bars are common structures in disc galaxies that have the ability to redistribute angular momentum and matter in their host galaxy, and are thought to be long-lived. This suggests that a comprehensive understanding of bars is needed to have a complete theory of galaxy evolution. A lot of work on this topic has already been done for strong bars, but studies on the effects of weak bars have been lacking. This is because strong bars are easier to identify and observe. I used morphological classifications obtained from Galaxy Zoo, together with data from SDSS, MaNGA, the Legacy Survey and ALFALFA to study both weak and strong bars. In Chapter 3 I looked at the global properties of galaxies to assess the effects that weak and strong bars have on their hosts in the context of galaxy evolution and I addressed whether weak and strong bars are fundamentally distinct physical phenomena. In Chapter 4, I studied the kinematics of bars by applying the Tremaine-Weinberg method. I investigated whether the kinematics of weak and strong bars are significantly different and I addressed the existence of ultrafast bars and the recently claimed tension with $\Lambda$CDM. Finally, in Chapter 5, I created radius profiles of weak and strong bars, as well as fast and slow bars, and investigated how they affect star formation in their hosts. For a detailed discussion and conclusions, please refer to the sections at the end of each individual chapter. However, in this chapter I will provide a brief overview of the most important points and highlight possible avenues of research that I wish to undertake in the future.

## 6.1 Stronger bars facilitate quenching

In Section 3.2, I showed that the conclusions that are typically made for bars in general only apply to strong bars. For example, the strong bar fraction is significantly higher in the red sequence than in the blue cloud, but this is not found for weak bars.

I have also found evidence that strong bars facilitate the quenching process in Section 3.4, as higher fibre SFRs, lower gas masses and shorter depletion timescales were found in strongly barred galaxies than in unbarred SF galaxies. Interestingly, this was not observed for weakly barred SF galaxies, suggesting that they are not able to facilitate quenching. These results are supported by the results in Section 5.1, where I used resolved star formation indicators (EW[H$\alpha$] and $\mathrm{D_n}4000$) to create radius profiles. I found that strong bars in SF galaxies have increased star formation in their centres and in the regions beyond the bar-end ($R \approx 1.2 - 1.5R_{\mathrm{bar}}$), while suppressing star formation in the arms of the bar ($R \approx 0.5R_{\mathrm{bar}}$) and in the outskirts of the galaxy. This was again not found for weakly barred galaxies, whose radius profiles were similar to those of unbarred galaxies.

These results confirm that strong bars are long-lived structures that sweep up and funnel gas from the galaxy towards the centre. Here, the gas is concentrated and is available to increase star formation and the rate of gas consumption, which will help to speed up the quenching process. Star formation is also increased in the region beyond the bar-end due to a high density of gas and low values of shear. Conversely, star formation is suppressed in the arms of the bar, as the gas flows along the arm, which induces high values of shear and increases velocity dispersion. Thus, strong bars are important structures that can affect their hosts in significant ways. In contrast, weak bars seem to not have a big effect on their hosts, as no evidence was found for any of the above happening in weak bars.

## 6.2 The kinematics of bars

In the previous section, I highlighted differences that were found between weakly and strongly barred galaxies using photometry and resolved star formation indicators, but I have not yet considered their kinematics. In Section 4.2, I measured the bar pattern speed, corotation radius and $\mathcal{R}$ for strongly and weakly barred galaxies and compared them to each other. I found that strongly barred galaxies have significantly lower values for the pattern speed and $\mathcal{R}$ than weakly barred galaxies. As simulations show that the bar pattern speed goes down as the bar evolves, these results imply that strong bars are older and more evolved structures than weak bars. Additionally, these results also show that strong bars are more likely to be formed by global bar instabilities, while weak bars are more likely to be triggered by tidal interactions, as simulations have linked $\mathcal{R}$ to the formation mechanism of the bar. This last statement could be verified observationally in future work by testing whether weakly barred galaxies are preferentially found in denser environments using data from SDSS, or from future large-scale surveys, such as Euclid (Euclid Collaboration et al., 2022) and the Legacy Survey of Space and Time (LSST, Ivezić et al., 2019), which is discussed in more detail in Section 6.5.

The value of $\mathcal{R}$ depends on a correctly estimated bar length. However, measuring the bar length is not straightforward. While I am confident in the accuracy and reproducibility of the bar lengths used in this thesis (see Section 2.2.2 for more details), it would be prudent to use other techniques to measure bar length in future work and recalculate $\mathcal{R}$ to make sure the results presented above are robust to the method used to measure bar lengths.

I have also found that only 11% of the bars in my sample are ultrafast, with only 2% having a $1\sigma$ upper limit with $\mathcal{R} < 1.0$ (i.e. only 2% of the sample is confidently within the ultrafast regime). This is significantly lower than what has been found by other studies. The overall distribution of $\mathcal{R}$ is higher than what is typically found, which also decreases the recently claimed tension with $\Lambda$CDM, as bars are thought to have high values of $\mathcal{R}$ due to dynamical friction on the bar caused by the dark matter (DM) halo. This is partly because of the inclusion of weak bars in this analysis, as weak bars have significantly higher values for $\mathcal{R}$ than strong bars. The median value of $\mathcal{R}$ of a study that only includes strong bars will underestimate the true median value of $\mathcal{R}$ of the entire population of barred galaxies.

Interestingly, $\mathcal{R}$ is significantly different for strong and weak bars, which implies possible differences in the DM fractions of strongly and weakly barred galaxies. This can be tested by generating Jeans Anisotropic Models (JAM, Cappellari, 2008) of the barred galaxies in my sample, which will help to constrain the DM fraction. This will be done in future work and will help to study the relationship between bar strength, bar kinematics and the DM halo in greater detail and possibly provide new insights to the aforementioned tension with $\Lambda$CDM. Additionally, the dependence of the pattern speed, corotation radius and $\mathcal{R}$ on the gas mass can also be tested using gas mass estimates from ALFALFA (see Section 2.1.4), to see whether gas plays a significant role in the kinematics of bars as well.

Finally, I found that the corotation radius is significantly larger for bars in quenching galaxies than for bars in SF galaxies, while this was not found for the pattern speed and $\mathcal{R}$. I studied the relationship between bar kinematics and quenching in Chapter 5, but I concentrated on the effects of $\mathcal{R}$. I want to keep studying bar kinematics and quenching in future work using data from MaNGA, but specifically focus on the corotation radius.

## 6.3 Fast and slow bars

I identified slow and fast bars in the section above, but it was unclear whether slow and fast bars affect their host differently in terms of star formation. I found evidence that slow bars have significantly higher amounts of star formation along the position angle of the bar than fast bars in SF galaxies in Section 5.2. However, the global star formation rates are not significantly different. This suggests that, while the global properties of the galaxy remain the same in galaxies with fast and slow bars, the kinematics of the bar governs where star formation occurs. This result is likely due to the difference in velocity between the bar-end and the gas in the disc being larger for slow bars than for fast bars, which implies that slow bars are more efficient at sweeping up and concentrating gas in the bar and creating gas-depleted regions. This hypothesis can be tested in the future with spatially resolved observations of gas in slow and fast bars in SF galaxies, which can be used to verify whether gas-depleted regions are more prevalent in SF galaxies with slow bars.

I have also found preliminary evidence that there is a synergistic effect between bar strength and bar kinematics, as a slow strong bar seems to affect its host more than a fast strong bar in terms of star formation.

However, a limiting factor of this analysis is the relatively small sample size, which makes it hard to make definitive statements. I want to measure $\mathcal{R}$ for a larger sample to further investigate the relationship between bar strength and bar kinematics in greater detail. This can be done in the future with upcoming IFU surveys, such as Hector (Bryant et al., 2020), which will be described in more detail in Section 6.5.

I have shown that the effects of a strong bar are more prevalent in high mass galaxies, compared to low mass galaxies (see Section 5.1.3). However, the effect of stellar mass on the radius profiles of fast and slow bars was not addressed in this thesis. The reason for this was again a limited sample size. This will be done in future work, once a larger sample size is obtained with upcoming surveys, as mentioned above.

## 6.4 Bar continuum

The results from Section 3.5 show that the differences between strong and weak bars in terms of fibre SFR disappear when accounting for the length of the bar. This observation first led to the conclusion that strong and weak bars are not physically distinct phenomena, but rather part of a continuum of bar types. On this continuum, bars range from 'weakest' to 'strongest', and many of the effects that are described above are found to scale with this continuum. For example, I concluded above that strong bars have higher fibre SFRs than weak bars. However, there exists a positive relation between bar length and fibre SFR, which shows that the longest (and strongest) bars tend to have the highest fibre SFR. Thus, with this bar continuum in mind, I concluded that the strongest bars facilitate quenching the most.

A few additional pieces of evidence found throughout this thesis support the idea of a bar continuum. First of all, no threshold was found in gas mass, depletion timescale, bar pattern speed, corotation radius and $\mathcal{R}$ that can be used to separate weak and strong bars to a satisfying degree. Instead, I find that many of these parameters are correlated with bar length. Finally, weakly barred and strongly barred galaxies with intermediate bar lengths look very similar and are hard to differentiate from each other, even though the ends of the continuum look very different.

Even though the median radius profile of EW[H$\alpha$] and $\mathrm{D_n}4000$ for strongly barred and weakly barred galaxies are very different, the results are still consistent with the idea of a bar continuum, as there is a large amount of variability associated with the plots. This scatter allows for the existence of many profiles in between the median profile of a weakly barred and strongly barred galaxy. There are two possible scenarios of how the profile of a bar might change as bars of increasing strength are considered. One possibility is that the features typically associated with a strong bar (i.e. increased star formation in the centre and in the region beyond the bar-end and suppression of star formation in the arms of the bar) become more pronounced as the bar under consideration becomes stronger. The alternative is that the probability of such a feature appearing increases with bar strength. This will be tested in future work by characterising the diversity of the profiles of galaxies of different bar types, instead of looking at the median profile of the entire population.

I have shown in Section 5.2 that the kinematics of the bar is important in the context of galaxy evolution, as fast and slow bars affect their hosts in different ways. This led me to suggest in Section 5.2.5.5 that a possible second axis can be added to the bar continuum. The first axis, which is described above, is based on morphological measurements, whereas the second axis would be based on kinematic measurements. This was suggested because $\mathcal{R}$, which is used to classify bars as fast or slow, is a continuous variable that has been shown to change over time in simulations. Thus, bars can become 'faster' or 'slower'. There are also significant populations of slow strong bars, fast strong bars, slow weak bars and fast weak bars, which suggests that information about both the kinematics and photometry of a galaxy is needed to fully characterise it. The results presented in Chapter 5 suggest that slow strong bars will affect their hosts the most. However, as mentioned before, a larger sample size is needed to accurately quantify the relationship between bar strength and bar kinematics and to see whether adding a second kinematic axis to the bar continuum makes sense. The validity of the kinematic bar continuum can also be tested by studying how specific parameters scale with $\mathcal{R}$, similarly to what I did with the morphological bar continuum and bar length in Section 3.5. For example, does the concentration of star formation along bars become more apparent when considering consistently slower bars (i.e. increasing $\mathcal{R}$)?

## 6.5 Future observations

There are many upcoming facilities that will help to study bars in even greater detail. For example, the James Webb Space Telescope (JWST, Gardner et al., 2006) can be used to study the epoch when bars first emerge and bar fractions at higher redshifts ($z \sim 2$, e.g. see Guo et al. 2022), which can help clarify the relationship between bars and mergers. Additionally, large-scale surveys, such as the upcoming Euclid mission (Euclid Collaboration et al., 2022) and LSST (Ivezić et al., 2019), will survey an estimated 15,000 deg$^2$ and 10,000 deg$^2$ of the sky, respectively. These observations will include a huge number of galaxies, many of which will be barred. These large surveys will help to investigate the properties of barred galaxies in much more detail. The expected full width at half maximum (FWHM) of LSST in the $r$-band is 0.73 arcsec (Ivezić et al., 2019), while it is $\sim$0.22 arcsec for Euclid in the visible bands (Euclid Collaboration et al., 2022). For reference, the FWHM of the $r$-band in DECaLS is 1.18 arcsec (Dey et al., 2019). Additionally, the $5\sigma$ detection limit of a point source of DECaLS is 23.54 in the $r$-band (Dey et al., 2019), while it is 24.35 and 26.2 for LSST and Euclid, respectively (Ivezić et al., 2019; Euclid Collaboration et al., 2022). The increased resolution and depth of these future surveys will help to detect more, smaller and fainter bars. This more complete sample of weak bars can be used to study barred galaxies in a wide range of environments and investigate the effect of environment on bar formation. This can help to verify the results of Section 4.6.2 that suggest that weak bars are more likely to be formed by tidal interactions.

However, for the work presented in this thesis, I believe it would be more interesting to have a larger sample of galaxies with reliable IFU data, which is needed to study the kinematics of barred galaxies, rather than just more photometric data. In this thesis, I have used data from MaNGA, which has IFU data for 11,273 galaxies. It would be possible to use other currently available IFU surveys, such as SAMI, which has surveyed 3,068 galaxies (Croom et al., 2021), and CALIFA, which has surveyed 667 galaxies (Sánchez et al., 2012, 2016c). However, including these two surveys will only modestly increase the final sample size. Due to multiple thresholds and quality restrictions (see Section 2.2.4.5 for more details), it was only possible to study the kinematics of 225 out of the 11,273 targets in MaNGA. Assuming a similar success rate for SAMI and CALIFA, the sample size would increase with only $\sim$75 new targets. One exciting future possibility involves the Hector instrument, which is a multi IFU spectrograph that will be placed on the 4m Anglo-Australian Telescope (AAT). Hector will be used to survey an estimated $\sim$15,000 galaxies in the southern hemisphere at low redshifts ($z < 0.1$) up to 2 effective radii (Bryant et al., 2020). Assuming a similar success rate as for MaNGA, Hector would increase the sample size with $\sim$300 galaxies, bringing the total estimated sample size for all four surveys combined up to $\sim$600 galaxies, which could be sufficient to help disentangle the effects of bar strength and bar kinematics.

The vast amounts of data that will be coming from all these different telescopes and surveys will help to clarify the remaining open questions that I outlined in the sections above. I am incredibly excited for the future and cannot wait to continue this research and see what can still be learned about galaxy evolution - and bars specifically.

# Chapter 7

# Epilogue: A series of unfortunate events

As mentioned in Section 6.5, more detailed observations of barred galaxies will be useful, especially to study the kinematics of bars. To this end, I was awarded telescope time on the 2.54m Isaac Newton Telescope (INT) at Roque de los Muchachos Observatory on the island of La Palma three times. I wanted to detect the presence of gas for a wide range of barred galaxies and infer potential gas flows caused by the bar. Furthermore, I wanted to test whether these gas flows are different for strongly and weakly barred galaxies, as was suggested by the results discussed in Section 5.1.5.1.

The galaxies selected for this had to satisfy multiple requirements. Firstly, it was made sure that these targets are not in MaNGA, CALIFA or SAMI to avoid unnecessary duplicate observations. However, they have to be in the MPA-JHU catalogue, so that we have reliable stellar mass and SFR estimates for them, which implies that their are also in SDSS. Additionally, they are all also detected in ALFALFA, to guarantee the presence of HI gas and maximise the chance of inferring gas flows. All galaxies are also selected to be star forming, as my previous work has shown the biggest differences between weak and strong bars are found in star forming galaxies (see Chapters 3 and 5). Additionally, the targets should be at low redshifts and as bright as possible, in order to minimise the exposure time. In total, I identified 7 strongly barred, 7 weakly barred and 7 unbarred galaxies, which are shown in Figure 7.1. The median redshift of the entire sample is 0.037, while the median r-band Petrosian magnitude from SDSS is 14.9. A blind offset and standard star was found for every individual target.

The intermediate dispersion spectrograph (IDS) on the INT is ideal for our science goals. It is a long-slit spectrograph that can be paired with a range of gratings. I decided to use to R300V grating together with the EEV10 detector, which combined

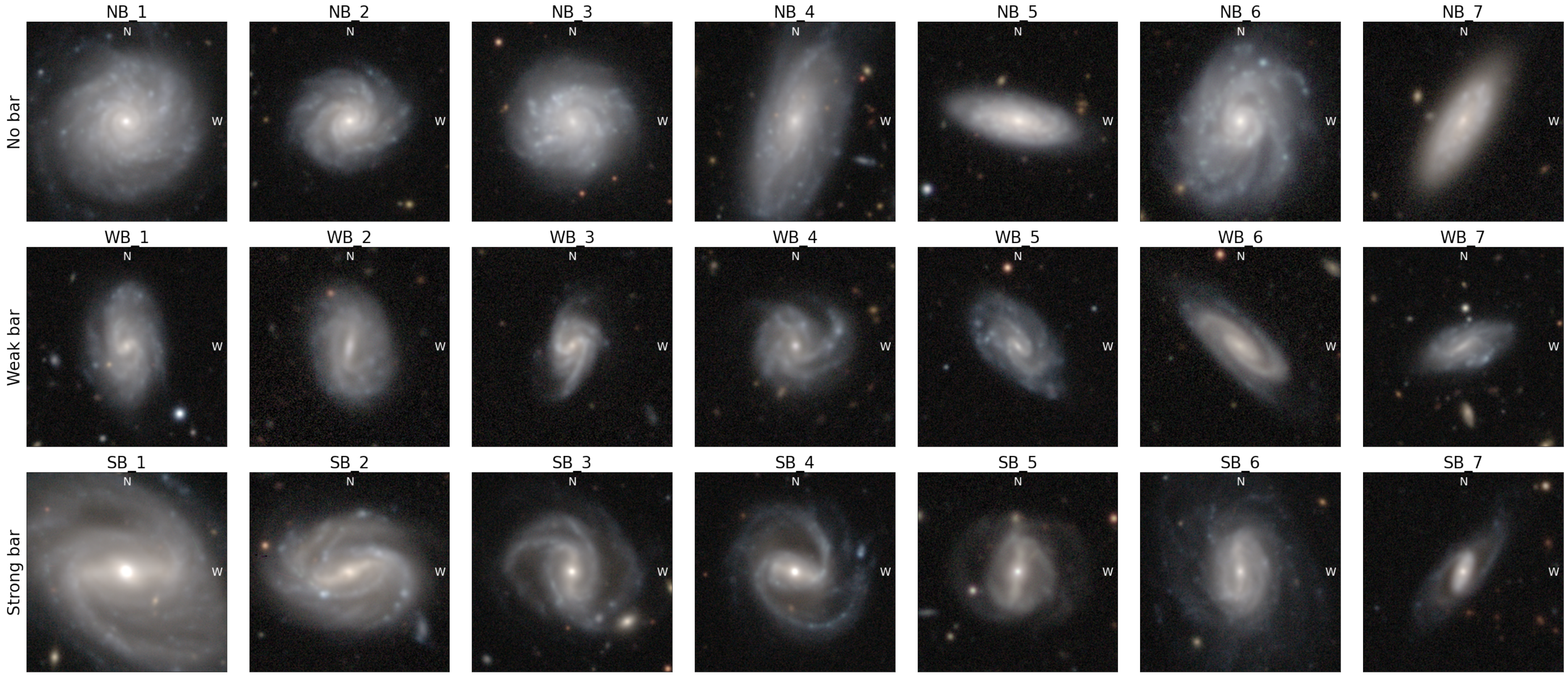

Figure 7.1: Postage stamps (64x64 arcsec) from the Legacy survey of the 21 targets selected for observation at the INT. I have selected 7 unbarred galaxies (abbreviated as 'NB', top row), 7 weakly barred galaxies ('WB', middle row) and 7 strongly barred galaxies ('SB', bottom row). The cardinal directions are shown in every image. The name of every target, which consists of the bar type (SB, WB or NB) and a number, is shown on top of every image.

have a large enough wavelength range to cover the H$\alpha$ region, which is emitted by ionised gas, while simultaneously also covering other interesting regions, such as the $D_n4000$ break, H$\beta$ and [O III] regions for our entire sample (roughly from 4000 Å to 7000 Å). The velocity of the gas can be derived from the spectra using the penalized Pixel-Fitting (pPXF) method (Cappellari & Emsellem, 2004; Cappellari, 2017). The combined estimated total exposure time (without overhead) in order to get a sufficiently high signal-to-noise ratio is 26.5 hours. For each of these targets, I want to place a slit parallel and perpendicular to the position angle of the bar, so that it was possible to compare the gas in the bar region with the disc region. The hypothesis is that we would detect more gas in the slit placed parallel to the bar than in the slit placed perpendicular to the bar, as the bar would concentrate gas in its arms. Furthermore, we expect this difference to be greater for strong bars than for weak bars. Finally, the resultant gas flows are also expected to be greater in strong bars than in weak bars.

I applied for telescope time on the INT with this project for the first time in the 2020B semester and I was awarded four dark nights (7 January - 10 January 2021). However, due to the rising safety concerns about COVID-19 in Europe around that time, we decided not to travel to the observatory ourselves. The support astronomers of the INT kindly offered to take the observations in our absence. Unfortunately, a few days before our scheduled observing run, storm Filomena started forming close to the Canary Islands (Smart, 2021) and caused snowfall and very low temperatures at the observatory site, which meant that none of our chosen targets could be observed. We even received news that the telescope dome had physically frozen shut, which is counterproductive for astronomical observations. Panels a and b in Figure 7.2 show the conditions at Roque de los Muchachos Observatory during this time.

In spite of this bad luck, I applied for telescope time again in the 2021B semester. This time, we were awarded five dark nights (29 September - 3 October 2021). However, 10 days before our observing run was supposed to start, a volcanic eruption occurred on the island on the Cumbre Vieja volcanic ridge (Carracedo et al., 2021). The observatory was covered in volcanic ash and the management team rightfully decided to cancel the planned observations, so again not a single one of our targets was observed. The extent of the volcanic plume and the cone of the volcano are shown in panels c and d of Figure 7.2. This was a case of extremely bad luck; Eff-Darwich et al. (2010) previously stated that the geological hazard of volcanic activity was found to be lowest at the Roque de los Muchachos Observatory, compared to other observatories around the world, such as El Teide Observatory on Tenerife, Mauna Kea on

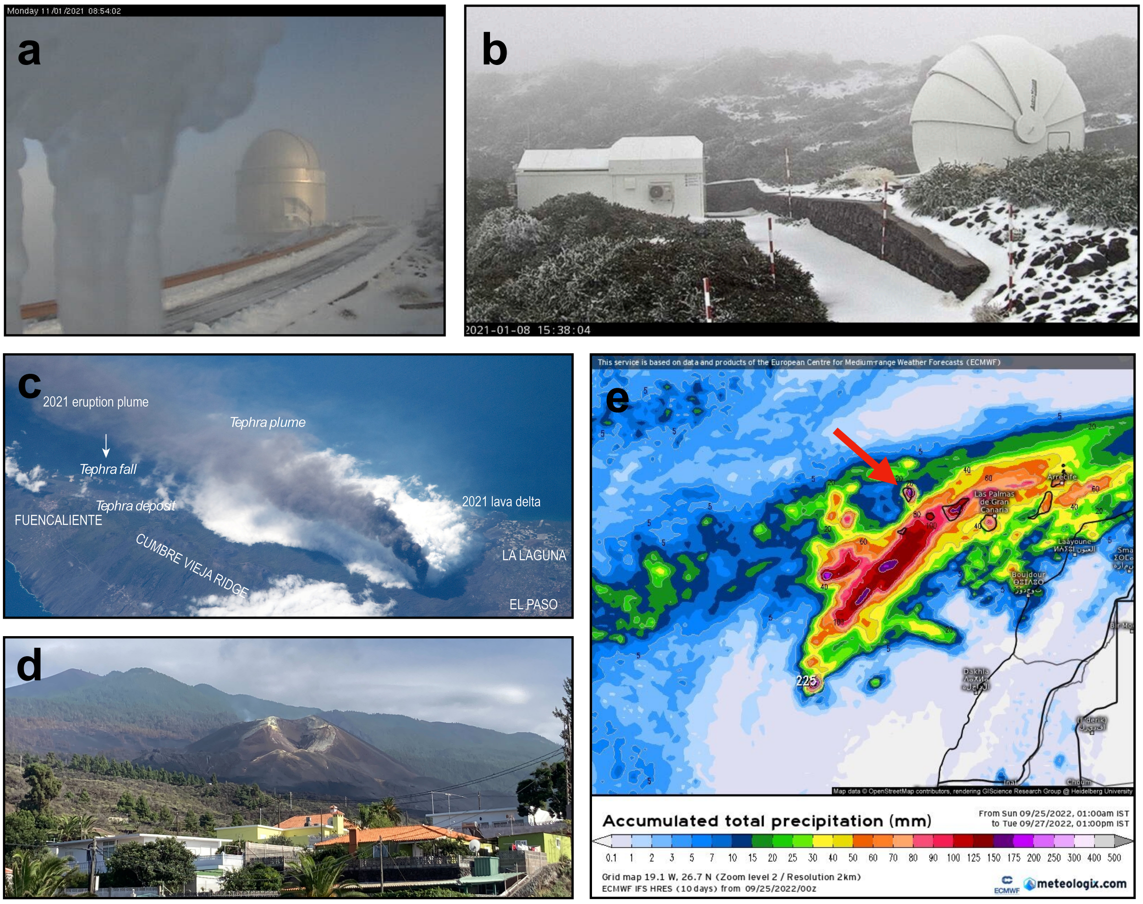

Figure 7.2: Panel a and b show the severity of the snowfall following storm Filomena at Roque de los Muchachos Observatory. The images were taken with the live webcams of the Roque de los Muchachos Observatory on 8 and 11 January 2021. Panel c is a photograph taken from the International Space Station on 4 October 2021 and shows the extent of the volcanic plume after the eruption. The original figure was taken from Carracedo et al. (2021). Panel d shows the volcano cone and the open crater. This picture was taken ∼1 year after the eruption by myself when we were on La Palma on 28 September 2022. Panel e shows the accumulated total precipitation between 25 September 2022 and 27 September 2022 caused by storm Hermine. The location of La Palma is indicated by the red arrow. The figure was taken from meteologix and is based on data from the European Centre for Medium-range Weather Forecasts (ECMWF).

Hawai‘i, Paranal in Chile and Cerro Ventarrones in Chile. As my bad luck surely must have run out by now, I applied for telescope time a third time in the 2022B semester and we were again awarded 5 dark nights (23 September - 27 September 2022). Everything seemed to go well and we flew down to La Palma. However, consistent with our previous luck, a tropical storm, named Hermine, appeared during our observations and caused unusual amounts of rainfall on the island (see panel e in Figure 7.2), which severely limited our observing time[1].

At this point, our observations have been thwarted by (in chronological order): a global pandemic, a snow storm, a volcanic eruption and a tropical storm. These findings are consistent with the results presented in Lund (2020), who found a significant correlation between their obtained telescope time and increased rainfall. Based on the results presented in this section, I would advise extreme caution to anyone that is considering to include me in future observing proposals, as there seems to be a very tight correlation between natural disasters occurring and me receiving observing time.

Due to the aforementioned storm Hermine, we were only able to observe 1 out of the 21 selected targets. The only target that was observed was the strongly barred galaxy named ‘SB_5’ in Figure 7.1. The calculated ideal exposure time for the target was 90 min, however due to inclement weather, this was reduced to 60 min. The target was observed in separate exposures of 15 min. We were able to observe the target for the full 60 min for the observations with the slit placed parallel to the bar. However, for the observations with the slit placed perpendicular to the bar, the sky started to become overcast after 30 min and we had to completely stop observing after 60 min. The resultant spectra are shown in Figure 7.3, respectively. The top panel shows the spectrum with the slit placed parallel to the bar, while the bottom panel shows the spectrum with the slit placed perpendicular to the bar. The slit width of each exposure was 6 arcsec, to make sure the entire bar could fit within the parallel slit. The spectra were gain corrected, bias subtracted, flatfield corrected, sky subtracted, normalised, wavelength calibrated and corrected for the redshift of the target. The reduction pipeline used is made publicly available and can be found here[2].

The dashed red vertical lines in both spectra in Figure 7.3 indicate where it is expected to see H$\alpha$ emission (at 6564 Å). The peak around this wavelength is clearly larger for the slit placed parallel to the bar than in the slit placed perpendicular to

---

[1] At least we made it to the island this time.

[2] `github.com/tobiasgeron/INT_data_reduction`

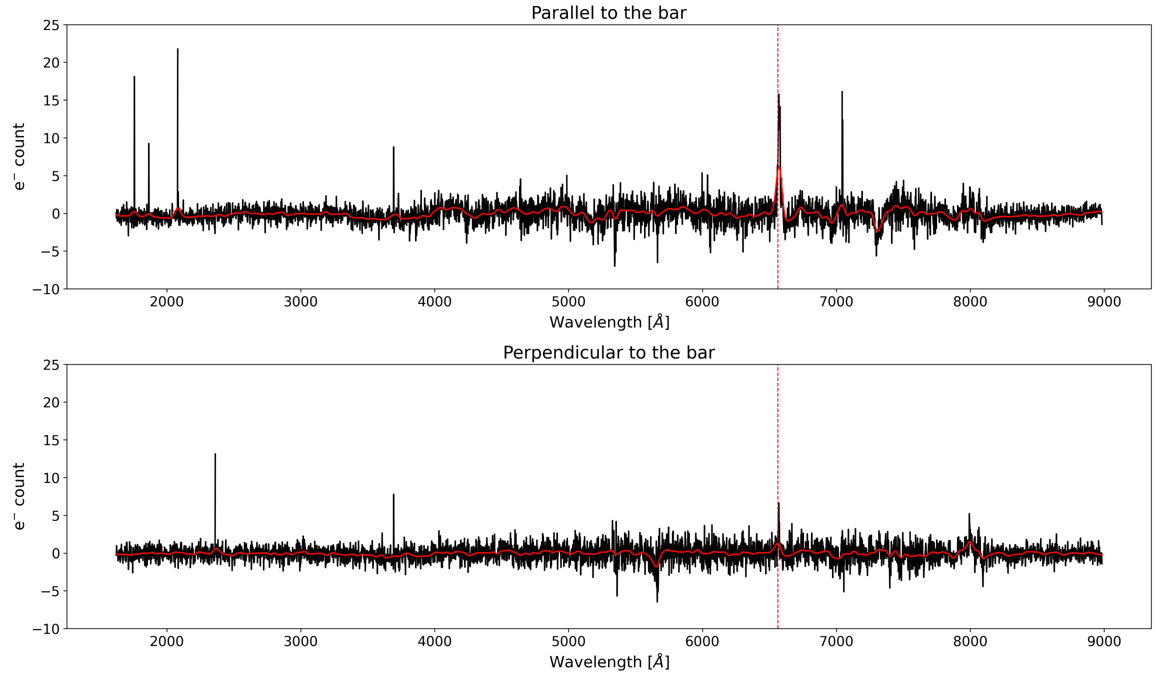

Figure 7.3: The spectra for SB_5 with the slit placed parallel to the bar (top panel) and perpendicular to the bar (bottom panel). The spectra (black line) have been gain corrected, bias subtracted, flatfield corrected, sky subtracted, normalised, wavelength calibrated and corrected for the redshift of the target. The red line is the smoothened version of the spectrum, using a Gaussian kernel with a standard deviation of 10. The dashed red vertical lines represent where it is expected to see H$\alpha$ emission (at 6564 Å). The H$\alpha$ peak is clearly more pronounced for the slit placed parallel to the bar, suggesting that there is more HII gas to be found in the arms of the bar than perpendicular to the bar.

the bar. This preliminary result is consistent with the hypothesis stated above and suggests the presence of more gas along the arms of the bar than elsewhere for this one target. However, it is also possible that the lower amounts of H$\alpha$ found in the perpendicular slit is because of the worse weather during these observations.

In conclusion, the kinematics of barred galaxies can be studied with detailed observations of barred galaxies (either with an IFU or with long-slit spectroscopy). Over the course of my DPhil, I have attempted to make such observations, although the quantity and quality of these observations has been limited due to multiple natural disasters. Nevertheless, the preliminary results presented in this section demonstrate the kind of observations that could be done in the future in order to better understand the differences in the kinematics between strongly and weakly barred galaxies.

# Bibliography

Abadi M. G., Moore B., Bower R. G., 1999, MNRAS, 308, 947

Abadi M. G., et al., 2003, ApJ, 591, 499

Abazajian K. N., et al., 2009, ApJS, 182, 543

Abdurro'uf et al., 2022, ApJS, 259, 35

Abraham R. G., van den Bergh S., Nair P., 2003, ApJ, 588, 218

Adelman-McCarthy J. K., et al., 2008, ApJS, 175, 297

Aguerri J. A. L., Beckman J. E., Prieto M., 1998, AJ, 116, 2136

Aguerri J. A. L., et al., 2000, A&A, 361, 841

Aguerri J. A. L., Debattista V. P., Corsini E. M., 2003, MNRAS, 338, 465

Aguerri J. A. L., Méndez-Abreu J., Corsini E. M., 2009, A&A, 495, 491

Aguerri J. A. L., et al., 2015, A&A, 576, A102

Ahumada R., et al., 2020, ApJS, 249, 3

Aihara H., et al., 2011, ApJS, 193, 29

Akins H. B., et al., 2022, ApJ, 929, 94

Alam S., et al., 2015, ApJS, 219, 12

Algorry D. G., et al., 2017, MNRAS, 469, 1054

Alonso-Herrero A., Knapen J. H., 2001, AJ, 122, 1350

Argence B., Lamareille F., 2009, A&A, 495, 759

Assef R. J., et al., 2018, ApJS, 234, 23

Athanassoula E., 1992a, MNRAS, 259, 328

Athanassoula E., 1992b, MNRAS, 259, 345

Athanassoula E., 2002, ApJ, 569, L83

Athanassoula E., 2003, MNRAS, 341, 1179

Athanassoula E., 2007, Astrophysics and Space Science Proceedings, 3, 195

Athanassoula E., et al., 1983, A&A, 127, 349

Athanassoula E., Lambert J. C., Dehnen W., 2005, MNRAS, 363, 496

Athanassoula E., Machado R. E. G., Rodionov S. A., 2013, MNRAS, 429, 1949

Baillard A., et al., 2011, A&A, 532, A74

Baldry I. K., et al., 2004, ApJ, 600, 681

Baldry I. K., et al., 2006, MNRAS, 373, 469

Baldwin J. A., Phillips M. M., Terlevich R., 1981, PASP, 93, 5

Balogh M. L., et al., 1999, ApJ, 527, 54

Bamford S. P., et al., 2009, MNRAS, 393, 1324

Banerji M., et al., 2010, MNRAS, 406, 342

Barazza F. D., Jogee S., Marinova I., 2008, ApJ, 675, 1194

Barnes J., Efstathiou G., 1987, ApJ, 319, 575

Barnes J. E., Hernquist L. E., 1991, ApJ, 370, L65

Beane A., et al., 2022, arXiv e-prints, p. arXiv:2209.03364

Becker R. H., White R. L., Helfand D. J., 1995, ApJ, 450, 559

Beckwith S. V. W., et al., 2006, AJ, 132, 1729

Bekki K., 1998, ApJ, 496, 713

Belfiore F., et al., 2018, MNRAS, 477, 3014

Belfiore F., et al., 2019, AJ, 158, 160

Bell E. F., et al., 2004, ApJ, 608, 752

Best P. N., Heckman T. M., 2012, MNRAS, 421, 1569

Bhambra P., Joachimi B., Lahav O., 2022, MNRAS, 511, 5032

Binney J., Tremaine S., 2008, Galactic Dynamics: Second Edition

Blanton M. R., et al., 2017a, AJ, 154, 28

Blanton M. R., et al., 2017b, AJ, 154, 28

Bluck A. F. L., et al., 2014, MNRAS, 441, 599

Bluck A. F. L., et al., 2022, A&A, 659, A160

Blumenthal G. R., et al., 1984, Nature, 311, 517

Bois M., et al., 2011, MNRAS, 416, 1654

Bournaud F., Combes F., 2002, A&A, 392, 83

Bournaud F., Combes F., Semelin B., 2005, MNRAS, 364, L18

Boylan-Kolchin M., Ma C.-P., Quataert E., 2005, MNRAS, 362, 184

Brammer G. B., et al., 2011, ApJ, 739, 24

Brinchmann J., Ellis R. S., 2000, ApJ, 536, L77

Brinchmann J., et al., 2004, MNRAS, 351, 1151

Bruzual G., Charlot S., 2003, MNRAS, 344, 1000

Bruzual A. G., 1983, ApJ, 273, 105

Bryant J. J., et al., 2020, in SPIE. p. 1144715

Bullock J. S., Boylan-Kolchin M., 2017, ARA&A, 55, 343

Bundy K., Ellis R. S., Conselice C. J., 2005, ApJ, 625, 621

Bundy K., et al., 2015, ApJ, 798, 7

Buta R., 1986, ApJS, 61, 609

Buta R., Block D. L., 2001, ApJ, 550, 243

Buta R. J., Zhang X., 2009, ApJS, 182, 559

Buta R. J., et al., 2015, ApJS, 217, 32

Buta R. J., et al., 2019, MNRAS, 488, 2175

Cappellari M., 2008, MNRAS, 390, 71

Cappellari M., 2016, ARA&A, 54, 597

Cappellari M., 2017, MNRAS, 466, 798

Cappellari M., Copin Y., 2003, MNRAS, 342, 345

Cappellari M., Emsellem E., 2004, PASP, 116, 138

Cappellari M., et al., 2007, MNRAS, 379, 418

Cappellari M., et al., 2011a, MNRAS, 413, 813

Cappellari M., et al., 2011b, MNRAS, 416, 1680

Cappellari M., et al., 2013, MNRAS, 432, 1709

Carles C., et al., 2016, MNRAS, 463, 1074

Carnall A. C., et al., 2023, MNRAS,

Carollo C. M., et al., 2007, ApJ, 658, 960

Carracedo J. C., et al., 2021, Geology Today, 38, 94

Casteels K. R. V., et al., 2013, MNRAS, 429, 1051

Catinella B., et al., 2018, MNRAS, 476, 875

Cervantes Sodi B., 2017, ApJ, 835, 80

Ceverino D., Klypin A., 2007, MNRAS, 379, 1155

Charlot S., Longhetti M., 2001, MNRAS, 323, 887

Cheng T.-Y., et al., 2020, MNRAS, 493, 4209

Cherinka B., et al., 2019, AJ, 158, 74

Cheung E., et al., 2013, ApJ, 779, 162

Cheung E., et al., 2015, MNRAS, 447, 506

Cisternas M., et al., 2013, ApJ, 776, 50

Cisternas M., et al., 2015, ApJ, 802, 137

Coelho P., Gadotti D. A., 2011, ApJ, 743, L13

Combes F., Sanders R. H., 1981, A&A, 96, 164

Comerford J. M., et al., 2020, ApJ, 901, 159

Condon J. J., et al., 1998, AJ, 115, 1693

Conselice C. J., 2003, ApJS, 147, 1

Conselice C. J., 2014, ARA&A, 52, 291

Conselice C. J., et al., 2003, AJ, 126, 1183

Contopoulos G., 1980, A&A, 81, 198

Contopoulos G., 1981, A&A, 102, 265

Contopoulos G., Papayannopoulos T., 1980, A&A, 92, 33

Corsini E. M., et al., 2007, ApJ, 659, L121

Courteau S., 1997, AJ, 114, 2402

Cox D. R., 1972, Journal of the Royal Statistical Society. Series B (Methodological), 34, 187

Cox T. J., Loeb A., 2008, MNRAS, 386, 461

Crain R. A., et al., 2015, MNRAS, 450, 1937

Cresci G., et al., 2009, ApJ, 697, 115

Croom S. M., et al., 2021, MNRAS, 505, 991

Cuomo V., et al., 2019, A&A, 632, A51

Cuomo V., et al., 2020, A&A, 641, A111

Cuomo V., et al., 2021, A&A, 649, A30

Curtis H., 1921, Bull. Nat. Res. Coun., 2, 194

Davidson-Pilon C., et al., 2020, CamDavidsonPilon/lifelines: v0.25.4, doi:10.5281/zenodo.4002777, `https://doi.org/10.5281/zenodo.4002777`

Davis M., et al., 1985, ApJ, 292, 371

Davis T. A., et al., 2015, MNRAS, 449, 3503

Davoust E., Contini T., 2004, A&A, 416, 515

Debattista V. P., 2003, MNRAS, 342, 1194

Debattista V. P., Sellwood J. A., 1998, ApJ, 493, L5

Debattista V. P., Sellwood J. A., 2000, ApJ, 543, 704

Debattista V. P., Williams T. B., 2004, ApJ, 605, 714

Debattista V. P., Corsini E. M., Aguerri J. A. L., 2002, MNRAS, 332, 65

Debattista V. P., et al., 2006, ApJ, 645, 209

Dekel A., Birnboim Y., 2006, MNRAS, 368, 2

Dey A., et al., 2016, in Ground-based and Airborne Instrumentation for Astronomy VI. p. 99082C

Dey A., et al., 2019, AJ, 157, 168

Díaz-García S., et al., 2016, A&A, 587, A160

Díaz-García S., et al., 2020, A&A, 644, A38

Dieleman S., Willett K. W., Dambre J., 2015, MNRAS, 450, 1441

Djorgovski S., Davis M., 1987, ApJ, 313, 59

Donnari M., et al., 2021, MNRAS, 500, 4004

Dressler A., et al., 1987, ApJ, 313, 42

Dreyer J. L. E., 1888, MmRAS, 49, 1

Drory N., et al., 2015, AJ, 149, 77

Duc P.-A., et al., 2011, MNRAS, 417, 863

Eff-Darwich A., et al., 2010, MNRAS, 407, 1361

Efstathiou G., Lake G., Negroponte J., 1982, MNRAS, 199, 1069

Efthymiopoulos C., et al., 2019, MNRAS, 484, 1487

Elbaz D., et al., 2011, A&A, 533, A119

Ellison S. L., et al., 2011, MNRAS, 416, 2182

Elmegreen B. G., Elmegreen D. M., 1985, ApJ, 288, 438

Elmegreen D. M., et al., 1991, A&A, 244, 52

Elmegreen B. G., et al., 1996, AJ, 111, 2233

Elmegreen B. G., Elmegreen D. M., Hirst A. C., 2004, ApJ, 612, 191

Emsellem E., et al., 2006, MNRAS, 365, 367

Emsellem E., et al., 2011, MNRAS, 414, 888

Emsellem E., et al., 2015, MNRAS, 446, 2468

Emsellem E., et al., 2022, A&A, 659, A191

Erwin P., 2004, A&A, 415, 941

Erwin P., 2005, MNRAS, 364, 283

Erwin P., 2018, MNRAS, 474, 5372

Erwin P., 2019, MNRAS, 489, 3553

Eskridge P. B., et al., 2000, AJ, 119, 536

Eskridge P. B., et al., 2002, ApJS, 143, 73

Euclid Collaboration et al., 2022, A&A, 662, A112

Faber S. M., Jackson R. E., 1976, ApJ, 204, 668

Faber S. M., et al., 2007, ApJ, 665, 265

Falcón-Barroso J., et al., 2011, A&A, 532, A95

Fall S. M., Efstathiou G., 1980, MNRAS, 193, 189

Fanali R., et al., 2015, MNRAS, 454, 3641

Fathi K., et al., 2009, ApJ, 704, 1657

Fillingham S. P., et al., 2016, MNRAS, 463, 1916

Fisher D. B., Drory N., 2011, ApJ, 733, L47

Flaugher B., et al., 2015, AJ, 150, 150

Flório V., Freire Júnior O., 2021, Physics in Perspective, 23, 85

Font J., et al., 2011, ApJ, 741, L14

Font J., et al., 2014, ApJS, 210, 2

Font J., et al., 2017, ApJ, 835, 279

Fragkoudi F., et al., 2021, A&A, 650, L16

Frankel N., et al., 2022, ApJ, 940, 61

Fraser-McKelvie A., et al., 2016, MNRAS, 462, L11

Fraser-McKelvie A., et al., 2020a, MNRAS, 495, 4158

Fraser-McKelvie A., et al., 2020b, MNRAS, 499, 1116

Freeman K. C., 1970, ApJ, 160, 811

Frenk C. S., White S. D. M., 2012, Annalen der Physik, 524, 507

Fujimoto Y., Tasker E. J., Habe A., 2014, MNRAS, 445, L65

Fujimoto Y., et al., 2020, MNRAS, 494, 2131

Gabbasov R. F., Repetto P., Rosado M., 2009, ApJ, 702, 392

Gadotti D. A., 2011, MNRAS, 415, 3308

Gadotti D. A., et al., 2007, MNRAS, 381, 943

Gajda G., Łokas E. L., Athanassoula E., 2017, ApJ, 842, 56

Galloway M. A., et al., 2015, MNRAS, 448, 3442

Garcia-Gómez C., et al., 2017, A&A, 601, A132

Gardner J. P., et al., 2006, Space Science Reviews, 123, 485

Garma-Oehmichen L., et al., 2020, MNRAS, 491, 3655

Garma-Oehmichen L., et al., 2022, MNRAS, 517, 5660

Gavazzi G., et al., 2015, A&A, 580, A116

Genzel R., et al., 2008, ApJ, 687, 59

George K., et al., 2019, A&A, 621, L4

Gerin M., Combes F., Athanassoula E., 1990, A&A, 230, 37

Géron T., et al., 2021, MNRAS, 507, 4389

Géron T., et al., 2023, MNRAS, 521, 1775

Gerssen J., Debattista V. P., 2007, MNRAS, 378, 189

Gerssen J., Kuijken K., Merrifield M. R., 1999, MNRAS, 306, 926

Gerssen J., Kuijken K., Merrifield M. R., 2003, MNRAS, 345, 261

Giovanelli R., et al., 2005, AJ, 130, 2598

Giuricin G., et al., 1993, ApJ, 407, 22

Gonçalves T. S., et al., 2012, ApJ, 759, 67

Graham A. W., Worley C. C., 2008, MNRAS, 388, 1708

Gunn J. E., et al., 1998, AJ, 116, 3040

Gunn J. E., et al., 2006, AJ, 131, 2332

Guo R., et al., 2019, MNRAS, 482, 1733

Guo Y., et al., 2022, arXiv e-prints, p. arXiv:2210.08658

Guth A. H., Pi S. Y., 1982, Physical Review Letters, 49, 1110

Haslbauer M., et al., 2022, ApJ, 925, 183

Hawking S. W., 1982, Physics Letters B, 115, 295

Haynes M. P., et al., 2011, AJ, 142, 170

Haynes M. P., et al., 2018, ApJ, 861, 49

Hayward C. C., et al., 2014, MNRAS, 442, 1992

Haywood M., et al., 2016, A&A, 589, A66

Hernandez O., et al., 2005, ApJ, 632, 253

Hilmi T., et al., 2020, MNRAS, 497, 933

Hilz M., et al., 2012, MNRAS, 425, 3119

Hirota A., et al., 2014, PASJ, 66, 46

Hocking A., et al., 2018, MNRAS, 473, 1108

Hohl F., 1971, ApJ, 168, 343

Hopkins A. M., Beacom J. F., 2006, ApJ, 651, 142

Hoskin M. A., 1976, Journal for the History of Astronomy, 7, 169

Hoyle B., et al., 2011, MNRAS, 415, 3627

Hoyle B., et al., 2012, MNRAS, 423, 3478

Hubble E. P., 1925, The Observatory, 48, 139

Hubble E. P., 1926, ApJ, 64, 321

Hubble E. P., 1936, Realm of the Nebulae

Huertas-Company M., et al., 2011, A&A, 525, A157

Huertas-Company M., et al., 2015, ApJS, 221, 8

Hunt L. K., et al., 2008, A&A, 482, 133

Hunter J. H. J., et al., 1988, ApJ, 324, 721

Inami H., et al., 2017, A&A, 608, A2

Ivezić Ž., et al., 2019, ApJ, 873, 111

Izquierdo-Villalba D., et al., 2022, MNRAS, 514, 1006

James P. A., Percival S. M., 2018, MNRAS, 474, 3101

Janowiecki S., et al., 2020, MNRAS, 493, 1982

Jedrzejewski R. I., 1987, MNRAS, 226, 747

Jiang Y.-F., et al., 2011, ApJ, 742, 68

Jiang L., et al., 2014, ApJS, 213, 12

Jogee S., et al., 2004, ApJ, 615, L105

Jogee S., Scoville N., Kenney J. D. P., 2005, ApJ, 630, 837

Johnson H. M., 1961, ApJ, 133, 314

Joye W. A., Mandel E., 2003, in Payne H. E., Jedrzejewski R. I., Hook R. N., eds, Astronomical Society of the Pacific Conference Series Vol. 295, Astronomical Data Analysis Software and Systems XII. p. 489

Kannappan S. J., et al., 2013, ApJ, 777, 42

Kauffmann G., 1996, MNRAS, 281, 487

Kauffmann G., et al., 2003, MNRAS, 341, 33

Kautsch S. J., 2009, PASP, 121, 1297

Kautsch S. J., et al., 2006, A&A, 445, 765

Kaviraj S., 2010, MNRAS, 406, 382

Kaviraj S., et al., 2011, MNRAS, 415, 3798

Kaviraj S., et al., 2012, MNRAS, 423, 49

Kaviraj S., et al., 2013, MNRAS, 429, L40

Kelly B. C., 2007, ApJ, 665, 1489

Kennicutt Robert C. J., 1998a, ARA&A, 36, 189

Kennicutt Robert C. J., 1998b, ApJ, 498, 541

Kennicutt R. C., Evans N. J., 2012, ARA&A, 50, 531

Khoperskov S., et al., 2018, A&A, 609, A60

Kim T., et al., 2015, ApJ, 799, 99

Kim T., et al., 2016, MNRAS, 462, 3430

Kim T., et al., 2021, ApJ, 922, 196

Knapen J. H., Shlosman I., Peletier R. F., 2000, ApJ, 529, 93

Kormendy J., 2013, in Falcón-Barroso J., Knapen J. H., eds, , Secular Evolution of Galaxies. p. 1

Kormendy J., Bender R., 1996, ApJ, 464, L119

Kormendy J., Kennicutt Robert C. J., 2004, ARA&A, 42, 603

Kormendy J., et al., 2010, ApJ, 723, 54

Krajnović D., et al., 2006, MNRAS, 366, 787

Krajnović D., et al., 2011, MNRAS, 414, 2923

Kraljic K., Bournaud F., Martig M., 2012, ApJ, 757, 60

Krishnarao D., et al., 2020, ApJ, 898, 116

Kruk S. J., et al., 2017, MNRAS, 469, 3363

Kruk S. J., et al., 2018, MNRAS, 473, 4731

Kruk S. J., et al., 2019, MNRAS, 490, 4721

Kuno N., et al., 2007, PASJ, 59, 117

Laine S., et al., 2002, ApJ, 567, 97

Lang M., Holley-Bockelmann K., Sinha M., 2014, ApJ, 790, L33

Lara-López M. A., et al., 2010, A&A, 519, A31

Laurikainen E., Salo H., 2002, MNRAS, 337, 1118

Laurikainen E., et al., 2013, MNRAS, 430, 3489

Law D. R., et al., 2015, AJ, 150, 19

Law D. R., et al., 2016, AJ, 152, 83

Law D. R., et al., 2021, AJ, 161, 52

Leavitt H. S., 1908, Annals of Harvard College Observatory, 60, 87

Leavitt H. S., Pickering E. C., 1912, Harvard College Observatory Circular, 173, 1

Lee Y. H., et al., 2022, ApJ, 926, 58

Leroy A. K., et al., 2021a, ApJS, 255, 19

Leroy A. K., et al., 2021b, ApJS, 257, 43

Li C., et al., 2009, MNRAS, 397, 726

Lin Y., et al., 2014, ApJ, 796, 98

Lin L., et al., 2020, MNRAS, 499, 1406

Lindblad P. A. B., Kristen H., 1996, A&A, 313, 733

Lintott C. J., et al., 2008, MNRAS, 389, 1179

Lintott C., et al., 2011, MNRAS, 410, 166

Łokas E. L., 2018, ApJ, 857, 6

Lotz J. M., et al., 2011, ApJ, 742, 103

Lund M. B., 2020, arXiv e-prints, p. arXiv:2003.13879

Lynden-Bell D., Kalnajs A. J., 1972, MNRAS, 157, 1

Madau P., Pozzetti L., Dickinson M., 1998, ApJ, 498, 106

Maeda F., et al., 2018, PASJ, 70, 37

Maeda F., et al., 2020a, MNRAS,

Maeda F., et al., 2020b, MNRAS, 493, 5045

Maeda F., et al., 2021, MNRAS, 502, 2238

Magaña-Serrano M. A., et al., 2020, Rev. Mex. Astron. Astrofis., 56, 39

Mancini C., et al., 2011, ApJ, 743, 86

Marinova I., Jogee S., 2007, ApJ, 659, 1176

Marleau F. R., Clancy D., Bianconi M., 2013, MNRAS, 435, 3085

Martin D. C., et al., 2007, ApJS, 173, 342

Martin G., et al., 2018, MNRAS, 476, 2801

Martin G., et al., 2020, MNRAS, 491, 1408

Martinet L., Friedli D., 1997, A&A, 323, 363

Martinez-Valpuesta I., Shlosman I., Heller C., 2006, ApJ, 637, 214

Martinez-Valpuesta I., Aguerri J., González-García C., 2016, Galaxies, 4, 7

Martinez-Valpuesta I., et al., 2017, MNRAS, 464, 1502

Masters K. L., et al., 2010, MNRAS, 405, 783

Masters K. L., et al., 2011, MNRAS, 411, 2026

Masters K. L., et al., 2012, MNRAS, 424, 2180

Masters K. L., et al., 2019, MNRAS, 487, 1808

Masters K. L., et al., 2021, MNRAS, 507, 3923

McAlpine S., et al., 2016, Astronomy and Computing, 15, 72

McAlpine S., et al., 2020, MNRAS, 494, 5713

Meidt S. E., et al., 2013, ApJ, 779, 45

Melvin T., et al., 2014, MNRAS, 438, 2882

Méndez-Abreu J., et al., 2012, ApJ, 761, L6

Mendez A. J., et al., 2011, ApJ, 736, 110

Menéndez-Delmestre K., et al., 2007, ApJ, 657, 790

Merrifield M. R., Kuijken K., 1995, MNRAS, 274, 933

Messier C., 1781, Connoissance des Temps, pp 227–267

Mihos J. C., Hernquist L., 1994, ApJ, 431, L9

Miwa T., Noguchi M., 1998, ApJ, 499, 149

Mo H. J., Mao S., White S. D. M., 1998, MNRAS, 295, 319

Momose R., et al., 2010, ApJ, 721, 383

Muñoz-Tuñón C., Caon N., Aguerri J. A. L., 2004, AJ, 127, 58

Naab T., et al., 2014, MNRAS, 444, 3357

Nair P. B., Abraham R. G., 2010a, ApJS, 186, 427

Nair P. B., Abraham R. G., 2010b, ApJ, 714, L260

Newnham L., et al., 2020, MNRAS, 492, 4697

Nimori M., et al., 2013, MNRAS, 429, 2175

Noeske K. G., et al., 2007, ApJ, 660, L43

Noguchi M., 1987, MNRAS, 228, 635

Oh S., Oh K., Yi S. K., 2012, ApJS, 198, 4

Oh K., et al., 2015, ApJS, 219, 1

Oh K., et al., 2018, ApJS, 235, 4

Okamoto T., Isoe M., Habe A., 2015, PASJ, 67, 63

Ostriker J. P., Peebles P. J. E., 1973, ApJ, 186, 467

Paccagnella A., et al., 2016, ApJ, 816, L25

Patel S. G., et al., 2011, ApJ, 735, 53

Patel S. G., et al., 2012, ApJ, 748, L27

Patsis P. A., Athanassoula E., 2019, MNRAS, 490, 2740

Paulino-Afonso A., et al., 2020, A&A, 633, A70

Peebles P. J. E., 1982, ApJ, 263, L1

Peng Y., Maiolino R., Cochrane R., 2015, Nature, 521, 192

Pérez I., Aguerri J. A. L., Méndez-Abreu J., 2012, A&A, 540, A103

Perlmutter S., et al., 1999, ApJ, 517, 565

Peschken N., Łokas E. L., 2019, MNRAS, 483, 2721

Piotrowska J. M., et al., 2022, MNRAS, 512, 1052

Planck Collaboration et al., 2016, A&A, 594, A13

Planck Collaboration et al., 2020, A&A, 641, A6

Polyachenko E. V., 2013, Astronomy Letters, 39, 72

Postman M., et al., 2005, ApJ, 623, 721

Price S. H., et al., 2022, A&A, 665, A159

Puerari I., Dottori H., 1997, ApJ, 476, L73

Rathore H., et al., 2022, MNRAS, 513, 389

Rautiainen P., Salo H., 2000, A&A, 362, 465

Rautiainen P., Salo H., Laurikainen E., 2008, MNRAS, 388, 1803

Regan M. W., Mulchaey J. S., 1999, AJ, 117, 2676

Reines A. E., Volonteri M., 2015, ApJ, 813, 82

Renaud F., et al., 2015, MNRAS, 454, 3299

Renzini A., Peng Y.-j., 2015, ApJ, 801, L29

Reynaud D., Downes D., 1998, A&A, 337, 671

Roshan M., et al., 2021a, MNRAS, 503, 2833

Roshan M., et al., 2021b, MNRAS, 508, 926

Ryan R. E. J., et al., 2008, ApJ, 678, 751

Sachdeva S., Saha K., 2016, ApJ, 820, L4

Sadler E. M., Gerhard O. E., 1985, MNRAS, 214, 177

Sahni V., Starobinsky A., 2000, International Journal of Modern Physics D, 9, 373

Saintonge A., et al., 2016, MNRAS, 462, 1749

Salim S., et al., 2007, ApJS, 173, 267

Sánchez-Blázquez P., et al., 2006, MNRAS, 371, 703

Sánchez-Menguiano L., et al., 2015, MNRAS, 450, 2670

Sánchez S. F., et al., 2012, A&A, 538, A8

Sánchez S. F., et al., 2016a, Rev. Mex. Astron. Astrofis., 52, 21

Sánchez S. F., et al., 2016b, Rev. Mex. Astron. Astrofis., 52, 171

Sánchez S. F., et al., 2016c, A&A, 594, A36

Sánchez S. F., et al., 2018, Rev. Mex. Astron. Astrofis., 54, 217

Sandage A., 1961, The Hubble Atlas of Galaxies

Sanders R. H., Tubbs A. D., 1980, ApJ, 235, 803

Scannapieco C., et al., 2009, MNRAS, 396, 696

Schawinski K., et al., 2009, MNRAS, 396, 818

Schawinski K., et al., 2010, ApJ, 711, 284

Schawinski K., et al., 2014, MNRAS, 440, 889

Schaye J., et al., 2015, MNRAS, 446, 521

Sellwood J. A., 1981, A&A, 99, 362

Sellwood J. A., Wilkinson A., 1993, Reports on Progress in Physics, 56, 173

Sempere M. J., et al., 1995, A&A, 296, 45

Seo W.-Y., et al., 2019, ApJ, 872, 5

Sérsic J. L., 1968, Atlas de Galaxias Australes

Shapiro K. L., et al., 2008, ApJ, 682, 231

Shapley H., 1921, Bull. Nat. Res. Coun., 2, 171

Shen J., Sellwood J. A., 2004, ApJ, 604, 614

Sheth K., et al., 2000, ApJ, 532, 221

Sheth K., et al., 2005, ApJ, 632, 217

Sheth K., et al., 2008, ApJ, 675, 1141

Sierra A. D., et al., 2015, MNRAS, 450, 1799

Simmons B. D., et al., 2013, MNRAS, 429, 2199

Simmons B. D., et al., 2014, MNRAS, 445, 3466

Siudek M., et al., 2018, A&A, 617, A70

Skibba R. A., et al., 2009, MNRAS, 399, 966

Skibba R. A., et al., 2012, MNRAS, 423, 1485

Skokos C., Patsis P. A., Athanassoula E., 2002a, MNRAS, 333, 847

Skokos C., Patsis P. A., Athanassoula E., 2002b, MNRAS, 333, 861

Smart D., 2021, Weather, 76, 98

Smee S. A., et al., 2013, AJ, 146, 32

Smethurst R. J., et al., 2015, MNRAS, 450, 435

Smethurst R. J., et al., 2019, MNRAS, 484, 3590

Smethurst R. J., et al., 2022, MNRAS, 510, 4126

Somerville R. S., et al., 2008, MNRAS, 391, 481

Sorai K., et al., 2012, PASJ, 64, 51

Sorensen S. A., Matsuda T., Fujimoto M., 1976, Ap&SS, 43, 491

Sparke L. S., Sellwood J. A., 1987, MNRAS, 225, 653

Sparre M., Springel V., 2016, MNRAS, 462, 2418

Sparre M., et al., 2015, MNRAS, 447, 3548

Speagle J. S., et al., 2014, ApJS, 214, 15

Speltincx T., Laurikainen E., Salo H., 2008, MNRAS, 383, 317

Spindler A., et al., 2018, MNRAS, 476, 580

Spinoso D., et al., 2017, MNRAS, 465, 3729

Spitzer Lyman J., Baade W., 1951, ApJ, 113, 413

Springel V., Di Matteo T., Hernquist L., 2005, ApJ, 620, L79

Stark D. V., et al., 2021, MNRAS, 503, 1345

Strateva I., et al., 2001, AJ, 122, 1861

Strauss M. A., et al., 2002, AJ, 124, 1810

Taranu D., Dubinski J., Yee H. K. C., 2015, ApJ, 803, 78

Toomre A., 1964, ApJ, 139, 1217

Trayford J. W., et al., 2017, MNRAS, 470, 771

Tremaine S., Weinberg M. D., 1984, ApJ, 282, L5

Tremonti C. A., et al., 2004, ApJ, 613, 898

Treuthardt P., et al., 2007, AJ, 134, 1195

Treuthardt P., et al., 2008, AJ, 136, 300

Trussler J., et al., 2020, MNRAS, 491, 5406

Tully R. B., Fisher J. R., 1977, A&A, 54, 661

Vera M., Alonso S., Coldwell G., 2016, A&A, 595, A63

Verley S., et al., 2007, A&A, 474, 43

Villa-Vargas J., Shlosman I., Heller C., 2010, ApJ, 719, 1470

Wake D. A., et al., 2017, AJ, 154, 86

Walker I. R., Mihos J. C., Hernquist L., 1996, ApJ, 460, 121

Walmsley M., et al., 2022, MNRAS, 509, 3966

Watanabe Y., et al., 2011, MNRAS, 411, 1409

Weiner B. J., Sellwood J. A., Williams T. B., 2001, ApJ, 546, 931

Weinzirl T., et al., 2009, ApJ, 696, 411

Westfall K. B., et al., 2019, AJ, 158, 231

Whitaker K. E., et al., 2010, ApJ, 719, 1715

Whitaker K. E., et al., 2021, Nature, 597, 485

White S. D. M., Frenk C. S., 1991, ApJ, 379, 52

White S. D. M., Rees M. J., 1978, MNRAS, 183, 341

Willett K. W., et al., 2013, MNRAS, 435, 2835

Williams G. G., et al., 2004, in Moorwood A. F. M., Iye M., eds, SPIE Vol. 5492, Ground-based Instrumentation for Astronomy. pp 787–798

Williams R. J., et al., 2009, ApJ, 691, 1879

Williams T. G., et al., 2021, AJ, 161, 185

Wright E. L., et al., 2010, AJ, 140, 1868

Wuyts S., et al., 2007, ApJ, 655, 51

Wyder T. K., et al., 2007, ApJS, 173, 293

Wyithe J. S. B., Loeb A., 2003, ApJ, 595, 614

Yan R., et al., 2016, AJ, 152, 197

York D. G., et al., 2000, AJ, 120, 1579

Zimmer P., Rand R. J., McGraw J. T., 2004, ApJ, 607, 285

Zou Y., et al., 2019, ApJ, 884, 23

Zurita A., et al., 2004, A&A, 413, 73

de Vaucouleurs G., 1948, Annales d'Astrophysique, 11, 247

de Vaucouleurs G., 1959, Handbuch der Physik, 53, 275

de Vaucouleurs G., 1960, ApJ, 131, 585

de Vaucouleurs G., 1963, ApJS, 8, 31

van Dokkum P. G., 2005, AJ, 130, 2647

van den Bergh S., 2002, AJ, 124, 782

*"For my part I know nothing with any certainty,*
*but the sight of the stars makes me dream."*

- Vincent Van Gogh